UNIVERSIDAD COMPLUTENSE DE MADRID

FACULTAD DE CIENCIAS MATEMÁTICAS

DEPARTAMENTO DE MATEMÁTICA APLICADA

TESIS DOCTORAL

Modelización y Optimización de Tratamientos Médicos en Radioterapia
(Modeling and Optimization of Radiotherapy Treatment Plans)

MEMORIA PARA OPTAR AL GRADO DE DOCTOR

PRESENTADA POR

Juan Carlos López Alfonso

Directores

Miguel Ángel Herrero García
Juan Bosco García Archilla
Luis Núñez Martín

Madrid, 2014

Departamento de Matemática Aplicada
Facultad de Ciencias Matemáticas
Universidad Complutense de Madrid

Modelización y Optimización de Tratamientos Médicos en Radioterapia

(Modeling and Optimization of Radiotherapy Treatment Plans)

Memoria para optar al grado de doctor

presentada por:

Juan Carlos López Alfonso

Bajo la dirección de:

Dr. Miguel Ángel Herrero García

Departamento de Matemática Aplicada, Facultad de Ciencias Matemáticas,

Universidad Complutense de Madrid, España

Dr. Juan Bosco García Archilla

Departamento de Matemática Aplicada II, Universidad de Sevilla, España

Dr. Luis Núñez Martín

Departamento de Radiofísica, Hospital Universitario Puerta de Hierro Majadahonda, Madrid, España

Madrid, Febrero de 2014

"To my parents and to my wife, Laura;
for their love and support.
They are the biggest asset of my life."

Agradecimientos

Quiero expresar mis más sinceros agradecimientos a todas aquellas personas que de una forma u otra me han apoyado y ayudado en mi trayectoria profesional, y más concretamente, en la culminación de la presente tesis doctoral.

En primer lugar a mis directores Dr. Miguel Ángel Herrero García, Dr. Juan Bosco García Archilla y Dr. Luis Núñez Martín. A Miguel A. Herrero García me gustaría agradecerle su exquisito trato, el tiempo invertido, su enorme paciencia y pragmatismo con el que ha abordado las distintas etapas de la investigación. De idéntica forma, me gustaría agradecerle a Juan Bosco García Archilla y Luis Núñez Martín toda su colaboración, así como la total confianza que han depositado en mí a lo largo de este período. Sin lugar a dudas sin ellos este trabajo no hubiera sido posible.

También agradecer al Dr. Reinaldo Rodríguez Ramos líder del grupo de investigación Mecánica de Sólidos de la Universidad de la Habana, así como a todos sus miembros, por guiarme y ayudarme durante mis primeros pasos en esta carrera investigadora. A los profesores Dr. Andreas Deutsch, Dr. Dirk Drasdo y Dr. Giuseppe Buttazzo por darme la gran oportunidad de trabajar con ellos y en sus respectivos grupos de investigación, lo cual ha sido un factor determinante en mi desarrollo científico. Al Dr. Nick Jagiella por su colaboración y las sucesivas discusiones científicas. Por otro lado, mi gratitud para los evaluadores externos e interno de esta tesis doctoral, Dr. Antonio Fasano, Dr. Haralampos Hatzikirou y Dr. Gerardo Oleaga por el magnífico trabajo realizado.

Para concluir quiero agradecer a toda mi familia, porque a pesar de no estar siempre presentes físicamente, me han estado apoyando incondicionalmente y haciendo que todo me resultara mucho más llevadero. Por último, agradecer a mis amigos de aquí y allá, que desde donde quiera que están siempre han confiado en mí y han sido un soporte fundamental.

A todos mi mayor reconocimiento y gratitud!

Publications

The results presented in this memoir have led to a series of publications and works in progress. They are listed here for reference:

- **J. C. L. Alfonso**, G. Buttazzo, B. García-Archilla, M. A. Herrero and L. Núñez (2012). "A class of optimization problems in radiotherapy dosimetry planning". Discr. Cont. Dyn. Systems B 17, 6; 1651-1672. doi:10.3934/dcdsb.2012.17.1651.

- **J. C. L. Alfonso**, N. Jagiella, M. A. Herrero, L. Núñez and D. Drasdo (2014). "Estimating dose painting effects in radiotherapy: a mathematical model". *Accepted in PLoS ONE, doi: 10.1371/journal.pone.0089380.*

- **J. C. L. Alfonso**, G. Buttazzo, B. García-Archilla, M. A. Herrero and L. Núñez (2014). "Selecting radiotherapy dose distributions by means of constrained optimization problems". *Accepted in Bulletin of Mathematical Biology, doi: 10.1007/s11538-014-9945-7.*

- **J. C. L. Alfonso**, M. A. Herrero and L. Núñez (2014). "A decision-support system to select tentative dosimetry plans in radiotherapy". *In Preparation.*

Table of Contents

Summary

In spite of the great efforts and progresses made over many years in the fight against cancer, improving the treatment, whence the prognosis of this disease remains one of the biggest challenges in medicine nowadays. Ever since the discovery of X-rays by Wilhelm Conrad Röntgen in 1895, radiotherapy has played a major role in the treatment of solid tumors for curative or palliative purposes. Radiotherapy techniques are designed to shed ionizing radiation to induce lethal damage in pathological tissues, while at the same time avoiding as much as possible undesirable side effects on nearby organs and healthy tissues. According to recent estimates, no less than 50% of all cancer patients receive radiotherapy during their illness, whether on its own or as an adjunct to chemotherapy, surgery or other medical techniques. Technical and methodological advances during the last century have allowed radiation oncologists and radiophysicists to achieve local tumor control in a considerable number of patients diagnosed with solid tumors. However, locoregional recurrence after therapies and the treatment of disseminated tumors remain a formidable problem in many cases. For these reasons, it is necessary to improve currently used diagnosis, planning and therapeutic techniques. In this context, the development of new mathematical models and more sophisticated computer-based procedures are expected to provide significant tools towards curing the disease whenever possible and to improve the patients quality of life in all cases.

The present memoir aims at developing mathematical models and computer-based procedures to assist in the decision-making process whereby actual radiotherapy treatment plans are selected. To that end, the plan of this work is described as follows. To introduce the main problems addressed in this work, an overview of the key principles involved in radiotherapy is provided in Chapter 1. In the first part of that Chapter a detailed description of the main steps in the treatment planning process is presented. Then some of the mathematical tools used in radiotherapy are briefly reviewed. In Chapter 2 a multi-parameter variational problem is proposed and analyzed whose solutions provide optimal radiation dose distri-

butions based on clinical and technological requirements. To obtain solutions of such mathematical model, different numerical and optimization methods have been implemented, and a detailed description of them is provided in Appendix A. In Chapter 3 a model of heterogeneous tumor growth based on specific biological and radiobiological properties is presented, and tumor response to different homogeneous and heterogeneous radiation dosimetries is investigated. Since intratumoral heterogeneity is widely considered to be a determinant factor in tumor progression and in particular in its recurrence after therapy, the study now performed supports a change in the current dosimetry strategy, which aims at delivering homogeneous, instead of heterogeneous, doses on target. In Chapter 4 a mathematical decision-aid tool is defined to assist clinicians and radiophysicists in the choice of actual treatment plans to be carried out, a process that to this day largely relies on the experience of the specialists in charge. The tool now provided permits to compare and evaluate tentative treatment plans for a same patient simulated on a commercial treatment planning system. To conclude, additional results as complement to those presented in Chapters 2 and 3 are provided in Appendices B and C respectively. Finally, the main results obtained in this work as well as future research directions are discussed in the final Chapter 5.

In summary, the work herein reported provides new mathematical models and computer-based procedures that could be combined with current techniques to improve radiotherapy outcomes. Such results should therefore be considered as auxiliary instruments to prepare and deliver better treatment plans, a goal of great importance both from scientific and social points of view.

Resumen

Introducción y Objetivos:

A pesar de los grandes avances realizados durante muchos años en la lucha contra el cáncer, mejorar el tratamiento, y por consiguiente el pronóstico de esta enfermedad sigue siendo uno de los mayores retos de la medicina en la actualidad. Desde el descubrimiento de los rayos X por Wilhelm Conrad Röntgen en 1895, la radioterapia ha jugado un papel destacado en el tratamiento de tumores sólidos, ya sea con fines curativos o paliativos. En la actualidad, no menos del 50% de los pacientes de cáncer reciben este tipo de tratamiento, ya sea por si solo o en combinación con quimioterapia o cirugía. Las técnicas de radioterapia buscan enviar radiación ionizante para inducir daños letales en tejidos patológicos, evitando en la medida de lo posible daños colaterales en tejidos sanos y órganos próximos. Los avances técnicos y metodológicos realizados durante el último siglo han permitido a oncólogos y radiofísicos conseguir control tumoral local para un número considerable de pacientes diagnosticados con tumores sólidos. Sin embargo, la recurrencia local tras la terapia y el tratamiento de tumores diseminados siguen representando problemas formidables en muchos casos. Por ello es necesario mejorar las técnicas actualmente usadas para el diagnóstico y la planificación de tratamientos. En este contexto se espera que el desarrollo de nuevos modelos matemáticos y de sistemas de cálculo más eficaces suministren importantes herramientas para curar la enfermedad cuando sea posible y para mejorar la calidad de vida de los pacientes en cualquier caso.

El objetivo de esta memoria es desarrollar modelos matemáticos y técnicas computacionales que permitan ayudar a decidir la elección de tratamientos de radioterapia. Para ello, el plan a seguir es el siguiente. En el Capítulo 1 se describen los principios básicos de la radioterapia que permiten definir el marco en el que se formulan los problemas que se abordarán en este trabajo. En concreto, en la primera parte de ese Capítulo se recuerdan los fundamentos básicos de la radioterapia, y a continuación se describen algunas herramientas matemáticas usadas en este campo. En el Capítulo 2 se propone y analiza una clase de problemas varia-

cionales multiparamétricos cuyas soluciones proporcionan distribuciones óptimas de radiación basadas en restricciones clínicas y tecnológicas. Para obtener soluciones de dicho modelo, han sido desarrollados diversos métodos numéricos y de optimización, que se describen en detalle en el Apéndice A. En el Capítulo 3, se presenta un modelo de crecimiento tumoral heterogéneo basado en hipótesis precisas de tipo biológico y radiobiológico, y se estudia la respuesta tumoral ante diferentes dosimetrías de radiación, tanto homogéneas como heterogéneas. Dado que la heterogeneidad intratumoral se considera un factor determinante en la progresión tumoral, y en particular en la recurrencia tras la terapia, el estudio realizado sugiere un cambio en la estrategia clínica actualmente seguida, que busca administrar dosis homogéneas en cualquier caso. En el Capítulo 4 se propone una herramienta de ayuda a la decisión para elegir el plan de radioterapia que ha de ser implementado, lo que hasta ahora se basa fundamentalmente en la experiencia del personal que ha de tomar la decisión. La herramienta propuesta permite comparar y evaluar diferentes planes alternativos para el mismo paciente, preparados mediante simuladores comerciales. Para concluir, en los Apéndices B y C se presentan resultados adicionales como complemento a los presentados en los Capítulos 2 y 3 respectivamente. Por último, los resultados obtenidos y sus posibles extensiones futuras se discuten en el Capítulo 5.

En resumen, este trabajo propone nuevos modelos matemáticos y procedimientos computacionales que pueden combinarse con las técnicas actuales para mejorar los resultados obtenidos con la radioterapia. Tales resultados pueden ser por tanto considerados como instrumentos auxiliares para preparar y administrar mejores tratamientos, un objetivo de gran importancia científica y social.

A continuación se describe con más detalle el contenido y resultados obtenidos en cada capítulo, así como las conclusiones del trabajo realizado.

Capítulo 1:

En este capítulo introductorio se presenta una panorámica breve y precisa del empleo de técnicas de radioterapia en el tratamiento de tumores sólidos, los fundamentos en que tales técnicas se basan y los problemas que su uso plantea en la práctica clínica. En particular, se hace especial énfasis en los modelos matemáticos basados en principios radiobiológicos que se utilizan a lo largo de este trabajo.

Capítulo 2:

Los pasos fundamentales en el proceso de planificación en radioterapia consisten en seleccionar para cada paciente diagnosticado con un tumor sólido: i) la dosis de prescripción en el tumor, ii) restricciones en las dosis de radiación suministradas a los órganos de riesgo circundantes y iii) un esquema de fraccionamiento especificando el número y frecuencia de las sesiones de tratamiento. En particular, la elección de la dosis de prescripción se basa principalmente en la experiencia clínica

acumulada en el tratamiento del tipo de tumor en consideración y los órganos de riesgo involucrados sin ninguna referencia directa a cuantificaciones radiobiológicas. Es importante remarcar, que modelos matemáticos desarrollados para estudiar el efecto de la radiación en la materia biológica existen hace bastante tiempo, y son ampliamente conocidos por los clínicos. Sin embargo la dificultad para obtener estimaciones in vivo de los parámetros radiobiológicos involucrados han restringido su uso directo en la clínica practica actual.

El objetivo de este Capítulo en primer lugar es proponer un modelo matemático para seleccionar distribuciones de dosis de radiación como soluciones de un problema variacional asumiendo que los principales parámetros radiobiológicos para el tumor y los órganos de riesgo circundantes involucrados son conocidos. En segundo lugar, se realiza un análisis detallado de la dependencia de tales soluciones en los parámetros seleccionados, y la manera en la que el uso de tales minimizadores podrían mejorar el proceso actual de toma de decisiones para seleccionar dosimetrías de radiación, cuando (como es generalmente el caso) solo información parcial de los parámetros radiobiológicos esta disponible. Una comparación entre las distribuciones de radiación propuestas con aquellas que son actualmente aplicadas a un número de casos clínicos sugiere que las soluciones del modelo matemático propuesto pueden ser de gran utilidad en el proceso de planificación de radioterapia para obtener mejores planes de tratamiento. Este modelo matemático puede ser aplicado a cualquier tipo de tumor con independencia de su localización, así como si diferentes regiones o varios tumores son identificados para un mismo paciente.

Capítulo 3:

La heterogeneidad tumoral es ampliamente considerada un factor determinante en la progresión de tumores y en particular en su recurrencia después de las terapias. Por desgracia, las técnicas médicas actuales no suministran información relevante acerca de la heterogeneidad tumoral mediante métodos no invasivos. Como consecuencia cuando la radioterapia es utilizada como una opción de tratamiento, las distribuciones de dosis de radiación son prescritas bajo la hipótesis que el tumor es de naturaleza homogénea.

El propósito de este Capítulo es precisamente explorar el efecto de diferentes dosis de radiación en tumores heterogéneos por medio de un modelo matemático donde el funcionamiento de cada célula es simulado de manera individual. Para esto, se ha considerado un caso donde solo dos fenotipos tumorales diferentes están presentes, los cuales se asumen que difieren en la duración del ciclo celular y sus propiedades radiobiológicas. En particular, como resultados de tales diferencias, la distribución espacial de los correspondientes fenotipos, por tanto de la resultante heterogeneidad, se puede predecir a medida que el tumor crece. Es decir, si el modelo de crecimiento tumoral se ejecuta desde una situación donde una mayoría de células tumorales (CC) y una minoría de células madres tumorales (CSC) están

inicialmente presentes y aleatoriamente distribuidas, entonces las CSCs quedan concentradas en la región interior del tumor a medida que este crece y mientras que la duración del ciclo celular de las CCs es menor que el de las CSCs y las CSCs siguen siendo una fracción menor respecto al número total de CCs en el tumor. Como consecuencia, y asumiendo además que las CSCs son más resistentes a la radiación que las CCs, las distribuciones heterogéneas pueden ser seleccionadas para aumentar la probabilidad de control tumoral suministrando mayores dosis de radiación a las regiones ocupadas por las células más radioresistentes. Por otro lado, también se obtiene que cuando se comparan con las distribuciones homogéneas utilizadas actualmente en la practica clínica, tales distribuciones heterogéneas proporcionan mejores resultados que sus correspondientes distribuciones homogéneas que administran la misma dosis total.

Capítulo 4:

Los planes de tratamiento en radioterapia son seleccionados por los radiofísicos y clínicos de entre un pequeño número de planes tentativos simulados en un sistema de planificación de tratamientos. En este trabajo se propone un procedimiento de ayuda a la decisión para asistir en la elección de planes de tratamiento. Esto se hace como se describe a continuación. Para cualquier plan tentativo de tratamiento se definen tres sub-índices asociados a las distribuciones de radiación: i) en el tumor, ii) órganos de riesgo circundantes y iii) tejido sano respectivamente. Estos sub-índices se combinan para obtener un índice global que proporciona un valor para cada plan tentativo de tratamiento. Para esto solo se utilizan los diagramas dosis volumen obtenidos a partir de los sistemas de planificación y la dosis de prescripción en el tumor. Este índice global proporciona una herramienta sencilla y fácil de usar para comparar diferentes planes dosimétricos de tratamiento que son muy similares respecto a los diagramas de dosis volumen. En particular, pequeñas diferencias en el número, ángulos de incidencia o intensidad de los ases de radiación proporcionan valores significativamente diferentes del índice global, así como de cada sub-índice que lo forma. Por otro lado, esta herramienta matemática puede ser implementada en cualquier sistema de planificación utilizado actualmente independientemente del tipo y localización del tumor, y además permite comparar planes tentativos obtenidos en diferentes sistemas de planificación o desarrollados mediante diferentes técnicas de irradiación.

En particular, esta herramienta matemática permite comparar de forma cuantitativa diferentes planes tentativos de tratamiento definidos para un mismo paciente. Para evaluar el funcionamiento de este procedimiento el plan tentativo sugerido por el índice global propuesto ha sido comparado con varios planes implementados para tratar a pacientes diagnosticados con tumores cerebrales. Para cada uno de estos casos clínicos tres estrategias diferentes de planificación fueron consideradas de las cuales una fue seleccionada y suministrada a cada paciente respectivamente. El valor del índice fue calculado para cada una de las estrategias

anteriormente mencionadas y un considerable grado de consciencia fue obtenido. Además, las razones de las posibles discrepancias cuando estas ocurren fueron discutidas. A fin de evaluar la información proporcionada por esta herramienta matemática, se ha examinado también una secuencia de planes de tratamiento hipotéticos para un paciente diagnosticado con cáncer de próstata, y se observó una clara correlación entre los resultados del índice global y la evaluación clínica realizada por los expertos.

Conclusiones:

Desde el descubrimiento de los rayos X hace más de cien años, el uso de la radiación ionizante en la medicina es cada vez mayor, tanto para asistir en el diagnóstico de enfermedades como una opción de tratamiento a pacientes con tumores. En particular, la radioterapia es en la actualidad una técnica ampliamente utilizada para tratar tumores sólidos. El tratamiento de estas enfermedades, y de los pacientes diagnosticados con cáncer en general, representa un desafío importante en términos científicos y sociales. Considerables avances científicos y tecnológicos realizados en los últimos años han dado lugar a una reducción significativa de la incidencia de tumores. Sin embargo, la recurrencia después de las terapias, así como el tratamiento de tumores diseminados o en etapas avanzadas de desarrollos sigue siendo un problema crítico en la práctica clínica.

Por otro lado grandes esfuerzos han sido realizados en el desarrollo de modelos matemáticos para ayudar en el proceso de planificación de tratamientos radioterápicos. En particular, se han propuesto diversos modelos basados en principios físicos y radiobiológicos, que han permitido mejorar el rendimiento de la radioterapia. Sin embargo, al preparar un plan de tratamiento en la práctica actual una serie de dificultades relacionadas con la elección de la dosis de prescripción y la forma en que esta debe ser suministrada deben aún ser superadas.

En esta memoria se han propuesto varios modelos matemáticos y métodos basados en ordenadores para ayudar a los clínicos y radiofísicos en el proceso de planificación de tratamientos. En primer lugar, en el Capítulo 2 se propone un modelo matemático para seleccionar distribuciones de dosis óptimas como soluciones (minimizadores) de un problema de optimización considerando restricciones clínicas y técnicas. Para estudiar este modelo matemático, se han considerado diferentes casos clínicos, donde se realizó una comparación de las distribuciones de dosis óptimas con las suministradas a cada paciente. Como resultado, cuando se compara con las dosimetrías aplicadas, las distribuciones de dosis óptimas propuestas representan mejores opciones de tratamiento, y por lo tanto pueden ser consideradas distribuciones óptimas contra las cuales los planes tentativos de tratamiento pueden compararse durante el proceso de planificación de la radioterapia. Por otro lado, el análisis de la dependencia de los parámetros del modelo en tales minimizadores permite proponer una estrategia para seleccionar las distribuciones de dosis de radiación, bajo el supuesto de que los parámetros radiobiológicos para los

tumores y órganos en riesgo implicados sólo se conocen parcialmente, una situación que es bastante común en la práctica clínica.

En el Capítulo 3 se investigó el efecto de la heterogeneidad del tumor en los resultados obtenidos con la radioterapia. Para ese fin, se considera un modelo matemático con el que se simula el crecimiento de tumores heterogéneos en los cuales dos fenotipos de células tumorales están presentes las cuales se diferencian en sus respectivas propiedades biológicas y radiobiológicas. En particular, como consecuencia de esas diferencias, la distribución espacial de tales fenotipos y por lo tanto de la heterogeneidad tumoral resultante se puede predecir a medida que el tumor avanza en su desarrollo. El uso de dicha información de heterogeneidad y los efectos de diferentes tratamientos heterogéneos han sido investigados. Se ha demostrado que dosimetrías heterogéneos se pueden seleccionar para mejorar el control tumoral al aumentar las dosis de radiación suministradas en la región ocupada por el fenotipo de células tumorales más radioresistentes. En consecuencia, se ha observado que tales dosimetrías heterogéneas proporcionan mejores resultados que sus respectivas homogéneas las cuales son utilizadas actualmente en la práctica clínica.

En el Capítulo 4 se ha propuesto una herramienta matemática de ayuda a la decisión para comparar y evaluar planes tentativos de tratamiento en radioterapia. Esta herramienta utiliza sólo los datos extraídos de los histogramas dosis volumen que ofrecen los sistemas de planificación de tratamientos y la dosis de radiación prescrita en el tumor. En particular, para evaluar la información proporcionada por esta herramienta se investigaron una serie de casos clínicos en retrospectiva. Además, un programa informático ha sido implementado, con el que los médicos y radiofísicos pueden comparar y analizar los diferentes planes tentativos. Es notable destacar que esta herramienta puede ser incorporada fácilmente en cualquier sistema de planificación de tratamientos y ser utilizada para evaluar cualquier técnica de radioterapia que proporciona histogramas de dosis volumen de los planes tentativos siendo simulados.

En resumen, esperamos que los modelos matemáticos propuestos en este trabajo proporcionen herramientas útiles en la práctica clínica de la radioterapia, un objetivo que ha estado siempre presente durante este estudio.

Chapter 1

Treatment planning process and mathematical modeling in radiation therapy

"... For the birth of something new, there has to be a happening. Newton saw an apple fall; James Watt watched a kettle boil; Röntgen fogged some photographic plates. And these people knew enough to translate ordinary happenings into something new ..."

Alexander Fleming (1881-1955)

1.1 Introduction

Despite advances made over the years, cancer is at the top of the mortality statistics in developed countries together with heart diseases [1]. For instance, in United States the five-year relative survival rate (age standardized) for individuals aged 15 and older, and for all tumor locations is about 65.9%, while for brain tumors is only 26.1% [2]. Cancer incidence worldwide amounted to about 14.1 million reported cases with 8.2 million deaths in 2012 [3]. Unfortunately, cancer impact is expected to keep on rising, with an estimated 21.6 million incidences and 13.1 million deaths in 2030 [3]. For these reasons a significant improvement on cancer

therapies is most needed to improve these sober predictions.

Radiotherapy, the use of ionizing radiation to destroy pathological tissues, currently plays an important role in the treatment of solid tumors. It is widely used both for curative (when therapy results in improved survival) or palliative (when cure is not possible and the aim pursued is symptomatic relief) purposes. More than 50% of all cancer patients receive radiotherapy at some point during the course of their illness, whether on its own or in combination with surgery, chemotherapy, immunotherapy or any other medical technique [4], [5], [6].

The clinical use of radiotherapy is based on our knowledge about radiobiology, which is the scientific field concerned with the effect of ionizing radiation on living matter. Research on this topic started almost immediately after the discovery of X-rays by Wilhelm Conrad Röntgen in 1895 (see for instance [7], [8]), which was received with extraordinary interest by the scientific community. Actually, within months of that discovery different medical systems were designed to use X-rays for diagnosis, and to treat skin lesions and hair diseases as well as cancer tumors [9], [10], [11]. However, at the beginning of the 20th century, radiotherapy was applied by means of relatively low-voltage machines and was mainly used to treat superficial tumors. Moreover, there was no accurate method of calculating the radiation dose emitted and delivered, and poor knowledge about radiobiological effects led to high morbidity, unexpected side effects and low tumor control [12]. Such outcomes prompted scientists to develop new techniques to deliver radiation and to investigate its effects on living tissues, specifically on healthy and malignant cells. See for instance [13], where a detailed description of advances in radiation physics, radiobiology and radiotherapy between 1895 and 1950 is provided.

The goal of any radiotherapy technique is to control or destroy tumor cells while at the same time keeping as low as possible unwanted side effects to the surrounding organs and healthy tissues [14], [15]. To a large extent, the success of radiotherapy relies on the fact that healthy cells recover better from radiation injury than cancer cells, since normal cells possess more efficient repair mechanisms than malignant ones [4]. This fact notwithstanding the effect of radiation in healthy tissues, that need to be spared, cannot be easily dismissed. In fact, it is not possible to deliver radiation from an external source to an internal tumor without inflicting

some damage to surrounding organs at risk (OARs). Indeed, ionizing radiation has to inevitably pass through healthy tissues on its way to the target in this case. However, due to the scientific and technological advances made over the last years, ionizing radiation can be used nowadays to treat deeper tumors with high precision and comparatively low side effects to neighboring organs. Powerful and sophisticated treatment techniques have been developed, which yield highly satisfactory results when applied to solid tumors caught at an early stage of their development. Some examples of these techniques are 3D Conformal Radiotherapy (3D-CRT), Intensity Modulated Radiation Therapy (IMRT) and Image-Guided Radiotherapy (IGRT) (see [16] and references therein for further details). On the other hand several types of ionizing radiation are currently used in clinical centers as for instance photons (gamma rays) and charged particles (electrons, protons, neutrons, carbon ions, etc.) delivered through particle accelerator devices (mainly Linear Particle Accelerators, LINAC) [17]. However, tumors at an advanced or disseminated stage remain out of control in most cases.

In current practice, to prepare a radiotherapy treatment plan a number of key issues have to be dealt with. To begin with, the tumor and critical healthy regions have to be identified as accurately as possible. To do this, use is made of medical imaging techniques, a field which has experienced impressive progress but where much improvement is still needed [18]. In particular, high-resolution methods for precisely identifying tumor are still lacking. As a consequence, clinicians usually select a security area around identified tumor regions, and refer to this enlarged volume as the Planning Target Volume (PTV) [14], [15]. This becomes the designated region to be irradiated. Having done this, a suitable radiation dose has to be prescribed and delivered on the PTV along a specified number of therapeutic sessions, which constitutes the so-called fractionation scheme.

Once the PTV and OARs have been sufficiently identified by means of medical imaging techniques, clinicians and radiophysicists are faced with the task of selecting and delivering an appropriate radiation dose distribution The choice of that distribution is made according to two general, and often conflicting, principles. First, it should be large enough over the PTV to achieve high tumor control, and at the same time it has to affect as little as possible neighboring OARs [19].

In many cases the radiation doses selected to achieve tumor control are close to the maximum values tolerated by neighboring healthy tissues. Therefore, the level of normal tissue morbidity will often limit the tumor control rate that may be achieved [20]. However, tolerance doses are not fixed, well-known values. In fact they differ for each organ and type of tissue. To this day, no procedure has been found to simultaneously achieve those goals in an optimal way. As a consequence, a given patient may well be assigned a different dosimetry plan depending on the clinical center where he/she is treated.

In addition to the previous considerations, when selecting a prescription dose over a PTV, additional issues have to be addressed. Among them, tumor heterogeneity is particularly relevant. Evidence accumulated during last years strongly suggests that tumor heterogeneity, that is the presence of several different tumor phenotypes in a given tumor, is a key factor in the development of resistance to radiotherapy [21], [22], [23]. As a consequence, increasing attention is being paid to "dose painting", a technique consisting in delivering different radiation dosimetries to different regions within a given tumor, so that irradiation be boosted in more radioresistant regions (for instance, hypoxic, quiescent, etc.) [24], [25], [26]. This strategy, which is in sharp contrast with the still prevailing homogeneous radiation dose delivery approach [14], [15], has been made possible by the availability of high-precision linear particle accelerators, and looks particularly promising in those cases where current techniques fail to provide sufficient tumor control. However, in order for dose painting to show its full power, detailed information is needed about the internal structure of the tumor to be irradiated. Such information should ideally be provided by medical imaging techniques. These however are not yet able to distinguish different radiosensitivity regions except in a few cases, commonly related to hypoxia effects. In view of current technical limitations, the question thus arises of providing tools to *i)* obtain as much information as possible about internal spatial tumor heterogeneity before a dosimetry is prescribed, *ii)* simulate the effects of dose painting therapies which take into account whatever heterogeneity data are available, and *iii)* compare such simulations with those corresponding to standard homogeneous dose distributions currently delivered in clinical practice.

Once the choice of a prescription dose has been made, the question remains of

how to accurately deliver it on the PTV. To do that, a standard strategy consists in using several radiation beams that converge at the PTV, which is therefore arrived at along a variable number of incidence angles and intensities. In general, the choice of the beam configuration is made by selecting one among several tentative cases simulated by means of treatment planning systems (TPS), computer simulators which are incorporated at the particle accelerator to be used [14], [15], [19]. Any such case is called a tentative treatment plan. The plan to be delivered is selected among these alternatives, but to this day no standard protocol for quantitatively comparing tentative plans has been agreed upon. In spite of this, during the last decades a number of quantitative indexes (also termed as figures of merit) have been proposed to assist in the selection of dosimetry plans (cf. for instance [27], [28], [29], [30], [31], [32], [33], [34], [35], [36], [37], [38] and [39]). Generally speaking, any such index assigns a score to a tentative plan according to its compliance with a specified criterion. However, the search for a single, optimal index to quantify and evaluate the quality of a radiotherapy treatment plan has been unsuccessful as yet.

In the next sections further details on the process of radiotherapy planning will be provided. These will yield a useful background for the mathematical problems to be discussed in this memoir, which will be introduced as well.

1.2 Radiotherapy treatment planning process

The purpose of this Section is to briefly describe the main principles and techniques involved in the radiotherapy treatment planning process as well as their application in current clinical practice.

The path followed by any radiotherapy-prescribed patient can be summarized as follows. The process begins with the diagnosis of a solid tumor with the help of medical imaging techniques, for which radiotherapy is considered advisable. To proceed further, an accurate distinction between tumor and nearby organs is a crucial task, because over-dosage of radiation can lead to severe side effects, while under-dosage reduces the probability of tumor control. Once the medical images have been analyzed, clinicians and radiophysicists should decide what type

of radiotherapy technique should be applied, the prescription radiation dose on the tumor, the fractionation scheme and the precise manner in which radiation should be delivered. These decisions depend on the type, stage and location of the tumor as well as on its radiosensitivity (response to radiation), the radiation tolerance of surrounding OARs, and the clinical history of the patient among other factors. Then a number of tentative treatment plans are simulated in a treatment planning system (TPS), a simulator incorporated to the linear particle accelerator that will be used. Finally, after comparing the tentative plans thus obtained, that which is expected to yield better results is selected and delivered.

1.2.1 Anatomical structures definition: medical imaging techniques

The development of medical imaging techniques began immediately after the discovery of X-rays by Röntgen in 1895. He noticed that these invisible rays can provide images of the interior of solid objects after they pass through them. Ever since, medical imaging techniques have become a key source of information in the design of radiotherapy treatment plans. The application of state-of-the-art radiotherapy techniques requires accurate tumor and organs delineation, as well as the intrinsic characterization of the tissues, facts which are strongly dependent on imaging techniques [40], [41]. For instance, Computed Tomography (CT) and Magnetic Resonance Imaging (MRI) provide anatomical information (see Figure 1.1), whereas Positron Emission Tomography (PET) allows to keep track of metabolic activity. In addition, different imaging techniques can be combined to create more complete and comprehensive images than none of them can offer alone. An example of that is the PET-CT technique, where functional images obtained by PET can be displayed together with anatomic imaging obtained by CT scanning (see Figure 1.2).

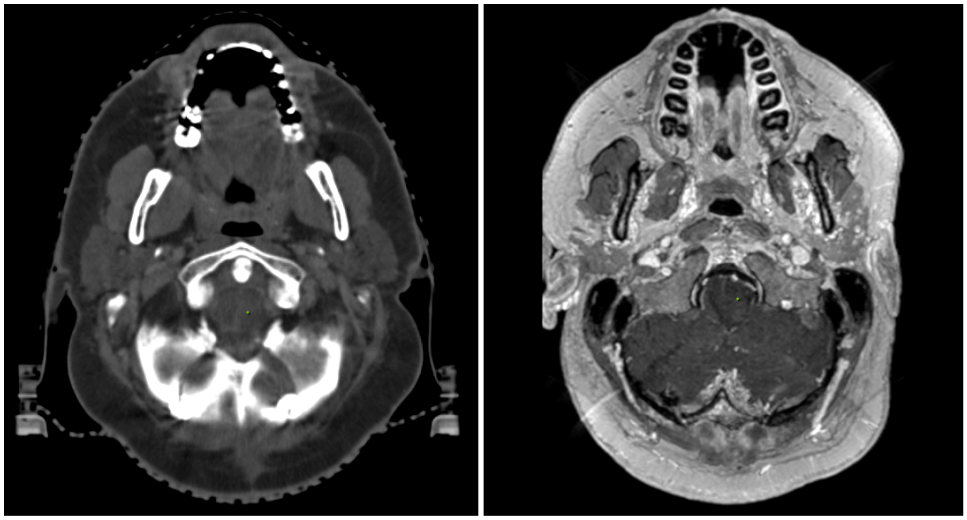

Figure 1.1. (Left) Magnetic Resonance Imaging (MRI) image compared with a Computed tomography (CT) image (right) for a same patient. Notice that MRI is better suited to distinguish soft tissues than CT, which is more appropriate to visualize dense tissues such as bones. [This image is used under permission of the Hospital Universitario Puerta de Hierro Majadahonda, Madrid, Spain].

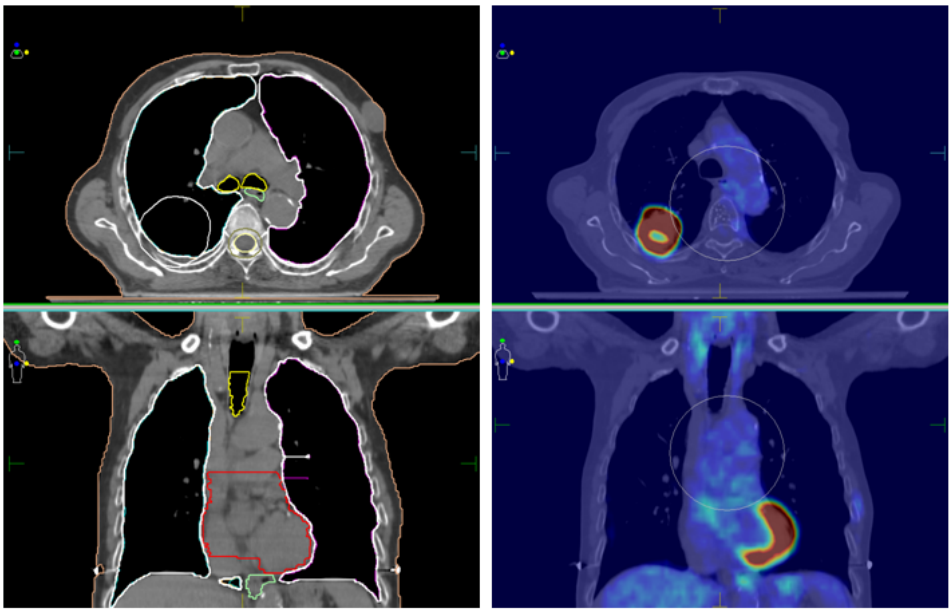

Figure 1.2. (Left) Computed tomography (CT) image compared with a combined PET-CT image (right) for a same patient. Notice that PET-CT scan reveals abnormal metabolic activity. [This image is used under permission of the Hospital Universitario Puerta de Hierro Majadahonda, Madrid, Spain].

Once a patient is diagnosed with a solid tumor for which radiotherapy is prescribed, clinicians and radiophysicists carefully analyze the available medical images in order to delineate the tumor and nearby OARs. This process is prone to a number of inaccuracies. On the one hand, these volumes are manually contoured on a 2D slice-by-slice basis, although modern treatment planning systems are able to automatically accomplish parts of this task for various critical structures. However, in almost all cases sharp identification of tumor boundaries remains a major challenge. For such reasons, the International Commission on Radiation Units (ICRU) has proposed several tumor and organ at risk volume definitions to assist in this part of the treatment planning process [14], [15].

The first such term is the gross tumor volume (GTV) commonly defined as "*the gross palpable or visible/demonstrable extent of location of malignant growth*" [15]. Due to inaccuracies inherent in tumor delineation, a clinical target volume (CTV) is next defined as follows: "*is the tissue volume that contains a demonstrable GTV*

and/or sub-clinical microscopic malignant disease, which has to be eliminated. This volume thus has to be treated adequately in order to achieve the aim of therapy, cure or palliation" [15]. In this case, CTV is usually drawn with an empirical margin added to the GTV of approximately 1 millimeter in order to consider different areas of spread of the tumor, which current imaging techniques are not able to detect. On the other hand, the planning target volume (PTV) is a new concept introduced specifically for the treatment planning process, which should include the CTV and accounts for uncertainties in patient positioning and alignment of treatment beams. "*The planning target volume (PTV) is a geometrical concept, and it is defined to select appropriate beam arrangement, taking into consideration the net effect of all possible geometrical variation, in order to ensure that the prescribed dose is actually absorbed in the CTV*" [15]. In Figure 1.3 a representation of a CTV and the corresponding PTV for a patient diagnosed with a brain tumor is provided.

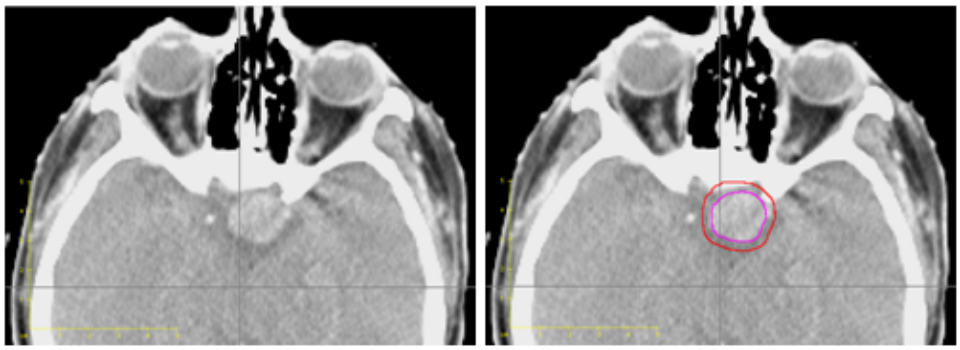

Figure 1.3. From left to right a CT image of a patient diagnosed with a brain tumor and the delineation of the CTV (purple) and the corresponding PTV (red). [This image is used under permission of the Hospital Universitario Puerta de Hierro Majadahonda, Madrid, Spain].

The process of contouring a tumor and the surrounding OARs is a crucial task during planning. In fact, small errors in this process may result in low tumor control and undesirable side effects to the patient. For that reason, low-resolution (corresponding to low-dose irradiation) images are sometimes taken in the course of treatment prior to every new therapeutic session. In fact, this strategy helps in a correct positioning of the patient before each session, so that a prescribed radiation dose will be delivered where required.

On the other hand, tumor heterogeneity is widely considered to be a determinant factor in radiotherapy outcomes [21], [22], [23]. Unfortunately, to this day only partial information can be derived about that feature by means of non-invasive, medical imaging techniques. Currently available information can be mainly used to distinguish various level of oxygen pressure within the tumor related to hypoxia processes [24], necrotic areas, or highly proliferating regions detected by means of PET techniques [42]. While undoubtedly important, such information is not enough to design therapies whose results could significantly improve those obtained by current standard procedures. As a consequence, when radiotherapy is used, radiation dosimetries are selected under the assumption that the malignancy targeted is of a homogeneous nature. Further improvements in imaging techniques are still required to increase the spatial and functional resolution of the internal tumor structure. Any additional information in this respect could be translated into a more efficient dosimetry planning.

In this work, a mathematical model has been proposed in an attempt to gain insight about the influence of tumor heterogeneity in radiotherapy treatment response. More precisely, in Chapter 3 a mathematical model is presented to investigate *i)* how the internal structure of a tumor could be predicted from the knowledge of key biological properties of the different phenotypes involved and *ii)* the way in which suitable heterogeneous radiation therapies can then be prepared that clearly outperform homogeneous dosimetries as those currently in use.

1.2.2 Selecting the prescription radiation dose and fractionation schemes

For any given patient, once the PTV and OARs have been delineated, radiation oncologists and radiophysicists prepare a treatment plan. To that end, the number of therapeutic sessions (fractionation scheme) and the prescription radiation dose (D_p) on the tumor should be specified. In particular, D_p depends on the type, location, stage and radiosensitivity of the tumor considered. Moreover, the radiation dose distribution to be applied should satisfy a set of clinical constraints on the dose prescribed on the PTV and on the maximum radiation deemed acceptable over neighboring OARs. These clinical requirements are selected by radiation

oncologists according to their clinical experience, without explicit reference to any underlying radiobiological or physical theory.

Selecting suitable clinical constraints is a key question. For instance, a high and homogeneously delivered radiation dose on the PTV, and a zero dose outside is obviously a desirable choice. However, this high-precision dosimetry is out of question due to limitations in the radiation equipment resolution. The prescription dose distribution has therefore to be selected by achieving a suitable balance between radiation doses delivered on PTV and on nearby OARs. In particular, a maximum and minimum dose as close as possible to D_p is sought on the PTV to achieve sufficient tumor control, while at the same time strict maximum limits on the doses on the surrounding OARs are always wanted. Dose-volume constraints may be also required on the volume fraction of the PTV and/or OARs that receives a dose above/below a given threshold value.

To address these issues, in Chapter 2 a mathematical model to find optimal radiation dose distributions satisfying clinical and technical requirements is formulated and discussed. The proposed dose distributions are given as solutions of a multi-parameter optimization problem of a variational nature, where high tumor control and low radiation doses on OARs are simultaneously sought-for.

Once the radiation dose distribution to be applied has been selected, a fractionation scheme should be defined. This process consists in dividing the total radiation dose into smaller fractions distributed on different sessions, so that at the end the total prescription dosimetry is delivered [14], [15]. The main motivation for dose fractionation is related with the concept of the 5 R's of radiotherapy: repair, repopulation, redistribution, re-oxygenation [43] and more recently, intrinsic radioresistance [44]. All of these are biological and radiobiological effects that occur in the time interval between treatment sessions. In particular, a fractionation protocol allows healthy cells time to recover, and thus benefits from the fact that tumor cells have generally less efficient repair mechanisms. In fact, there is a dependence of tumor radiosensitivity on the cell cycle phases, as well as on the level of cell oxygenation. For instance, since hypoxic cells are more resistant to radiation than well-oxygenated cells [45], fractionation also permits that tumor cells reoxygenate and enter into other cell cycle phases, where they become more

radiosensitive [46]. In addition to these cellular processes, fractionation is also supported by clinical experience related to the radiation tolerance of nearby OARs.

As to the number of sessions in which a selected dosimetry is delivered, different fractionation protocols are currently used in radiotherapy, according to the amount of radiation per fraction and to the number of treatment sessions per day [47]. For instance, hyperfractionated schemes prescribe more than one session per day with low radiation doses. Hypofractionated dosimetries give large radiation doses per session instead, but fewer sessions are scheduled than in the former case. Some brain tumors are usually treated with a very high radiation dose in a single session. This technique is known as Stereotactic Radiosurgery, which in some clinical cases can provide acceptable results in terms of tumor control. It should be noted that for similar tumors fractionation schemes may vary between different clinical centers and even between individual radiophysicists in a same center, although in general standard protocols achieved by consensus are widely (if not universally) followed. For instance, in current clinical practice a standard fractionation scheme for adults diagnosed with brain tumors as Meningioma, or Glioblastoma Multiforme (GBM) consists in $1.8Gy$ to $2.0Gy$ per day, 5 days a week along 28-30 sessions with weekend interruptions [48], [49]. Here Gy stands for Gray, a standard unit for absorbed ionizing radiation dose (1 Gy being 1 Joule per Kilogram) [50].

1.2.3 Radiation delivery

Radiation may be delivered externally or internally depending on the type of radiotherapy technique selected. In the case of external beam radiotherapy (EBRT) the radiation is sent to the tumor from an external machine. On the other hand, internal radiotherapy or Brachytherapy consists in the implantation of small radiation sources known as seeds in or as near as possible to the tumor. Furthermore, radiation can also be delivered as radioactive tracers (generally short-lived isotopes linked to chemical compounds), which emit gamma rays from within the body. These isotopes can be administered by injection, inhalation or orally, as in the case of thyroid and mouth cancers.

External beam radiotherapy EBRT, the technique underpinning the models

studied in this work, is applied by means of linear particle accelerators (LINAC), which are able to deliver radiation even at deeply-seated tumors (see Figure 1.4). In combination with sophisticated techniques of treatment, LINACs have enabled radiation oncologists and radiophysicists to significantly reduce side effects while at the same time improving the precision and efficiency of the therapy. In particular, treatment plans are applied to a patient positioned on a computer-controlled couch that can rotate, while LINAC delivers ionizing radiation from a gantry that can turn around a central axis. This enables variable positioning of couch and gantry, so that radiation beams can be focused on the PTV center to achieve a cumulative radiation effect, so that the exposure of nearby healthy tissues and OARs is significantly reduced. For each beam incidence angle (defined by the position of couch and gantry) the LINAC delivers radiation, which passes through a multi-leaf collimator (MLC). This device that consists of a number of pairs of metal leaves moving along channels into the path of radiation to block out different parts of the beam. This allows radiation beams to better fit to the shape of the tumor (see Figure 1.5).

Figure 1.4. A linear particle accelerator (LINAC). [This image is used under permission of the Hospital Universitario Puerta de Hierro Majadahonda, Madrid, Spain].

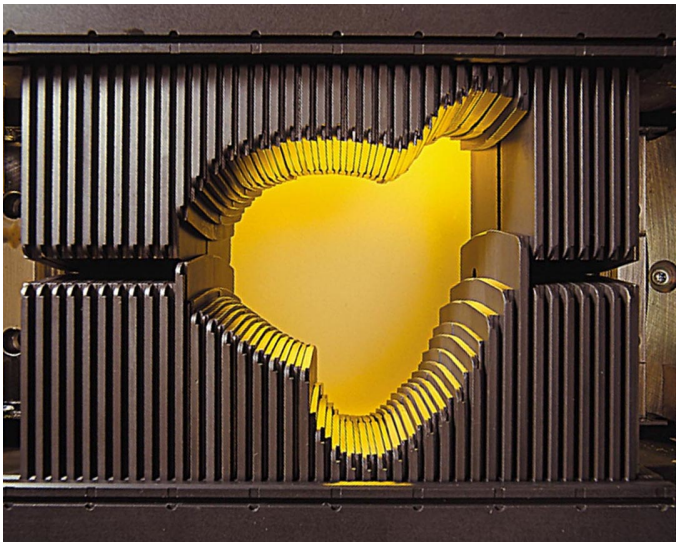

Figure 1.5. A multi-leaf collimator (MLC).

On the other hand, delivery of radiation is particularly difficult in areas that keep moving during a treatment session, such as the thoracic and abdominal regions affected by breathing. In those cases, immobilization of patients is important, particularly in the case of small tumors, where a slight shift in position can move the target out of the beams path. For this reason, several devices are currently used to prevent movement (i.e. molds, masks and stereotactic head or body frames). These are custom-made individually to fit the patient body or head, and are used during each treatment session. Moreover, different techniques may also be applied to keep track of the medical images obtained before any session treatment starts, including low-resolution images, skin markers, laser lights, infrared cameras, X-rays positioners, etc.

Several modalities of external beam therapy are currently used in clinical practice (see [15], [51], [52] and references therein) and some of them are briefly described as follows:

◦ **Three-Dimensional Conformal Radiation Therapy (3D-CRT)** uses computers and advanced imaging techniques (such as CT, MRI and/or PET scans) to create 3D digital data sets of the tumor and adjacent organs. These data are used to deliver highly "conformed" (focused) radiation beams to a tumor by means

of multi-leaf collimators (MLC) and field shaping blocks. Since radiation beams are very precisely focused, nearby healthy tissue receives little radiation. In 3D-CRT, the planning process is directly determined, meaning that radiophysicists decide the beam configuration (number, incidence angles, shapes and weights of radiation beams) and the TPS provides the resulting dose distribution.

◦ **Intensity Modulated Radiation Therapy (IMRT)** is an advanced form of 3D-CRT that allows radiation to be shaped to fit complex tumor geometries (for instance, concave tumor shapes surrounding organs at risk as the spinal cord or the brain stem). To do that, each radiation beam can be decomposed into many "beamlets" and the intensity of each beamlet can be adjusted individually. This intensity modulation is achieved by moving the leaves in the MLC during the course of treatment, which produces radiation fields with non-uniform intensities. In IMRT dose distributions are inversely determined. This means that radiophysicists select the clinical requirements to be met, and then the TPS produces, by means of different optimization algorithms, a series of beam intensities as close as possible to the desired prescription goals. IMRT technique allows higher radiation doses to be delivered to the tumor, potentially increasing tumor control or eradication.

◦ **Image-Guided Radiation Therapy (IGRT)** consists in using medical imaging (such as CT, ultrasound or X-rays) before or during the course of a treatment session to improve the precision and accuracy of radiation delivery. This technique is used to treat tumors in areas that are prone to movement while breathing, as thoracic cavity for example. In general, all patients undergo at least a CT scan as part of the treatment planning process, but further imaging test are seldom performed during treatment. The imaging information obtained allows radiophysicists to compare earlier images (obtained during the simulation) with the images taken just before treatment session starts. Then, any necessary adjustments regarding the patient position and/or treatment plan (beam configuration) can be made in order to better fulfill clinical requirements. In particular, IGRT is often used in conjunction with IMRT or any other advanced modality of high-precision radiotherapy.

In standard fractionated radiation therapy the same prescribed radiation dose distribution is applied in each treatment session. However, changes occurring be-

tween sessions are receiving increasing attention. Since variations in tumor size during treatment can have dosimetric impact, advanced radiotherapy protocols that utilize IMRT and IGRT further stress the need for periodic plan adaptation, which is often referred to as Adaptive Radiation Therapy (ART). Session dosimetries in ART will thus be reconsidered after evaluation of tumor changes resulting from the previous sessions. However, efficient tools are yet to be developed to allow for better tumor control resulting from sequential feedback on the evolution of the tumor as treatment proceeds.

1.3 Mathematical modeling in radiotherapy

As in many medical fields, mathematical modeling plays an important role in radiotherapy. In fact, several mathematical models, based on physical and radiobiological principles, have been developed to estimate and improve treatment outcomes. The topics addressed by these models includes estimating the radiation effects on healthy and malignant tissues, quantifying tumor control and side effects on critical structures, improving the accuracy and precision of radiation delivery techniques, optimizing the treatment planning process, assisting in the decision-making process and comparing different tentative treatment plans. This Section is devoted to a brief description of the mathematical models in radiotherapy that are pertinent for the purpose of this work.

1.3.1 Estimating the effect of ionizing radiation on cells: the Linear Quadratic model

To understand the effect of ionizing radiation on cells, it is crucial to know the mechanisms by which ionizing particles interact with living tissues, and in particular the differences in radiation response between malignant and healthy cells.

In general, ionizing radiation produces harmful effects on all types of cells. The action of ionizing particles on cell structures is of a stochastic character. This means that an ionizing particle that hits at a cell may, or may not, produce a measurable effect. When the latter occurs, it will produce a damage whose importance

may be highly variable. In particular, radiation damage on cells depends on the amount and type of radiation, the exposure time and the nature of the irradiated tissue. Most importantly, radiation can damage the cell DNA (Deoxyribonucleic Acid), which plays a crucial role in cell activity and viability [45], [47]. More precisely, changes induced in the DNA structure may result in chromosomal aberrations and genetic mutations with various effects, from modifications in normal cell behavior to cell death. At the molecular level, the two most important lesions in the genome induced by radiation are related with the number and location of strand breaks in the double DNA helix (see Figure 1.6). More precisely, these lesions are single-strand breaks (SSB) and double-strand breaks (DSB). SSB may be repaired in a comparatively easy way by using the remaining intact strand as a template to restore the original genetic information. However, DSBs are more difficult to repair, and often result in cell death, even when produced in a smaller proportion than SSB [47], [53].

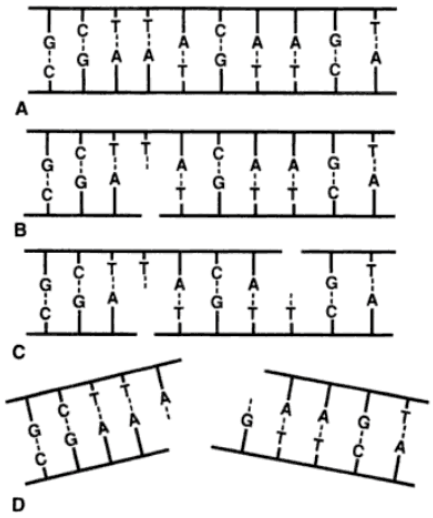

Figure 1.6. Representation of single-strand breaks (SSB) and a double-strand break (DSB) induced by ionizing radiation in the DNA structure. From top to bottom, *i)* representation of the undamaged strands of the DNA, *ii)* a single break in one strand, *iii)* two single strand breaks in two different locations and *iv)* a double-strand break. [Reproduced from E. J. Hall et al. *"Radiobiology for the radiologist"* 2006, see reference [47]].

To this day, the most widely used mathematical tool to measure the effects of

ionizing radiation on cell populations is the so-called Linear Quadratic (LQ) model (cf. for instance [53], [54], [55], [56]). Interestingly, the LQ model was heuristically deduced from empirical data of cell survival curves [57]. Only years after its formulation was the LQ formula derived as an asymptotic limit of a dynamical system describing the kinetics of radiation damage production, repair and misrepairs [58].

The LQ model states that for a given cell aggregate (either malignant or healthy), the surviving fraction of cells after receiving a radiation dose D is given by

$$SF(D) = e^{-(\alpha D + \beta D^2)}, \tag{1.1}$$

The linear and quadratic terms in the exponent of (1.1) are respectively related to cell damage induced by single and double DNA strand breaks. The positive parameters α and β in (1.1) (the so-called radiosensitivity parameters) depend of the specific cell line under consideration. It has been suggested that $SF(2)$, the surviving cell fraction after receiving a radiation dose of $2.0Gy$, is an important figure to predict the effects of radiation on a given tumor (see [53], [59] and [60] for a comparison with other commonly used radiobiological models). According to that principle, low (respectively high) values of $SF(2)$ would indicate good (respectively poor) expected results for a given radiotherapy treatment. However no rationale for that fact (nor any precise determination of the corresponding threshold values of $SF(2)$) has been substantiated as yet.

Obviously, a precise knowledge of radiosensitivity parameters α and β is a prerequisite to obtain useful clinical information from the LQ model. Unfortunately, the task of estimating such parameters meets a number of significant difficulties. As a matter of fact, most values reported in the literature are obtained upon irradiation either of *in vitro* growing cells taken from tumor samples or of cultures of healthy cell lines. A major drawback towards direct clinical use of the LQ model is that there is no consensus on the values of these parameters for many of the cell lines (either malignant or healthy) studied, and there are many tumor lines and healthy tissues for which such parameters have not even been reported as yet. Therefore, use of values of the radiosensitivity parameters α and β should be made

with extreme caution.

On the other hand, the LQ model has been extended to include relevant aspects involved in radiotherapy as for instance repopulation, the time course between treatments, dose-rate effects and hypersensitivity (see [56] and references therein). Further details will be omitted here, and the reader is referred instead to [61] for a comprehensive review on this topic.

1.3.2 Optimization in radiotherapy

Optimization techniques have been extensively used with successful results in many medical fields, and particularly in radiotherapy (see for instance [62], [63], [64], [65]). In this context the term optimization can be used for different purposes. For instance, at a general level optimization may be considered as a process leading to selecting a treatment plan that maximizes the probability of tumor control with comparatively low side effects in the nearby organs at risk and healthy tissues. In technical terms, the search for such a treatment plan is often divided into a sequence of steps, many of which involve large-scale mathematical programming problems that require particular optimization techniques to be solved.

Clearly, such techniques depend on the type of objective functions that need to be optimized at any step of the process. These are often divided into those of a physical or biological nature. In a recent AAPM group report [66] the following can be read:

"... Until recently, the quality of a radiotherapy treatment (RT) plan has been judged by physical quantities, that is, dose and dose-volume (DV) parameters, thought to correlate with biological response rather than by estimates of the biological outcome itself. It is widely recognized that the DV criteria, which are merely surrogate measures of biological responses, should be replaced by biological indices in order for the treatment process to more closely reflect clinical goals of RT. Developments in our understanding of advantages and limitations of existing dose-response models begin to allow the incorporation of biological concepts into a routine treatment planning process ..."

As observed above, physical optimization methods look for radiation dose dis-

tributions satisfying criteria as high tumor coverage and low dose deposition on organs at risk, but the biological response to radiation of the tumor and organs at risk is not explicitly taken into account [62], [67], [68]. For instance, under-dosing a very small volume of the tumor might not have a significant effect on the objective value of a physical-based treatment plan, but tumor control might be largely diminished in that case. On the other hand, radiobiological methods focus on the biological and radiobiological effects resulting from the radiation dose distributions selected [69], [70], [71], [72]. For instance, tolerance to radiation of the OARs and tumor radiosensitivity will be now given priority with respect to dose conformity over PTV, which is a constraint of a physical nature.

Optimization techniques in radiotherapy are relevant both for direct and inverse planning, which were briefly mentioned in the context of the external beam radiation therapies considered in Section 1.2.3. The forward optimization approach, which is mostly used nowadays in clinical practice, is a trial-and-error process where radiophysicists change the radiation beam configuration: incidence angles, intensities (fluence), number of beams... and consequently the resulting radiation dose distribution, in an attempt to satisfy some prescribed clinical criteria [73], [74], [75], [76], [77], [78]. Availability of high computer power in commercial TPS has turned inverse planning into a competitive alternative. In this last procedure, which is usually harder to handle from a mathematical point of view, predetermined clinical criteria are used as an input to produce the radiation beam configuration that satisfies as much as possible the prescription goals [79], [80], [81], [82], [83].

Commonly used optimization methods for forward and inverse planning are linear and nonlinear programming, mixed-integer programming and dynamic programming (see [62], [74], [76], [77], [84], [85], [82], [83] for further details). Variables used by such optimization methods include number, intensities and incidence angles of radiation beams (see Figure 1.7), beam modulation through a multi-leaf collimator (MLC) and parameters related to fractionation schemes (number of treatment sessions, radiation dose per session, patient positioning, etc.). Solving these optimization problems remains in many cases is a formidable challenge due to the huge size of its solution space.

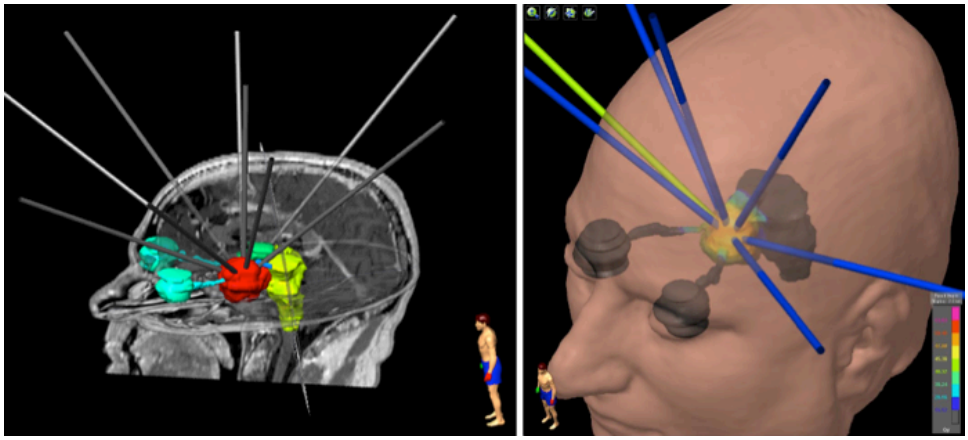

Figure 1.7. Representation of two different radiation beam configurations on a treatment planning system over a CT scan (left) and in a three-dimensional reconstruction of the head of the same patient (right). [This image is used under permission of the Hospital Universitario Puerta de Hierro Majadahonda, Madrid, Spain].

Radiobiological optimization is one of the main research directions of this work. Specifically, in Chapter 2 an optimization model to select optimal radiation dose distributions based on radiobiological principles is described. The model includes in its formulation compliance with current clinical and technical restrictions. Moreover a procedure is proposed to use it as comparison standard when only partial information on radiosensitivity parameters is available.

1.3.3 Assessing and comparing treatment plans

In radiotherapy, for any patient diagnosed with a solid tumor the treatment to be applied is expected to achieve high tumor control and to induce little side effects on neighboring critical regions. To achieve those goals, a number of tentative treatment plans (usually two or three) are simulated (or a unique plan is defined and successively modified) on a commercial treatment planning system (TPS) until the result is found close enough to clinical prescription. In general, the tentative plans considered differ only from each other in small variations in the number, incidence angles or intensity of radiation beams converging on the tumor. To this day no standard, computerized system seems to be in use to assist in such decision process, which largely relies on the clinical experience of the radiophysicists in

charge. Moreover, such choice, even when made by experienced specialists, is subject to considerable uncertainty due to the absence of quantitative standards to grade and evaluate alternative plans.

For any tentative treatment plan being considered, commercial TPSs provide a 3D view of the tumor and organs at risk obtained by different medical imaging techniques (see Figure 1.7 in Section 1.3.2), dose volume histograms (DVHs) for each anatomical structure involved, and the isodose curves over the whole treatment domain. A cumulative DVH is a plot of the volume of a given structure that receives at least a certain radiation dose. For instance, stating that $V(D = y) = x$ means that $x\%$ of the total volume under consideration receives at least the $y\%$ of a normalized dose value (see Figure 1.8). On the other hand, the isodose curves are closed lines bounding regions where radiation dose is larger or equal than a given value (see Figure 1.8). Out of all tentative plans considered, the choice of the actual treatment plan is then made upon comparison (by inspection) of the DVHs and isodose curves for each tentative plan considered, independently of any subsequent radiobiological calculations.

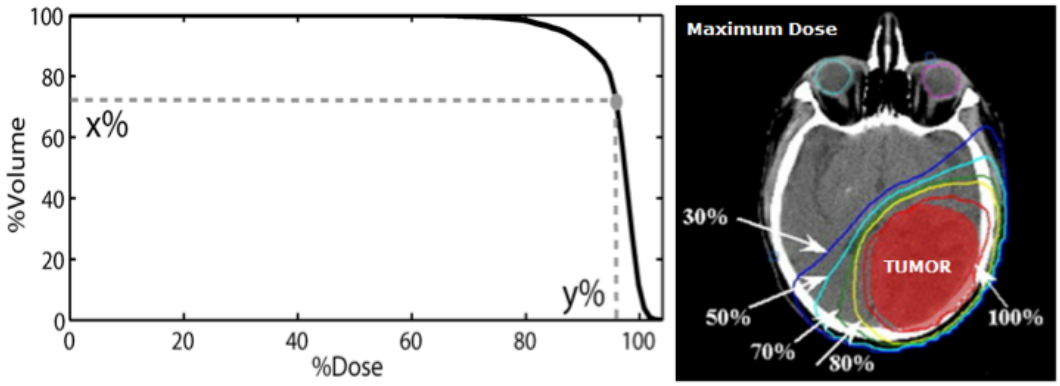

Figure 1.8. Representation of a normalized dose volume histogram (DVH) for a PTV (left) and isodose curves corresponding to a maximum radiation dose for a brain tumor (right). [This image is used under permission of the Hospital Universitario Puerta de Hierro Majadahonda, Madrid, Spain].

The underlying evaluation and comparison process just described is highly subjective and prone to inaccuracies. For this reason, several quantitative indexes (also

termed as figures of merit) have been proposed to assist in the selection of tentative plans. For instance, some well-known figures of merit in radiotherapy planning are the Homogeneity Index (HI) and the Conformity Index (CI). In particular, HI basically computes the ratio between the maximum dose and the prescription dose in the PTV, so that values close to 1 correspond to largely homogeneous dose distributions within the target [27], [29], [32]. On the other hand, CI can be defined as the ratio between two particular isodose regions within the PTV. For instance, typical choices are the volume fraction of the PTV receiving the prescription dose and the total PTV volume (see also [27], [28], [30], [31], [32]).

Besides HI and CI, different indexes have been proposed to assess dosimetry plans paying attention to dose coverage, conformity and dose gradient as separate or global scores [27], [28], [29], [30], [31], [32], [33], [34], [35], [36], [37] and [38]. However, most of such figures have been reported to suffer from limitations. In particular, the models proposed may introduce false positives (see [27], [29], [32] for a detailed discussion on HI and CI), may not be sensitive to small modifications sequentially introduced, they often depend on many parameters (cf. for instance [31], [33], [37], [39]), provide ambiguous scoring due to averaging effects [34] and are generally not easy to implement [38]. Furthermore, in some of these cases no value normalization is performed, which renders difficult the interpretation of the results obtained.

Clearly, any figure of merit permits to evaluate a tentative plan according to its compliance with a criterion specific to that figure. In the absence of widely accepted quantitative criteria as a standard, different persons may possibly make different choices from the same set of DVHs, isodose curves and radiobiological features. As a consequence, different clinicians may suggest different actions for a given patient, which makes difficult to properly estimate applied therapies from a statistical point of view.

Bearing these facts in mind, in Chapter 4 a mathematical tool is proposed to assist clinical personnel when it comes to estimate the consequences of modifications, however small, on any tentative treatment plan under consideration. The proposed user-friendly decision-support tool is easy to handle and uses exclusively the information of DVHs for each structure defined in a treatment plan and the

corresponding prescription dose on the tumor. The figure proposed is intended to better understand the differences between the alternatives being considered, and no attempt is made to modify the priorities made by the person who has to apply the treatment.

1.4 Discussion

In most clinical cases, cancer is a threatening disease and any improvement in the diagnosis, planning and treatment techniques will result in great benefits for patients. This is a compelling reason to pay more attention to mathematical modeling and computer-based techniques, which could be helpful to predict and provide relevant quantitative clinical information. In consequence, many researchers worldwide are developing advanced mathematical methods to contribute to the fight against cancer, a goal towards the studies conducted in this memoir intend to contribute.

In this Chapter basic principles and techniques involved in the radiotherapy treatment planning process have been described in connection to the main problems that will be addressed in this work. In particular, a brief description of medical imaging modalities used for diagnosis and therapeutic purposes, the principles followed to select the prescription dose distribution and fractionation schemes in current clinical practice, and the most used radiation delivery techniques has been briefly recalled. On the other hand, some of the mathematical models used in radiotherapy have been reviewed. More precisely, the basic Linear Quadratic model describing the effect of radiation on tissues has been has been recalled. Moreover, some aspects of radiotherapy optimization as well as some of the figures of merit proposed to evaluate and compare the quality of different tentative treatment plans have been also reviewed.

The main goal of this memoir is to provide new mathematical and computer-based tools to assist in the decision-making process in radiotherapy treatment planning process, a brief description of which has been presented. More precisely, the issue of whether an optimal radiation dose distribution can be determined under given clinical and technological constraints is addressed in Chapter 2. To

this end, a theoretical definition of radiation dose distributions, given as the solution of a suitable multi-parametric variational problem is proposed. The choice proposed will be shown to be suitable for personalized patient treatment, since it allows for assigning different radiation dosimetries for different clinical priorities. On the other hand, increasing attention is being paid to tumor heterogeneity as a key factor in tumor prognosis. Unfortunately, current clinical and experimental techniques are unable to probe deeply enough into tumor heterogeneity by non-invasive procedures. In Chapter 3 a mathematical model of tumor growth with spatial intratumoral heterogeneity is investigated. Specifically, a simplified situation is assumed, where only two tumor cell phenotypes are present, which strongly differ in their respective cell cycle duration and radiosensitivity properties. It is shown that such difference in phenotype behaviours permit to predict the internal distribution of both phenotypes as tumor grows. As a consequence, heterogeneous radiation dosimetries could be planned which are shown to yield better results in terms of local tumor control than the homogeneous ones currently pursued in clinical practice. On the other hand, a decision-aid tool based the prescription radiation dose and on the DVHs obtained from a TPS has been proposed in Chapter 4 to estimate any tentative treatment plan. In this manner, different plans can be compared and evaluated in a quantitative way. Finally, in Chapter 4 some concluding remarks and future research directions are discussed.

Chapter 2

Selecting radiation therapy dose distributions by means of constrained optimization problems

"... Mathematics is one of the most significant manifestations of the love of wisdom. On the one hand, there are no boundaries in mathematical thought and imagination, but on the other hand there is the reality that the world is made of things both visible and invisible and that mathematics is the unique science with the capacity to pass from the observations of visible things to the imagination of things invisible. This is perhaps the secret of the strength of mathematics ..."

Ennio De Giorgi (1928-1996)

2.1 Abstract

The main steps in planning radiotherapy consist in selecting for any patient diagnosed with a solid tumor *i)* a prescribed radiation dose on the tumor, *ii)* bounds on the radiation side effects on nearby organs at risk and *iii)* a fractionation scheme specifying the number and frequency of therapeutic sessions during treatment. In particular, the choice of a prescription radiation dose and bounds on the radiation doses are mostly based on clinical experience accumulated on the specific type of

tumor and organs at risk involved, without any direct reference to quantitative radiobiological assessment. Interestingly, mathematical models for the effect of radiation on biological matter exist long since, and are widely acknowledged by clinicians. However, the difficulty to obtain accurate *in vivo* measurements of the radiobiological parameters involved has severely restricted their direct application in current clinical practice.

The goal of this Chapter is first to propose a mathematical model to select radiation dose distributions as solutions (minimizers) of suitable variational problems, under the assumption that key radiobiological parameters for tumors and organs at risk involved are known. Second, by analyzing the dependence of such solutions on the parameters involved, the manner in which the use of those minimizers could improve current decision-making processes to select clinical dosimetries is then discussed, when (as is generally the case) only partial information on model radiosensitivity parameters is available. A comparison of the proposed radiation dose distributions with those actually delivered in a number of clinical cases strongly suggests that solutions of the proposed mathematical model can be instrumental in deriving good quality tests to select radiotherapy treatment plans in rather general situations. This model can be applied for any type of tumor regardless of its location, as well as if different intratumoral regions or several tumors are identified for a same patient.

2.2 Introduction

A crucial step in planning radiotherapy is the choice of the radiation dose distribution to be delivered during treatment to a patient diagnosed with a solid tumor. Standard clinical practice requires radiation dose distributions to be as close as possible to a prescribed radiation dose (D_p) homogeneously distributed over the Planning Target Volume (PTV), while unwanted side effects on surrounding organs at risk (OARs) and healthy tissues (HT) should be kept as low as possible. Addressing such often conflicting goals is the aim of the dosimetry planning process, where the number and frequency of therapeutic sessions, clinical constraints on the radiation dose reaching nearby OARs and the D_p on the tumor are selected, and the manner in which the resulting treatment plan has to be delivered is specified.

In particular, selecting D_p depends on the type, location and size of each tumor under consideration and on its expected radiosensitivity (that is, its estimated resistance to radiation). As a matter of fact, sparing radiation delivery to critical structures is the most important limiting factor in radiotherapy treatments [53]. Indeed, an important consideration is that the radiation dose selected to achieve tumor control should depend on that tolerated by nearby organs and healthy tissues. Therefore, normal tissue morbidity will often set a limit to the cure rate that may be achieved [20]. On the other hand, radiation does not affect different organs in the same way. In fact, its effect will depend of the organ architecture (serial, parallel or combination of them) and the intrinsic radiosensitivity among other factors. As consequence, estimating the effect of radiation on anatomical structures (both pathological and physiological) is thus a key feature in the radiotherapy planning process. To this day, the accepted theoretical foundation for that purpose is the Linear Quadratic (LQ) model (see Section 1.3.1 in Chapter 1 and [53], [54], [55], [56]). Since the LQ model is an essential ingredient in the optimization problem formulated in this Chapter, some of its main features are recalled as follows.

According to the LQ model, for any given cell aggregate, the surviving fraction of cells (either malignant or healthy) after a radiation dose D has been delivered there can be estimated by means of equation (1.1) in Chapter 1. Radiosensitivity parameters are thus specific for any anatomical or pathological structure considered, and this represents a major obstacle towards their efficient clinical use, particularly in the case of malignancies. As a matter of fact, and in spite of intrinsic variability between patients, extensive (although by no means exhaustive) data have been gathered for the values of α and β in healthy human tissues [88], [89]. However, in what concerns tumors, the situation is less satisfactory (see for instance [90] for Glioblastoma Multiforme (GBM) tumor cell lines and [91] for prostate carcinoma cell lines). To begin with, most data available have been gathered from *in vitro* grown cell cultures obtained from animal trials or from patient samples, and it is widely accepted that *in vivo* values might considerably differ from their *in vitro* counterparts. Furthermore, an additional difficulty to ascertain their precise values is represented by tumor heterogeneity [21], [22]. In fact, most developed tumors contain different tumor subpopulations, each possessing

different sensitivity properties to radiotherapy (or to other therapies) [23]. To this day, no efficient, non-invasive technique exists which could sort out neither the spatial distribution of such subpopulations within a tumor, nor their different radiosensitivity parameters. Thus, in spite of equation (1.1) being considered as a cornerstone in theoretical radiobiology, in current clinical practice radiation doses prescribed on tumors are selected without making direct use of such formula to estimate radiation effects.

However, indirect albeit highly significant use of the LQ model has found a relevant place in current clinical practice in the context of dose fractionation [55], [60]. Fractionation schemes were introduced to facilitate recovery in organs and healthy tissues affected by radiation and led to the concept of Biological Effective Dose (BED) (see for instance [53], [92]), which is defined as follows. Suppose that a total radiation dose D is prescribed on a tumor, which is equally distributed into a number of n sessions, at any of which a single dose d is delivered. Assuming that treatment session effects are independently accumulated, the quantity in the exponent of equation (1.1) (usually termed as the log cell kill) will read

$$E = n(\alpha d + \beta d^2).$$

Thus, when d is small and n large, the main contribution to E is contained in its linear part. BED is then defined as follows

$$BED = \frac{E}{\alpha} = D\left(1 + \frac{d}{(\alpha/\beta)}\right). \tag{2.1}$$

Therefore, when tumor cell repopulation between treatment sessions is neglected, BED represents the radiation dose required for a given effect if the total dose D were delivered by means of small doses per fraction. As a consequence, BED quantitatively estimates the biological dose delivered to a tissue characterized by a given (α/β) ratio, by means of a particular combination of dose per fraction d and total radiation dose D. Notice that BED does not depend on α and β separately, but on their ratio (α/β), which is the dose at which cell killing by the linear and quadratic terms in (1.1) are equal. Clearly, for any fixed dose D, the same BED can be achieved with different fractionation schemes. Clinical experience accumulated on fractionation effects over years led to a classification of tissues (in-

cluding tumors) into Early-responding (ER) and Late-responding (LR) ones [47], [93]. Roughly speaking, ER tissues show only limited changes when a dose is fractionated into a number of treatment sessions, a common clinical practice, whereas LR tissues display large changes due to fractionation. Using the definition of BED in (2.1), it turns out that such effects are respectively associated with large (in the case of ER tissues) and small (for LR tissues) values of the ratio (α/β) [53], [94]. In spite of acknowledging that precise values of (α/β) ratios are rarely known in human tissues, for each particular type of tumor clinicians use some accepted figures for such ratio when selecting the particular fractionation scheme to be carried out. For instance, it is common to take $\alpha/\beta = 10Gy$ for early responding tissues and most tumors, and $\alpha/\beta = 2Gy - 3Gy$ for late responding ones. These values are usually arrived at in a statistical way from data obtained from clinical practice (see for instance [95], [96] for (α/β) ratios reported for different organs and tumors).

As argued in Chapter 1, to minimize collateral damage on OARs and HT, a standard radiotherapy strategy consists in selecting several radiation beams that converge at the PTV, which is therefore arrived at along a variable number of incidence angles, with possibly different intensities along each beam configuration. In general, the choice of any such configuration is made by selecting one among several tentative cases simulated by means of treatment planning systems (TPS) [15], [53]. Current practice consists in simulating a (usually small) number of tentative plans corresponding to different beam configurations. After comparing the plans thus obtained, that which is expected to yield better results is selected. As a matter of fact, simulated tentative plans usually differ from each other in small variations in the number, incidence angles or intensity of radiation beams converging on the PTV. Indeed, the choice of the treatment plan to be applied in any particular case relies mainly on a personal decision by the responsible clinician according to his/her own professional experience.

To remedy the uncertainties surrounding this decision process, during the last decades a number of quantitative figures of merit have been proposed to assist in this planning process (see Section 1.3.3 in Chapter 1 for further details). More precisely, some well-known figures of merit in radiotherapy are the Homogeneity Index

(HI) and the Conformity Index (CI) (see [27], [29], [32] for a detailed discussion on HI and CI). The conventionally used HI is usually defined as follows

$$HI = \frac{D_M}{D_p}, \tag{2.2}$$

where D_M is the maximum radiation dose delivered in the PTV, and D_p is the prescribed radiation dose. In most clinical cases, good homogeneity, corresponding to HI close to one, is often sought for [29]. On the other hand, the CI proposed by the Radiation Therapy Oncology Group (RTOG) [27] is given as

$$CI = \frac{V_{RI}}{V}, \tag{2.3}$$

where V_{RI} is the volume of a (selected) reference isodose and V is the volume of the planning target, so that a value of CI close to one is considered to provide a good conformation with respect to the reference isodose considered (see [32] for a review). In addition to these, several indexes have been proposed to assess dosimetry plans, however figures of merit (2.2) and (2.3) have been widely used to compare radiation effects in tumors in current clinical practice.

In this Chapter mathematical modeling and computer simulations are used to select radiation dose distributions according to the information about radiosensitivity parameters available in each given clinical case. Mathematical models of tumor growth and therapy have been extensively studied during last years: see for instance [97], [98], [99], [100], [101], [102], [103], as well as the reviews [104], [105]. Radiotherapy modeling has been reviewed in [56], [62] and specific issues of that field have been studied in [106], [107], [108], [109], [110], [111], [112]. In particular, the impact of radiation on the spatio-temporal dynamics of tumor spheroids has been discussed in [112] (see also [113]), where the effect of radiation on cell cycle synchronization is discussed, as well as in [109], where radiosensitivity parameters identification has been addressed. The impact of re-oxygenation in tumor sensitivity is discussed in [114]. An image-based kinetic algorithm to model tumor response to therapy has been described in [115], and specific models for the response of brain tumors to a given radiation dose (including in particular dose fractionation effects) have been proposed and discussed in [116], [117].

Let us now describe more in detail the plan and structure of this Chapter. To begin with, a mathematical model to obtain optimal radiation dose distributions satisfying clinical and technical requirements has been proposed and discussed. More precisely, in Section 2.3 a multi-parameter variational problem is formulated whose minimizers provide optimal choices for a radiation dose distribution when all radiosensitivity parameters α and β of the LQ model are known (see related works [106], [110]). In particular, the functional to be minimized represents a weighted sum of radiobiological effects, directly related to PTV coverage and OARs and HT sparing, evaluated according to the LQ model. In addition, standard clinical and technological constraints are also accounted for. The situation considering volumetric constraints on the fraction of a PTV and/or OARs that receive a radiation dose above of a given threshold value is also investigated, since these are issues of great clinical interest [15].

Then, in Section 2.4 theoretical results related to existence and uniqueness properties of solutions are provided. When doing so, in Section 2.5 the dependence of previously obtained minimizers on radiosensitivity parameters is explored to propose a strategy to select a dose distribution when the ratio (α/β) (but not the separate values of α and β) are known for tumors present. Roughly speaking (see that Section for details), suitable volumetric constraints on OARs are imposed and then increase the weight assigned to the PTV dosimetry in the functional to obtain a dose distribution whose radiobiological effects could hardly be improved, even if the precise values of α and β for the tumor involved were known. Moreover, when compared with actual dosimetries delivered in some clinical cases reported, the radiation dose distribution thus selected is shown to be a better option. Therefore, the dosimetry thus selected can be considered an optimal choice against which tentative treatment plans should be compared during the radiotherapy planning process. This Chapter is then concluded with a final Section 2.6, where the main results of this work are summarized and future research directions are highlighted. Finally, in Appendices A and B the numerical discretization of the proposed model and additional computer simulations of the clinical cases considered are provided respectively.

2.3 A theoretical model: radiation dose distributions as minimizers of a variational problem

In this Section a mathematical model that provides radiation dose distributions according to precise radiobiological principles is formulated. To begin with, consider a three-dimensional domain $\Omega \subset \mathbb{R}^3$ where different radiosensitivity cell populations may coexist, and $\Omega_i = \Omega_1, \ldots, \Omega_n$ $(1 \leq i \leq n)$ and $\Omega_j = \Omega_{n+1}, \ldots, \Omega_m$ $(n+1 \leq j \leq n+m)$ denote the subset of Ω occupied by tumor and organs at risk/healthy tissues respectively. Thus, $\Omega = \bigcup_{i=1}^{n} \Omega_i \bigcup_{j=n+1}^{n+m} \Omega_j$, where the sets Ω_i and Ω_j are mutually disjoint. The effect of radiation in each of these regions will be estimated by means of the LQ model (1.1), namely

$$SF_k(D(\mathbf{x})) = e^{-(\alpha_k D(\mathbf{x}) + \beta_k D(\mathbf{x})^2)}, \qquad k = 1, \ldots, n+m, \tag{2.4}$$

where $D(\mathbf{x})$ is the amount of radiation delivered at any point $\mathbf{x} \in \Omega$ and (α_k, β_k) are the radiosensitivity parameters of the regions considered. In the sequel, tumor regions (respectively, OAR and HT regions) will be indexed by i (respectively, by j).

For a given set $\Omega_k \subset \Omega$, $(k = 1, \ldots, n+m)$, $X_{\Omega_k}(\mathbf{x})$ represents the characteristic function defined as follows

$$X_{\Omega_k}(\mathbf{x}) = \begin{cases} 1 & \text{if } \mathbf{x} \in \Omega_k \\ 0 & \text{otherwise} \end{cases} . \tag{2.5}$$

Let us now consider the following multi-parameter variational problem: find $D(\mathbf{x})$ defined in Ω, such that $D(\mathbf{x})$ minimizes the following functional

$$J(D(\mathbf{x})) = \sum_{i=1}^{n} w_i \int_{\Omega} X_{\Omega_i} SF_i(D(\mathbf{x}))\, d\mathbf{x} + \sum_{j=n+1}^{n+m} w_j \int_{\Omega} X_{\Omega_j} \left(1 - SF_j(D(\mathbf{x}))\right)\, d\mathbf{x} + a \int_{\Omega} |\nabla D(\mathbf{x})|^2\, d\mathbf{x}, \tag{2.6}$$

subject to the following constraints

$$|\nabla D(\mathbf{x})| \leq C_1 \quad \text{in } \Omega, \tag{2.7}$$

$$C_2 \leq D(\mathbf{x}) \leq C_3 \quad \text{in } \Omega, \tag{2.8}$$

$$C_{m_k} \leq D(\mathbf{x}) \leq C_{M_k} \quad \text{in } \Omega_k, \quad k = 1, \ldots, m+n, \tag{2.9}$$

$$|\{\mathbf{x} \in \Omega_i : D(\mathbf{x}) > C_{V_i}\}| \geq \delta_i |\Omega_i|, \quad i = 1, \ldots, n, \tag{2.10}$$

$$|\{\mathbf{x} \in \Omega_j : D(\mathbf{x}) \geq C_{V_j}\}| \leq \delta_j |\Omega_j|, \quad j = n+1, \ldots, n+m, \tag{2.11}$$

where w_k (respectively, C_1, C_2, C_3, C_{m_k}, C_{M_k}, C_{V_k} and a) for ($k = 1, \ldots, m+n$) are given positive (respectively, nonnegative) real numbers, the functions X_{Ω_i} and X_{Ω_j} are defined in (2.5), $SF_i(D(\mathbf{x}))$ and $SF_j(D(\mathbf{x}))$ represent the surviving cell fraction given by the LQ model of the *ith* and *jth* region respectively (see equation (2.4)), and where $|\cdot|$ in (2.10) and (2.11), when applied to a measurable set, denotes its volume.

A solution (if any) $D(\mathbf{x})$ of functional (2.6) subject to constraints (2.7)–(2.11), henceforth referred to as (P) for short, is called a minimizer function of the corresponding problem. Concerning the meaning of the various terms in (2.6) and constraints (2.7)–(2.11), a few remarks are in order. To begin with, it should be noticed that the quantities

$$\int_{\Omega} X_{\Omega_i} SF_i(D(\mathbf{x}))\, d\mathbf{x} = \int_{\Omega_i} SF_i(D(\mathbf{x}))\, d\mathbf{x} \equiv |\Omega_i(D(\mathbf{x}))|$$

$$\int_{\Omega} X_{\Omega_j}(1 - SF_j(D(\mathbf{x})))\, d\mathbf{x} = \int_{\Omega_j}(1 - SF_j(D(\mathbf{x})))\, d\mathbf{x} \equiv |\Omega_j(D(\mathbf{x}))|$$

for $i = 1, \ldots, n$ and $j = n+1, \ldots, n+m$, represent the volume of the malignant and healthy regions Ω_i and Ω_j after receiving a dose $D(\mathbf{x})$ respectively, so that for instance, $|\Omega_k(D(\mathbf{x}))| \leq |\Omega_k|$ for $(k = 1, \ldots, m+n)$. The first and second term in the right of (2.6) represent a weighted estimate of the changes in the surviving cell fractions of the subsets occupied by each tumor and organ at risk/healthy tissue after irradiation. In particular, the first term in the right of (2.6) represents a tumor control term, and can account for possible tumor heterogeneity. On the other hand, the second term there represents organs at risk side effects. As a matter of fact, one may aim at achieving different effects in different regions by appropriately selecting the weight parameters w_k for $(k = 1, \ldots, n+m)$ in (2.6).

On the other hand, (2.7) is a constraint related to the resolution limit achieved by the radiation equipment being used (for instance, linear particle accelerators), whereas (2.8)–(2.11) corresponds to minimum and maximum radiation bounds over the regions considered, and are added to meet clinical requirements (where obviously one has to impose $C_2 \leq C_{m_k}, C_{M_k}, C_{V_k} \leq C_3$, for $(k = 1, \ldots, n+m)$). In addition, when $a > 0$, the last term in (2.6), provides a global gradient bound that complements the pointwise bound in (2.7). Notice that constants in this model have to be compatible, in the sense that the class of admissible, differentiable functions $D(\mathbf{x})$ satisfying (2.7)–(2.11) should be nonempty, an assumption to be retained henceforth. Moreover, for ideal cases of the volumetric constraints (2.10) and (2.11), a good selection is to fix values of $C_{V_i} = C_3 - \epsilon$, for $(i = 1, \ldots, n)$ and $C_{V_j} = C_2 + \epsilon$, for $(j = n+1, \ldots, m)$, where $\epsilon > 0$ is sufficiently small, and where δ_i $(i = 1, \ldots, n)$ (respectively, δ_j $(j = n+1, \ldots, m)$) for $0 \leq \delta_i, \delta_j \leq 1$ should be as close to 1 (respectively, to 0) as possible (say for instance, $\delta_i \approx 0.9$ and $\delta_j \approx 0.1$). In this formulation, the sets Ω_i and Ω_j are assumed to be time-independent. Indeed, this is a reasonable hypothesis if repopulation effects are assumed to occur at a

much slower time scale than that corresponding to radiation delivery.

2.4 Theoretical results of the variational problem

The problem (P) just stated can be studied by means of classical methods in the Calculus of Variations (see for instance [118], [119]). In particular, the existence of at least one minimizer can be readily obtained under very general assumptions. The proposed problem has bounded solutions with generalized bounded derivatives. More precisely, they belong to the space $W^{1,\infty}(\Omega)$ of all bounded functions $D(x)$ on Ω that satisfy a Lipschitz property, namely

$$|D(\mathbf{x}) - D(\mathbf{y})| \leq K|\mathbf{x} - \mathbf{y}|, \quad \forall \mathbf{x}, \mathbf{y} \in \Omega,$$

for a suitable constant K. The notation $W_0^{1,\infty}(\Omega)$ is used for the subclass of functions in $W^{1,\infty}(\Omega)$ that vanish on the boundary $\partial\Omega$ of Ω (see for instance [120] for properties of such spaces). In particular, for the problem consisting of minimizing (2.6) under constraints (2.7)–(2.9) one has the following result.

Theorem 1. *Let $D_0(\mathbf{x})$ be any given function in $W^{1,\infty}(\Omega)$, where Ω is a bounded, open set in $\mathbb{R}^d$ $(d \geq 1)$ with Lipschitz boundary $\partial\Omega$. Then, there exists at least one $D(\mathbf{x}) \in W^{1,\infty}(\Omega)$ such that the functional (2.6) achieves its minimum in the set*

$$\mathcal{K} = \big\{ D(\mathbf{x}) \in W^{1,\infty}(\Omega) : (D(\mathbf{x}) - D_0(\mathbf{x})) \in W_0^{1,\infty}(\Omega) \\ \text{and (2.7)-(2.9) } \textit{hold} \big\}.$$

Any such function $D(\mathbf{x})$ is said to be a minimizer of (2.6) in $\mathcal{K}$.

Proof. It is readily seen that the functional given in (2.6) is lower semicontinuous (l.s.c) on the space $W^{1,\infty}(\Omega)$ endowed with the uniform convergence. Thus, existence of at least one minimizer follows from the fact that the associated functional

$$J^*(D) = J(D) + \mathcal{I}_{\mathcal{K}}(D), \tag{2.12}$$

where $\mathcal{K}$ is as in the statement of the Theorem 1 and $\mathcal{I}_{\mathcal{K}}(D) = 0$ when $D \in \mathcal{K}$, $\mathcal{I}_{\mathcal{K}}(D) = +\infty$ otherwise, is also l.s.c on $W^{1,\infty}(\Omega)$ with respect to the uniform convergence, since $\mathcal{K}$ is compact for the uniform convergence. Then a minimizer of (2.12) (hence for the problem under consideration consisting of minimizing (2.6) under constraints (2.7)–(2.9)) exists by classical results, (cf. for instance [118], [119]). □

Besides constraints (2.7)–(2.9), a common clinical requirement consists in imposing volumetric constraints on the percentage of a tumor region (respectively, an organ at risk or healthy tissue) that is expected to receive no less (respectively, no more) than a threshold radiation dose. Let us now suppose that the volumetric constraints (2.10), (2.11) are compatible in the sense recalled above. Then a variational problem as that considered in Theorem 1 continues to have minimizers when volumetric constraints are imposed in addition to those already considered in (2.7)–(2.9). More precisely, there holds.

Theorem 2. *Let Ω, Ω_i, Ω_j and $D_0(\mathbf{x})$ be as in Theorem 1, and assume that in addition to (2.7)–(2.9), compatible volumetric constraints (2.10)–(2.11) are imposed. Then, there exists at least one $D(\mathbf{x}) \in W^{1,\infty}(\Omega)$ such that the functional (2.6) achieves its minimum in the set*

$$\widehat{\mathcal{K}} = \big\{ D(\mathbf{x}) \in W^{1,\infty}(\Omega) : (D(\mathbf{x}) - D_0(\mathbf{x})) \in W_0^{1,\infty}(\Omega), \\ D(\mathbf{x}) \text{ satisfies } (2.7) - (2.9), (2.10) \text{ and } (2.11) \big\}.$$

Proof. It is quite similar to that of Theorem 1. In particular, the functional

$$J^*(D) = J(D) + \mathcal{I}_{\widehat{\mathcal{K}}}(D) \tag{2.13}$$

is l.s.c on the space $W^{1,\infty}(\Omega)$ endowed with the uniform convergence, since $\widehat{\mathcal{K}}$ is compact for that convergence. This yields the existence of minimizers of (2.13) (hence for the problem under consideration consisting of minimizing (2.6) under constraints (2.7)–(2.11)). □

Therefore, from Theorems 1 and 2 the existence of at least one minimizer of the

problem (2.6)–(2.11) has been obtained. However, to achieve uniqueness, suitable restrictions on the upper and lower bounds in (2.8) have to be imposed, which turn out to be related with the radiosensitivity parameters of the corresponding structures. In particular, there holds.

Theorem 3. *Let Ω, Ω_i and Ω_j be as in Theorems 1 and 2. Then for any choice of positive (respectively, nonnegative) constants w_k for $(k = 1, \ldots, n+m)$ (respectively a) and for any compatible choice of constants in (2.7)–(2.11), the variational problem (P) consisting of minimizing (2.6) under constraints (2.7)–(2.11) has a unique minimizer provided that*

$$\begin{aligned} C_2 &> \max_{1\le i\le n}\left\{-\frac{\alpha_i}{2\beta_i}+\sqrt{\frac{1}{2\beta_i}}\right\}, \\ C_3 &< \min_{n+1\le j\le n+m}\left\{-\frac{\alpha_j}{2\beta_j}+\sqrt{\frac{1}{2\beta_j}}\right\}, \end{aligned} \tag{2.14}$$

where (α_i, β_i) (respectively, (α_j, β_j)) are the radiosensitivity parameters of the regions Ω_i $(1 \le i \le n)$ (respectively, Ω_j $(n+1 \le j \le n+m)$).

Proof. Uniqueness for the problem under consideration consisting of minimizing (2.6) under constraints (2.7)–(2.11) is guaranteed whenever the functional in (2.6) happens to be strictly convex. To achieve this result, it suffices to show that, when finite, the integrand in (2.6) is strictly convex as a function of $\nabla D(\mathbf{x})$ and $D(\mathbf{x})$. In view of the particular form of (2.6), one just needs to show that

$$\begin{aligned} \frac{\partial^2}{\partial D^2} SF_i(D(\mathbf{x})) > 0, \quad (1 \le i \le n), \\ \frac{\partial^2}{\partial D^2}(1 - SF_j(D(\mathbf{x}))) > 0, \quad (n+1 \le j \le n+m). \end{aligned} \tag{2.15}$$

A quick computation reveals that

$$\frac{\partial^2}{\partial D^2} SF_i(D(\mathbf{x})) = e^{-(\alpha_i D(\mathbf{x}) + \beta_i D(\mathbf{x})^2)}((\alpha_i + 2\beta_i D(\mathbf{x}))^2 - 2\beta_i)$$

$$= \left(e^{-(\alpha_i D(\mathbf{x}) + \beta_i D(\mathbf{x})^2)}\right) \cdot 4\beta_i^2 \left(D(\mathbf{x})^2 + \frac{\alpha_i}{\beta_i} D(\mathbf{x}) + \frac{\alpha_i^2 - 2\beta_i}{4\beta_i^2}\right) \tag{2.16}$$

$$\equiv 4\beta_i^2 \left(e^{-(\alpha_i D(\mathbf{x}) + \beta_i D(\mathbf{x})^2)}\right) g_i(D(\mathbf{x})).$$

Therefore, in order to satisfy the first set of inequalities in equation (2.15), one needs to have $g_i(D(\mathbf{x})) > 0$ for $(1 \leq i \leq n)$, such that

$$D(\mathbf{x}) > \frac{1}{2}\left(-\frac{\alpha_i}{\beta_i} \pm \sqrt{\left(\frac{\alpha_i}{\beta_i}\right)^2 - \left(\frac{\alpha_i^2 - 2\beta_i}{\beta_i^2}\right)}\right)$$

$$\Downarrow$$

$$D(\mathbf{x}) > \frac{1}{2}\left(-\frac{\alpha_i}{\beta_i} \pm \sqrt{\frac{2}{\beta_i}}\right),$$

which certainly holds provided that

$$D(\mathbf{x}) > D_i^m = \left\{-\frac{\alpha_i}{2\beta_i} + \sqrt{\frac{1}{2\beta_i}}\right\}, \qquad \text{for} \quad (i = 1, \ldots, n). \tag{2.17}$$

From equation (2.16) it also follows that the second inequality in equation (2.15) is satisfied whenever one has

$$D(\mathbf{x}) < D_j^M = \left\{-\frac{\alpha_j}{2\beta_j} + \sqrt{\frac{1}{2\beta_j}}\right\}, \qquad \text{for} \quad (j = n+1, \ldots, n+m). \tag{2.18}$$

Putting together equations (2.17) and (2.18) the result follows. Therefore, the integrand in (2.6) is strictly convex when inequalities (2.14) are satisfied. This in turn implies the strict convexity of $J(D(\mathbf{x}))$ in (2.6), whereupon uniqueness follows. □

Remark 1. *The case $a = 0$ is admissible in Theorem 3, since the constraint $|\nabla D(\mathbf{x})| \leq C_1$ in (2.7) then provides enough compactness to pass to the limit in the corresponding functional.*

Remark 2. *Theorems 1 and 3 can be considered to yield existence and uniqueness in cases where constraints (2.9) are imposed on some specified open subsets of Ω. For instance, for $(k = 1, \ldots, n + m)$, let Ω_k be a family of open sets such that $\Omega_k \subset \Omega$ and the sets Ω_k are mutually disjoint. Let C_{m_k} and C_{M_k} be nonnegative constants such that $C_2 \leq C_{m_k} \leq C_{M_k} \leq C_3$ for $(k = 1, \ldots, n + m)$, and consider now the minimization problem (P') consisting in solving (P) under the following additional conditions*

$$C_{m_k} \leq D(\mathbf{x}) \leq C_{M_k} \quad in \quad \Omega_k, \quad k = 1, \ldots, n + m. \tag{2.19}$$

Then, under the assumption that constants C_1, C_2, C_3, C_{m_k} and C_{M_k} are compatible (that is, assuming that there exist differentiable functions $D(\mathbf{x})$ in Ω satisfying (2.7)–(2.8) and (2.19)) there exists a unique solution of the new minimization problem (P') provided that conditions (2.14) hold.

2.5 Planning under radiobiological uncertainty

This Section is devoted to discuss how to use the minimizers of the model previously formulated as a guide to select appropriate radiation dose distributions when only partial information about tumor radiosensitivity parameters is available. To begin with, the manner in which radiotherapy treatment plans are currently selected in clinical practice is briefly recalled.

2.5.1 How are clinical radiation dosimetries planned?

For any given patient diagnosed with a solid tumor, once the number and frequency of therapeutic sessions, volumetric and dose constraints on the PTV and/or OARs have been established, and the radiation dose to be delivered on the PTV has been prescribed, radiophysicists are required to prepare a treatment plan as close as possible to the previously defined requirements. To that end, they simulate a few

different tentative treatment plans on a treatment planning system (TPS), operating on the same linear particle accelerator (LINAC), which will deliver radiation to the patient.

For any such tentative plan, the TPS being used provides cumulative dose-volume histograms (DVH) for each structure involved, as well as isodose curves over the whole treatment domain. A DVH summarizes 3D dose distributions in a 2D graphical format and isodose curves are closed lines bounding regions where radiation dose is larger or equal than a given value (see Figure 1.8 in Chapter 1). After comparing the tentative plans thus prepared, that which is expected to be closer to the clinical prescription requirements is selected and delivered to the patient. Such comparison, and therefore the resulting choice of a treatment plan, is made mainly by inspection of the DVHs and isodose curves for each tentative plan considered. A key point to be noticed is that tentative plans usually differ from each other in small variations in the number, incidence angles or intensity of the radiation beams converging on a PTV. As a consequence, the corresponding DVHs and isodose curves for different tentative plans may look quite close to each other. This makes it difficult, even to a trained eye, to tell by mere inspection which one may yield better results. To illustrate this issue, Figure 2.1 shows actual DVHs corresponding to two tentative treatment plans for a same patient.

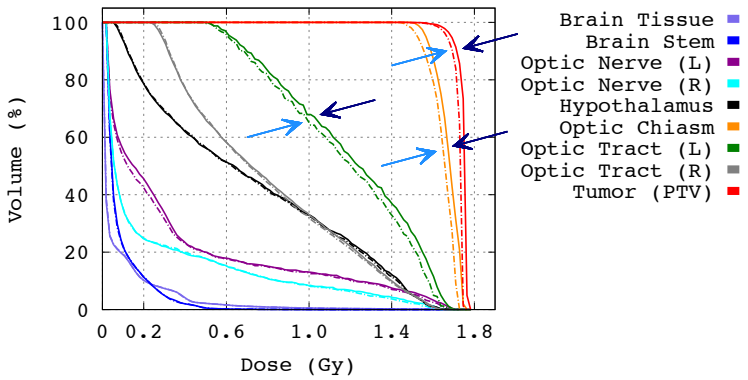

Figure 2.1. Superposed dose volume histograms (DVHs) of two tentative treatment plans (solid and dashed lines respectively) for a same patient. Same color arrows correspond to the same tentative plan. Notice that the plan pointed in light blue is better for the OARs indicated, but worse for the PTV in the case considered.

At this juncture, it is worth remarking on the values assigned to tentative plans in Figure 2.1 by figures of merit as Homogeneity Index (HI) and Conformity Index (CI) recalled at the introductory Section 2.2. Let us denote by A (respectively by B) the plan corresponding to solid (respectively dashed) lines in Figure 2.1. One readily checks that the maximum radiation dose received by the PTV is about $1.77Gy$ for plan A and $1.74Gy$ for plan B. Accordingly, the corresponding HI in (2.2) is equal to 0.98 for plan A and 0.96 for plan B. Moreover, the CI in (2.3) measured with respect to the reference isodose corresponding to 95% of the prescription radiation dose ($1.8Gy$) is equal to 0.91 for plan A and 0.84 for plan B respectively. Therefore, if attention is paid on effect achieved on the PTV, it appears that plan A is better than plan B, both in terms of radiation dose homogeneity and conformity on the tumor.

On the other hand, the maximum radiation dose received by the Hypothalamus, Optic Chiasm and left Optic Tract is equal to $1.68Gy$, $1.75Gy$ and $1.69Gy$ for plan A, and $1.65Gy$, $1.71Gy$ and $1.66Gy$ for plan B respectively. Moreover, 15% of the volume of such organs received at least a radiation dose of $1.35Gy$, $1.73Gy$ and $1.58Gy$ for plan A, and $1.33Gy$, $1.69Gy$ and $1.54Gy$ for plan B respectively. Therefore, out of the two cases considered, plan B is better than plan A with respect to OARs sparing.

In general, no direct reference to the radiobiological effects induced by each tentative treatment plan is made when the dosimetry to be applied is selected. However, information about radiosensitivity of the anatomical structures involved is implicitly used whenever a fractionated radiation dosimetry is prescribed, a standard therapeutic choice for most tumors. Indeed, as discussed at the introductory Section 2.2, a fractionated scheme depends among other factors on the characterization of the tumor considered as ER or LR tissue, which is known to be correlated with the respective (α/β) ratio.

2.5.2 Numerical simulations for minimizers. Comparison with a clinical case

To proceed further, in this Section the solutions of the theoretical model formulated in Section 2.3 are considered and the way in which efficient numerical approxima-

tions to them can be obtained is described.

Since solutions to the variational problem described in Section 2.3 cannot be represented in a closed form, to analyze their performance an efficient numerical approximation for them has to be provided, so that their corresponding DVHs and isodose curves could be readily obtained. Furthermore, to be able to compare with actual clinical cases, such numerical approximations need to be obtained under the same technical requirements satisfied by linear particle accelerators used to treat the patients selected. Therefore, to obtain suitable numerical solutions of model (2.6)-(2.11) a first step consists in data processing from the particular TPS used in each case.

Then, to illustrate these results let us discuss how the solution of the proposed variational problem compares with a clinical case of a patient diagnosed with a centrally-located brain tumor (Meningioma), where the PTV and several surrounding OARs have been delineated by clinicians and radiophysicists (see Figure 2.2 and 2.3). This is part of a larger study conducted over ten patients diagnosed with Meningioma, which are reported in Appendix B. Such type of tumors have been selected since, due to its internal location, they are surrounded by several OARs that have to be spared as much as possible. In this case, technical data were obtained from the TPS used, *iPlan RT Dose 4.1.1, BrainLAB AG Germany*. These data were retrieved in the form of DICOM (**D***igital* **I***maging and* **CO***mmunication in* **M***edicine*) files, a standard for handling and transmitting information in medical imaging [121]. These files have been interpreted through appropriate software (CERR, **C***omputational* **E***nvironment for* **R***adiotherapy* **R***esearch*, see [122] for further details).

Having done this, a three-dimensional Delaunay triangulation [123] of the whole domain of simulation (considered as healthy tissue, namely Brain tissue), the OARs involved and the PTV as defined by radiophysicists and clinicians in the same treatment planning system is created (see Figure 2.2). For that purpose an open-source C++ library (CGAL, *The* **C***omputational* **G***eometry* **A***lgorithms* **L***ibrary*, [124], [125]) has been used, which provides easy access to efficient and reliable computational geometric algorithms. It should be noted that in the corresponding numerical simulations the same points defined in the TPS and the same defini-

tion of each structure involved have been considered. In this way, minimizers are obtained in the same domain, and under the same conditions, that were assumed during the actual treatment planning process.

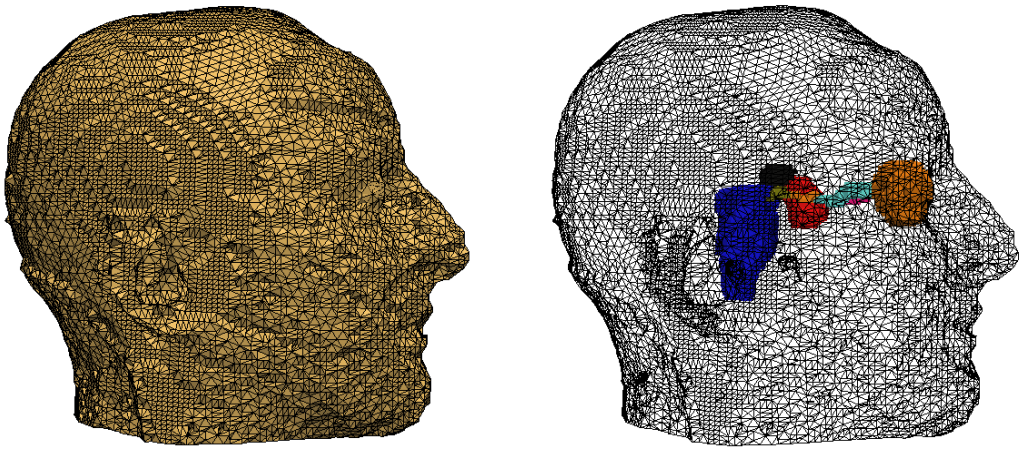

Figure 2.2. From left to right a three-dimensional domain reconstruction for the clinical case considered, the three-dimensional Delaunay triangulation created over the whole domain of simulation, and the representation of the PTV and OARs involved.

Figure 2.3. Three-dimensional reconstruction of the PTV and OARs involved. Notice that the PTV is represented in red.

To approximate the minimizers of the model given by (2.6)-(2.11), the finite element method has been used (see for instance [126], [127], [128] and [129]). That

is, the key idea is look for a minimizer $D(x)$ that is a continuous function in Ω and linear in every tetrahedron of the three-dimensional triangulation implemented (see Appendix A where a detailed description of the numerical discretization and computational implementation is provided). This last property implies that its value on every tetrahedron is defined by the value at its vertices, and the fact that $D(x)$ is continuous implies that the value at a vertex is unique, independently of how many tetrahedrons the vertex belongs to. In fact, denoting by $x_1, \ldots, x_{n_v}$ the vertices of the triangulation (the domain points defined in the TPS), and writing for simplicity, $d_1 = D(x_1), \ldots, d_{n_v} = D(x_{n_v})$, it is customary to express $D(x)$ as follows

$$D(x) = d_1\varphi_1(x) + \ldots + d_{n_v}\varphi_{n_v}(x), \quad x \in \tau, \tag{2.20}$$

where for $i = 1, \ldots, n_v$, $\varphi_i(x)$ denotes the nodal basis function (continuous in Ω and linear in every tetrahedron) associated to vertex x_i, which takes value one on the vertex x_i and zero on the remaining vertices (see for instance Section 1.4 in [127], Section 2.3 in [128] and Section 1.4 in [129]). Therefore, substituting (2.20) in the model (2.6)-(2.11), then the problem of finding the minimizer $D(x)$ reduces to a nonlinear constrained optimization problem (see Chapter 15 in [130]) in the variables $d_1, \ldots, d_{n_v}$ (see also Appendix A).

Solving this optimization problem requires the computation of the integrals in (2.6) and their partial derivatives with respect to $d_1, \ldots, d_{n_v}$. This can be done by summing the contributions to the integrals on every tetrahedron, contributions which can be computed in a standard and well-established way (see Section 1.8 in [127], and Section 2.2.3 and 2.3.3 in [128]). Observe also that since $D(x)$ is linear in every tetrahedron, constraints (2.8) and (2.9) reduce to $C_2 \leq d_l \leq C_3$ and $C_{m_k} \leq d_l \leq C_{M_k}$ for $l = 1, \ldots, n_v$ and $k = 1, \ldots, n + m$, respectively. Similarly, since $\nabla D(x)$ is constant on every tetrahedron, constraint (2.7) reduces to requiring that in each tetrahedron τ is expressed as follows

$$\left(\sum_{x_l \in \tau} d_l \nabla\varphi_l\right)^2 \leq C_1^2, \quad l = 1, \ldots, n_v.$$

Again, it is easy to compute $\nabla\varphi_i$ in every tetrahedron following standard pro-

cedures as in Section 2.2 in [128]. Concerning the volumetric constraints (2.10) and (2.11), it should be noted that their computation reduces to estimate the fraction of volume that receives a radiation dose higher than C_{V_k} of those tetrahedrons in the triangulation which belong to the region considered. In particular, to do that three general cases should be considered: *i)* the value of D in the four vertices is larger than C_{V_k} for $k = 1, \ldots, m+n$, *ii)* the value of D is larger than C_{V_k} in one vertex and smaller in the remaining three vertices and *iii)* the value of D is larger than C_{V_k} in two vertices and smaller in the other two vertices. For instance, let us consider only one tetrahedron, then for the case *i)* the portion of volume that receives a radiation dose higher than C_{V_k} is precisely the volume of this tetrahedron, while for *ii)* and *iii)* is the portion of its volume receiving a radiation dose higher than C_{V_k}. Therefore, volumetric constraints (2.10) and (2.11) can be computed from an iterative process over each tetrahedron in the region considered based in the cases described above (see Appendix A for further details).

To numerically solve the corresponding nonlinear constrained optimization problem, the C++/Fortran open-source optimization package (IPOPT, **I***nterior* **P***oint* **OPT***imizer*) has been used, which is a numerical library for large-scale nonlinear optimization [131]. Since this package does not include linear algebra routines, IPOPT has been coupled with PARDISO solver [132], [133], which is a high-performance and memory-efficient C++ library for solving large sparse symmetric and non-symmetric linear systems of equations on shared-memory and distributed-memory multiprocessors.

2.5.3 The case of equally important anatomical structures

Let us continue with the study started in Section 2.5.2, which corresponds to a patient treated with Intensity Modulated Radiation Therapy (IMRT) [15], [19]. The radiosensitivity parameters required for application of the LQ model for different OARs involved in this clinical case are given in Table 2.1 (see also [89]). Since appropriate data are not always available, non-reported radiosensitivity parameters have been selected as follows: *i)* Hypothalamus parameters have been taken equal to those of the Brain Stem, which are known and *ii)* Optic Tracts parameters are assumed equal to those of the Optic Nerve. While such assignment has been made

according to anatomical proximity, it should be stressed that the results that follow do not depend on the precise values taken for such parameters. Actually, the process to be described below will be shown to be robust with respect to changes in all radiosensitivity parameters involved.

Organ	$\alpha/\beta(Gy)$	$\alpha(Gy^{-1})$	$\beta(Gy^{-2})$
Brain Tissue	2.1	0.0499	0.0238
Brain Stem	2.1	0.0491	0.0234
Eye	1.2	0.0686	0.0572
Retina	3.0	0.0439	0.0146
Optic Nerve	3.0	0.0586	0.0195
Optic Chiasm	3.0	0.0251	0.0084

Table 2.1. Radiosensitivity parameters of the Linear Quadratic (LQ) model (2.4). Values of (α/β), α and β for OARs and HT (Brain tissue) are provided (see [89]).

Concerning the PTV, and in line with what has been said at the introductory Section 2.2, for Meningioma (a well-known late responding tissue [134], [135]) a value of the ratio $\alpha/\beta = 3.7Gy$ has been considered. This is consistent with the conventional radiotherapy fractionation scheme selected to treat this type of tumors, that is a total prescription dose of $50.4Gy$, delivered in 28 diary treatment sessions 5 days a week with weekend interruptions, which corresponds to a prescription dose (D_p) of $1.8Gy$ per session [48], [136]. Thus, the constants in constraints (2.8) and (2.9) were selected as $C_2 = C_{m_k} = 0.0Gy$ and $C_3 = C_{M_k} = 1.8Gy$ for $(k = 1, \ldots, n+m)$, in agreement with clinical requirements considered for this clinical case. On the other hand, the bound of the gradient in (2.7) ($C_1 = 3.0Gy/cm$) was estimated from the TPS data used to simulate the tentative plans prepared for that patient, and was accordingly imposed in numerical simulations. To do that, the maximum change of the radiation gradient in the applied radiation dose distribution simulated in the TPS for the whole treatment domain was computed, which has a dimension of about $17.37cm \times 23.31cm \times 20.83cm$. In this way, it is possible to ensure that the resulting simulation keeps to clinical requirements, and satisfies the same operational restrictions that the linear particle accelerator actu-

ally used in that radiotherapy treatment applied. However, it is not assumed that values of radiosensitivity parameters α or β are separately known for the tumor type considered. Therefore, the impact of various possible choices of such parameters (compatible with the restriction $\alpha/\beta = 3.7Gy$) on the radiobiological effects induced by the corresponding minimizer in the PTV, OARs and HT is explored. It should be noticed that in the simulations described in this Chapter the parameter a in (2.6) has been assumed equal to zero (see [110] where different results of a related, two-dimensional model considering $a > 0$ has been described).

To do this, the PTV is supposed homogeneous and assume that shrinkage of tumor region and sparing OARs are deemed equally important by clinicians, so that all weights w_1 and w_j $(2 \leq j \leq m+1)$ in (2.6) are taken equal to one. Consider first the case where no volumetric constraints (2.10) and (2.11) are imposed. Then, results describing the performance of the minimizer of (2.6)-(2.9) for different values of α when $\alpha/\beta = 3.7Gy$ are reported in Table 2.2 and Figure 2.4.

Parameter	$\alpha = 0.95Gy^{-1}$	$\alpha = 0.85Gy^{-1}$	$\alpha = 0.70Gy^{-1}$	$\alpha = 0.40Gy^{-1}$	$\alpha = 0.25Gy^{-1}$	$\alpha = 0.10Gy^{-1}$
SF_2	0.05	0.07	0.12	0.29	0.46	0.73
$D_{PTV100\%}$	$1.1403Gy$	$1.1584Gy$	$1.1946Gy$	$1.2127Gy$	$1.1765Gy$	$0.9955Gy$
PTV_{Dp}	52.57%	54.07%	55.79%	57.50%	55.75%	46.87%
$CI_{Dp95\%}$	0.67	0.68	0.71	0.73	0.70	0.62
Brain Tissue*	$1.1584Gy$	$1.1765Gy$	$1.2127Gy$	$1.2489Gy$	$1.1946Gy$	$1.0679Gy$
Optic Nerve (L)*	$0.6878Gy$	$0.6937Gy$	$0.7240Gy$	$0.7582Gy$	$0.7059Gy$	$0.5611Gy$
Optic Nerve (R)*	$0.3439Gy$	$0.3620Gy$	$0.3982Gy$	$0.4344Gy$	$0.3863Gy$	$0.3077Gy$
Hypothalamus*	$0.7421Gy$	$0.7602Gy$	$0.7964Gy$	$0.8326Gy$	$0.7783Gy$	$0.6154Gy$
Optic Chiasm*	$1.0860Gy$	$1.1122Gy$	$1.1503Gy$	$1.1765Gy$	$1.1484Gy$	$1.0317Gy$
Optic Tract (L)*	$0.7421Gy$	$0.7602Gy$	$0.7964Gy$	$0.8145Gy$	$0.7783Gy$	$0.6878Gy$
Optic Tract (R)*	$0.6697Gy$	$0.6878Gy$	$0.7582Gy$	$0.7964Gy$	$0.7240Gy$	$0.4887Gy$

Table 2.2. Dependence of induced radiobiological effects on the values of α for $\alpha/\beta = 3.7Gy$ when $w_1 = w_j = 1$ for $(2 \leq j \leq m+1)$. SF_2 represents the surviving cell fraction at $2.0Gy$ on the PTV given by the LQ model (2.4). ($D_{PTV100\%}$) Maximum radiation dose received at least by 100% of the PTV. (PTV_{Dp}) Percentage of the PTV receiving the prescribed radiation dose ($1.8Gy$). ($CI_{Dp95\%}$) Conformity Index (CI) for the isodose corresponding to 95% of the prescription radiation dose on the PTV. (*) Maximum radiation dose received by the OARs considered.

Concerning the results presented in Table 2.2, a few remarks are in order. To begin with, in all these simulations the HI is equal to 1. This is due to the fact that the maximum radiation received by the PTV is equal to the prescription radiation dose ($1.8Gy$). On the other hand, for the applied treatment plan the maximum

radiation on the PTV and the HI are equal to $1.77Gy$ and 0.98 respectively. In addition the maximum radiation dose received at least by 100% of the PTV in the applied treatment plan is $1.63Gy$, while for simulations described in Table 2.2 such value ranges from $0.99Gy$ to $1.21Gy$. Moreover, the CI for the isodose corresponding to 95% of the prescription radiation dose for values of α considered in Table 2.2 ranges from 0.62 to 0.73, which are smaller than that obtained with the applied treatment plan (CI equal to 0.95). Therefore, in spite that the radiation dose delivered at the PTV with the applied treatment is smaller than that provided in these simulations, the radiation coverage of the PTV for the applied treatment plan is higher than that achieved with the simulations in Table 2.2.

On the other hand, the maximum radiation dose delivered with the applied treatment plan to the Brain tissue, left Optic Nerve, right Optic Nerve, Hypothalamus, Optic Chiasm, left Optic Tract and right Optic Tract are equal to $1.75Gy$, $1.58Gy$, $1.51Gy$, $1.53Gy$, $1.73Gy$, $1.52Gy$ and $1.57Gy$ respectively (to be compared to values on Table 2.2). Therefore, simulations described in Table 2.2 deliver less radiation to OARs (see Figure 2.4) than the actually implemented treatment plan.

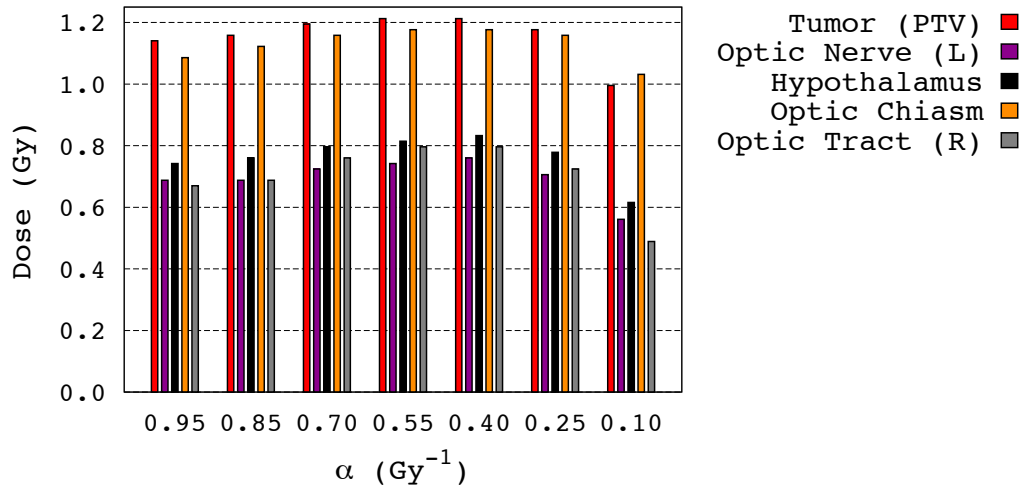

Figure 2.4. Maximum radiation dose received by some OARs considered in Table 2.2. Maximum radiation dose received at least by 100% of the PTV is also shown. Parameters considered as in Table 2.2.

Summing up, concerning tumor control, simulations in Table 2.2 do not perform

better than the treatment plan applied to the patient, although less radiation dose is delivered on the OARs with them than was achieved with the applied treatment plan. From this result follows that, to improve minimizers performance, an increase in the weight corresponding to the PTV dosimetry in (2.6) should be required. This strategy will be explored in detail in the following sections.

As a matter of fact, the results presented in Table 2.2 and Figure 2.4 suggest a strategy to select an optimal radiation dose distribution as a standard for comparison with tentative treatment plans. Namely, the first step may be to fix the maximum damage considered acceptable in OARs, and then select the value of α for which damage inflicted at the PTV is larger. Then, no matter what the precise value of α for that patient is, a radiation dose distribution that cannot be improved under the assumptions made on OARs damage is eventually obtained. In particular, this point will be addressed in detail in Section 2.5.6. Before doing it, though, some remarks on the meaning of the corresponding simulations are in order.

2.5.4 Uniqueness of minimizers revisited. (Pseudo)-minimizers

The simulations described in the previous Section 2.5.3 were done according to the process sketched in Section 2.5.2. When doing so, a basic theoretical background is provided in Theorems 1, 2 and 3 in Section 2.4. However, while the existence result therein obtained is quite general, the uniqueness conditions in (2.14) of Theorem 3 are not satisfied by all values of α considered in Table 2.2. In particular, for the ratio α/β considered, there is a threshold value α_c of α such that for values below that threshold inequalities in (2.14) are no longer compatible with the choices of clinical bounds C_2 and C_3 made so far. In particular, and since $\alpha_c = 0.54Gy^{-1}$, it is not possible to take $C_2 = 0.0Gy$ in (2.14) if α is small enough, as depicted in Figure 2.5.

Therefore, if an α value below that threshold is selected, it is not possible to guarantee any longer that the numerical algorithm will converge to a minimizer of the proposed variational problem. However, in all cases examined, the algorithm used does converge to a radiation dose function when it runs over the discretized

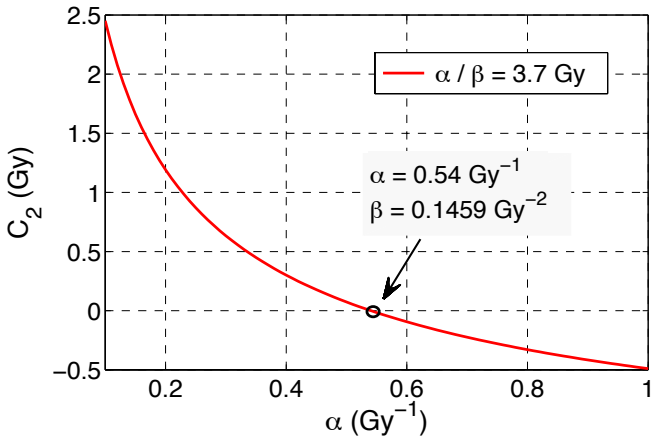

Figure 2.5. Uniqueness threshold for minimizers (see Theorem 3 in Section 2.4). For the ratio $\alpha/\beta = 3.7Gy$, the value of the lower bound C_2 in (2.14) is represented in terms of α. Notice that $C_2 = 0.0Gy$ cannot be imposed for values of α below $\alpha_c = 0.54Gy^{-1}$, which is indicated by an arrow.

mesh used by the TPS where the actual dosimetry was implemented. Thus, a function $D(x)$ is numerically computed in that case that need not be an approximation to a minimizer, but still will be shown to provide a better treatment choice when compared with the actual dosimetry delivered. In particular, such $D(x)$ will be referred as a pseudo-minimizer of the variational problem under consideration. In the sequel, all numerical approximations will correspond either to actual minimizers (when uniqueness requirements are met) or to pseudo-minimizers when they fail to do so. For the ease of notation, the term minimizer will be often used in either case.

2.5.5 Increasing the weight on PTV dosimetry

To explore how the proposed variational model can be fine-tuned to suit different clinical priorities, let us next consider the case where weights w_j $(2 \leq j \leq m+1)$ in (2.6) are kept equal to one over the OARs involved, whereas w_1, the corresponding coefficient over the PTV dosimetry, is allowed to increase. More precisely, to see how sensitive the results are to different choices of w_1, let us assume as before that $\alpha/\beta = 3.7Gy$, select this time the value $\alpha = 0.10Gy^{-1}$, and compute the minimizer of (2.6)-(2.9) for increasing values of w_1. Table 2.3 contains the values obtained

in such cases, and Figure 2.6 shows how radiobiological effects on some OARs and the PTV described in Table 2.3 change as w_1 increases.

Parameter	$w_1 = 1.0$ $w_j = 1.0$	$w_1 = 2.5$ $w_j = 1.0$	$w_1 = 5.0$ $w_j = 1.0$	$w_1 = 7.5$ $w_j = 1.0$	$w_1 = 10$ $w_j = 1.0$
$D_{PTV100\%}$	$0.9955Gy$	$1.2670Gy$	$1.4480Gy$	$1.5104Gy$	$1.5565Gy$
PTV_{Dp}	46.87%	61.68%	73.96%	80.30%	83.46%
$CI_{Dp95\%}$	0.62	0.77	0.88	0.92	0.94
Brain Tissue*	$1.0679Gy$	$1.3213Gy$	$1.4661Gy$	$1.5267Gy$	$1.5746Gy$
Optic Nerve (L)*	$0.5611Gy$	$0.8145Gy$	$1.0136Gy$	$1.0317Gy$	$1.0859Gy$
Optic Nerve (R)*	$0.3077Gy$	$0.5068Gy$	$0.5792Gy$	$0.7240Gy$	$0.7783Gy$
Hypothalamus*	$0.6154Gy$	$0.8688Gy$	$1.0498Gy$	$1.1222Gy$	$1.1583Gy$
Optic Chiasm*	$1.0317Gy$	$1.2127Gy$	$1.2851Gy$	$1.3575Gy$	$1.3936Gy$
Optic Tract (L)*	$0.6878Gy$	$0.9231Gy$	$1.0498Gy$	$1.1946Gy$	$1.2115Gy$
Optic Tract (R)*	$0.4887Gy$	$0.8145Gy$	$0.9593Gy$	$1.0136Gy$	$1.1221Gy$

Table 2.3. The effect of increasing radiation weight over PTV when weights over OARs are kept constant and equal to one, where $\alpha = 0.10Gy^{-1}$ and $\alpha/\beta = 3.7Gy$. ($D_{PTV100\%}$) Maximum radiation dose received at least by 100% of the PTV. (PTV_{Dp}) Percentage of the PTV receiving the prescribed radiation dose ($1.8Gy$). ($CI_{Dp95\%}$) Conformity Index (CI) for the isodose corresponding to 95% of the prescription radiation dose on the PTV. (*) Maximum radiation dose received by the OARs considered.

A quick glance at Table 2.3 reveals that radiation coverage on the PTV increases with w_1 and the same happens with the maximum radiation dose received at least by 100% of the PTV. Moreover, the radiation delivered over all OARs considered is higher than in the case where $w_1 = 1$, although still less than that corresponding to the applied treatment plan (see Section 2.5.3).

Let us now select the PTV weight equal to its largest value in Table 2.3 ($w_1 = 10$) and explore how the values reported in the previous Tables 2.2 and 2.3 change with α. As it turns out, the radiation coverage now obtained over the PTV is similar to that provided in the applied treatment plan, but less radiation doses on the OARs are delivered than in the applied treatment (see Section 2.5.3). The corresponding results are represented in the Table 2.4.

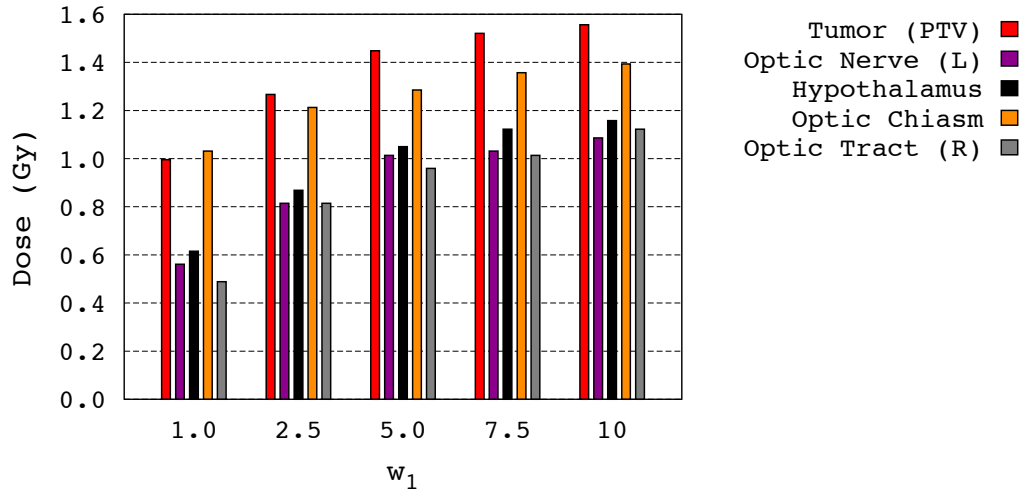

Figure 2.6. Dependence of radiobiological effects for some OARs and the PTV in the cases considered in Table 2.3. Maximum radiation dose received by some OARs is represented. Maximum radiation dose received at least by 100% of the PTV is also shown.

Parameter	$\alpha = 0.95Gy^{-1}$	$\alpha = 0.85Gy^{-1}$	$\alpha = 0.70Gy^{-1}$	$\alpha = 0.40Gy^{-1}$	$\alpha = 0.25Gy^{-1}$	$\alpha = 0.10Gy^{-1}$
$D_{PTV100\%}$	$1.5928Gy$	$1.6108Gy$	$1.6389Gy$	$1.6691Gy$	$1.6443Gy$	$1.5565Gy$
PTV_{Dp}	84.66%	86.93%	89.86%	92.73%	91.83%	83.46%
$CI_{Dp95\%}$	0.96	0.97	0.98	0.99	0.98	0.94
Brain Tissue*	$1.6109Gy$	$1.6289Gy$	$1.6470Gy$	$1.6731Gy$	$1.6525Gy$	$1.5746Gy$
Optic Nerve (L)*	$1.1041Gy$	$1.1583Gy$	$1.1765Gy$	$1.2127Gy$	$1.1946Gy$	$1.0859Gy$
Optic Nerve (R)*	$0.7844Gy$	$0.7964Gy$	$0.8145Gy$	$0.8507Gy$	$0.8507Gy$	$0.7783Gy$
Hypothalamus*	$1.1946Gy$	$1.2126Gy$	$1.2488Gy$	$1.2670Gy$	$1.2489Gy$	$1.1583Gy$
Optic Chiasm*	$1.4118Gy$	$1.4167Gy$	$1.4298Gy$	$1.4480Gy$	$1.4313Gy$	$1.3936Gy$
Optic Tract (L)*	$1.2127Gy$	$1.2307Gy$	$1.2569Gy$	$1.3032Gy$	$1.2952Gy$	$1.2115Gy$
Optic Tract (R)*	$1.1765Gy$	$1.2015Gy$	$1.2341Gy$	$1.2851Gy$	$1.2670Gy$	$1.1221Gy$

Table 2.4. The impact of changing α for a comparatively large value of $w_1 = 10$ when w_j $(2 \leq j \leq m+1)$ are kept equal to one, and $\alpha/\beta = 3.7Gy$. $(D_{PTV100\%})$ Maximum radiation dose received at least by 100% of the PTV. (PTV_{Dp}) Percentage of the PTV receiving the prescribed radiation dose $(1.8Gy)$. $(CI_{Dp95\%})$ Conformity Index (CI) for the isodose corresponding to 95% of the prescription radiation dose on the PTV. (*) Maximum radiation dose received by the OARs considered.

An inspection of Table 2.4 reveals that if $\alpha = 0.40Gy^{-1}$ is now selected, the corresponding pseudo-minimizer provides the higher effect on the PTV, and delivers

less radiation doses on the OARs involved than the applied treatment. A comparison of the results obtained with this choice ($\alpha = 0.40Gy^{-1}$, $w_1 = 10$, $w_j = 1$ for $2 \leq j \leq m+1$) and those corresponding to the actually applied treatment plan can be seen in Figure 2.7.

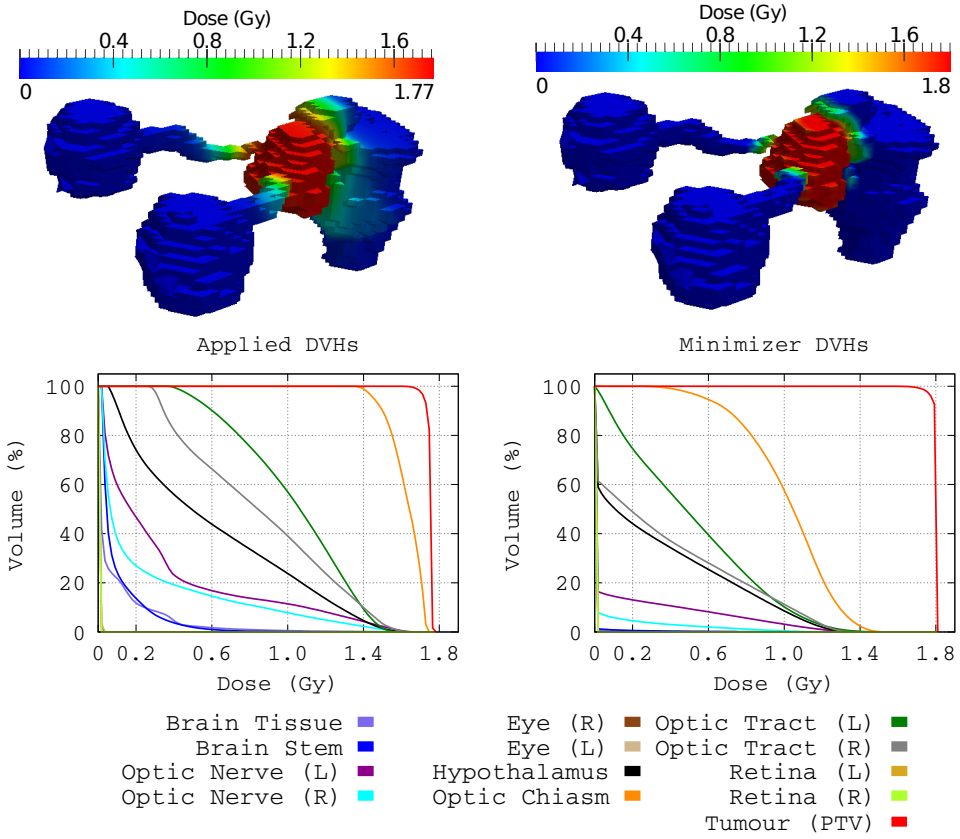

Figure 2.7. Top: A comparison of the applied radiation dose distribution (left) and the minimizer dose distribution (right) obtained from model where $w_1 = 10$, w_j $(2 \leq j \leq m+1)$ are kept equal to one and $\alpha = 0.40Gy^{-1}$. From left to right the radiation dose distributions (3D) over the OARs, HT and the PTV. Bottom: Dose volume histograms (DVHs) of the applied (left) and minimizer (right) dose distributions for each OAR, HT and the PTV.

At this juncture it should be remarked that the better performance of the minimizer considered when compared to the actual treatment delivered is not restricted to the particular choice of α made. Actually, a similar pattern is displayed when other values of α are selected instead (see Table 2.4). Details corresponding to some of those alternative choices can be found in the Appendix B.

2.5.6 Volumetric constraints and alternative treatment planning strategies

In general, the dosimetry obtained in the previous case when $w_1 = 10$, $w_j = 1$ for $2 \leq j \leq m+1$ and $\alpha = 0.40Gy^{-1}$ might be too harsh on OARs compared to what was obtained with the simulations in Section 2.5.3 for $w_1 = w_j = 1$ (see Tables 2.2 and 2.4). This is due to the fact that, in the case just considered, obtaining large radiation coverage over the PTV was assigned the highest priority, and side effects were not given a similar importance. In many clinical settings, however, clinicians insist on enforcing strong sparing effects over OARs. This can be done for instance by considering multiple pointwise constraints as in (2.9). A detailed study on the performance of a related, two-dimensional model considering such constraints has been described in a previous work (see [110] for further details).

An alternative which is very appealing to clinicians consists in imposing volumetric constraints on the dose delivered to the PTV and/or OARs as those considered in (2.10), (2.11) and discussed in Theorem 2. Remarkably, considerable volumetric constraints are obtained as a token from the pointwise constraints on the radiation dose imposed in Theorem 1. For instance, in the numerical simulation discussed above for the case $w_1 = 10$, $w_j = 1$ $(2 \leq j \leq m+1)$ and $\alpha = 0.40Gy^{-1}$ (see Figure 2.7 and Table 2.4), where no volumetric constraints were a priori imposed, no more than 15% of the Hypothalamus, right Optic Tract and Optic Chiasm receive a radiation dose higher than $0.83Gy$, $0.92Gy$ and $1.25Gy$ respectively (see Figure 2.7). However, when more stringent volumetric constraints are needed, one has to explicitly include such requirements in the statement of the variational problem under consideration, and then make use of Theorem 2. As an example, below is reported a result for the case where parameter values C_1, C_2, C_3, (α/β), α, w_1 and w_j $(2 \leq j \leq m+1)$ are as in the case under consideration, and the following volumetric constraints (2.10), (2.11) are considered: no more than 15% of the Hypothalamus and right Optic Tract should receive a radiation dose higher than $0.70Gy$, and no more than 15% of the Optic Chiasm should receive a radiation dose higher than $0.80Gy$.

DVHs and 2D slices of isodose curves of this numerical simulation when volumetric constraints are imposed and a comparison with the previous one without

volumetric constraints, are displayed in Figure 2.8 when $w_1 = 10$, $w_j = 1$ for $2 \leq j \leq m+1$ and $\alpha = 0.40Gy^{-1}$.

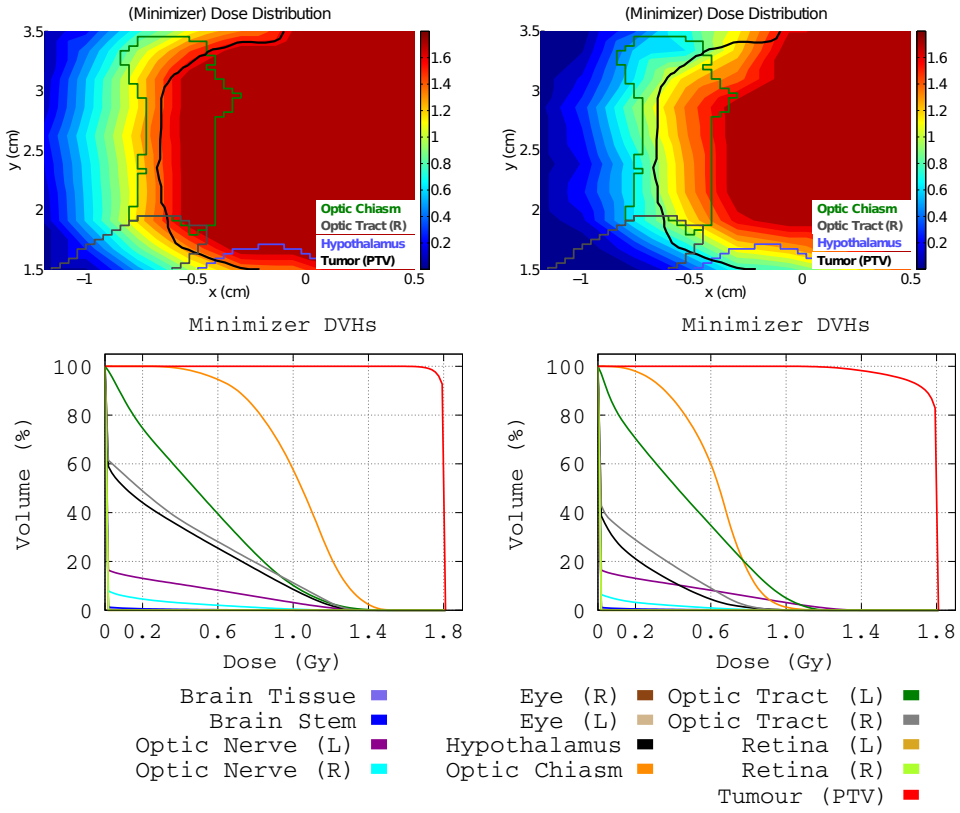

Figure 2.8. Isodose curves in a 2D slice and dose volume histograms (DVHs) of the minimizer radiation dose distributions discussed in the previous Section 2.5.5 without volumetric constraints (left) and that simulated in this Section 2.5.6 with volumetric constraints (right) for each OAR, HT and the PTV. In both cases $w_1 = 10$, $w_j = 1$ when $2 \leq j \leq m+1$ and $\alpha = 0.40Gy^{-1}$.

A quick glance at Figure 2.8 reveals that the minimizer obtained under volumetric constraints provides a lower effect on PTV than that obtained when such restrictions are ignored. For instance, the maximum radiation dose received at least by 100% of the PTV and the percentage of the PTV receiving the prescribed radiation dose ($1.8Gy$) are respectively equal to $1.6691Gy$ and 92.73% for the simulation without volumetric constraints, and equal to $1.1946Gy$ and 82.92% for that with volumetric constraints. However, the former has lower side effects on OARs than the second minimizer, as expected from the volumetric constraints required.

Since it is not possible to obtain arbitrarily large tumor coverage and arbitrarily small OARs irradiation at the same time, the following strategy for dosimetry selection is suggested by the results shown in this Section 2.5.4. For simplicity, let us restrict in the following to the case where PTV is considered homogenous, as is the situation in current clinical practice:

1) Once a value of the ratio (α/β) had been selected in agreement with the diagnosed tumor type and fractionation scheme chosen, select arbitrarily one value of α, set all weights w_1 and w_j $(2 \leq j \leq m+1)$ in (2.6) equal to one as a standard to start with, and impose pointwise constraints in (2.7)-(2.9) according to TPS resolution capabilities (in the case of (2.7)) and following clinical prescriptions (in the case of (2.8) and/or (2.9)). Then select volumetric constraints (2.10) and/or (2.11) deemed suitable on OARs, HT and the PTV involved. These volumetric constraints (2.11) will impose at once a limit on the side effects retained admissible.

Notice that stringent pointwise and volumetric restrictions need not always be imposed in all OARs considered. On the other hand, in some clinical settings different levels of priority for OARs sparing could be considered. In that case different values for weights w_j $(2 \leq j \leq m+1)$ in (2.6) should be selected. As a matter of fact, the larger the number of OARs subject to such constraints, and the stronger the requirements thereby imposed, the lower the maximum effect on PTV turns out to be.

2) If the minimizer obtained after solving the variational problem under the conditions listed in *Step 1* provides enough tumor coverage, let us proceed to *Step 3* below. If however further impact on PTV is needed, allow w_1 to increase while keeping all other weights w_j $(2 \leq j \leq m+1)$ as before. As w_1 grows, it may happen that a value for that parameter is reached so that tumor coverage saturates, in that no further impact is achieved when is w_1 further increased. Then, let us keep the value of w_1 for which saturation is first observed, and continue to *Step 3*.

Alternatively, it may occur that the desired tumor coverage cannot be achieved by increasing w_1 unless the choice of pointwise and/or volumetric constraints imposed in *Step 1* is weakened. If this is the case, a compromise has to be achieved between both requirements. For instance, a large enough value of w_1 may be

considered, which is still compatible with the restrictions considered in *Step 1*, or reduce the constraints imposed on some of the OARs previously considered.

3) After *Step 1* and *Step 2* have been fulfilled, let us next provide simulations for the minimizers corresponding to various values of α, keeping the ratio (α/β) and the remaining model parameters constant as in *Step 1*. Out of them, which yields better coverage of the PTV and less side effects on the OARs under the pointwise and volumetric constraints retained must be eventually selected. Then, this radiation dose distribution will be defined as optimal in that clinical case, and propose it as a standard with respect to which tentative treatment plans should be compared.

The previous argument naturally leads to an important question. Namely, one may wonder how can we tell which of two given tentative plans simulated on a TPS is closer to a given dosimetry, as that resulting from *Step 1* to *Step 3* above. A way in which this can be done is by means of figures of merit as the indexes HI or CI recalled before. More precisely, one could state that a tentative plan is close to the optimal dosimetry suggested if the difference between the respective indexes HI and/or CI (or any other figure of merit reported) is small enough. The issue of deciding which figure of merit is more adequate to account for actual clinical requirements is far from being settled, and is currently being the subject of active research. In particular, in Chapter 4 this issue is addressed in detail where a decision-aid tool is proposed.

2.6 Discussion

In this Chapter the possibilities offered by mathematical modeling and computer simulations to assist radiophysicists and clinicians to improve current decision-making processes to treat solid tumors by means of radiotherapy have been explored. To this end, more attention has been paid on a key aspect, namely how to obtain a theoretical radiation dose distribution that provides a standard against which tentative plans should be compared.

To address such issue, the case when radiosensitivity parameters for tumor and neighboring organs at risk are known have been first considered, and a theoretical

definition of a radiation dose distribution based on current radiobiological criteria has been proposed. Such dose distribution is given as the solution of a suitable variational problem recalled in Section 2.3. It should be noted that such problem includes among its hypotheses common clinical requirements (as bounds on maximum and minimum dosage over the anatomical structures considered) on one hand, as well as technical constraints on the clinical linear particle accelerators (for instance, their operative resolution) on the other. Therefore, the dosimetry obtained from the study of that problem could be computed on treatment planning systems (TPS) for linear particle accelerators currently in use. Moreover, the choice proposed is suitable for personalized patient treatment, since it allows for computing different dosimetries for different therapeutic priorities.

Then, this theoretical result has been used to propose a possible strategy to assist in the choice of clinical dosimetries when only partial information on radiosensitivity parameters for the PTV is available, as is often the case in current clinical practice. Specifically, the case of a homogenous tumor (i.e. consisting of a single tumor cell population), for which only the ratio (α/β) is known, has been discussed. In many cases a value for such ratio is suggested from clinical experience resulting from the use of different fractionation schemes to treat a particular type of tumor. Conversely, when such ratio has been obtained experimentally (usually *in vitro*) the corresponding result can be used to select a type of fractionation scheme suitable for the tumor under consideration. In that case, a strategy consisting in *Step 1* to *Step 3* has been implemented in the previous Section 2.5.6 to eventually obtain an optimal radiation dose distribution with which tentative plans simulated over the corresponding TPS should be compared.

The way in which this comparison should be done deserves a detailed study, which goes beyond the scope of this Chapter. Actually, TPS are not equipped with sophisticated decision-aid tools to quantify the radiobiological impact of modifications, whether large or small, on the tentative plans considered. To this it should be added that current operational limitations establish a tough limit on the number of tentative treatment plans that can be prepared for a single patient. However, selection procedures can be implemented at once without introducing new tools or principles in the field. Indeed, one may pick up any of various quantitative esti-

mators that are used in radiotherapy for that purpose. For instance, the standard Homogeneity Index (HI), defined as the ratio between the maximum and minimum radiation dose over a given anatomical structure could be considered, and decide that, out of the number of tentative plans simulated, the best one is that for which the value of the HI over the PTV is closer to the corresponding value for the minimizer obtained after *Step 1* to *Step 3* before. The novelty here is that minimizers of the proposed optimization problem suggest a reference value for HI (that of the radiation dose distribution arrived at by means of this approach) to compare with. Even in so simple a form, easy to translate into a user-friendly software, such a procedure could be helpful in current decision-making processes.

To illustrate this method, the proposed radiation dose distributions have been compared with that actually delivered in ten clinical cases; see Section 2.5 for a thorough study of one of these cases, and the Appendix B for a description of results for the remaining nine patients considered. In all cases such studies were performed keeping to the same specifications of the linear particle accelerator which was actually used, as well as to the clinical requirements (say, on maximum and minimum radiation dose per session) specified by clinicians. Moreover, it is apparent from the previous discussion that both the proposed mathematical model in Section 2.3, and the proposed strategy for dosimetry selection presented in Section 2.5.6 are robust with respect to changes in all model parameters involved.

To conclude, some remarks on the assumptions made, as well as on future research directions are commented as follows. In Section 2.3 the PTV has been assumed homogeneous since that was the assumption made by clinicians in the treatments provided. However, this approach could be extended to deal with heterogeneous tumors as soon as sufficient information on *in vivo* tumor heterogeneity is available (see [110] for a previous work related to such issue). As a matter of fact, in the absence of such information, which is still out of reach in current clinical practice, standard radiotherapy protocols all over the world continue to consider tumors as homogeneous in structure, as in the cases herein considered. This model can be easily extended for the case where different PTVs are defined for a same patient. Moreover, radiation dose distributions can be simulated for any type of

tumor regardless of its location insofar information on radiosensitivity parameters of nearby critical structures are known.

A second and far reaching question concerns the way in which tentative plans could be prepared to better fit a theoretical radiation dose distribution. Clinical technology seems to have reached a sufficient level of sophistication to permit a major breakthrough in this respect. However, a key limitation stems from the fact that only limited information on radiosensitivity parameters for tumors is currently available [53], and without a comprehensive library of such parameters no theoretical link can be directly established between experimental dosimetries and radiobiological effects. While this issue requires of sustained experimental exploration, mathematical methods can nevertheless help in making appropriate decisions under considerable parametric uncertainty. The approach presented in Section 2.3 could provide a step in this direction. Needless to say, new decision strategies should be developed to further enhance the efficiency of optimization protocols as those described in this Chapter.

Chapter 3

Estimating dose painting effects in radiotherapy: a mathematical model

"... A great discovery solves a great problem, but there is a grain of discovery in the solution of any problem. Your problem may be modest, but if it challenges your curiosity and brings into play your inventive faculties, and if you solve it by your own means, you may experience the tension and enjoy the triumph of discovery ..."

George Pólya (1887-1985)

3.1 Abstract

Tumor heterogeneity is widely considered to be a determinant factor in tumor progression and in particular in its recurrence after therapy. Unfortunately, current medical techniques are unable to deduce clinically relevant information about tumor heterogeneity by means of non-invasive methods. As a consequence, when radiotherapy is used as a treatment of choice, radiation dosimetries are prescribed under the assumption that the malignancy targeted is of a homogeneous nature.

The purpose of this Chapter is precisely that of exploring the effects of different radiation dose distributions on heterogeneous tumors by means of an individual cell-based model. To that end, a case is considered where two tumor cell phenotypes are present, which have been assumed to strongly differ in their respective

cell cycle duration and radiosensitivity properties. In particular, as a result of such differences, the spatial distribution of the corresponding phenotypes, whence the resulting tumor heterogeneity can be predicted as growth proceeds. That is, if the model of tumor growth starts from a situation where a majority of ordinary cancer cells (CCs) and a minority of cancer stem cells (CSCs) are initially present and randomly distributed, then CSCs become concentrated at an inner region as tumor grows, as long as CSC cycle is significantly longer than that of CCs and CSCs remain a small fraction of the total tumor population. As a consequence, and assuming also that CSCs are more resistant to radiation than CCs, heterogeneous dosimetries can be selected to enhance tumor control by boosting radiation in the region occupied by the more radioresistant tumor cell phenotype. It is also shown that, when compared with homogeneous dose distributions as those being currently delivered in clinical practice, such heterogeneous radiation dosimetries fare always better than their homogeneous counterparts.

3.2 Introduction

Technical and methodological advances have allowed radiation oncologists to achieve local tumor control in a considerable number of patients. However, locoregional recurrence (LRR) remains a problem in many clinical settings. For example, a recent study in patients with Stage III lung cancer found a 5-year LRR rate of 31% [137]. In Glioblastoma Multiforme (GBM), the most common and aggressive malignant primary brain tumor, LRR approaches 90% [138]. In such critical cases, radiotherapy usually results in an initial shrinkage of malignancies, followed by a subsequent growth recovery that cannot be checked even by resorting to larger radiation doses.

The onset of radioresistance, and its resulting poor prognosis, is strongly correlated with the development of significant intratumoral heterogeneity. For that reason, there is growing interest in the clinical significance of tumor heterogeneity. In different works have been recently demonstrated extensive genetic variations in tumor cells due to intratumoral evolution [139], [140]. Moreover, tissue-level heterogeneity due to variations in vascular density and blood flow has been long since evident in clinical medical imaging (see for instance Figure 3.1). In recent

years, accumulating evidence suggests that tumor heterogeneity is a key factor in the development of therapeutic resistance and therefore in radiation therapy outcomes [21], [22], [23]. As a consequence, increasing attention is being paid to "dose painting" (or "dose sculpting"), a technique which consists in prescribing different radiation dosimetries to different regions within a given tumor, so that irradiation be boosted in more radioresistant (for instance, hypoxic, quiescent, etc.) regions [24], [25].

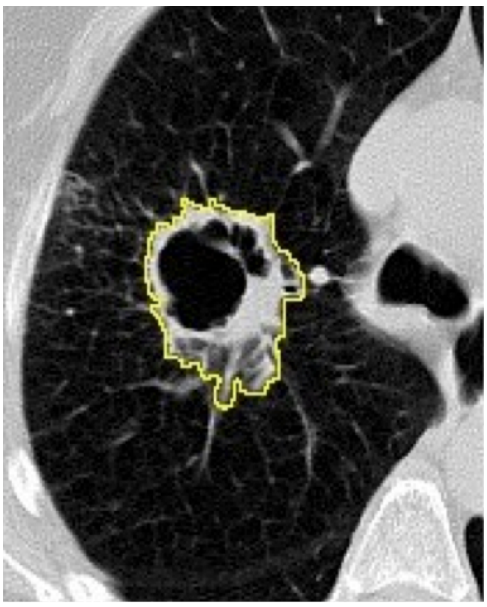

Figure 3.1. CT scan of lung showing a cancer in the right upper lobe (circled) with regions of necrotic (dead) and viable tissue (Courtesy of Dr. Robert Gatenby).

The work reported in this Chapter intends to yield some insight into these issues. More precisely, in the sequel a mathematical model for heterogeneous tumor growth is formulated, and the effects of various radiation dose distributions on it are investigated by means of computer simulations. Specifically, a situation where two tumor cell phenotypes, cancer cell (CC) and cancer stem cell (CSC), are present at an early stage, when the tumor consists of about 10^5 cells in total has been considered. Concerning CCs and CSCs, the following assumptions are made *i)* CSCs represent only a small percentage of the total number of cells at that stage (say, about 15%), *ii)* CSCs have a significantly longer cell cycle duration than CCs

and can replicate indefinitely, while CCs can perform only a limited number of cell divisions, and *iii)* CCs and CSCs show quite different resistance to radiation, CSCs being more radioresistant than CCs. These biological and radiobiological features have been reported in the literature, specifically for Glioblastoma Multiforme (GBM), where there is mounting evidence of CSCs presence in GBM tumors (cf. for instance [23], [141], [142], [143]). Growth of the heterogeneous tumor thus resulting is simulated by means of an agent-based model in which each cell is individually represented [144], [145]. Tumor growth is kept track of until a size of approximately 10^6 cells is attained, which roughly corresponds to a spheroid of about 1 cubic millimeter in size, a typical volume in multi-cellular spheroids (MCS) *in vitro* growth. At that stage, different (homogeneous and heterogeneous) radiation dose distributions are simulated using the Linear Quadratic (LQ) model [53], [54], [55], [56], and their effects compared.

An interesting consequence of *i)* and *ii)* above is then shown to be that, as tumor grows, most of the CSCs concentrate themselves within the tumor core, irrespective of their initial distribution at an earlier stage. This fact, which will be described to be inversely correlated with cell migration rates, when migration is not inhibited by cell-cell adhesion (which is the case, for instance, after cells undergo an epithelial-mesenchymal transition (EMT) [146]), is then used together with *iii)* to simulate the effects of different radiation dosimetries to achieve tumor control, or in the case where this cannot be obtained, to compare tumor heterogeneity (seen as an indicator of malignancy in terms of the proportion of CSCs) before and after treatment has been delivered. In this context, it will be shown that for a given amount of radiation, heterogeneous dose distributions, where different radiation doses are delivered at different regions of the tumor according to the presence of more radioresistant cells there, invariably fare better than homogeneous ones when sufficient information about tumor spatial heterogeneity is available. In the case herein reported, such information will be shown to follow from assumptions *i)* and *ii)* above. It should be noticed that hypotheses *i)*, *ii)* and *iii)* are amenable to experimental validation, at least *in vitro*.

This work can be considered as a preliminary step towards analyzing preclinical models where larger tumors (of the order of cubic centimeters) should be dealt

with, several tumor cell phenotypes would simultaneously be present (possibly as a consequence of mutations) as tumor expands, and vascular networks, immune response, and hypoxic and necrotic effects are also taken into account. While the case herein considered is still far from that situation, the simplicity of the setting selected allows to stress the consequences derived from the minimal number of biological and radiobiological assumptions made on the tumor cell phenotypes involved. This last is particularly relevant in view of the scarcity of *in vivo* biological parameter measures available. Scaling results up to larger tumor sizes, as well as increasing phenotypic and anatomical complexity appear as feasible within the same approach, but only after key biological data retrievable by non-invasive probing had been identified, and their impact on tumor growth elucidated, an objective toward this work intends to contribute.

It should be noted that considerable attention is being currently paid to mathematical modeling as a tool towards designing patient-tailored and adaptive therapies; see for instance [146], [147], [148], [149], [150], [151], [152], [153], [154] and [155]. In particular, radiotherapy modeling and simulations have been addressed in [54], [56], [107], [108], [112], [156], [157], [158] and [159], as well as in [111], [116] and [117] where GBM cases are considered. Mathematical models and computer simulations on the impact of the presence of CSCs in tumor therapies have been discussed in [107], [160] and more recently in [111], where focus is made in a GBM case. It is worth to be stressed, however that in the cases previously mentioned, the total number of cells simulated (and thus the resulting structural complexity) remained way below that of the computer simulations arrived at in this work.

In summary, in Sections 3.3 and 3.4 the tumor growth mechanism considered and the mathematical model thereof are described respectively. In Section 3.5 the effects of different homogeneous and heterogeneous radiation dose distributions on tumors resulting from different model parameter sets are investigated. Finally, a discussion on the results obtained and their clinical implications make then the content of the concluding Section 3.6.

3.3 Tumor cell phenotypes assumptions

In this Section the assumptions made on the tumor cell phenotypes considered are described in details. To begin with, for definiteness model parameter values corresponding to Glioblastoma Multiforme (GBM) cell lines have been used [90], [161], [162]. More precisely, a heterogeneous tumor where two different phenotypes coexist at an early stage is considered, where it is assumed a preponderant (approximately 85% of the total tumor volume) proportion of a tumor cell phenotype denoted as CC (cancer cell) coexisting with a second tumor cell phenotype CSC (cancer stem cell), randomly distributed, that roughly represents 15% of the total population at that stage. Both phenotypes CC and CSC are supposed to possess markedly different biological and radiobiological properties.

3.3.1 Cell cycle duration

The duration of cell cycle for CCs is significantly shorter than that of CSCs. In particular, CCs are assumed to divide every 26 hours. Then, for tumor cell phenotype CSC three cases have been considered, corresponding respectively to a CSC cycle duration of 96 hours (four days), 72 hours (three days) and 48 hours (two days). Moreover, CCs are assumed to divide a maximum of 15 times, while CSCs are able to replicate indefinitely.

Concerning the cell cycle duration property, it is currently assumed that CSCs proliferate at a slower pace than ordinary cancer cells (see for instance [142], [163], [164], [165], [166], [167], [168], [169], [170] and [171]). Actually, as observed in the references previously quoted, slow-cycling is to be expected from CSCs since such cells belong to tumor phenotypes that are highly resistant to current therapies (radiotherapy, chemotherapy or combined) and these are targeted at killing cycling cells. On the other hand, recent *in vivo* experiments in a mouse model of Glioblastoma to identify and isolate CSCs through genetically engineered mice demonstrate the presence of a small pool of slow-cycling and highly tumorigenic cells that retain long-term self-renewal ability [170], [172]. It should be remarked that cell cycle durations of $24h$-$26h$ for GBM have been reported [90], [111], [173], although considerably different cell cycle durations, which in particular include the

values herein considered for CSCs, have been noticed as well [90], [174]. Concerning the assumption on the maximum number of CCs replications (see for instance [175]), the value 15 has been selected [107], [176], [177], but the results obtained continue to hold if this number is slightly changed. Actually, an arbitrary increase in CSC cycle duration is always compatible with such results, as long as CC cycle duration continues to be significantly faster.

In the course of tumor growth, each of the previous tumor cell phenotypes may transiently enter in a quiescent, non-proliferating stage, due to contact inhibition. Moreover, replication of CCs is always supposed to be symmetric. On the other hand, CSCs have been assumed to sustain either symmetric or asymmetric division, in which case one CSC and one CC will result from replication. Evidence for asymmetric division for CSCs, has been reported in [178], [179], [180]. Since reliable estimates about actual probabilities of asymmetric division p_a do not seem to be available as yet, computer simulations will be performed for different choices of that model parameter, namely $p_a = 0.75$, $p_a = 0.50$ and $p_a = 0.25$ (cf. for instance [107], [176]).

3.3.2 Response to radiation

When irradiated, CSCs are significantly more resistant to radiation than CCs. As a matter of fact, CSCs have been described as a comparatively small subpopulation that is highly radioresistant [141], [143], [176], [181]. Radioresistance and surviving cell fractions are estimated by means of the standard Linear Quadratic (LQ) model (see Section 1.3.1 in Chapter 1 and [53], [54], [55], [56]) given by

$$SF(D) = e^{-\xi(\alpha D + \beta D^2)}, \tag{3.1}$$

where ξ is a parameter introduced, as in [107], to distinguish the different radiosensitivities of the proliferating and quiescent states for CCs and CSCs. Actually, cells in a quiescent state (in the $G0$ cell cycle phase) are known to be more resistant to radiation than their non-quiescent counterparts [182].

It should be noticed that, when estimating the impact of radiation according to the LQ model, what matters is the particular combination of α and β that ap-

pears in (3.1), which provides the surviving cell fractions, rather than the separate values of α and β by themselves. For definiteness, in the sequel $\alpha = 0.48Gy^{-1}$, $\beta = 0.02Gy^{-2}$ and $\xi_{p1} = 1.00$ for proliferating CCs have been taken. These radiosensitivity parameters have been reported in [162], where *in vitro* estimates on surviving cell fractions at $2.0Gy$, $SF(2)$, can be found for different GBM cell lines (see also [183]); similar values for α and β have been recently proposed in [111]. In particular, $SF(2) = 0.36$ for proliferating CCs in this case (to be compared to the value $SF(2) = 0.44$ corresponding to α and β parameters proposed in [111]). For quiescent CCs, $\xi_{q1} = 0.85$ has been taken, so that the corresponding value is $SF(2) = 0.42$. For proliferating CSCs the value $\xi_{p2} = 0.30$ ($SF(2) = 0.73$) is considered, whereas for quiescent CSCs the value $\xi_{q2} = 0.20$ ($SF(2) = 0.81$) is selected. Also, such surviving cell fraction ranges at $2.0Gy$ have been observed and reported in the literature (cf. [111], [183], [184]). It should be remarked that the results described in this Chapter continue to hold when the values selected for the radiosensitivity parameters α and β undergo considerable variations, which in particular include the ranges considered in the references quoted above. As a matter of fact, once these assumptions are made, the proposed model is shown to be quite robust with respect to changes in its parameters.

3.4 A three-dimensional (3D) model of stochastic tumor growth

Different mathematical models of tumor growth and its radiation response have been reported in the literature. For instance, tumor growth models and radiation effects with continuous and discrete populations have been reviewed in [104], [185], [186] (see also [112], [156], [157], [158], [187], [188], [189], [190] for more details). On the other hand, the effects of different radiation dosimetries have been considered in [107], [112], [156], also in [110], [111] for fractionated radiotherapy and in [106] for a case of stereotactic radiosurgery. However, little seems to be known concerning mathematical modeling and computer simulations on the effects of heterogeneous radiation dose distributions on heterogeneous tumors, as in the case herein examined.

The model of tumor growth implemented in this Chapter is as follows. Within the growing tumor, both tumor cell phenotypes, CC and CSC, will be subject to the same kinetic rules. More precisely, following [144], [191], [192], a three-dimensional cellular automata (CA) model for tumor growth is developed, where each cell is considered as an individual agent. In particular, each cell (whether CC or CSC) occupies a single node in a 3D unstructured lattice (a lattice with no rotational or translational symmetry [192]) thus avoiding symmetry artifacts. Cell division, migration, apoptosis (programmed death) and lysis (removal of debris) have been included and are represented by stochastic processes. Accordingly, each kinetic rule is characterized by a rate, and the governing equation to be solved is a multivariate master equation (see equation (3.2)). Figures 3.2 and 3.3 show a sketch of the processes included and a scheme describing the possible actions that a cell is able to perform in the mathematical model respectively (for further details, see Appendix C). Nutrient-limited growth is not accounted for in this model. This issue, as well as others, could be included at the expense of increasing complexity by adding degrees of freedom in the computer simulations, but they are not expected to play a significant role in a tumor cell colony of the size considered, which may be assumed to be fully oxygenated [191]. At any rate, for tumors of the size considered in this work the assumption made is not unlikely. For instance, *NIH3T3* cells form tumors of size larger than $1\,cm^3$ without apparent necrotic core even though micro-lesions may be observed [191].

As to the rules of the model of tumor growth, proliferation is only possible for cells located at a node having at least one free neighbor in the lattice. In the case that all neighbor sites are occupied, a cell enters in a quiescent state due to contact inhibition. However, quiescence is abandoned, and cells return to their normal state, as soon as one of the surrounding nodes becomes free. Proliferation, apoptosis, migration and lysis are modeled as stochastic processes occurring with certain rates. A Poisson process has been assumed for each individual stochastic process and a master equation for the change of the probability of the multi-cellular configuration at time t (denoted by the variable Z) in terms of the multi-cellular configuration in another state $Z^{'}$ at time $t^{'}$ is then used. It reads as follows

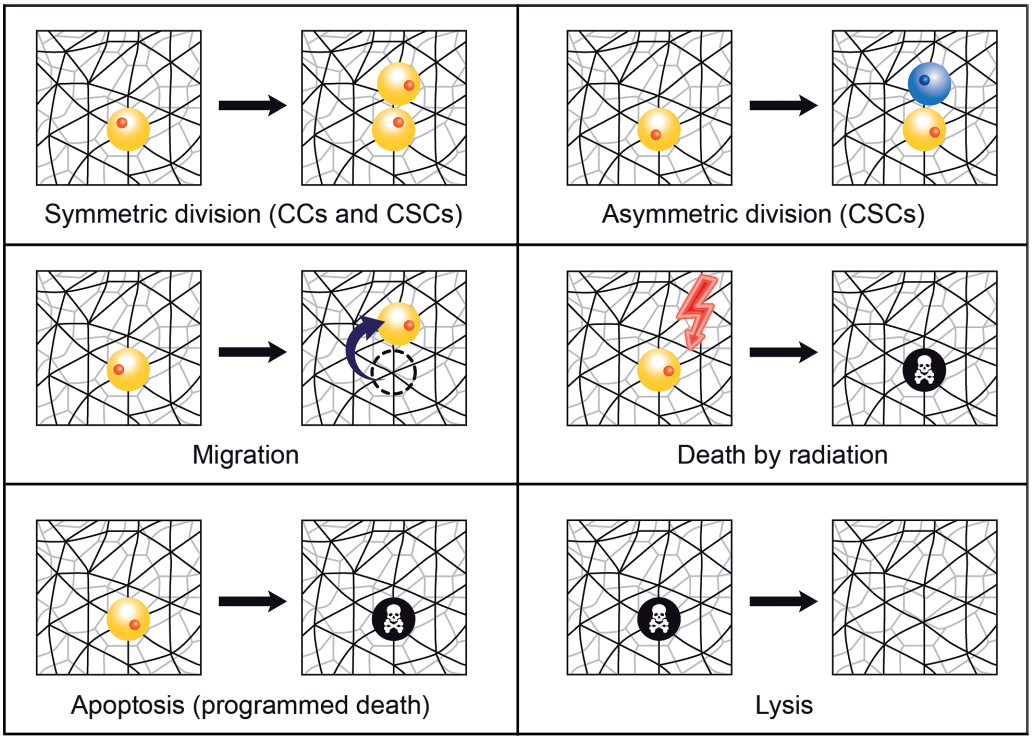

Figure 3.2. Cell processes mimicked in the model of tumor growth. Schematic representation of the cell processes considered in the model of tumor growth (symmetric and asymmetric division, migration, death by radiation, apoptosis (programmed death) and lysis (removal of debris)). Notice that CSCs can perform all these cell processes, while replication of CCs is always supposed to be symmetric. See Appendix C for further details.

$$\frac{dP(Z,t|Z^{''},t^{''})}{dt} = \sum_{Z^{'}} r_{Z^{'}\to Z} P(Z^{'},t|Z^{''},t^{''}) - r_{Z\to Z^{'}} P(Z,t|Z^{''},t^{''}), \tag{3.2}$$

where $p(Z,t|Z^{''},t^{''})$ denotes the conditional probability of finding the multi-cellular configuration Z at time t given the configuration was $Z^{''}$ at time $t^{''}$, $r_{Z\to Z^{'}}$ being the transition rate from configuration Z to $Z^{'}$. Notice that the master equation (3.2) is a balance equation. Indeed, the first term on the right of (3.2) is a gain term that summarizes all transitions that increase the probability of finding the corresponding multi-cellular system in configuration Z. On its turn, the second term in the right describes transitions that move the system away from

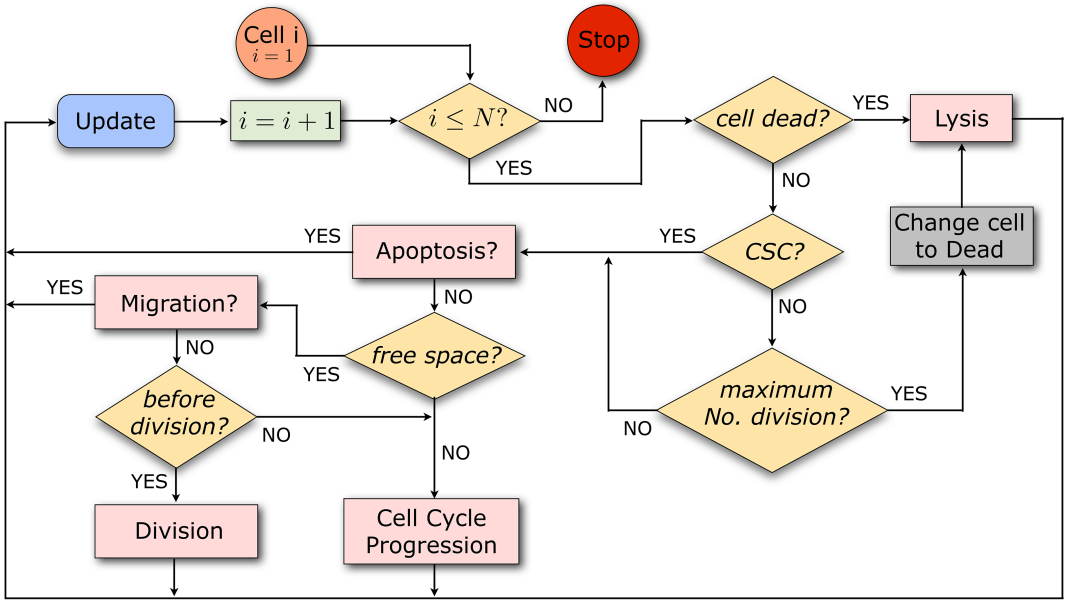

Figure 3.3. Scheme showing the possible actions that a cell is able to perform in the model of tumor growth. As long as the population size is below a prescribed maximum N, it is first tested whether a cell is dead. If so, it undergoes lysis at a certain rate. Alive cells are classified according to CSCs and CCs; CCs die and are subject to lysis with a certain rate once they have performed the maximum number of cell divisions prescribed. CCs not having yet reached the maximum number of cell divisions and CSCs can undergo apoptosis. Those cells that do not go through apoptosis can migrate if free space is available. If they do not migrate and have sufficiently advanced in the cell cycle, they divide. If those cells have not yet reached the end of G2-phase, then they continue to progress in the cell cycle. Cells with no free space available at neighboring sites can only progress in the cell cycle. Concerning radiation effects, cells are picked randomly and killed according to the corresponding surviving cell fraction estimate. See Appendix C for details on the technical implementation of the model algorithm.

Z, and thus represents a loss term. Equation (3.2) can be numerically solved if the initial condition $p(Z, t = 0) = \delta(Z_0)$ is given, where Z_0 denotes the initial multicellular (in this case, tumor cells) configuration. A configuration is determined by the spatial distribution of cells and the state of each cell (proliferating, quiescent, etc.). In this model both CCs and CSCs are able to migrate with the same rate. Migration is mimicked by a hopping process allowing any cell to move from one lattice site to a free neighbor lattice site. In case several free neighbor lattice sites exist, one of them is randomly chosen. In this work, two different migration rates

(k_{mig}) have been considered, a comparatively low rate ($0.025\,h^{-1}$) in the range obtained from the cell diffusion constant [144] as outlined in the Appendix C, and a higher rate ($1.75\,h^{-1}$) as estimated *in vitro* in [111] for a GBM cell line. These will be respectively referred to as low and high migration rates in the sequel. It should be stressed that in this model is only considered the case where the motion of a cell from one lattice site to another does not depend on the contact energy between neighboring cells, but only on the availability of space. In that case, the higher the migration rate, the stronger the cell dispersion is. If however cell-cell adhesion would be considered, migrating cells would tend to fill holes and cavities [192], and migration will lead instead to tumor compactification. Thus, it is assumed that in the current setting this case is substantially included in very low migration cases.

On the other hand, CCs and CSCs undergo programmed cell death (apoptosis) (see for instance [107]). Disposal of cellular debris resulting from apoptosis is carried out by a lysis process [193], for which a lysis rate $k_{lys} = 0.035h^{-1}$ (about $30h$) has been assumed. This is about 10-fold less than phagocytosis (digestion of cellular debris by macrophages) observed *in vivo* in [194], but within the range reported for *in vitro* cultures $0.002h^{-1}$ for *Hybridoma VO 208* cell line [195] to $0.07h^{-1}$ for *Fibrobacter succinogenes* [196].

The master equation (3.2) has been numerically solved by means of the so-called Gillespie algorithm [197], (also called kinetic Monte-Carlo algorithm or Bortz-Kalos-Lebowitz algorithm [198], see Appendix C for more details). Notice that one advantage of using a lattice model is the possibility of extending the same formalism at larger scales by permitting more than one cell to occupy a single lattice site [191]. In order to simulate the resulting biological effect when a radiation dose D is delivered, the surviving cell fraction is computed for each tumor cell phenotype according to the LQ model (3.1), taking into account the state of each cell, proliferating or quiescent. Surviving cells are randomly selected out of the total cell number involved. In the next Section it is shown a typical starting point (about 10^5 cells) in the computer simulations to be described below, as well as the resulting tumor once a size of about 10^6 cells has been reached under the kinetic rules just described, and before the radiotherapy treatment is applied. For convenience of the reader, in Table 3.1 all parameter values used in this mathematical

model to simulate the tumor growth and radiation response are provided.

Description	Symbol	Value/Range	Source
Migration rate	k_{mig}	$0.025\,h^{-1}$ / $1.75\,h^{-1}$	[144], [111]
Apoptosis rate	k_{apt}	$4.17 \times 10^{-4}\,h^{-1}$	[107]
Lysis rate	k_{lys}	$0.035\,h^{-1}$	*(Assumed)*
Radiosensitivity (LQ model)	α	$0.48\,Gy^{-1}$	[162]
Radiosensitivity (LQ model)	β	$0.02\,Gy^{-2}$	[162]
Radiosensitivity (LQ model): Proliferating (CC)	ξ_{p1}	1.00	[183],[184]
Radiosensitivity (LQ model): Quiescent (CC)	ξ_{q1}	0.85	[183],[184]
Radiosensitivity (LQ model): Proliferating (CSC)	ξ_{p2}	0.30	[183],[184]
Radiosensitivity (LQ model): Quiescent (CSC)	ξ_{q2}	0.20	[183],[184]
CC cycle duration	τ_{cc}	$26h$	[90]
CSC cycle duration	τ_{csc}	$48h$, $72h$, $96h$	*(Assumed)*
Asymmetric division probability (CSC)	p_a	0.75, 0.50, 0.25	*(Assumed)*
Maximum number of cycle divisions (CC)	$---$	15	[107],[176]

Table 3.1. Model parameters used in computer simulations of tumor growth and radiotherapy treatments. Values for those parameters not found in the literature were assumed (see detailed explanation for lysis rate). In the remaining cases (asymmetric division probability and CSC cycle duration) some values were assumed, and the impact of different parameter sets on the resulting effects was subsequently analyzed.

3.5 Results: computer simulations of tumor growth and radiotherapy

In this Section the impact of different irradiation strategies in tumors that grow according to the process previously described is analyzed and compared by means of computer simulations. To begin with, a standard protocol is simulated in homogenous tumors where only CCs are present. While doing so, heterogeneous tumors are considered and several homogeneous and heterogeneous radiation dose distributions are simulated using standard fractionation protocols. To conclude, a case of hyperfractionation as well as protocols with low total radiation doses are also investigated.

3.5.1 Standard fractionation protocols

As a reference case, let us first consider the effect on a fully monoclonal tumor (containing only CCs) of a therapeutic irradiation protocol, consisting of 30 sessions of $2.0Gy$, each being homogeneously delivered on the tumor. According to standard radiotherapy scheduling, sessions are distributed into 6 weeks, each week including five sessions from Monday to Friday separated by 24 hours intervals, and with a 72 hours interval from Friday to next Monday in the following week (with weekend interruptions). The total radiation dose delivered with this treatment is thus $60Gy$. This is currently considered a standard radiotherapy treatment for most GBM tumors [49], [199], [200]. The corresponding process is illustrated in Figure 3.4, both for the cases of low and high migration rate, under current assumption that migration is not inhibited by cell-cell adhesion. Figure 3.4 shows that tumor prior to treatment grows from week 1 to approximately week 5 for the low migration case, and just in one week in the case of high migration, until a size of about 10^6 cells is attained. Notice that the growth time of the tumor decreases with the migration rate due to the decreasing effect of contact inhibition inside the tumor. Then radiation therapy treatment starts, and accordingly tumor cell number diminishes during the first week (with small re-growth between each daily session and weekend interruptions, as represented by the knots in the straight line in the plot, see Figure 3.4). The pattern just described is reproduced until tumor eradication is achieved at the end of the radiotherapy treatment in these cases.

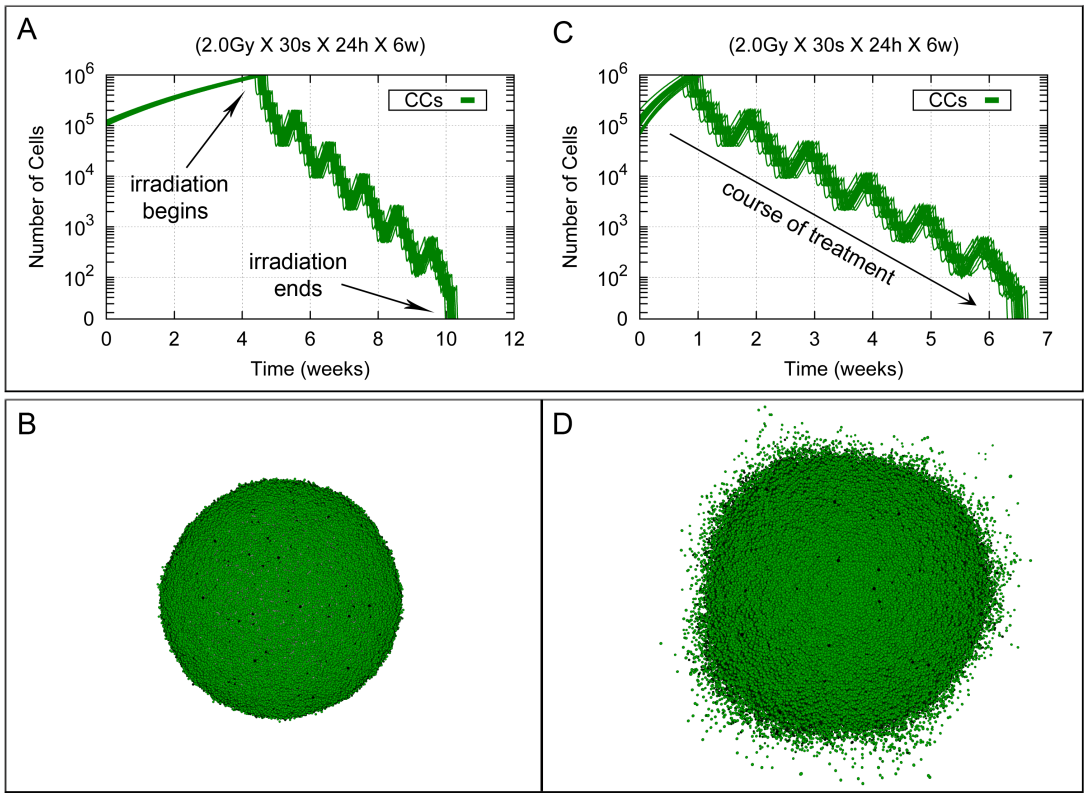

Figure 3.4. Standard radiotherapy treatment in a homogeneous tumor for the low and high migration cases. Cell growth curves are shown corresponding to homogeneous tumor growth for the low and high migration cases when only CCs are present (see respectively (A) and (C)). Tumor growth is allowed unchecked from a size of about 10^5 cells until about 10^6 cells are present, which approximately occurs at day 30 (respectively at day 7) since the beginning of the process. Then, a homogeneous treatment corresponding to 30 sessions of $2.0Gy$ each is delivered. In all cases, sessions are scheduled along 6 weeks separated by 24 hours intervals except for weekends, where a 72 hours interval is allowed. Radiotherapy treatment is thus completed 40 days afterwards its beginning (about 70 and 47 days since the initial stage respectively). Data corresponding to 20 simulations (with different seeds of a random number generator) are presented. Notice that the vertical coordinate is represented in a logarithmic scale. In (B) and (D) tumor stages are represented when radiation therapy is started (about 10^6 cells in total) for the low and high migration cases respectively. Depicted in dark and light green are proliferating and quiescent CCs. Dead cells are represented in black.

A heterogeneous tumor containing the two tumor cell phenotypes is now considered. Starting from an initial configuration where 10^5 cells are present, out of which approximately 85% are CCs and 15% are CSCs, tumor growth is allowed until a size of about 10^6 cells is reached (see Figures 3.5 and 3.6). Then the impact of homogeneous and heterogeneous radiation dose distributions is modeled, and computer simulation results are compared in the cases where asymmetric division probabilities p_a for CSCs are $p_a = 0.75$, $p_a = 0.50$ and $p_a = 0.25$, the CSC cycle duration is taken to be $96h$, $72h$ and $48h$, and the low and high migration rates are considered. The results obtained will show that the standard irradiation protocol described before fails now to achieve tumor control in any of the cases considered. To compare the dynamics of the tumor resulting after irradiation with respect to its pre-treatment stage, computer simulations are stopped once the pre-treatment population size of about 10^6 cells is again obtained.

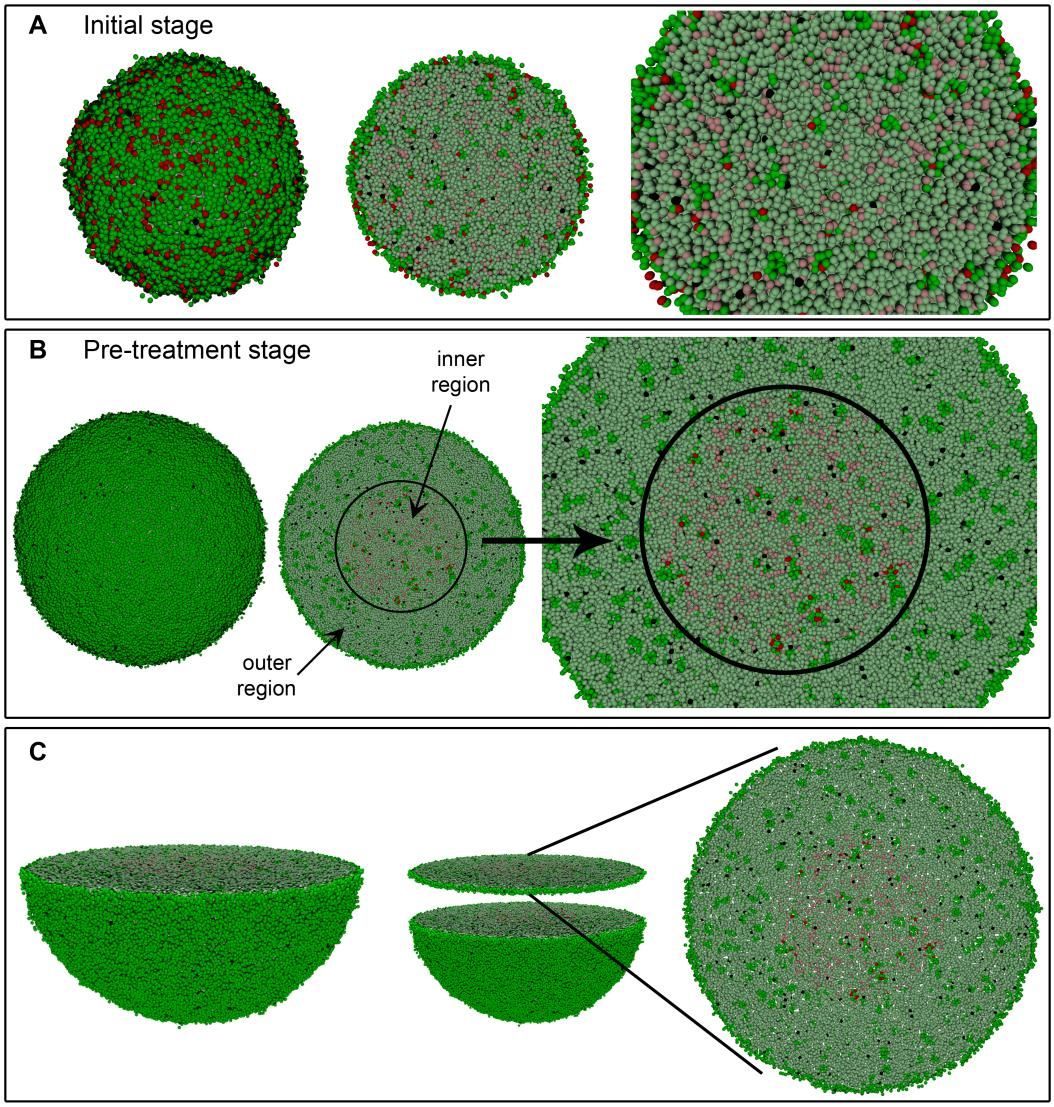

Figure 3.5. Simulated growth of a heterogeneous tumor with the low migration rate. Depicted in dark and light green (respectively, dark and light red) are proliferating and quiescent CCs (respectively, proliferating and quiescent CSCs). Dead cells are represented in black. (A) An initial stage where about 10^5 cells, distributed into tumor cell phenotypes CC (85%) and CSC (15%), are present. (B) Tumor stage when radiation therapy is started (about 10^6 cells in total). In the middle image, the location of the inner region where 100% of CSCs are concentrated is shown for the case when $p_a = 0.25$ and CSC cycle duration equal to $96h$. A 3D transversal cut is performed in the middle of solid figures (A) and (B) (left), so that its interior could be seen (middle and right) respectively. (C) Representation of the transversal cut showed in (B) for a slice of two cell diameters. Notice the little space existing between cells.

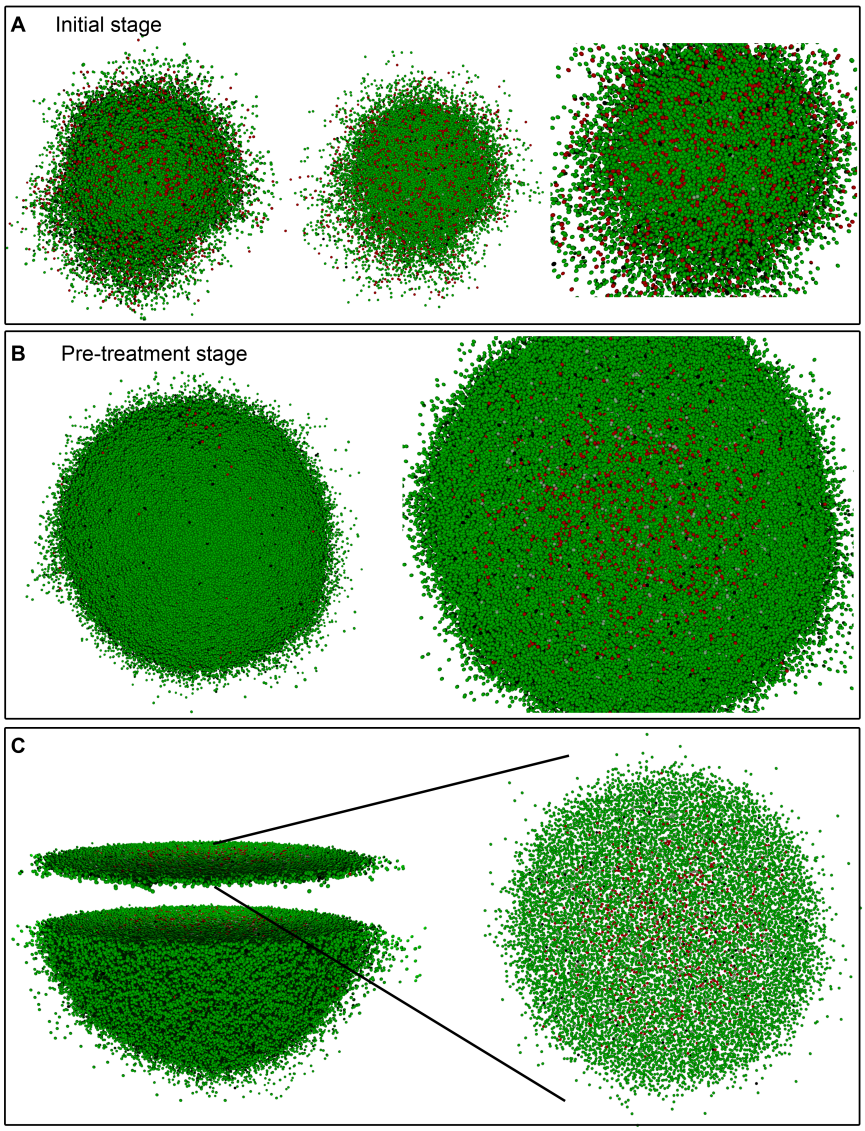

Figure 3.6. Simulated growth of a heterogeneous tumor with the high migration rate. Depicted in dark and light green (respectively, dark and light red) are proliferating and quiescent CCs (respectively, proliferating and quiescent CSCs). Dead cells are represented in black. (A) An initial stage where about 10^5 cells, distributed into tumor cell phenotypes CC (85%) and CSC (15%), are present. (B) Tumor stage when radiation therapy is started (about 10^6 cells in total). In the right image, the spatial distribution of CCs and CSCs is shown for the case when $p_a = 0.25$ and CSC cycle duration equal to $48h$. A 3D transversal cut is performed in the middle of solid figure (B) (left), so that its interior could be seen (right). (C) Representation of the transversal cut showed in (B) for a slice of two cell diameters. Notice the comparatively large (with respect to Figure 3.5) space observed between cells.

As shown in Figure 3.5, for $p_a = 0.25$, CSC cycle duration equal to $96h$ and the low migration rate, the more radioresistant tumor cell phenotype CSC is confined within an inner, smaller region when irradiation is started. Such spatial CSCs distribution is neither a priori imposed, nor a consequence of the specific CSC cycle duration or the asymmetric division probability considered (see Table 3.2). It is due instead to the difference of the CSC and CC cycle durations. Indeed, a robust emerging feature is now observed. Namely, due to asymmetric division CSCs produce a certain fraction of CCs. Both CCs and CSCs then compete for resources including free space at the tumor border [144], [201]. For sufficiently small micro-motility, that competition is controlled by cell replication. As CCs proliferate faster than CSCs, they have a selective advantage in the competition for free space and will eventually outcompete the CSCs in the border region of the tumor, if (as it happens in this case) to achieve such dominance less replications are needed than the maximum number that CCs can perform. The precise timing depends on the relation of the cell cycle duration for CSCs vs. CCs, p_a, and the fraction of CSCs in the initial population at 10^5 cells (notice that this fraction would itself be determined by p_a and CSC cycle duration if the 10^5 cells would already have emerged by replication from a single initial CSC).

Therefore, for a low migration rate, CSCs will be contact-inhibited by the fast proliferating CCs. As a consequence, CSCs will remain confined in an inner region in that case. Actually, on assuming a cell diameter of $20\mu m$, the diameter of the tumor in all cases is then of about $2680\mu m$ (with a standard deviation of $56\mu m$ over 20 simulations performed for each parameter set considered) and the volume of this inner region where 100% of CSCs are located varies from the 15% to 25% of the total tumor volume, when asymmetric division probability and the CSC cycle duration are allowed to change (see Table 3.2, and Figures in the Appendix C).

	$p_a = 0.75$		$p_a = 0.50$		$p_a = 0.25$	
τ_{csc}	**Diameter**	**CSCs**	**Diameter**	**CSCs**	**Diameter**	**CSCs**
96h	1426.3 μm	16871	1488.6 μm	18718	1513.5 μm	20448
	[41.07 μm]	[56.12]	[43.24 μm]	[71.33]	[53.70 μm]	[77.30]
72h	1473.6 μm	17125	1539.3 μm	19366	1587.8 μm	21092
	[40.85 μm]	[67.50]	[58.67 μm]	[102.07]	[40.45 μm]	[85.48]
48h	1498.1 μm	17785	1595.9 μm	19829	1682.2 μm	21953
	[47.21 μm]	[62.45]	[73.16 μm]	[88.98]	[47.74 μm]	[140.16]

Table 3.2. Estimates of the tumor inner region diameter and number of CSCs before irradiation for the low migration case. Diameter is that of an inner sphere where 100% of CSCs are located. CSCs number is computed before radiation therapy treatment starts. Within brackets the corresponding standard deviations are also provided. Data corresponding to 20 simulations (with different seeds of a random number generator) for each case considered. See also Figures in the Appendix C for further details.

On the other hand, when the high migration rate is considered, CSCs are not fully concentrated in an inner region of the tumor (see Figure 3.6 for $p_a = 0.25$ and CSC cycle duration equal to $48h$). However, it is possible to define an inner region where at least 80% of CSCs are located (see Figure 3.7). When asymmetric division probability and CSC cycle duration are allowed to change in the parameter range considered, this inner region approximately represents between 21% to 40% of the volume where 90% of cells, both CCs and CSCs, are located (see Table 3.3, and Figures in the Appendix C). In this case, the diameter of the tumor for all cases is about $5294\mu m$ (with a standard deviation of $778\mu m$ over 20 simulations performed for each parameter set considered). In Tables 3.2 and 3.3 the number of CSCs just before treatment starts is shown, so that its dependence with migration rate, asymmetric division probability and CSC cycle duration can be observed. Actually, the number of CSCs existing before treatment starts is a key factor to estimate tumor resistance to radiation therapy, as will be described below.

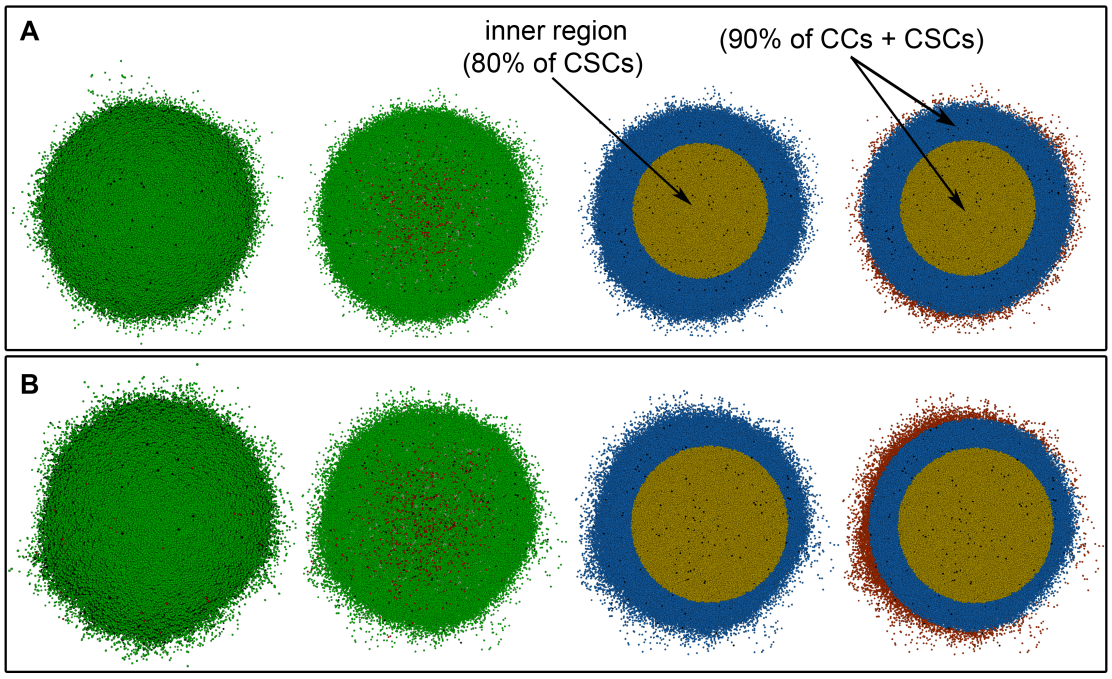

Figure 3.7. Spatial distribution of CSCs for a heterogeneous tumor with the high migration rate. From left to right tumor stage when radiation therapy is started (about 10^6 cells in total) with the high migration rate, 3D transversal cut in the middle of the tumor, region where 80% of CSCs are located (yellow) and region where 90% of total cells (CCs and CSCs) are located (yellow and blue). (A) For the case $p_a = 0.75$ and (B) for $p_a = 0.25$ considering CSC cycle duration equal to $48h$. Depicted in dark and light green (respectively, dark and light red) are proliferating and quiescent CCs (respectively, proliferating and quiescent CSCs). Dead cells are represented in black.

	$p_a = 0.75$		$p_a = 0.50$		$p_a = 0.25$	
τ_{csc}	**Diameter**	**CSCs**	**Diameter**	**CSCs**	**Diameter**	**CSCs**
96h	1857.4 μm	20454	1986.9 μm	27916	2035.6 μm	35087
	[74.72 μm]	[256.53]	[51.30 μm]	[811.67]	[77.80 μm]	[1066.54]
72h	1906.2 μm	21178	2043.1 μm	28847	2158.7 μm	37686
	[54.46 μm]	[322.63]	[78.51 μm]	[861.47]	[94.21 μm]	[859.31]
48h	1983.8 μm	21944	2139.3 μm	30119	2294.8 μm	41629
	[69.64 μm]	[506.92]	[81.17 μm]	[872.98]	[62.60 μm]	[1040.65]

Table 3.3. Estimates of the tumor inner region diameter and number of CSCs before irradiation for the high migration case. Diameter is that of an inner sphere where 80% of CSCs are located. CSCs number is computed before radiation therapy treatment starts. Within brackets the corresponding standard deviations are also provided. Data corresponding to 20 simulations (with different seeds of a random number generator) for each case considered. See also Figures in the Appendix C for further details.

Bearing these facts in mind, it turns out that tumor control can be obtained in all cases when a radiation boost is applied at such internal regions. More precisely, in the case of low migration tumor control can be achieved for CSC cycle durations equal to $96h$ and $72h$, when $2.5Gy$ (for the case $p_a = 0.75$), $2.9Gy$ (for $p_a = 0.50$) and $3.3Gy$ (for $p_a = 0.25$) are respectively delivered within the largest inner sphere containing 100% of CSCs, and $2.0Gy$ is delivered in the rest of the tumor, according to the former standard fractionation protocol (5 days a week along 30 sessions at 24 hours intervals except for weekends). However, when CSC cycle duration is equal to $48h$, tumor eradication is not possible with these heterogeneous therapies under the same conditions. In that case, to obtain tumor control, the dose delivered in the inner region has to be raised to $2.7Gy$, $3.4Gy$ and $3.9Gy$ respectively (see Table 3.4 and the Appendix C). Notice that these radiation doses increase as asymmetric division probability decreases.

		Heterogeneous therapy		Homogeneous therapy	
p_a	τ_{csc}	No Control	Control	No Control	Control
0.75	**96h**	$---$	$2.0Gy - 2.5Gy^{(1)}$	$2.10Gy^{(1)}$	$2.5Gy$
			$[63.0Gy]$	$[63.0Gy]$	$[75.0Gy]$
	72h	$---$	$2.0Gy - 2.5Gy^{(2)}$	$2.10Gy^{(2)}$	$2.5Gy$
			$[63.0Gy]$	$[63.0Gy]$	$[75.0Gy]$
	48h	$2.0Gy - 2.5Gy^{(3)}$	$2.0Gy - 2.7Gy^{(4)}$	$2.10Gy^{(3)}$ / $2.12Gy^{(4)}$	$2.7Gy$
		$[63.0Gy]$	$[63.6Gy]$	$[63.0Gy]$ / $[63.6Gy]$	$[81.0Gy]$
0.50	**96h**	$---$	$2.0Gy - 2.9Gy^{(5)}$	$2.15Gy^{(5)}$	$2.9Gy$
			$[64.5Gy]$	$[64.5Gy]$	$[87.0Gy]$
	72h	$---$	$2.0Gy - 2.9Gy^{(6)}$	$2.17Gy^{(6)}$	$2.9Gy$
			$[65.1Gy]$	$[65.1Gy]$	$[87.0Gy]$
	48h	$2.0Gy - 2.9Gy^{(7)}$	$2.0Gy - 3.4Gy^{(8)}$	$2.19Gy^{(7)}$ / $2.30Gy^{(8)}$	$3.4Gy$
		$[65.7Gy]$	$[69.0Gy]$	$[65.7Gy]$ / $[69.0Gy]$	$[102Gy]$
0.25	**96h**	$---$	$2.0Gy - 3.3Gy^{(9)}$	$2.23Gy^{(9)}$	$3.3Gy$
			$[66.9Gy]$	$[66.9Gy]$	$[99.0Gy]$
	72h	$---$	$2.0Gy - 3.3Gy^{(10)}$	$2.27Gy^{(10)}$	$3.3Gy$
			$[68.1Gy]$	$[68.1Gy]$	$[99.0Gy]$
	48h	$2.0Gy - 3.3Gy^{(11)}$	$2.0Gy - 3.9Gy^{(12)}$	$2.32Gy^{(11)}$ / $2.47Gy^{(12)}$	$3.9Gy$
		$[69.6Gy]$	$[74.1Gy]$	$[69.6Gy]$ / $[74.1Gy]$	$[117Gy]$

Table 3.4. Classification of heterogeneous and homogeneous radiation therapies for the low migration case. In all cases, treatment sessions were scheduled along 6 weeks separated by 24 hours intervals except for weekends, where a 72 hours interval is allowed. Data corresponding to 20 simulations (with different seeds of a random number generator) are presented. In the heterogeneous therapies, radiation doses are specified both for the outer (left) and inner (right) tumor regions, each case being indexed from (1) to (12). The averaged dose for any of the previous cases is labeled with the same number in the columns corresponding to homogeneous therapies. Within brackets the total dose of the radiation therapy treatment is also provided. See Tables and Figures in the Appendix C for further details.

Consider now the same heterogeneous therapies for the case of high migration and select an inner region where 80% of CSCs are located. Considering these heterogeneous therapies for each case as before, tumor control is now obtained only for $p_a = 0.75$ with CSC cycle durations of $96h$ and $72h$. This is due to the fact that *i)* the high migration rate permits less contact inhibition, which in turn allows for rapid re-growth, and *ii)* there are about 20% of CSCs which only receive a radiation dose of $2.0Gy$. Therefore, to obtain tumor control it is not only necessary to increase the radiation dose in the inner region, but also in the outer

one (see Table 3.5 and the Appendix C). The radiation doses of the heterogeneous therapies required to obtain tumor control are provided for each case of migration rate considered in Tables 3.4 and 3.5. The respective temporal evolution of the number of each tumor cell phenotype is shown in Figure 3.8 (A), (C), (E) and (G) for different values of asymmetric division probability, migration rate and CSC cycle duration.

		Heterogeneous therapy		**Homogeneous therapy**	
p_a	τ_{csc}	**No Control**	**Control**	**No Control**	**Control**
0.75	**96h**	$---$	$2.0Gy - 2.5Gy^{(1)}$	$2.10Gy^{(1)}$	$2.5Gy$
			$[63.0Gy]$	$[63.0Gy]$	$[75.0Gy]$
	72h	$---$	$2.0Gy - 2.5Gy^{(2)}$	$2.11Gy^{(2)}$	$2.5Gy$
			$[63.3Gy]$	$[63.3Gy]$	$[75.0Gy]$
	48h	$2.0Gy - 2.5Gy^{(3)}$	$2.2Gy - 2.7Gy^{(4)}$	$2.13Gy^{(3)}$ / $2.33Gy^{(4)}$	$2.7Gy$
		$[63.9Gy]$	$[69.9Gy]$	$[63.9Gy]$ / $[69.9Gy]$	$[81.0Gy]$
0.50	**96h**	$2.0Gy - 2.9Gy^{(5)}$	$2.3Gy - 2.9Gy^{(6)}$	$2.23Gy^{(5)}$ / $2.45Gy^{(6)}$	$2.9Gy$
		$[66.9Gy]$	$[73.5Gy]$	$[66.9Gy]$ / $[73.5Gy]$	$[87.0Gy]$
	72h	$2.0Gy - 2.9Gy^{(7)}$	$2.6Gy - 2.9Gy^{(8)}$	$2.25Gy^{(7)}$ / $2.70Gy^{(8)}$	$2.9Gy$
		$[67.5Gy]$	$[81.0Gy]$	$[67.5Gy]$ / $[81.0Gy]$	$[87.0Gy]$
	48h	$2.0Gy - 2.9Gy^{(9)}$	$2.8Gy - 3.4Gy^{(10)}$	$2.29Gy^{(9)}$ / $3.00Gy^{(10)}$	$3.4Gy$
		$[68.7Gy]$	$[90.0Gy]$	$[68.7Gy]$ / $[90.0Gy]$	$[102Gy]$
0.25	**96h**	$2.0Gy - 3.3Gy^{(11)}$	$2.4Gy - 3.3Gy^{(12)}$	$2.36Gy^{(11)}$ / $2.65Gy^{(12)}$	$3.3Gy$
		$[70.8Gy]$	$[79.5Gy]$	$[70.8Gy]$ / $[79.5Gy]$	$[99.0Gy]$
	72h	$2.0Gy - 3.3Gy^{(13)}$	$2.7Gy - 3.3Gy^{(14)}$	$2.43Gy^{(13)}$ / $2.90Gy^{(14)}$	$3.3Gy$
		$[72.9Gy]$	$[87.0Gy]$	$[72.9Gy]$ / $[87.0Gy]$	$[99.0Gy]$
	48h	$2.0Gy - 3.3Gy^{(15)}$	$3.4Gy - 3.9Gy^{(16)}$	$2.52Gy^{(15)}$ / $3.60Gy^{(16)}$	$3.9Gy$
		$[75.6Gy]$	$[108Gy]$	$[75.6Gy]$ / $[108Gy]$	$[117Gy]$

Table 3.5. Classification of heterogeneous and homogeneous radiation therapies for the high migration case. In all cases, treatment sessions were scheduled along 6 weeks separated by 24 hours intervals except for weekends, where a 72 hours interval is allowed. Data corresponding to 20 simulations (with different seeds of a random number generator) are presented. In the heterogeneous therapies, radiation doses are specified both for the outer (left) and inner (right) tumor regions, each case being indexed from (1) to (16). The averaged dose for any of the previous cases is labeled with the same number in the columns corresponding to homogeneous therapies. Within brackets the total dose of the radiation therapy treatment is also provided. See Tables and Figures in the Appendix C for further details.

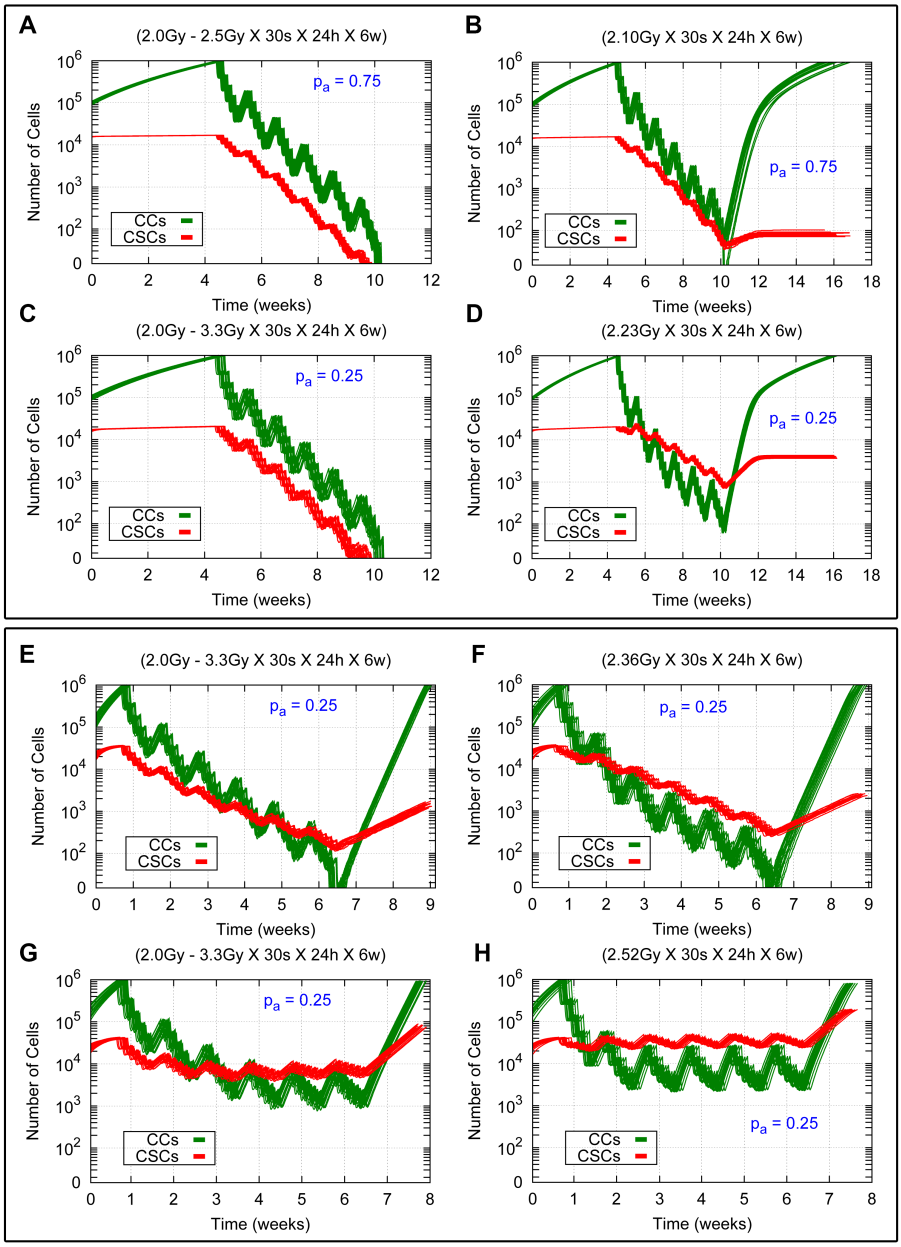

Figure 3.8. **Comparing heterogeneous and averaged homogeneous radiation therapies in a heterogeneous tumor for different model parameter sets.** Cell survival curves for 20 simulations (with different seeds of a random number generator) in the cases $p_a = 0.75$ and $p_a = 0.25$ for CSC cycle durations equal to $96h$ and $48h$ with the high and low migration rates are shown. The time evolution for CCs and CSCs is represented in green and red respectively. (A, C, E, G) Results for heterogeneous therapies consisting of $2.5Gy$ and $3.3Gy$ in the inner sphere and $2.0Gy$ in the rest of the tumor. (B, D, F, H) Results for the related averaged homogeneous therapies corresponding to $2.10Gy$, $2.23Gy$, $2.36Gy$ and $2.52Gy$ respectively. (A, B, C, D) Results for the cases $p_a = 0.75$ and $p_a = 0.25$ with the low migration rate and CSC cycle duration equal to $96h$. (E, F, G, H) Results for the case $p_a = 0.25$ with the high migration rate and CSC cycle durations equal to $96h$ (E, F) and $48h$ (G, H). In all cases 30 sessions are scheduled along 6 weeks, separated by 24 hours intervals except for weekends, where a 72 hours interval is allowed. Radiation is applied when the total cell count is about 10^6 cells. Notice that the vertical coordinate is represented in a logarithmic scale.

It may appear at first glance that the successful results obtained for heterogeneous dosimetries could be a consequence of the overall radiation dose delivered over the tumor being larger than that administered according the standard irradiation protocol ($2.0Gy$ a day, 5 days a week at 24 hours intervals, with weekend interruptions and $60Gy$ in total). However, heterogeneous dosimetry turns out to be crucial to achieve tumor control. In particular, tumor control fails to be attained when an averaged homogeneous dose (AD) is delivered, corresponding to the same global radiation energy as in the heterogeneous dosimetry, carried out along a similar scheduling. The corresponding AD is given by

$$AD = D_{in}\left(\frac{V_{in}}{V_{tot}}\right) + D_{out}\left(\frac{V_{out}}{V_{tot}}\right), \tag{3.3}$$

where V_{in}, V_{out} are the volume of the internal sphere and the remaining shell considered; D_{in}, D_{out} are the radiation doses delivered over the internal and external regions just described, and V_{tot} is the total volume of the tumor. In the case of low migration the inner region is that where 100% of CSCs are located (see Table 3.2 for values of the diameter of this inner region for each case) and the volume of the outer region is computed with respect to the average diameter of the tumor at the beginning of the radiotherapy treatment ($2680\mu m$). However, for the case of high migration the inner region is now selected as that where 80% of CSCs are located (see Table 3.3 for further details). Indeed, since some cells are now isolated far from the tumor bulk, instead of defining the tumor radius as the distance from its center of mass to the farthest cell, to compute the averaged dose the volume of the tumor is now considered as that of the region where 90% of total cells (CCs and CSCs) are located, where the diameter is about $3120\mu m$ (with a standard deviation of $186\mu m$ over 20 simulations performed for each parameter set considered). The reason for this assumption is that it will yield a higher AD than that obtained when considering the maximum diameter of the tumor ($5294\mu m$), which will extend to regions sparsely occupied by tumor cells. Hence the averaged homogeneous therapies thus derived will deliver higher radiation doses than those that would be obtained if the outer shell were defined as that where all tumor cells are contained.

The averaged dose (AD) per session according to equation (3.3) is shown in

Tables 3.4 and 3.5, for each of heterogeneous therapies described before. These AD vary from $2.10Gy$ to $2.32Gy$ for the low migration case and from $2.10Gy$ to $2.52Gy$ in the case of high migration for the asymmetric division probabilities and CSC cycle durations considered. Notice that the total radiation doses delivered by these averaged homogeneous therapies are higher than $60Gy$ (the value corresponding to the standard irradiation protocol) for all cases. The total radiation doses corresponding to these new dosimetries range between $63.0Gy$ to $69.6Gy$ for the case of low migration and $63.0Gy$ to $75.6Gy$ for the high migration case. Some of these results are illustrated in Figure 3.8 (B), (D), (F) and (H). On the other hand, in Figure 3.9, further details of the time evolution of the tumor colony are provided during and after an homogeneous radiation therapy delivering an $AD = 2.10Gy$ for $p_a = 0.75$ and $AD = 2.23Gy$ for $p_a = 0.25$ with the low migration rate and CSC cycle duration of $96h$. The cases $p_a = 0.25$ with the high migration rate and CSC cycle durations of $96h$ and $48h$, an $AD = 2.36Gy$ and $AD = 2.52Gy$ respectively are also included. Notice that in the case of high migration (Figure 3.9 (B)) more cells remain isolated at the end of the treatment compared with the case of low migration (Figure 3.9 (A)). In that Figure, when tumor control is not achieved, computer simulations are performed until the surviving tumor reaches a size approximately equal to 10^6 cells, the number of cells it had before radiotherapy started.

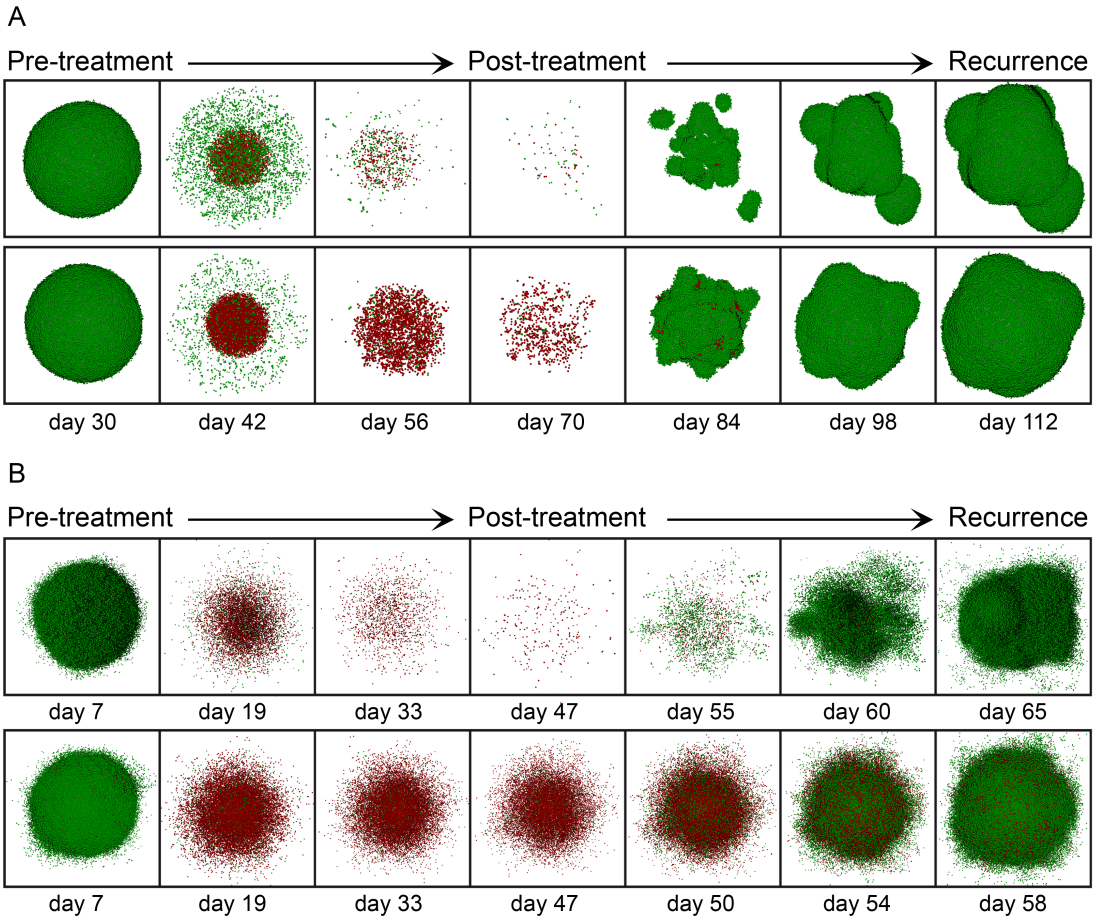

Figure 3.9. Time evolution of tumor growth during and after averaged homogeneous radiation therapies. (A) A homogeneous dose of $2.10Gy$ for the case $p_a = 0.75$ is delivered (Top), and a homogeneous dose of $2.23Gy$ for $p_a = 0.25$ is instead applied (Bottom), assuming in both cases of (A) the low migration rate and CSC cycle duration equal to $96h$. (B) A homogeneous dose of $2.36Gy$ is delivered (Top) and a homogeneous dose of $2.52Gy$ (Bottom) for the case $p_a = 0.25$ with the high migration rate and CSC cycle durations equal to $96h$ (Top) and $48h$ (Bottom). In all cases (A, B) a standard scheduling (30 sessions along 6 weeks separated by 24 hours intervals except for weekends) was applied. From left to right in sequential order the tumor before radiotherapy treatment starts, its state after sessions 10, 20 and 30, and three stages corresponding to recurrence during the period covered (where about 10^6 cells is again obtained) are shown. Depicted in dark and light green (respectively, dark and light red) are proliferating and quiescent CCs (respectively, proliferating and quiescent CSCs). Dead cells are not represented.

Tables 3.4 and 3.5 reveal that tumor recurrence occurs in all cases for a homogeneous therapy delivering the corresponding average dose (AD). Besides, the number of CSCs in the tumor at the end of the radiotherapy treatment decreases with p_a and CSC cycle duration (see Figure 3.10, and Tables in the Appendix C). In the case of low migration, for the heterogeneous therapies failing to achieve tumor control, the number of CSCs remaining alive at the end of the recurrence tumor stage is 107, 1785 and 4457 respectively, with the corresponding standard deviations being 8.53, 78.31 and 232.67 (see Figure 3.10 (A) to compare with the corresponding averaged homogeneous therapies). These values correspond to the cases $p_a = 0.75$, $p_a = 0.50$ and $p_a = 0.25$ with a CSC cycle duration of $48h$. On the other hand, in Figure 3.10 (B) the number of CSCs at the end of the recurrence tumor stage is provided in the case of high migration for the heterogeneous therapies delivering $2.5Gy$ (for the case $p_a = 0.75$), $2.9Gy$ (for $p_a = 0.50$) and $3.3Gy$ (for $p_a = 0.25$) in the inner region, and $2.0Gy$ in the rest of the tumor. Notice that, even when tumor control cannot be achieved with the heterogeneous therapies, the corresponding averaged homogeneous therapies always have more CSCs at the end of the recurrence tumor stage (see Figure 3.10 (C)). Moreover, in some cases that number of CSCs is larger than before the treatment started, resulting in more radioresistant tumors after treatment (see Appendix C for further details).

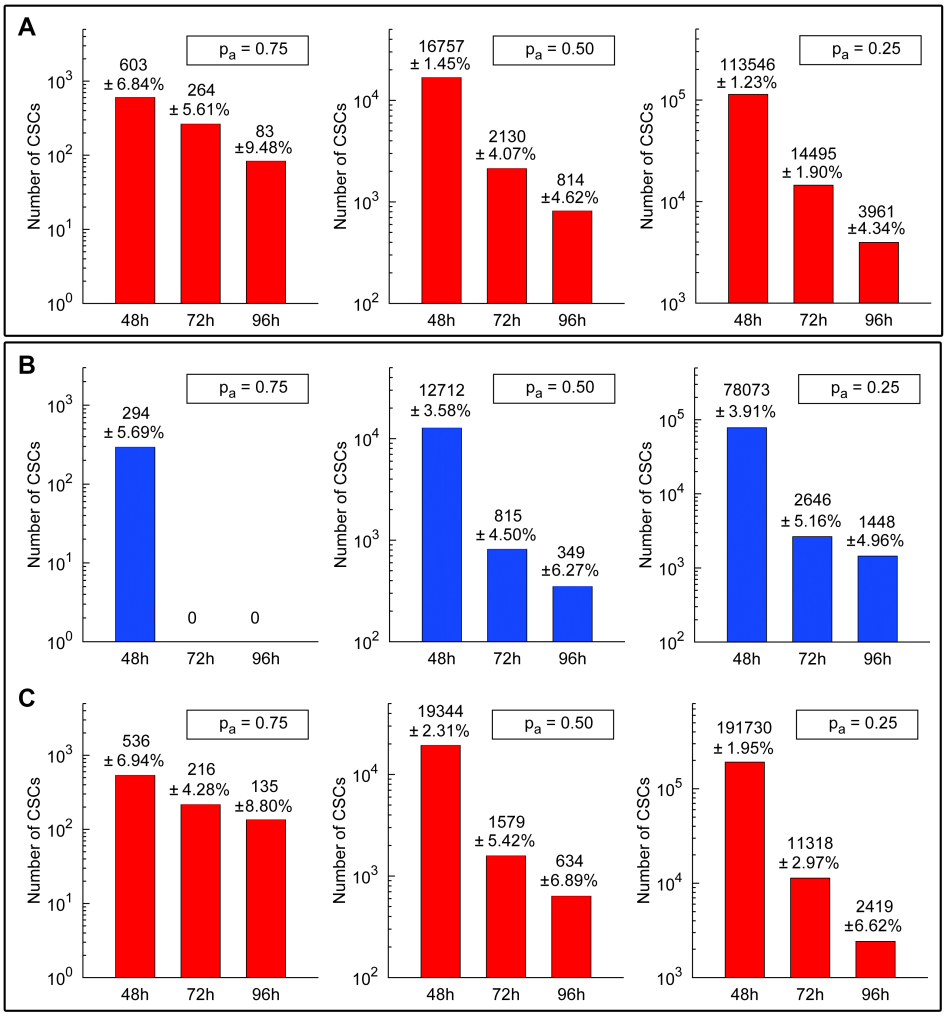

Figure 3.10. Estimates on the total number of CSCs at the end of the recurrence tumor stage for heterogeneous and averaged homogeneous radiation therapies. Number of CSCs at the end of the recurrence tumor stage (where about 10^6 cells is again obtained) and the corresponding standard deviations after performing 20 simulations in each case (with different seeds of a random number generator) are shown. (A) For averaged homogeneous therapies corresponding to heterogeneous therapies consisting of $2.5Gy$, $2.9Gy$ and $3.3Gy$ in the inner sphere and $2.0Gy$ in the rest of the tumor for the cases $p_a = 0.75$, $p_a = 0.50$ and $p_a = 0.25$ (left, middle, right) assuming the low migration rate and CSC cycle durations equal to $48h$, $72h$ and $96h$ (see Table 3.4). (B) For heterogeneous therapies consisting of $2.5Gy$, $2.9Gy$ and $3.3Gy$ in the inner sphere and $2.0Gy$ in the rest of the tumor (Top) and the corresponding averaged homogeneous therapies (Bottom) for the cases $p_a = 0.75$, $p_a = 0.50$ and $p_a = 0.25$ (left, middle, right) with the high migration rate and CSC cycle durations equal to $48h$, $72h$ and $96h$ (see Table 3.5). In all cases (A, B, C), a standard scheduling (30 sessions along 6 weeks separated by 24 hours intervals except for weekends) was applied. Notice that the vertical coordinate is represented in a logarithmic scale. See Tables in the Appendix C for further details.

Therefore, to achieve full eradication of a tumor consisting of two different tumor cell phenotypes, heterogeneous dosimetry is crucial. Actually, the choice of a minimal radiation dose sufficient to achieve tumor control depends on the value of p_a, the CC and CSC cycle durations and on the internal spatial distribution of CSCs. In Tables 3.4 and 3.5, the heterogeneous radiation therapies needed to achieve tumor control are described, and the corresponding averaged homogeneous therapies are also provided. Interestingly, the corresponding averaged homogeneous therapies in each case fail to obtain tumor control (see also Tables in the Appendix C). Moreover, homogeneous therapies needed to obtain tumor control are also provided in Tables 3.4 and 3.5. One readily sees that in all cases higher total radiation doses are needed for homogeneous than for heterogeneous therapies.

On the other hand, considering that for all choices of model parameters the AD is higher than $2.0Gy$, this implies that tumor recurrence will also occur for the standard irradiation protocol ($2.0Gy$ a day, 5 days a week at 24 hours intervals, with weekend interruptions and $60Gy$ in total) for each case of p_a, migration rate and CSC cycle duration considered. In terms of the number of remaining CSCs after treatment is completed, recurrence is certainly weaker when AD is delivered than for the standard fractionation protocol, as one could expect from the comparative increase in radiation delivery. Moreover, tumor control cannot be achieved for each case of p_a, migration rate and CSC cycle duration considered even when the homogeneous therapy delivering the average radiation dose is rescheduled in 7 days a week along 30 sessions at 24 hours intervals, without weekend interruptions (see Figure 3.11 for some examples of averaged homogeneous therapies with this fractionation protocol).

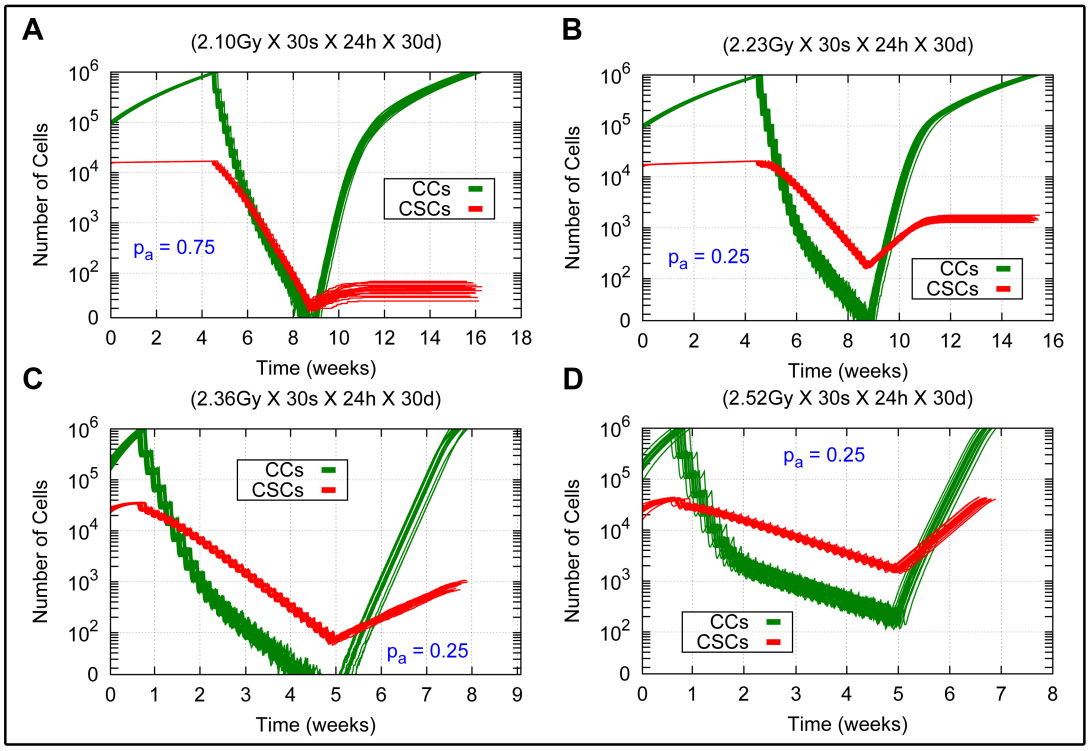

Figure 3.11. Comparing averaged homogeneous radiation therapies without weekend interruptions. Cell survival curves for 20 simulations (with different seeds of a random number generator) are shown. (A) Averaged dosimetries consisting of $AD = 2.10Gy$ for $p_a = 0.75$ and (B) $AD = 2.23Gy$ for $p_a = 0.25$, both for the low migration case and CSC cycle duration equal to $96h$. (C, D) Averaged homogeneous therapies consisting of $AD = 2.36Gy$ and $AD = 2.52Gy$ for the case $p_a = 0.25$ with the high migration rate and CSC cycle durations equal to $96h$ and $48h$ respectively. The time evolution of CCs and CSCs are represented in green and red respectively. In all cases (A, B, C, D), sessions were scheduled 7 days a week separated by 24 hours intervals along 30 sessions (without weekend interruptions). Notice that the vertical coordinate is represented in a logarithmic scale.

3.5.2 Hyperfractionation and lower total radiation doses

Since in many clinical scenarios radiation doses are mostly limited by damage inflicted at neighboring organs at risk and healthy tissues, it is important to estimate what amount of tumor control can be achieved when radiation dose distributions

are kept as low as possible. In what follows, a heterogeneous therapy for which the average radiation dose is approximately equal to $60Gy$, and a case of hyperfractionation (a type of scheduling consisting of comparatively many sessions, usually more than 1 per day, with low radiation doses [47], [53], see Section 1.2.2 in Chapter 1; cf. [202] for a specific study on GBM tumors) are considered. As a result, it will be shown that in these cases a heterogeneous radiation dose distribution also yields better results than its averaged homogeneous equivalent, even when tumor control is not achieved.

Consider first the case of low migration, CSC cycle duration equal to $96h$ and where the value of the total radiation dose is a bit less than $60Gy$ for heterogeneous therapies consisting of $2.3Gy$ for $p_a = 0.75$, $p_a = 0.50$ and $p_a = 0.25$ within the largest inner sphere containing 100% of CSCs and $1.8Gy$ in the rest of the tumor delivered 5 days a week along 30 sessions at 24 hours intervals with weekend interruptions. Computer simulations show that these radiation dosimetries fare better than their averaged homogeneous versions, where total AD lies between $56Gy$ and $57Gy$ for the values of p_a considered (see Figure 3.12 (A), (B) and (C)). On the other hand, similar results can be obtained for a lower total radiation dose when the time lapse between treatment sessions is also shortened. More precisely, consider the same cases but now for heterogeneous therapies consisting of $1.7Gy$ within the largest inner sphere containing 100% of CSCs and $1.2Gy$ in the rest of the tumor, delivered in two sessions per day, 5 days a week along 30 sessions 12 hours intervals, with weekend interruptions. While tumor control is not achieved, tumor radioresistance, measured in terms of the final proportion of CSCs, turns out to be lower for heterogeneous dosimetries than their averaged versions (see Figure 3.12 (D), (E) and (F)). Notice that in this case, the total averaged doses delivered by the heterogeneous dosimetries considered are much smaller than $60Gy$ (between $38Gy$ and $39Gy$ for the values of p_a considered).

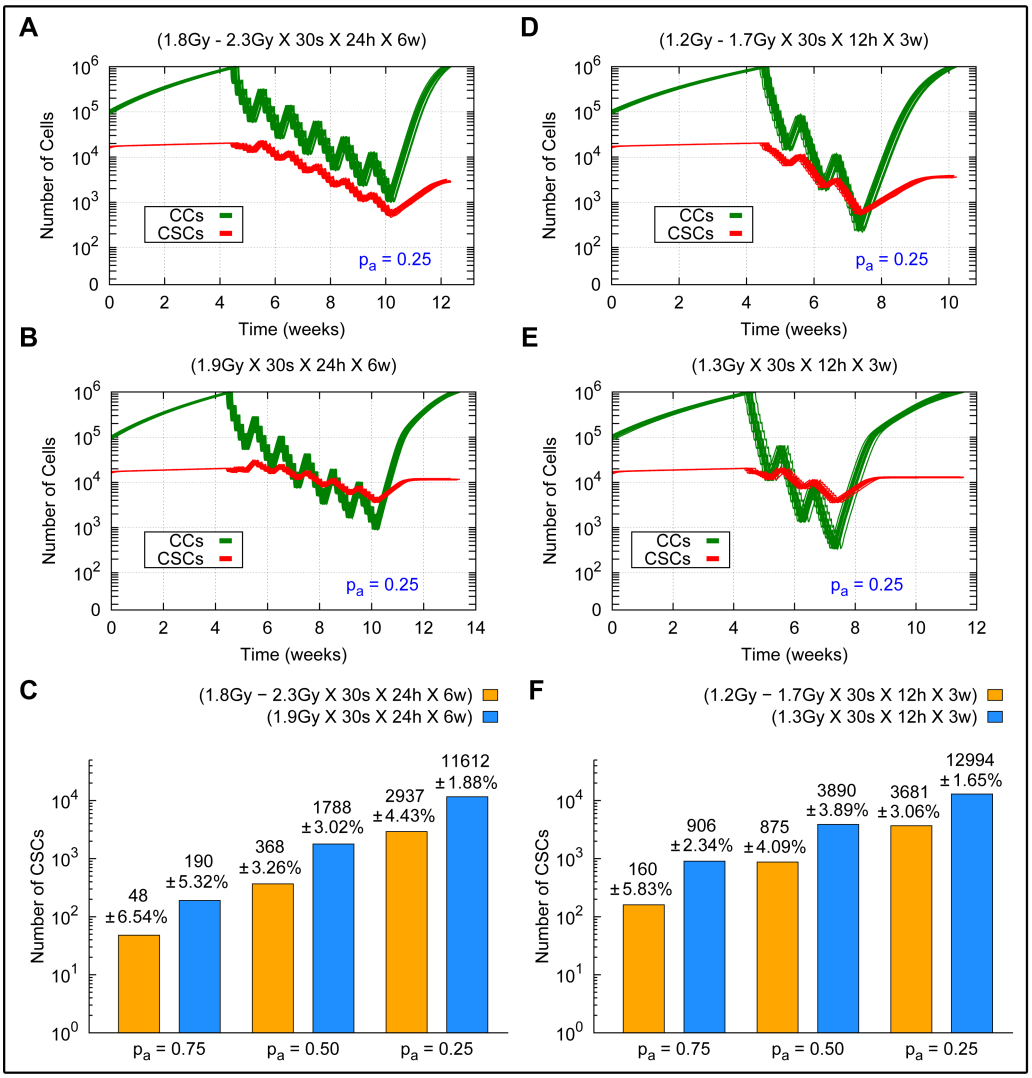

Figure 3.12. Comparing the effects of lower radiation dosimetries with and without hyperfractionation. Cell survival curves for 20 simulations (with different seeds of a random number generator) are shown in the case $p_a = 0.25$ for the low migration case and CSC cycle duration equal to $96h$. (Top) From left to right heterogeneous therapies consisting of $2.3Gy$ (A) and $1.7Gy$ (D) in the inner sphere, and $1.8Gy$ (A) and $1.2Gy$ (D) in the rest of the tumor respectively. (Middle) From left to right the averaged homogeneous therapies corresponding to $1.9Gy$ (B) and $1.3Gy$ (E) are represented. Radiation dose delivery been made according to 5 days a week, 30 sessions in total, at 24 hours (A, B) and at 12 hours (D, E) intervals with weekend interruptions. The time evolution of CCs and CSCs is represented in green and red respectively. (Bottom) Number of CSCs and the corresponding standard deviations at the end of the recurrence tumor stage (where about 10^6 cells is again obtained) for heterogeneous (yellow) and averaged homogeneous (blue) radiation therapies (C, F). Notice that the vertical coordinate is represented in a logarithmic scale.

Figure 3.12 shows that there is tumor recurrence in all cases. However, it turns out that the number of CSCs remaining at the end of the recurrence tumor stage after radiation therapy is lower than that existing prior to therapy in all cases. Thus, tumors surviving this therapy can be considered as less radioresistant than they were before radiation therapy started. An inspection of Figure 3.12 (C) and (F) quickly shows that in these current cases heterogeneous therapies yield better results than its averaged homogeneous counterparts previously discussed. For completeness, estimates on the total number of CSCs after treatments are concluded and recurrence appears for each case of p_a considered are provided (see Figure 3.12).

3.5.3 Dependence of results on model parameters: some remarks

To conclude this Section some remarks on the dependence of the model of tumor growth described, and the results derived from its analysis, on data and parameters assumed are provided as follows.

To begin with, the results obtained are not restricted to the figure selected (15%) for the proportion of CSCs within the tumor at the initial stage. In fact, they continue to hold as long as the more radioresistant tumor cell phenotype CSC represents a small percentage of the total tumor cell count. A particularly interesting limit case is that when tumor growth starts from a single CSC. Then for each value of p_a (0.75, 0.50, 0.25), CSC cycle duration ($96h$, $72h$ and $48h$) and migration rate k_{mig} ($0.025h^{-1}$, $1.75h^{-1}$) considered, the number of CSCs present when tumor has reached a size of about 10^6 cells (just before radiation treatment starts) is smaller than that corresponding to the cases considered in this work. For instance, in the case of CSC cycle duration equal to $48h$, $p_a = 0.25$, for the low and high migration cases the number of CSCs before the treatment starts is about 5956 and 14316 (with standard deviations of 129 and 530 over 20 simulations performed for each parameter set considered) respectively. The corresponding values for the case considered in this work are 21953 and 41629 respectively (see Tables 3.2 and 3.3). Moreover, the internal region where CSCs remain confined is smaller ($1120\mu m$ and $1840\mu m$ with standard deviations of $39.7\mu m$ and $71.4\mu m$ over 20 simulations

performed for each parameter set considered, respectively) than that reported in Tables 3.2 and 3.3. Hence any radiotherapy treatment that achieves tumor control in the cases considered also does so for tumors staring from a single CSC under assumptions above.

On the other hand, the assumption that the duration of cell cycle for CSCs is significantly longer than that of CCs has been used, a hypothesis commonly assumed in the literature (cf. for instance [142], [163], [164], [165], [166], [167], [168], [169], [170] and [171]). This fact notwithstanding, the proposed model can be used to examine also the opposite situation, that is the case where CSC cycle duration is equal or smaller than that of ordinary CCs. As an example, the cases where CSC cycle lasts 26 hours (respectively 18 hours), which is equal to (respectively less than) the 26 hours cell cycle selected for CCs have been considered. As one can expect, the inner core where most CSCs remain concentrated is now larger than when slow-cycling CSCs is assumed. In particular, in the case of low migration and for a CSC cycle duration of $26h$, such internal regions (where 100% of CSCs are located) range from 20% to 83% of the total tumor volume for values of p_a equal to 0.75, 0.50 and 0.25. Besides, when CSC cycle duration is taken to be $18h$ that internal volume further expands, ranging now between 23% and 100% of the total tumor volume. Additional details, including the number of CSCs present when tumor size reaches about 10^6 cells and the case of high migration, are provided in the Appendix C.

A case which has not been addressed in this work is cancer cell plasticity, a hypothesis that has been advanced to better understand the onset of resistance after therapy; see for instance [203], [204] and [205]. According to this scenario, in addition to CSCs giving raise to CCs by asymmetric division, a (supposedly small) percentage of CCs may transform to a CSC phenotype, possibly as a reaction to radiation therapy. Although little quantitative information about this process seems to be available as yet, including such type of process in this model is possible. To support this statement, a particular example has been studied. Specifically, a model situation where a small percentage of CCs are transformed to CSCs along the radiation treatment has been examined. As expected, any increase in the number of CSCs results in increased malignancy, measured in terms of higher

resistance to radiation therapy. However, the main conclusion obtained in this work that heterogeneous, tumor-adapted radiation therapies fare better than their corresponding averaged homogeneous versions continues to hold. Details on this study can be found in the Appendix C.

3.6 Discussion

Tumor heterogeneity is being increasingly recognized as a key obstacle to achieve successful tumor control, either by means of radiotherapy, chemotherapy or through the use of combined therapies. Indeed, it is well known that tumors at an advanced stage contain different tumor subpopulations, which might have been generated as a consequence of sequential mutations of one initial clonogenic line, or could result from the presence of cancer stem cells. Moreover, it is expected that such cell phenotypes may considerably differ in their biological and radiobiological properties, and in particular in their resistance to radiation (cf. for instance [23], [112], [141], [175], [206], [207]).

Accordingly, it has been proposed that the clinical prognosis of a given tumor would critically depend on the information that may be gathered about its internal heterogeneity, and more precisely, about the identification of regions within it with different sensitivities to a given therapy. In principle, once the spatial distribution of the various cell phenotypes coexisting in a tumor is known, and the resistance to therapy of each of these regions had been estimated, personalized strategies complementary to (or as a substitute to) surgery, could be designed to improve chances of clinical success. The latter can be understood either as total tumor eradication (the standard paradigm as of today) or as achieving instead a stable, chronically-controlled tumor burden where less aggressive lines keep at bay more resistant ones [208]. In either case, significant information towards a personalized treatment would be inferred from knowledge of the internal, non-homogeneous structure of a tumor and the resulting differences in therapy resistance corresponding to the regions thus identified.

In this work, a mathematical model of tumor growth has been proposed to gain insight about two key issues: how heterogeneity unfolds in a growing tumor, and

what type of radiation dosimetry is best suited to achieve control in heterogeneous tumors. Concerning the first issue, it has been described that substantial information about the evolution of spatial heterogeneity within a tumor can be retrieved from knowledge of a few key biological properties of the tumor cell phenotypes involved. In particular, it has been shown that the first place that a difference in cell cycle duration between a majority of ordinary cancer cells (CCs) and a minority of comparatively slow-cycling cancer stem cells (CSCs) leads to a concentration of CSCs in regions that can be a priori estimated. In the cases just discussed, such regions consist in an internal core within an expanding tumor, but the result would apply to other geometries as well. In particular, it can be extended to larger tumors with corrugated shapes and boundaries.

As has already been mentioned, the key assumption that CSCs have longer replication times than CCs is commonplace in the literature (see [142], [163], [164], [165], [166], [167], [168], [169], [170] and [171]). As a matter of fact, such assumption is naturally associated to the consideration of CSCs as a subpopulation of tumor cells which is able to rescue tumor growth after therapies have been delivered. This is related to the fact that standard radiation therapies preferentially target dividing cells (which are more radiosensitive), and thus spare those that have slower cycles or remain quiescent. Notice that the cell cycle duration could in principle be estimated, at least *in vitro*, for all cell phenotypes known to appear in a given tumor. Importantly, the spatial heterogeneity pattern thus observed does not depend so much on the precise values of such biological parameters, but rather on the fact that they are significantly different for the tumor cell phenotypes involved. As a consequence, the result obtained is robust with respect to fluctuations in cell cycle duration due to systemic factors.

A second result obtained is that, once information about functional heterogeneity had been obtained, tumor-tailored radiation dosimetries can be designed to improve the treatment outcome. As has been shown, heterogeneous radiation dosimetries do better than homogeneous ones when regions occupied by different radioresistant tumor subpopulations can be identified, and this is the case when more radioresistant phenotypes replicate at a lower pace than less resistant ones. Again, this is a standard assumption of the CSC theory of tumor resistance to

therapies. Interestingly, this result holds when the more radioresistant phenotype is able to sustain unlimited replication as in the case of CSCs, as opposed to the limited number of replications commonly assumed on CCs. The previous statement holds true, no matter the type of scheduling considered (with or without weekend interruptions) or the precise result pursued, being it total tumor eradication, controlled recurrence or palliative treatment. It should be noticed that the comparative advantage of heterogeneous radiation dose distributions deserves some consideration, since to this day homogeneous dosimetries continue to be those being commonly implemented worldwide.

It is worth to stress that the model described in this Chapter is quite robust with respect to changes in data and parameter values. In particular, the conclusions arrived in this work remain in force when CSC and CC cycle durations undergo considerable changes, as long as CSC cycle is significantly slower than that of CCs. Also, CCs and CSCs migration rates are allowed to undergo substantial changes (corresponding for instance to slow and fast migration processes) as far as both tumor cell phenotypes share a similar migration rate. Moreover, the results obtained continue to hold when changes in the choice of the radiosensitivity parameters α and β in (3.1) are allowed, or when different fractions of the minority phenotype (CSC) are assumed. For instance, such results are not confined to the choice made for the assumed percentage (15%) of CSCs present at an early stage of tumor growth. They continue to hold if a different figure for that proportion is taken, as long as CSCs remain a small fraction of the total tumor population at that stage.

On the other hand, cancer cell plasticity has recently received considerable attention [203], [204], [205]. As a consequence, a particular example where in addition to CCs being generated by CSCs with asymmetric division, a small percentage of CCs are transformed to CSCs as a consequence of radioresistance to therapy has been investigated. The main result obtained in this work that heterogeneous, tumor-adapted radiation therapies fare better than their corresponding averaged homogeneous versions continues to hold in this case.

To conclude a discussion on some of the limitations of this work, as well as on possible extensions thereof is provided as follows. To begin with, more research

is needed to understand the possible mechanisms that can be responsible for slow cycling of CSCs. Particularly relevant in this context would be to ascertain if slow cycling can, at least in some cases, be established as an intrinsic property of CSCs or if it could alternatively be induced by systemic feedback in the course of tumor growth. Interestingly, even if CSCs are assumed to cycle faster than CCs, the proposed model still shows that heterogeneous dosimetries adapted to the resulting tumor heterogeneity continue to outperform standard homogenous therapies currently in use.

A general conclusion that follows from this study is that detailed information about intratumoral heterogeneity is needed in order to implement efficient dose-painting techniques in clinical practice. In particular, in this work a clear dependence on tumor heterogeneity of the radiation doses needed to achieve tumor control has been obtained. In fact, the inner tumor regions where more radioresistant tumor cell phenotype remains confined are shown to strongly depend on CSC cycle duration and their probability of asymmetric division. In the particularly unfavorable assumption of fast CSCs cycling, this region may rank from 20% to 100% of the total tumor volume. In this latter situation, a worst-case scenario corresponding to a high and homogeneous radiation dose being prescribed and only limited by neighboring organs at risk tolerance, is recovered that corresponds to current clinical practice. The results obtained in this work suggest that such situation could be considerably improved in many cases if and when sufficient information about key different biological and radiobiological properties of the tumor cell phenotypes present in a given tumor is available, be it either by estimating patient-specific parameters or by means of medical imaging techniques.

Finally, it looks feasible from a mathematical viewpoint to address within this framework situations where larger tumors are considered, a number of cell phenotypes coexist there due to mutations, and other effects (immune response, nutrient limitation, etc.) are accounted for. For example, the modeling framework selected in this work permits simulations to be scaled up to cubic centimeter sizes, though at the expense of lower spatial and functional resolution, and more computing resources. It can also be used to construct hybrid models, zooming in at the cell scale in regions of interest. In particular, it has be chosen to represent each cell

individually to exclude averaging effects when studying the relation between tumor heterogeneity and simulated radiation outcomes. However, this work could provide a starting point towards the study of the more general situations described above.

Chapter 4

A decision-support system to select dosimetry plans in radiotherapy

"... The lack of real contact between mathematics and biology is either a tragedy, a scandal, or a challenge, it is hard to decide which ..."

Gian-Carlo Rota (1932-1999)

4.1 Abstract

Radiotherapy treatment plans are selected by radiophysicists and clinicians out of a small number of tentative plans simulated on a commercial treatment planning system (TPS). In this work, a decision-aid procedure to assist in the choice of the plan to be applied has been proposed. This is done as follows. For any tentative plan, three different estimates of radiation dose distributions are defined on the planning target volume, nearby organs at risk and healthy tissue respectively. These are then combined to build a figure of merit, the Dose Distribution Index (DDI), which provides a score for any such tentative plans. To do that, only dose volume histograms (DVHs) obtained from TPSs and the radiation dose prescribed on the tumor are used. DDI provides a straightforward, user-friendly tool to compare different radiation dosimetry plans with similarly looking DVHs. In fact, small differences in the number, incidence angles or intensities of radiation beams, yield significantly different scores for each of the partial indexes in the DDI. On the

other hand, DDI can be computed for any type of treatment planning system in use, irrespective of tumor type and localization, and allows to compare dosimetry plans obtained from different commercial planning systems or corresponding to different irradiation techniques.

In particular, using DDI several tentative plans for a given radiotherapy patient, each corresponding to a different radiation dose distribution, can be quantitatively compared. In order to test this methodology, the plan suggested by the DDI was compared with those actually implemented in a number of centrally-located brain tumor patients. For any of them, three different planning strategies were considered, out of which one was selected and eventually delivered. The DDI was then computed for any of those alternative choices, and a considerable degree of coincidence was observed. Besides, the reason for possible discrepancies, when they occurred, was discussed. To further assess the information provided by this tool, a sequence of hypothetical treatment plans for one prostate cancer patient was also examined, and a clear correlation between DDI scores and clinical assessment was observed.

4.2 Introduction

A key question in radiotherapy clinical practice is how to deliver by means of the devices actually in use (linear particle accelerators, LINACs) a radiation dose distribution that meets clinical requirements in a satisfactory manner. To that end, a LINAC commercial treatment planning system (TPS) is used, on which several tentative treatment plans for any diagnosed patient are tried, one of which is eventually selected. This last is expected to achieve best tumor control, and to induce little side effects on neighboring critical regions. However, TPSs are not equipped with standard decision-aid tools to quantify the difference between two tentative plans, nor the impact of small modifications on any of the tentative plans considered. The choice of a dosimetry plan is therefore made after examination of a few plans, or of successive modifications of a unique tentative plan, simulated in a TPS. Therefore, in the absence of widely accepted quantitative criteria, different persons may possibly make different choices from the same set of dose volume histograms (DVHs). As a consequence, different specialists may suggest different

treatment plans for a given patient, which makes difficult to establish a standard planning procedure to compare radiotherapy results. In fact, the differences in DVHs and isodose curves corresponding to different tentative plans are usually small, and thus a merely subjective selection made among them may not be easy to justify (see Figure 4.1 below and Figure 2.1 in Chapter 2). Therefore the development of user-friendly, computer-assisted decision tools could be quite useful as a benchmark quality test for clinical decisions.

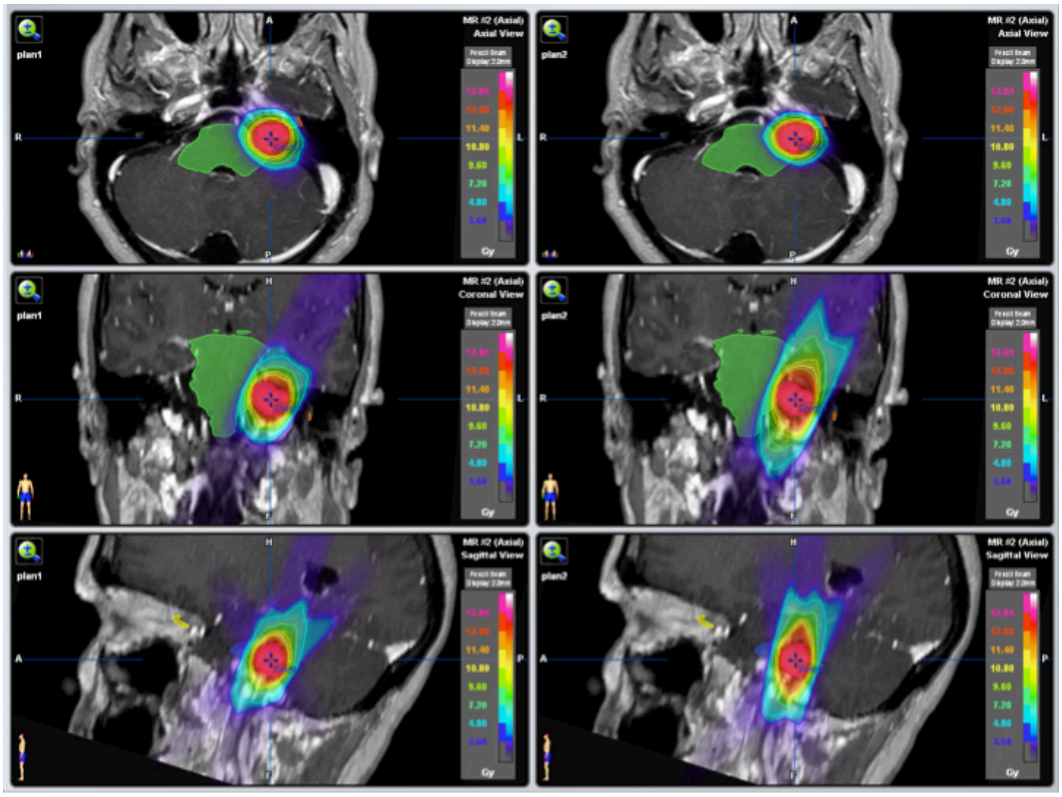

Figure 4.1. From left to right: magnetic resonance images (MRI) of radiation isodose curves corresponding to two different external beam radiotherapy tentative plans for a same patient. [This image is used under permission of the Hospital Universitario Puerta de Hierro Majadahonda, Madrid, Spain].

As discussed in Chapter 1, the search for a single figure of merit to quantify the quality of a radiotherapy treatment plan has been actively pursued, with only partial success to this day. During that process, several figures have been proposed to assess dosimetry plans, paying attention to radiation dose coverage, conformity

and dose gradient as separate or combined overall scores (see for instance [27], [28], [29], [30], [31], [32], [33], [34], [35], [36], [37] and [38]). However, all such figures have been reported to suffer from different limitations. In particular, the indexes proposed may introduce false positives (cf. [27], [29], [32] for a detailed discussion on HI and CI), are not sensitive to small modifications sequentially introduced (a common situation in the planning process), depend on many parameters (cf. [31], [33], [37], [39]), provide ambiguous scoring due to averaging effects [34], are difficult to extend for any type of TPS, and often are not easy to implement [38].

In this Chapter a decision-aid tool to assist in the choice of a radiotherapy treatment plan is proposed. Such tool uses only data extracted from the DVHs provided by commercial TPSs and the radiation dose prescribed on the PTV. Specifically, the DDI consists in a global score that will be formulated in Section 4.3. In Section 4.4 the DDI is computed in a series of clinical cases as part of a retrospective study. These correspond to centrally-located brain tumors, situated at internal regions close to several organs at risk (OARs), and for which different tentative treatment plans were simulated by means of a TPS: *iPlanRT Dose v4.1 TPS (BrainLAB AG, Germany)*. In each situation, three tentative plans were simulated for each patient, one of which was eventually selected. Such plans will be graded by means of the DDI and that which scores best will be selected and then compared with the actually implemented treatment plan. While considerable agreement between both choices is observed, discrepancies are also noticed, and some underlying patterns are identified when this occurs. On the other hand, to further assess the information provided by the DDI, a sequence of hypothetical treatment plans for one prostate cancer patient is also discussed. In this case, any such plan can be clinically evaluated in an easy way, and a good agreement between clinical assessment and DDI scores is observed. Finally in Section 4.5 a user-friendly graphic interface to implement the DDI in a TPS is presented. In fact, by means of this computer application, radiophysicists can compare and analyze different tentative plans in a straightforward way, and comparison output data can be displayed and saved for future statistic analysis. A discussion on the main results can be found in a concluding Section 4.6.

4.3 A decision-aid tool: the Dose Distribution Index

As mentioned above, differences between tentative treatment plans are often small. Moreover, the large amount of parameters to be considered during the planning process renders deciding among simulated alternatives a very difficult task. In this Section a decision-aid system, consisting of a Dose Distribution Index (DDI) to provide a quantitative estimate on any tentative treatment plan, is formulated. In this manner, different plans can be compared in a precise way. This quantitative index (DDI) accounts for the main dosimetry features (radiation dose coverage, conformity and homogeneity) considered in clinical practice and allows to quantitatively compare the results of even minor changes introduced in a tentative dosimetry plan. One can at once realize the separate impact on PTV, OARs and HT of any such modification, and use this information as a guidance to improve any given tentative plan.

For convenience of the reader, before defining the Dose Distribution Index, a table describing the parameters used in its formulation is provided (see Table 4.1).

Symbol	Description
D_p	Prescription radiation dose on the PTV
$D_{p\%}$	Percentage of the D_p
D_M	Maximum dose received for each structure involved
D_m	Maximum dose received at least by 100% of the PTV
N	Number of OARs involved
$\|PTV\|$	Volume of the planning target
$\|OARV_i\|$	Volume of the *ith* OAR
$\|HTV\|$	Volume of the HT
$V_T(D)$	DVH curve of the PTV
$V_{O,i}(D)$	DVH curve of the *ith* OAR
$V_H(D)$	DVH curve of the HT
$w_{O,i}$	Weight of the *ith* OAR term
w_T	Weight of the PTV subindex
w_O	Weight of the OARs subindex
w_H	Weight of the HT subindex

Table 4.1. Quantities used to define the DDI.

In particular, DDI is defined as a weighted sum of three main terms, which respectively measure radiation dose distributions within the PTV, OARs and HT for a given tentative treatment plan. The first of those terms estimates how well the proposed radiation dose distribution covers the PTV. In fact, it computes the ratio between the area under the dose-volume curves for the DVH considered, and that corresponding to the ideal case of constant prescription dose (D_p) uniformly delivered over the PTV (see Figure 4.2). Such a perfect conformation provides the best coverage of the PTV and would yield a value of one for that ratio. In this way, an estimate is obtained of the deviation with respect the case of perfect conformation over the PTV, which corresponds to $D_m = D_p = D_M$. On the other hand, the curvature in the DVH may be useful to compare different critical dosimetry points. For that reason, a factor (D_m/D_M) is also introduced. Thus, the PTV term (I_T) for a tentative plan is defined as follows

$$I_T = \left| 1 - \left(\left(\frac{\int_0^{D_M} V_T(D)\, dD}{D_p \cdot |PTV|} \right) \cdot \left(\frac{D_m}{D_M} \right) \right) \right|. \tag{4.1}$$

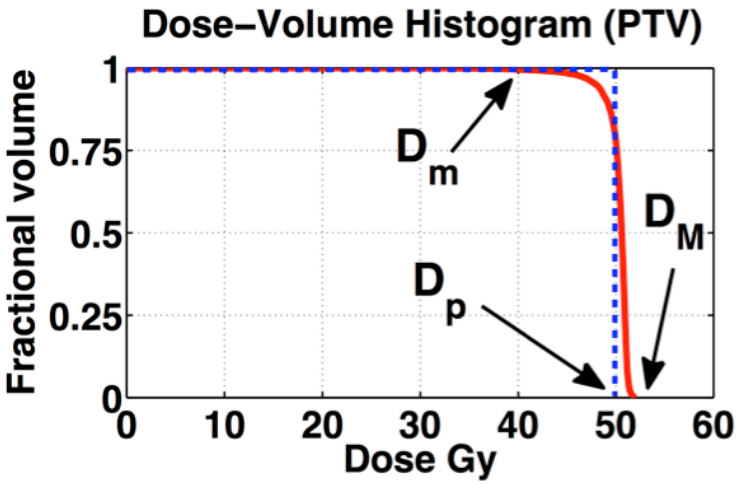

Figure 4.2. A DVH corresponding to a PTV where some of the parameters in Table 4.1 are indicated.

Notice that an optimal treatment plan over the PTV would yield $I_T = 0$. This case corresponds to a homogeneously irradiated tumor with a prescription dose D_p, which is the aim in current clinical practice.

On the other hand, in the case of OARs and HT considered in the second and third terms at the DDI, the idea is quite similar, but now the ideal cases correspond to a situation where the area under the DVH is close to zero, meaning that the radiation dose received by these critical structures is very low (see Figure 4.3). Moreover, the ratio $(D_M/D_{p\%})$ is included in order to weight the radiation dose received by OARs and HT against a fixed percentage of the prescribed dose $(D_{p\%})$ on the PTV. Clearly, one aims at situations when these ratios are also close to zero. The subindexes for OARs (4.2) and HT (4.3) will be referred as I_O and I_H respectively, and are defined as follows

$$I_O = \frac{1}{N}\sum_{i=1}^{N}\left[w_{O,i}\cdot\left(\frac{\int_0^{D_M} V_{O,i}(D)\,dD}{D_{p\%}\cdot|OARV_i|}\right)\cdot\left(\frac{D_M}{D_{p\%}}\right)\right] \tag{4.2}$$

and

$$I_H = \left(\frac{\int_0^{D_M} V_H(D)\,dD}{D_{p\%}\cdot|HTV|}\right)\cdot\left(\frac{D_M}{D_{p\%}}\right). \tag{4.3}$$

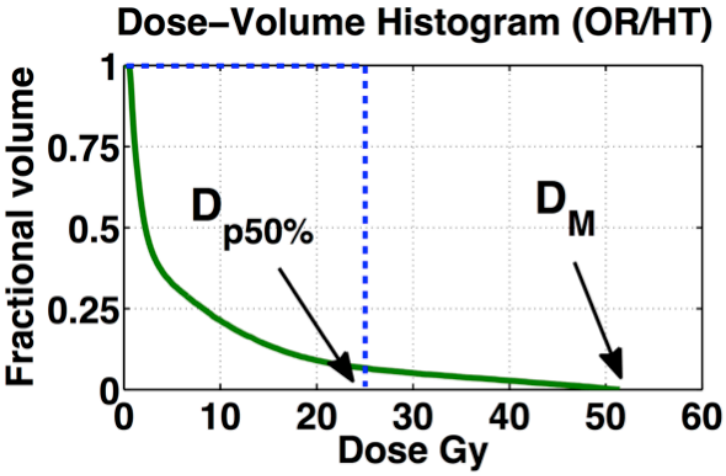

Figure 4.3. DVHs corresponding to an OAR or HT where some of the parameters in Table 4.1 are indicated.

In what concerns OARs and HT terms, an optimal treatment plan would yield $I_O = I_H = 0$, which would result in no irradiation on such critical structures. These three subindexes (4.1)-(4.3) are combined to obtain the Dose Distribution Index defined as follows

$$DDI = w_T \cdot I_T + w_O \cdot I_O + w_H \cdot I_H, \tag{4.4}$$

where w_T, w_O and w_H are weight parameters to enhance the relative importance of each term in (4.1), (4.2) and (4.3) respectively. Notice that different weights may

also be associated to different OARs in (4.2). An ideal treatment plan would give $DDI = 0$, which corresponds to perfect irradiation on the PTV and no irradiation at all over the OARs and HT. It should be noted that DDI could be easily extended to include several PTVs, similarly to what has been done for the OARs in (4.2). For instance, this may be the case when a heterogeneous PTV is considered and non-homogeneous radiation doses are required on it [19].

In order to evaluate how the DDI would work in clinical practice, a retrospective study has been performed over a number of clinical cases already treated in Hospital Universitario Puerta de Hierro Majadahonda, Madrid, Spain. In this study, 30 patients diagnosed with centrally-located brain tumors (14 Meningioma, 10 Neuroma and 6 Adenocarcinoma) were selected. In all cases, several OARs are closely located to the PTV. For any patient, three tentative plans were prepared and recorded during the ordinary treatment planning process over the same TPS: *iPlan RT Dose 4.1.1 (BrainLAB AG, Germany)*. Out of the three tentative plans considered, one was selected and delivered. This tentative plan will be referred in the following as the applied plan (AP). For any fixed choice of weight parameters, the plan achieving the lowest DDI value is obtained, (the DDI plan, referred as $DDIp$). Then the selected AP and the $DDIp$ were compared. The corresponding study is described below.

4.4 Results: comparing different dosimetries of clinical cases

A first result is that if all weight parameters in (4.2) and (4.4) are set all equal to one (so that dose impact on PTV, OARs and HT are considered as equally important), AP and $DDIp$ agree in 18 out of the 30 cases considered. This suggests that in the remaining 12 cases different importance has been assigned to different anatomical structures during the planning process. To make this point precise, the cases where AP and $DDIp$ did not coincide were examined. In 11 of these 12 cases AP can be shown to agree with a $DDIp$ if values of weights in (4.4) are not assumed to be all equal to one. Thus AP and $DDIp$ will still coincide in most of such cases if dose impact on PTV, OARs and HT are no longer assumed as equally important.

As shown in Table 4.2 if two such parameters are equal to one, a value of the third weight can be obtained such that the corresponding $DDIp$ agrees with that actually applied in 11 of the 12 cases under consideration. There remains a case where no such weight combination exists, although AP and $DDIp$ eventually agree if two (not just one) of the weight parameters in (4.4) are allowed to be different from one.

$\boldsymbol{w_T}$	1.0	1.0	1.5	1.0	1.5	1.0	2.0	1.0	1.0	1.1	1.0
$\boldsymbol{w_O}$	2.5	1.0	1.0	1.0	1.0	0.5	1.0	0.5	1.0	1.0	0.5
$\boldsymbol{w_H}$	1.0	0.5	1.0	2.0	1.0	1.0	1.0	1.0	0.5	1.0	1.0

Table 4.2. A list of possible values of weight parameters in (4.4) for which $DDIp$ and AP agree when only two of them are set equal to one.

It should be noted that the choice of weights in Table 4.2 does not need to be unique. Therefore the same dosimetry plan can be selected upon different assumptions on the relative importance attributed to impact achieved on PTV, OARs and HT.

To illustrate further the use of the DDI to monitor tentative treatment plans, the following case is now examined. A patient with prostate cancer has been selected, for whom four different tentative plans are examined. Specifically, the following cases have been sequentially considered *i)* two parallel and opposite beam fields, *ii)* three beam fields, *iii)* five beam fields and *iv)* seven beam fields, and DDI values were computed for any of them. In all situations, conformal beam technique was used to clearly observe the dose distribution changes for the different tentative plans, and to avoid optimization compensation possibly introduced by intensity-modulated radiation therapy (IMRT) techniques than can blur this test. The calculation was run using a commercial TPS: *XiO 4.62.00 (CMS-ELEKTA)*. For simplicity, only some of the organs at risk involved (Bladder, Rectum and Penile Bulb) as well as the PTV (see Figure 4.4) will be considered. As can be expected, when the number of fields increases the score of these tentative plans (measured by means of the corresponding term in (4.4)) over the OARs decreases.

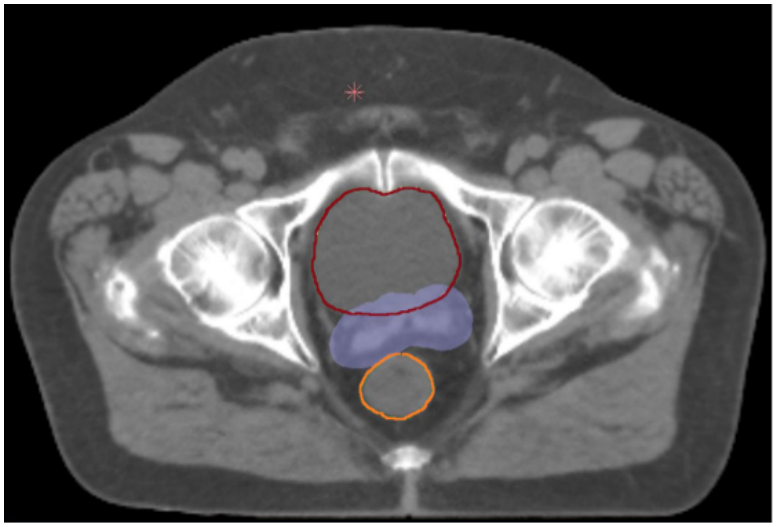

Figure 4.4. A CT scan of a patient diagnosed with prostate cancer, where Bladder (red), Rectum (orange) and PTV (purple) are represented. [This image is used under permission of the Hospital Universitario Puerta de Hierro Majadahonda, Madrid, Spain].

The first case (Plan A), where only two opposite fields have been used, produces the greatest effect on the PTV, but turns out to be the worst with respect to OARs (see Figure 4.5). As the number of fields increases, radiation effects on the OARs are sequentially reduced, but so is the effect on the PTV.

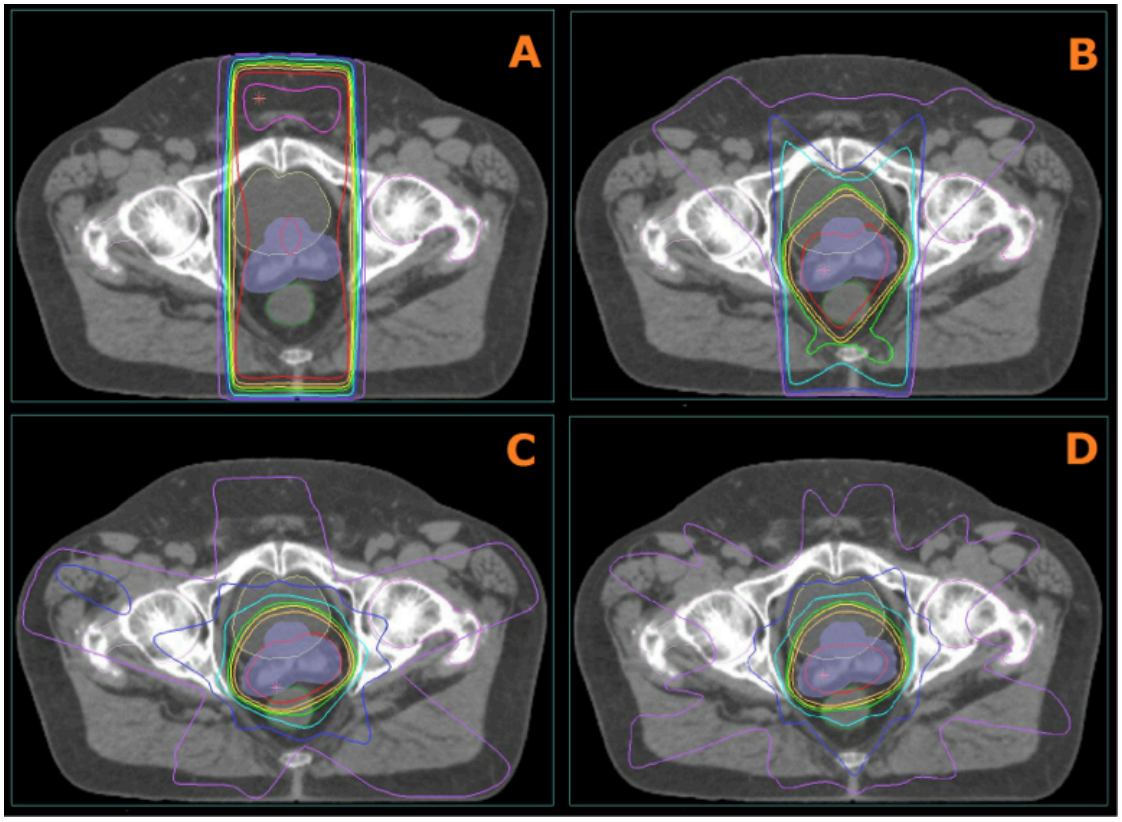

Figure 4.5. Representation of OARs and the PTV for a patient diagnosed with prostate cancer (Bladder (red), Rectum (orange) and PTV (purple)). Isodose curves (corresponding respectively to 30%, 50%, 70%, 85%, 90% and 95% of the prescription dose (D_p)) for each tentative plan: A) two parallel and opposite fields, B) three fields, C) five fields and D) seven fields are provided. [This image is used under permission of the Hospital Universitario Puerta de Hierro Majadahonda, Madrid, Spain].

An inspection of the DVHs for each tentative plan shows that if the effect on the PTV is given total priority, the best choice corresponds to Plan A, followed (in this order) by Plans B, C and D (see Figure 4.6). On the contrary, when lowering effects on OARs were given highest priority; the best choice would be Plan D, followed by Plans C, B and A, respectively (see Figure 4.7).

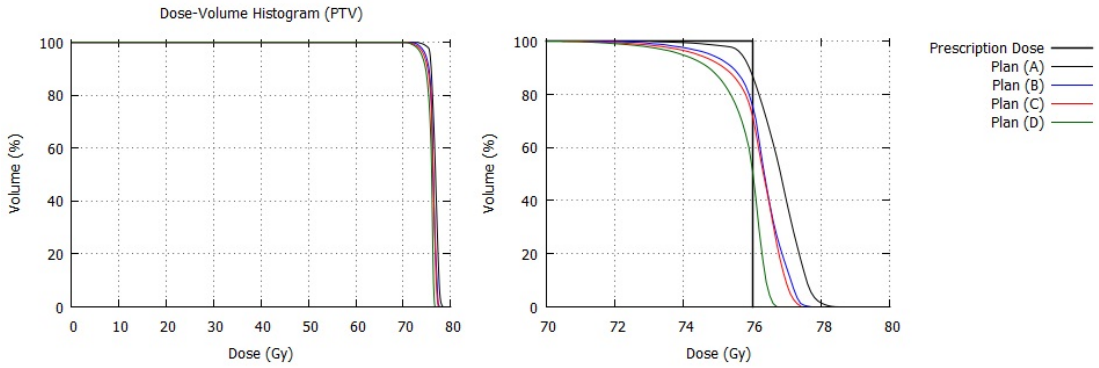

Figure 4.6. (Left) DVHs of the PTV for each tentative treatment plan. (Right) A magnification of previous DVHs to better display effects corresponding to higher radiation doses. Notice that the tentative treatment plan with larger effect on the PTV is Plan A followed by Plan B, Plan C and Plan D respectively.

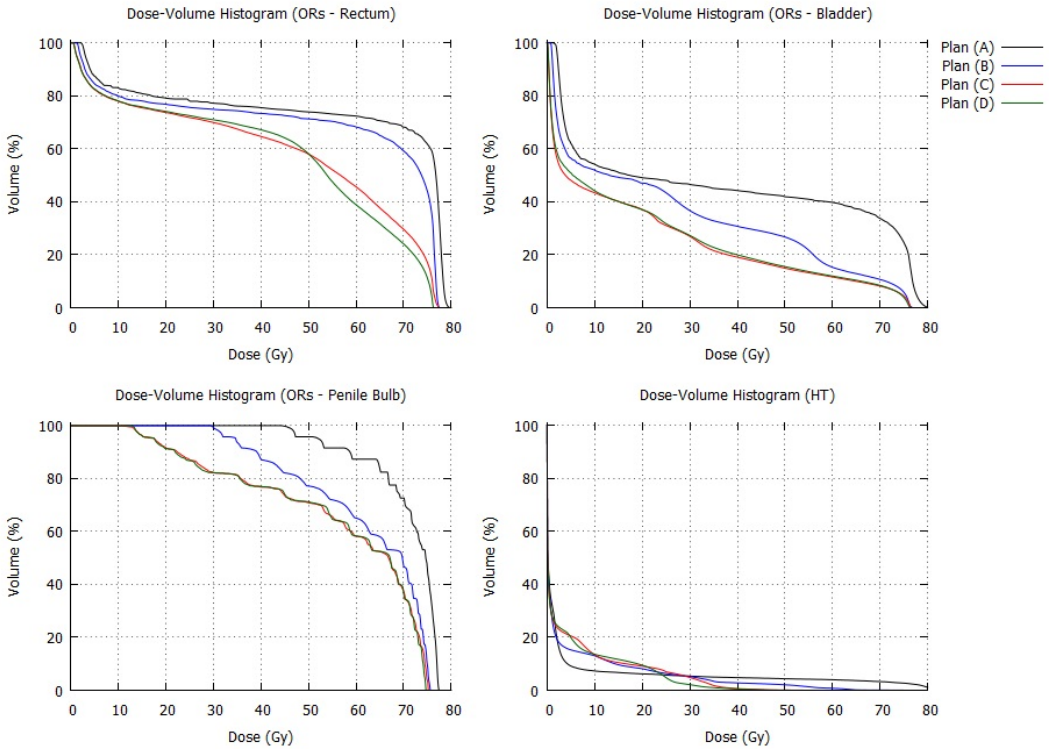

Figure 4.7. DVHs corresponding to OARs and HT for each tentative treatment plan in the case considered. Notice that the tentative treatment plan with less effect on the OARs and HT is Plan D followed by Plan C, Plan B and Plan A respectively.

Finally, in Table 4.3 the values of the proposed DDI in (4.4) and each term (4.1)-(4.3) for these tentative plans are given. In particular, when all weights in (4.2) and (4.4) are considered equal to one the best tentative plan turns out to be Plan D, which produces lowest effect on OARs, but has the lowest effect on the PTV as well. However, if tumor control (hence impact over the PTV) is retained as the primary goal, the best choice is Plan A. In fact, Table 4.3 shows that the values provided by each term in (4.4) are consistent with information provided by the corresponding DVHs.

	$I_{T,i}$	$I_{O,i}$	$I_{H,i}$	DDI
Plan A	0.0437	1.8105	0.2685	2.1226
Plan B	0.0580	1.5697	0.1872	1.8149
Plan C	0.0672	1.5859	0.1216	1.7746
Plan D	0.0705	1.4527	0.1092	1.6324

Table 4.3. Values of each term (4.1), (4.2) and (4.1) and the DDI (4.4) for the four tentative plans (when all weights are equal to one in (4.2) and (4.4)) of the example considered.

It should be mentioned that these results are part of a preliminary study to check the performance of the DDI on different clinical situations. Currently, a more exhaustive investigation of the performance of this tool in current clinical practice is being conducted. To do that, a user-friendly graphic interface has been created, where clinicians and radiophysicists can easily compare several tentative treatment plans in daily clinical practice. In the next Section more details about this software are provided.

4.5 A user-friendly graphic interface

In order to make simpler the use of the Dose Distribution Index in current clinical practice, a computer application has been programmed. This software, referred as $DDIapp$ for simplicity, is a tool to compare tentative plans defined on a commercial TPS. $DDIapp$ only uses the DVHs and the D_p on the PTV as external data defined in the planning process. The functionality of this decision-aid tool can

be accessed by a graphical user-interface (GUI) that includes, as its main feature, visualization and analysis of the comparison results (see Figure 4.8). The intuitive graphical interface of *DDIapp* follows a natural workflow and does not require programming for its use. In the following, this user-friendly software to compare different tentative plans is described and its main features are highlighted.

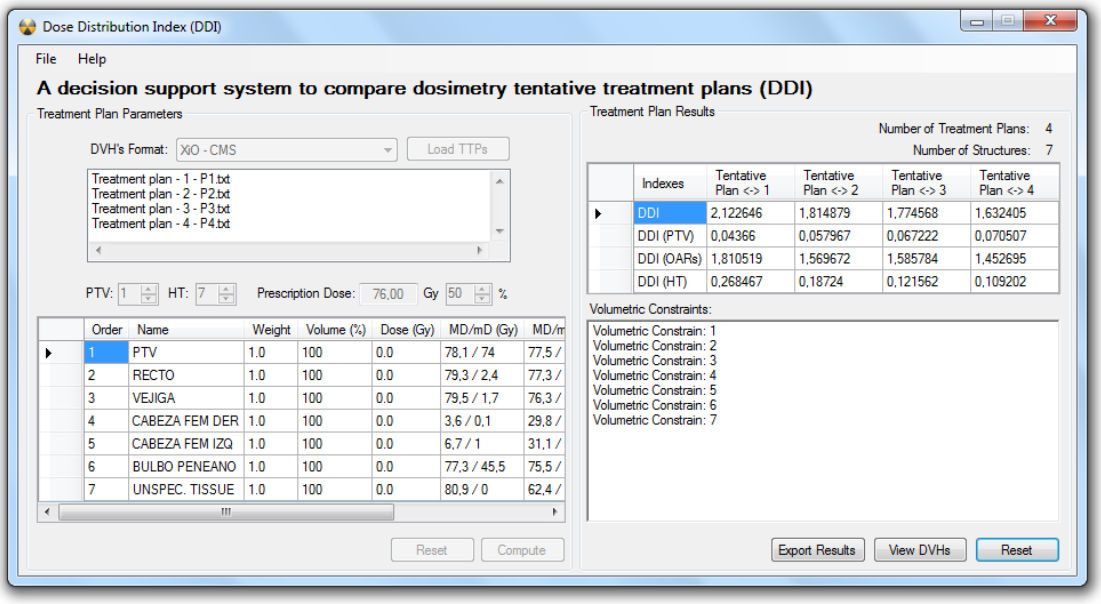

Figure 4.8. *DDIapp* graphical user interface (GUI).

To begin with, the first step to use *DDIapp* is to import the data files containing the information of the DVHs of each tentative plan that will be compared. In general, TPSs are equipped with options to export the DVHs of any tentative plan in different output formats, which are used as input data in the *DDIapp*. As required by radiophysicists, *DDIapp* is able to interpret these formats without requiring an edition of these files by the user. This simple feature is very useful to save time and make the comparison process easier. It should be noted that *DDI* is designed to compare tentative plans prepared for a same patient. Thus such plans should have the same number of structures, and be planned considering the same D_p on the PTV. Once the information of the DVHs has been introduced, the user has to provide the parameters of the *DDI* and the D_p. In addition, some dose volume constraints can be defined in order to account for further clinical

requirements as explained below. Then the comparison results are obtained, and can be visualized and saved for further discussion.

The graphical user interface of *DDIapp* provides a number of options to assist radiophysicists and clinicians in the process of analyzing tentative treatment plans (see Figure 4.9).

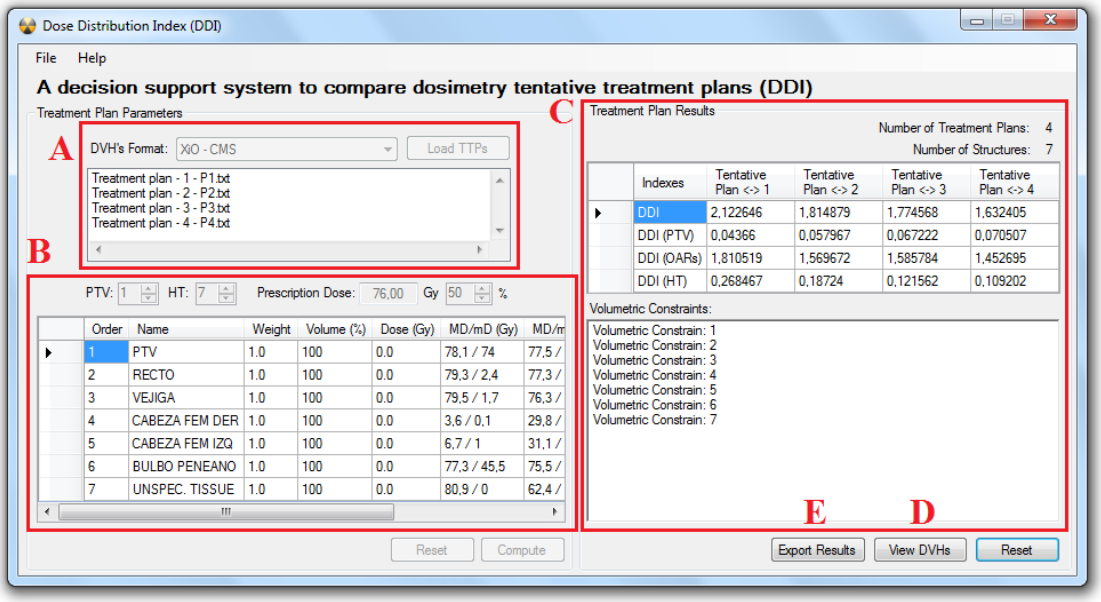

Figure 4.9. *DDIapp* graphical user interface and the representation of modules: data files import (A), parameters editor (B) and comparison viewer (C). The dose volume histograms viewer (D) and export result files (E) options are also provided.

The main features of the *DDIapp* are described as follows:

A. Data files import: At this moment, *DDIapp* is able to interpret the DVH data files provided by different TPSs currently in use in Hospital Universitario Puerta de Hierro. DVHs can be exported both in an accumulative or differential form, which can be handled by *DDIapp* without requiring an edition of these files by the user. Therefore, different tentative plans for a same patient defined in any of such TPSs can be compared.

B. Parameters editor: Once the DVH data files have been loaded, all structures defined on the corresponding tentative plans are listed. At that moment, the

user should provide the value of all parameters involved in the comparison process. To begin with, the HT and PTV have to be selected. Then, the D_p defined in the planning process has to be provided. Moreover, the weights used in the definition of the DDI (see (4.2) and (4.4)) for each OAR, HT and PTV can be selected to consider different clinical requirements. In addition, for each tentative plan and each structure involved a dose volume constraint can be incorporated. For instance, it may be required that 95% of the PTV should receive less than a given radiation dose. These constraints do not have influence in the calculation of the DDI. In fact, by means of dose volume constraints radiophysicists can pay attention to relevant aspects on the DVH plots and decide which tentative plan (if any) satisfies such constraints.

C. Comparison viewer: The comparison results are represented in two forms. In the first, the values of the PTV (4.1), OARs (4.2) and HT (4.3) terms, and the DDI (4.4) are provided. Then, the tentative plans can be sorted by each of these terms and compared. On the other hand, for each tentative plan a description of the dose volume constraints (if required) is provided. In particular, to repeat the process changing any of the parameters or to add another tentative plan, there is no need to re-enter all the information. Only the parameters that the user wants to modify should be fed in.

D. Dose volume histograms visualization tool: For user convenience, $DDIapp$ is equipped with a tool that provides a visualization of the DVHs of tentative plans being compared (see Figure 4.10). DVHs can be viewed in an accumulative or differential form. On the other hand, for comparison purposes several DVHs for different tentative plans can be superposed to better realize the differences between them.

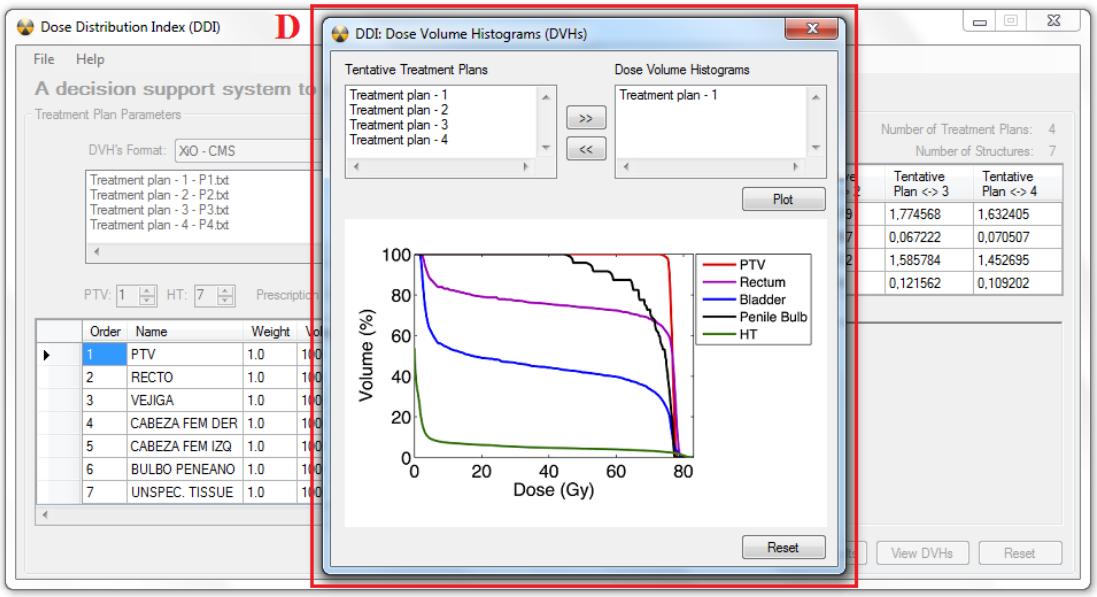

Figure 4.10. Dose volume histograms visualization tool (see also Figure 4.9).

E. Exporting result files: To save the workspace for future uses, an additional tool is provided (see Figure 4.11), where a file with the whole information of the current process can be saved. In a similar way, *DDIapp* can restore these workspace files starting the process exactly in the same point.

The programming language used to implement this software was C++, which has a wide range of compilers that run on many different platforms that support it. Moreover, codes that exclusively use the C++ standard library can be executed on many environments. On the other hand, procedures to interpret more DVH output files generated from different TPSs can be included in a simple way keeping to the same general process.

In summary, this user graphic interface provides all features of the *DDI* in an easy and simple way. The radiophysics department of Hospital Universitario Puerta de Hierro is currently testing this software, an exhaustive and detailed study of its use in current radiotherapy clinical practice is being prepared. The results obtained from this study will be reported in future works.

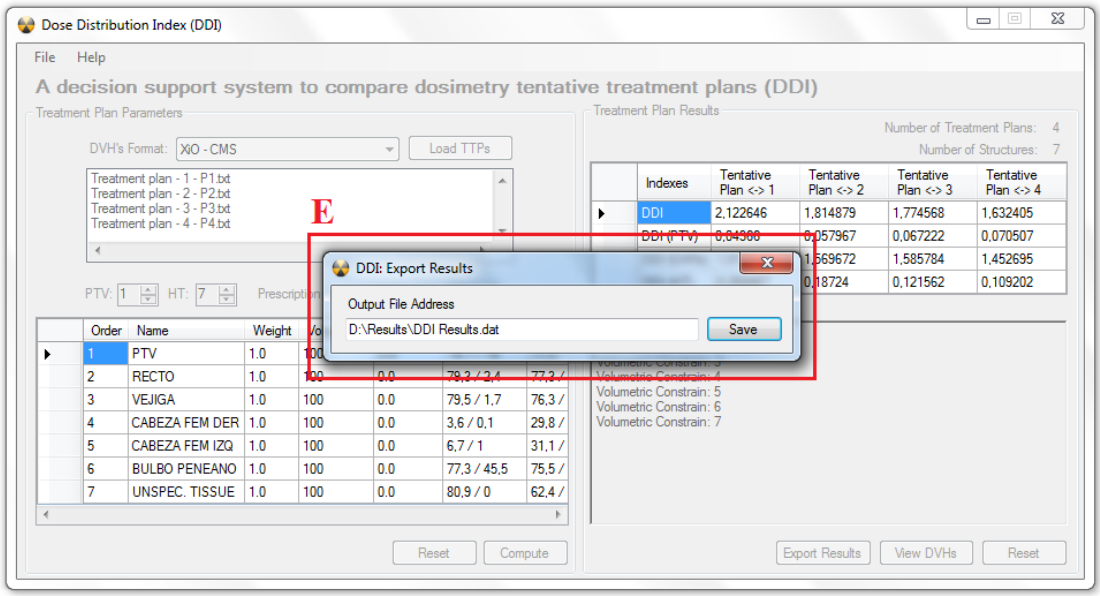

Figure 4.11. Exporting result files (see also Figure 4.9).

4.6 Discussion

The availability of commercial treatment planning systems allows radiophysicists and radiation oncology departments to virtually explore different dosimetry plans for each radiotherapy patient. In any such plan, detailed information concerning DVHs and isodose curves is provided. However, TPSs are not equipped with standard decision-aid tools to quantify the impact of small modifications on the tentative plans considered. The choice of a dosimetry plan is therefore made after examination of a few tentative plans, or of successive modifications of a unique plan, simulated in a commercial TPS.

Bearing these facts in mind, in this Chapter a decision-aid tool (DDI) has been presented to assist clinical personnel to estimate the consequences of modifications, however small, on any tentative plan under consideration. The decision-support tool thus provided is easy to handle and uses exclusively the information of DVHs and the D_p on the PTV exported from a TPS. It also permits simultaneously considering the particular results of the different subindexes of the DDI corresponding to different radiation dose distributions and the DVHs involved.

It should be remarked that DDI is not meant to be a replacement for personal decisions along the treatment planning process. Instead, it is expected to provide a better assessment of the impact of such decisions over the anatomical and pathological regions considered. In particular, the DDI will not tell the planning person what his/her choice of dosimetry plan should be, nor what criteria should be assumed to produce such plan. Instead, DDI provides precise estimates on the differences between priorities made and the tentative plans thus resulting. Actually, for any given patient, different practitioners may pursue different, and occasionally conflicting goals: prioritizing impact on PTV in some cases, insisting on palliative considerations and therefore on saving OARs and HT in others. DDI is not intended to change their priorities, but to help them to precisely assess the consequences of their choices. On the other hand, it should be stressed that computing the DDI is straightforward, and can be easily done and displayed on a TPS simultaneously to the plotting of the corresponding DVHs. Moreover, the DDI is very sensitive to small dosimetry variations, is easily implemented and can be obtained for any type of TPS. It may also be used to compare plans obtained from different TPSs. Furthermore, the proposed DDI can be derived for any irradiation source (photons, protons, etc.) or radiotherapy technique (IMRT, 3DCRT, etc.) that provide DVHs of the radiation dose distributions for the tentative plans being simulated.

To give an idea of what DDI can actually accomplish, a retrospective study has been presented, corresponding to 30 patients diagnosed with centrally-located brain tumors. In each case, three tentative plans were simulated and recorded, out of which one was eventually delivered. Then, for a given set of weight parameters the applied plan (AP) and that providing the lowest DDI score ($DDIp$), were compared. Moreover, a clinical case of prostate cancer has been also considered and variations on the impact of tentative plans on PTV, OARs and HT have been monitored by the DDI as the number of fields considered changes. In view of the previous results, it appears that the implementation of the DDI in any type of TPS being used in clinical centers could improve reliability standards in selecting treatment plans.

Finally, the DDI proposed in this Chapter can be combined with the mathe-

matical model described in Chapter 2 to improve the radiotherapy planning process. In fact, these tools are aid-decision systems, which permit to define and compare different radiation dose distributions, which is one of the main tasks in clinical practice. In particular, having discussed on a precise definition of prescription radiation dose distributions as proposed in Chapter 2, it is natural to wonder how one could prepare a radiotherapy treatment plan where the dose distribution is as close as possible to an optimal prescription dose. While it is not possible to provide a general solution to that problem, this user-friendly tool can be used to decide, out of a given number of tentative plans, which one is closer to delivering the radiation dose distribution deemed optimal in each case.

Chapter 5

Conclusions

"... But there is another reason for the high repute of mathematics: it is mathematics that offers the exact natural sciences a certain measure of security which, without mathematics, they could not attain ..."

Albert Einstein (1879-1955)

Since the discovery of X-rays more than one hundred years ago, use of ionizing radiation in medicine has become pervasive, both to assist in diagnosis and as a treatment choice for tumor patients. In particular, radiotherapy is now a common clinical technique to treat solid tumors. The treatment of these diseases, and that of cancer patients in general, represents a major challenge on scientific and social terms. Considerable scientific and technological advances made over the last years have led to a significant reduction in tumor morbidity. However, tumor recurrence after therapy, as well as treatment of tumors at advanced or disseminated stages remains a critical problem in clinical practice.

On the other hand large efforts have been devoted to the development of mathematical models to assist in the radiotherapy treatment planning process. In particular, several models based on physical and radiobiological principles have been proposed, which have permitted to improve radiotherapy performance. However, when preparing a treatment plan in current practice, a number of difficulties related to the choice of prescription dose and the manner in which this has to be

delivered have to be overcome.

In this memoir some mathematical models and computer-based methods have been proposed to assist clinicians and radiophysicists during the treatment planning process. To begin with, in Chapter 2 a mathematical model was proposed to select optimal radiation dose distributions as solutions (minimizers) of a constrained optimization problem satisfying common clinical and technical constraints. To illustrate this approach, several clinical cases were considered, and a comparison of the proposed optimal dose distributions with those actually delivered was performed. As a result, when compared with actual dosimetries delivered in such clinical cases, the proposed optimal dose distributions are shown to be better options, and can thus be considered optimal choices against which tentative treatment plans should be compared during the radiotherapy planning process. In fact, these results strongly suggest that solutions of this mathematical model can be instrumental in deriving good quality tests to select radiotherapy treatment plans in rather general clinical situations. On the other hand, analysis of the dependence of such minimizers on model parameters allows to propose a strategy to select radiation dose distributions, under the assumption that key radiobiological parameters for tumors and organs at risk involved are only partially known, a situation which is quite common in clinical practice.

In Chapter 3 the effect of tumor heterogeneity in radiotherapy treatment outcomes was investigated. To that end, a mathematical model for heterogeneous tumor growth was considered where two tumor cell phenotypes are present, which strongly differ in their respective biological and radiobiological properties. In particular, as a consequence of those differences, the spatial distribution of such phenotypes and hence of the resulting tumor heterogeneity can be predicted as growth proceeds. Using such heterogeneity information the effects of different heterogeneous (dose painting) therapies have been investigated. It has been shown that heterogeneous dosimetries can be selected to enhance tumor control by boosting radiation in the region occupied by the more radioresistant tumor cell phenotype. Consequently, it has been observed that such heterogeneous radiation dosimetries fare always better than their homogeneous counterparts that are currently used in clinical practice.

In Chapter 4 a mathematical aid-decision tool to compare and evaluate radiotherapy tentative treatment plans has been proposed. Such tool uses only data extracted from the dose volume histograms provided by commercial treatment planning systems and the prescribed radiation dose on the tumor. In particular, to assess the information provided by the proposed aid-system, a number of actual clinical cases were investigated in retrospect. In addition, a computer application has been implemented, where clinicians and radiophysicists can easily compare and analyze different tentative plans. It should be stressed that this tool can be easily incorporated on any commercial treatment planning system and used to assess any radiotherapy technique that provides dose volume histograms of the tentative plans being simulated.

Summing up, the proposed mathematical models are expected to provide some help towards improving radiotherapy clinical practice, a goal that has been always present during this study.

Appendix A

Numerical discretization of variational problems

A.1 A general functional defined in an infinite dimensional function space

In this Appendix, a detailed numerical discretization of a class of general problems formulated in the field of Calculus of Variations is presented. See for instance [118] and [119] for further details of such problems. In particular, this discretization is used to numerically solve the problem (2.6)–(2.11) formulated in Chapter 2.

To begin with, let us consider a general functional $J(v)$ defined in an infinite dimensional function space $\mathcal{X}$, that is

$$J(v) = \int_{\Omega} f(\mathbf{x}, v(\mathbf{x}), \nabla v(\mathbf{x}))\, d\mathbf{x},$$

where f is a sufficiently smooth function, so that the corresponding integral makes sense. The problem of finding the minimizer function $u \in \mathcal{X}$, for which $J(u) \leq J(v)$ for all functions $v \in \mathcal{X}$ defined in Ω and $\mathbf{x} \in \Omega$, can be briefly expressed in the following form

$$J(u) = \min_{u \in \mathcal{X}} J(v), \tag{A.1}$$

where in what follows, solutions of the problem (A.1) will be referred as minimizers for short.

Unfortunately, most of this type of problems do not have an analytic expression of the minimizer function $u \in \mathcal{X}$, even though its existence and uniqueness are known in advance, as well as many of its properties. Therefore, it will be necessary to resort efficient numerical techniques and optimization methods in order to approximate $u \in \mathcal{X}$. The simplest way to do that is to consider a finite dimensional function space, or better yet, a family $(V_h)_{0<h<h_0}$ of finite dimensional function spaces that, as $h \to 0$, better approximate the elements of $\mathcal{X}$. In particular, the procedure to numerically approximate minimizers of the problem (A.1) will be presented and discussed through this Appendix.

In what follows, it will be going from the formulation of most general problems towards main aspects to numerically solve the problem (2.6)–(2.11) (referred as (P) for short). For this purpose, the formulation of the Finite Element Method (FEM) (cf. for instance [128], [127] and [126]) and an optimization method are considered. Then, Sections A.2 - A.6 are devoted to present the definitions and numerical procedures used to find solutions (minimizers) of the problem (P). While doing so, Section A.7 is focused on the numerical discretization and the corresponding mathematical formulation. Moreover, particular attention is paid to the key issues related with the computational implementation, as well as the existence and uniqueness properties of solutions of the resulting discrete problem.

A.2 The finite element method for nonlinear functionals

To start, let us first consider the problem of finding the function u defined in the infinite dimensional function space

$$\mathcal{X} \equiv W^{1,\infty}(\Omega) = \{v \in L^\infty(\Omega) : \partial v_{x_i} \in L^\infty(\Omega),\, i = 1, ..., n\}\,, \tag{A.2}$$

for $\Omega \subset \mathbb{R}^3$, such that u minimizes the following functional

$$J(v) = \int_{\Omega} |\nabla v(\mathbf{x})|^2 \, d\mathbf{x} + \int_{\Omega} f(v(\mathbf{x})) \, d\mathbf{x}, \tag{A.3}$$

where $\mathbf{x} \in \mathbb{R}^3$, $J(u) \leq J(v)$ for all $v \in \mathcal{X}$ defined in Ω and $f : \Omega \to \mathbb{R}^n$ is a nonlinear function.

Then, to approximate the minimizers of functional $J(v)$ in (A.3), a finite dimensional function space V_h of dimension n_h has been considered, which is an approximation of the infinite dimensional function space for which $J(v)$ makes sense, that is, $\mathcal{X}$ in (A.2). Let $\{\varphi_1, \ldots, \varphi_{n_h}\}$ be a basis of V_h, then for any function $v_h \in V_h$, v_h can be written as a unique linear combination of the elements of such basis, that is

$$v_h(\mathbf{x}) = \sum_{j=1}^{n_h} v_j \varphi(\mathbf{x}). \tag{A.4}$$

As it is customary, the first term of the functional (A.3) can be expressed as $a(v, w)$ for functions $v, w \in \mathcal{X}$, where a is the symmetric bilinear form given by

$$a(v, w) = \int_{\Omega} \nabla v(\mathbf{x}) \cdot \nabla w(\mathbf{x}) \, d\mathbf{x}. \tag{A.5}$$

As consequence, in view of (A.4) the bilinear form $a(v, w)$ can be expressed as follows

$$a(v_h, w_h) = a\left(\sum_{i=1}^{n_h} v_i \varphi_i, \sum_{j=1}^{n_h} w_j \varphi_j\right) = \sum_{i,j=1}^{n_h} v_i a(\varphi_i, \varphi_j) w_j,$$

for the corresponding functions $v_h, w_h \in V_h$.

On the other hand, denoting by $A_h = (a_{ij})_{1 \leq i,j \leq n_h}$ the symmetric square matrix of dimension $(n_h \times n_h)$, usually referred as the stiffness matrix, with elements

$$a_{ij} = a(\varphi_i, \varphi_j) = \int_{\Omega} \nabla \varphi_i(\mathbf{x}) \cdot \nabla \varphi_j(\mathbf{x}) \, d\mathbf{x}, \quad 1 \leq i, j \leq n_h,$$

that is, the matrix of the bilinear form $a(v_h, w_h)$ on the basis $\{\varphi_1, \ldots, \varphi_{n_h}\}$, then it is possible to express the following

$$a(v_h, w_h) = \underline{v}_h^T A_h \underline{w}_h,$$

where for any function $v_h \in V_h$, $\underline{v}_h \in \mathbb{R}^{n_h}$ denotes the vector of values

$$\underline{v}_h = \begin{bmatrix} v_h(\mathbf{x}_1) \\ \vdots \\ v_h(\mathbf{x}_{n_h}) \end{bmatrix}.$$

In the same way, the second term of the functional (A.3) can be expressed as follows

$$F_h(v_h) = \int_\Omega f\left(\sum_{j=1}^{n_h} v_j \varphi_j(\mathbf{x})\right) \, d\mathbf{x},$$

where $F_h : \mathbb{R}^{n_h} \to \mathbb{R}$ and $v_h \in V_h$.

Therefore, for any function $v_h \in V_h$ the value of $J(v_h)$ can be expressed in the following form

$$J(v_h) = \underline{v}_h^T A_h \underline{v}_h + F_h.$$

A.3 The finite dimensional function spaces and the corresponding nodal basis functions

In this Section, a definition of the finite dimensional function spaces V_h and the expression of their nodal basis functions $\{\varphi_1, ..., \varphi_{n_h}\}$ are provided. To do that, the first step is to consider a three-dimensional triangulation

$$\mathcal{T}_h = \{\tau_i\}_{i=1}^{n_t}$$

of the domain $\Omega \subset \mathbb{R}^3$, with n_n vertices and n_t elements (for instance, tetrahedrons in $\mathbb{R}^3$). The subindex h refers to the diameter of the triangulation, defined as the length of the longest edge of all tetrahedrons, that is, the longest distance between two vertices on $\mathcal{T}_h$. It should be noted that, a triangulation of Ω is a partition of this domain into elements, in this case tetrahedrons. On its turn, tetrahedrons

must cover the closure of Ω but no more, and must fulfill the following rule: *"if two tetrahedrons have some intersection, it is either on common vertex or a common full face"*. In particular, two different tetrahedrons do not overlap.

The finite dimensional function spaces V_h considered in this work have been the well-known piecewise linear elements, which are continuous functions in Ω, such that are linear on each tetrahedron $\tau \in \mathcal{T}_h$ and given by

$$V_h = \left\{ v \in C(\tau) : v_{|_\tau} \in \mathbb{P}^1(\tau), \quad \forall \tau \in \mathcal{T}_h \right\},$$

where $\mathbb{P}^1$ represents the set of polynomials of degree less than or equal to one. Observe that, if the values on the vertices of the triangulation $\mathcal{T}_h$ are fixed, then there exists a unique function $v_h \in \mathcal{T}_h$ with those values on such vertices. Therefore, an element of $\mathcal{T}_h$ is uniquely determined by its values on the set of vertices of the triangulation.

The next step is to show the expression of the nodal basis functions $\{\varphi_1, \ldots, \varphi_{n_h}\}$ in terms of the independent variable $\mathbf{x} \in \Omega$, which satisfy the following property

$$\varphi_i(\mathbf{x}_j) = \delta_{ij} = \begin{cases} 1 & \text{if } i = j \\ 0 & \text{if } i \neq j \end{cases}. \tag{A.6}$$

Since the nodal basis functions have been defined elementwise, let us consider an arbitrary tetrahedron $\tau \in \mathcal{T}_h$ as represented in Figure A.1, where the coordinates of its vertices are as follows

$$\mathbf{x}_1 = \begin{bmatrix} x_1 \\ y_1 \\ z_1 \end{bmatrix} \quad \mathbf{x}_2 = \begin{bmatrix} x_2 \\ y_2 \\ z_2 \end{bmatrix} \quad \mathbf{x}_3 = \begin{bmatrix} x_3 \\ y_3 \\ z_3 \end{bmatrix} \quad \mathbf{x}_4 = \begin{bmatrix} x_4 \\ y_4 \\ z_4 \end{bmatrix}.$$

Then, for instance, the basis function φ_4 associated to the vertex $\mathbf{x}_4$ on the tetrahedron τ can be defined by means of the equation of the plane $p_4(x, y, z) = 0$ that passes through the nonaligned remaining three vertices $\mathbf{x}_1$, $\mathbf{x}_2$ and $\mathbf{x}_3$, which is as follows

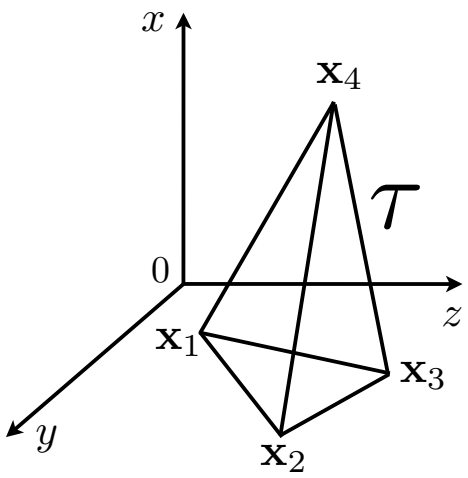

Figure A.1. Representation of an arbitrary tetrahedron τ with vertices $\mathbf{x}_1$, $\mathbf{x}_2$, $\mathbf{x}_3$ and $\mathbf{x}_4$ on a triangulation $\mathcal{T}_h$.

$$p_4(x,y,z) \equiv \begin{vmatrix} x-x_1 & x_2-x_1 & x_3-x_1 \\ y-y_1 & y_2-y_1 & y_3-y_1 \\ z-z_1 & z_2-z_1 & z_3-z_1 \end{vmatrix} = 0,$$

where $|\cdot|$ denotes the determinant of any arbitrary square matrix. Notice that equation $p_4(x,y,z)$ is a linear function, equal to zero in the vertices $\mathbf{x}_1$, $\mathbf{x}_2$ and $\mathbf{x}_3$, and nonzero in $\mathbf{x}_4$. Thus, dividing the equation $p_4(x,y,z)=0$ by the value of the corresponding function evaluated on $\mathbf{x}_4$ results in a linear function equal to one in $\mathbf{x}_4$ and zero in the remaining vertices, that is

$$\varphi_4(x,y,z) = \frac{p_4(x,y,z)}{p_4(x_4,y_4,z_4)} \tag{A.7}$$

and expressed in terms of its coordinates as follows

$$\varphi_4(x,y,z) = \frac{\begin{vmatrix} x-x_1 & x_2-x_1 & x_3-x_1 \\ y-y_1 & y_2-y_1 & y_3-y_1 \\ z-z_1 & z_2-z_1 & z_3-z_1 \end{vmatrix}}{\begin{vmatrix} x_4-x_1 & x_2-x_1 & x_3-x_1 \\ y_4-y_1 & y_2-y_1 & y_3-y_1 \\ z_4-z_1 & z_2-z_1 & z_3-z_1 \end{vmatrix}}. \tag{A.8}$$

Moreover, observe that the basis function φ_4 satisfies the property (A.6). Similarly, it is possible to obtain the expression of the basis functions φ_1, φ_2 and φ_3 on the arbitrary tetrahedron $\tau \in \mathcal{T}_h$. Notice also that, in this way the expressions of the nodal basis functions on every tetrahedron τ in the triangulation $\mathcal{T}_h$ can be obtained.

A.4 Computation of integrals on a triangulation

This Section is devoted to introduce the procedure to approximate an integral defined in Ω by means of the triangulation $\mathcal{T}_h = \{\tau_i\}_{i=1}^{n_t}$ in the finite dimensional function space V_h. The key idea is to replace the original integral by a finite sum of integrals over each tetrahedron $\tau \in \mathcal{T}_h$. To do that, let us recall the bilinear form $a(v, w)$ for functions $v, w \in \mathcal{X}$ of equation (A.5) given by

$$a(v,w) = \int_{\Omega} \nabla v(\mathbf{x}) \cdot \nabla w(\mathbf{x})\, d\mathbf{x} = \int_{\Omega} (v_x w_x + v_y w_y + v_z w_z)\, dx\, dy\, dz,$$

where this bilinear form can be expressed as a finite sum of integrals over each tetrahedron of the triangulation $\mathcal{T}_h$ as follows

$$a(v,w) = \sum_{j=1}^{n_t} \left[\int_{\tau_j} (v_x w_x + v_y w_y + v_z w_z)\, dx\, dy\, dz \right]. \tag{A.9}$$

Denoting by $a_\tau(v, w)$ the bilinear form restricted to a tetrahedron $\tau \in \mathcal{T}_h$, that is

$$a_\tau(v,w) = \int_{\tau} \nabla v(\mathbf{x}) \cdot \nabla w(\mathbf{x})\, d\mathbf{x}, \tag{A.10}$$

then the bilinear form $a(v, w)$ of equation (A.9) can be expressed as follows

$$a(v,w) = \sum_{j=1}^{n_t} a_{\tau_j}(v,w). \tag{A.11}$$

As a result, notice that the stiffness matrix $A_h = (a(\varphi_i, \varphi_j))_{1 \leq i,j \leq n_n}$ of dimension $(n_n \times n_n)$ can be written in the following form

$$A_h = A_{\tau_1} + A_{\tau_2} + \ldots + A_{\tau_{n_t}}, \tag{A.12}$$

where A_{τ_k} for $(k = 1, \ldots, n_t)$ is the matrix of the bilinear form $a_{\tau_k}(v, w)$, that is

$$A_{\tau_k} = (a_{\tau_k}(\varphi_i, \varphi_j))_{1 \leq i,j \leq n_n}.$$

On the other hand, the second term of the functional (A.3) given by

$$F(v) = \int_{\Omega} f(v(\mathbf{x}))\, d\mathbf{x},$$

can also be expressed as the sum of the contributions of the tetrahedrons τ in the triangulation $\mathcal{T}_h$ to the corresponding integral defined in Ω, which is then given by

$$F(v) = \sum_{j=1}^{n_t} \int_{\tau_j} f\left(v(\mathbf{x})\right)\, d\mathbf{x} = \sum_{j=1}^{n_t} F_{\tau_j}(v), \tag{A.13}$$

where

$$F_{\tau}(v) = \int_{\tau} f\left(v(\mathbf{x})\right)\, d\mathbf{x}. \tag{A.14}$$

Therefore, the problem of computing an integral defined in Ω is reduced to compute the contributions to such integral of the tetrahedrons in the triangulation $\mathcal{T}_h$. In particular, in what follows, the way to compute the integrals (A.10) and (A.14) on an arbitrary tetrahedron $\tau \in \mathcal{T}_h$ is described.

A.5 Assembling the stiffness matrix

As pointed out in the previous Section, the stiffness matrix A_h can be decomposed in a finite sum of the matrices A_{τ_j} for $(j = 1, \ldots, n_t)$ in the triangulation $\mathcal{T}_h =$

$\{\tau_i\}_{i=1}^{t}$ (see (A.12) for further details). Therefore, the way to obtain a matrix A_τ of the bilinear form a_τ for an arbitrary tetrahedron $\tau \in \mathcal{T}_h$ is now outlined. To do that, let us consider an arbitrary tetrahedron τ with vertices $\mathbf{x}_1$, $\mathbf{x}_2$, $\mathbf{x}_3$ and $\mathbf{x}_4$, and the function $v \in V_h$ restricted to τ. Let us also consider the corresponding nodal basis functions φ_1, φ_2, φ_3 and φ_4 associated to these vertices. Thus, taking into account that v is linear in τ, means that

$$v(\mathbf{x}) = \sum_{i=1}^{4} v(\mathbf{x}_i)\varphi_i(\mathbf{x}),$$

where by introducing the vector

$$\underline{v} = \begin{bmatrix} v(\mathbf{x}_1) \\ v(\mathbf{x}_2) \\ v(\mathbf{x}_3) \\ v(\mathbf{x}_4) \end{bmatrix} \tag{A.15}$$

and the mapping whose components are the nodal basis functions given by

$$\widehat{\varphi}(\mathbf{x}) = \begin{bmatrix} \varphi_1(\mathbf{x}) \\ \varphi_2(\mathbf{x}) \\ \varphi_3(\mathbf{x}) \\ \varphi_4(\mathbf{x}) \end{bmatrix}, \quad \mathbf{x} \in \tau,$$

then the function $v(\mathbf{x})$ can be expressed as follows

$$v(\mathbf{x}) = \underline{v}^T \widehat{\varphi}(\mathbf{x}), \qquad \mathbf{x} \in \tau.$$

Therefore, in order to compute the integral of the bilinear form $a_\tau(v, v)$ defined in (A.10), the partial derivatives of $v(\mathbf{x}) = \underline{v}^T \varphi(\mathbf{x})$ with respect to x, y and z should be also computed, and these are

$$v_x = \underline{v}^T \widehat{\varphi}_x, \quad v_y = \underline{v}^T \widehat{\varphi}_y, \quad v_z = \underline{v}^T \widehat{\varphi}_z, \tag{A.16}$$

where

$$\widehat{\varphi}_x = \begin{bmatrix} \partial_x\varphi_1 \\ \partial_x\varphi_2 \\ \partial_x\varphi_3 \\ \partial_x\varphi_4 \end{bmatrix}, \quad \widehat{\varphi}_y = \begin{bmatrix} \partial_y\varphi_1 \\ \partial_y\varphi_2 \\ \partial_y\varphi_3 \\ \partial_y\varphi_4 \end{bmatrix}, \quad \widehat{\varphi}_z = \begin{bmatrix} \partial_z\varphi_1 \\ \partial_z\varphi_2 \\ \partial_z\varphi_3 \\ \partial_z\varphi_4 \end{bmatrix}.$$

Then, substituting (A.16) into the bilinear form $a_\tau(v, v)$ in (A.10) gives the following

$$a_\tau(v, v) = \int_\tau ((\underline{v}^T\widehat{\varphi}_x)^2 + (\underline{v}^T\widehat{\varphi}_y)^2 + (\underline{v}^T\widehat{\varphi}_z)^2)\, dx\, dy\, dz. \tag{A.17}$$

On the other hand, taking into account that for each point $\mathbf{x} \in \tau$ the expression $(\underline{v}^T\widehat{\varphi}_x)$ is a scalar value, then

$$\underline{v}^T\widehat{\varphi}_x = (\underline{v}^T\widehat{\varphi}_x)^T = \widehat{\varphi}_x^T\underline{v},$$

where in the last equality, the property that the transpose of a scalar value is equal to itself has been used. Thus, the square of this last expression can be written as follows

$$(\underline{v}^T\widehat{\varphi}_x)^2 = (\underline{v}^T\widehat{\varphi}_x)(\widehat{\varphi}_x^T\underline{v}) = \underline{v}^T\widehat{\varphi}_x\widehat{\varphi}_x^T\underline{v}. \tag{A.18}$$

Arguing similarly for the remaining terms under the integral sign in (A.17), then

$$a_\tau(v, v) = \underline{v}^T E\underline{v}, \tag{A.19}$$

where the matrix E, which is usually known as the elementary matrix, is given by

$$E = \int_\tau \left(\widehat{\varphi}_x\widehat{\varphi}_x^T + \widehat{\varphi}_y\widehat{\varphi}_y^T + \widehat{\varphi}_z\widehat{\varphi}_z^T\right)\, dx\, dy\, dz. \tag{A.20}$$

Notice that, for each tetrahedron $\tau \in \mathcal{T}_h$ there are only four nonzero nodal basis functions, so the dimension of the matrix E is (4×4). Observe also that

$$E = \begin{pmatrix} a_\tau(\varphi_1,\varphi_1) & a_\tau(\varphi_1,\varphi_2) & a_\tau(\varphi_1,\varphi_3) & a_\tau(\varphi_1,\varphi_4) \\ a_\tau(\varphi_2,\varphi_1) & a_\tau(\varphi_2,\varphi_2) & a_\tau(\varphi_2,\varphi_3) & a_\tau(\varphi_2,\varphi_4) \\ a_\tau(\varphi_3,\varphi_1) & a_\tau(\varphi_3,\varphi_2) & a_\tau(\varphi_3,\varphi_3) & a_\tau(\varphi_3,\varphi_4) \\ a_\tau(\varphi_4,\varphi_1) & a_\tau(\varphi_4,\varphi_2) & a_\tau(\varphi_4,\varphi_3) & a_\tau(\varphi_4,\varphi_4) \end{pmatrix}, \tag{A.21}$$

that is, the elements of the matrix E are the values of a_τ in those basis functions that are nonzero in the tetrahedron τ.

Indeed, the matrix E can be computed by a change of variables to the reference tetrahedron τ_0 (see Figure A.2), where τ_0 is the unit tetrahedron defined by one point in the origin and one on each coordinate axis in a cartesian grid at the value one. This change of variables has been implemented by means of an affine transformation Ψ.

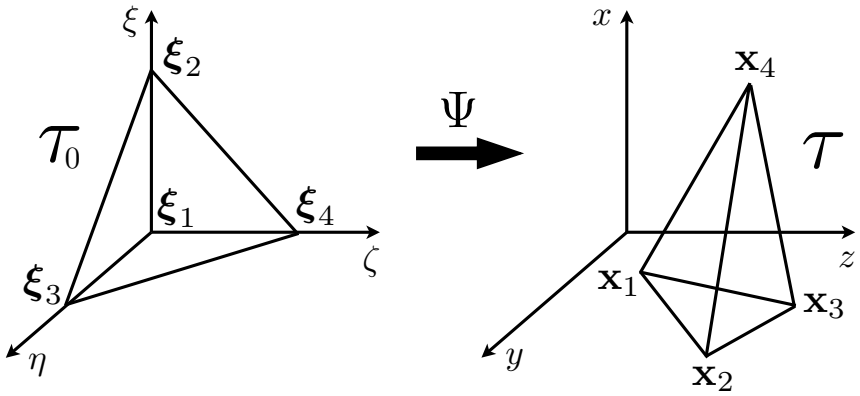

Figure A.2. A schematic representation of an affine transformation Ψ which allows to express an arbitrary tetrahedron τ with vertices $\mathbf{x}_1$, $\mathbf{x}_2$, $\mathbf{x}_3$ and $\mathbf{x}_4$ in the coordinate system (x, y, z) (right) in terms of the reference tetrahedron τ_0 with vertices $\boldsymbol{\xi}_1$, $\boldsymbol{\xi}_2$, $\boldsymbol{\xi}_3$ and $\boldsymbol{\xi}_4$ in the coordinate system (ξ, η, ζ) (left).

More precisely, let us consider the reference tetrahedron τ_0, which is defined by the following vertices $\boldsymbol{\xi}_1$, $\boldsymbol{\xi}_2$, $\boldsymbol{\xi}_3$ and $\boldsymbol{\xi}_4$ in the coordinate system (ξ, η, ζ) given by

$$\boldsymbol{\xi}_1 = \begin{bmatrix} 0 \\ 0 \\ 0 \end{bmatrix}, \quad \boldsymbol{\xi}_2 = \begin{bmatrix} 1 \\ 0 \\ 0 \end{bmatrix}, \quad \boldsymbol{\xi}_3 = \begin{bmatrix} 0 \\ 1 \\ 0 \end{bmatrix}, \quad \boldsymbol{\xi}_4 = \begin{bmatrix} 0 \\ 0 \\ 1 \end{bmatrix}.$$

Then, the vertices $\mathbf{x}_1$, $\mathbf{x}_2$, $\mathbf{x}_3$ and $\mathbf{x}_4$ of an arbitrary tetrahedron τ can be obtained

from the reference tetrahedron τ_0 by means of the affine transformation $\Psi(\boldsymbol{\xi})$ in the following form

$$\boldsymbol{\xi} \mapsto \mathbf{x} = \Psi(\boldsymbol{\xi}) = \mathbf{x}_1 + [\mathbf{x}_2 - \mathbf{x}_1, \mathbf{x}_3 - \mathbf{x}_1, \mathbf{x}_4 - \mathbf{x}_1]\boldsymbol{\xi} \tag{A.22}$$

or expressed in terms of their components as follows

$$\boldsymbol{\xi} = \begin{bmatrix} \xi \\ \eta \\ \zeta \end{bmatrix} \mapsto \mathbf{x} = \begin{bmatrix} x \\ y \\ z \end{bmatrix} = \begin{bmatrix} x_1 \\ y_1 \\ z_1 \end{bmatrix} + \begin{bmatrix} x_2 - x_1 & x_3 - x_1 & x_4 - x_1 \\ y_2 - y_1 & y_3 - y_1 & y_4 - y_1 \\ z_2 - z_1 & z_3 - z_1 & z_4 - z_1 \end{bmatrix} \begin{bmatrix} \xi \\ \eta \\ \zeta \end{bmatrix}.$$

Notice that, the differential of $\Psi(\boldsymbol{\xi})$ with respect to $\boldsymbol{\xi}$ is the constant square matrix given by

$$D\Psi = \begin{bmatrix} x_\xi & x_\eta & x_\zeta \\ y_\xi & y_\eta & y_\zeta \\ z_\xi & z_\eta & z_\zeta \end{bmatrix} = \begin{bmatrix} x_2 - x_1 & x_3 - x_1 & x_4 - x_1 \\ y_2 - y_1 & y_3 - y_1 & y_4 - y_1 \\ z_2 - z_1 & z_3 - z_1 & z_4 - z_1 \end{bmatrix},$$

where hence the inverse matrix of $D\Psi$ is expressed as follows

$$D\Psi^{-1} = \begin{bmatrix} \xi_x & \xi_y & \xi_z \\ \eta_x & \eta_y & \eta_z \\ \zeta_x & \zeta_y & \zeta_z \end{bmatrix},$$

which is also constant. In particular, the entries of the matrix $D\Psi^{-1}$ are easily computed by the Cramer's rule. For instance, $\xi_x = \frac{(y_3-y_1)(z_4-z_1)-(z_3-z_1)(y_4-y_1)}{J}$, where $J = |D\Psi|$ is the determinant of the Jacobian matrix given by

$$\begin{aligned} J = {} & (x_2 - x_1)(y_3 - y_1)(z_4 - z_1) + (x_3 - x_1)(y_4 - y_1)(z_2 - z_1) + \\ & (x_4 - x_1)(y_2 - y_1)(z_3 - z_1) - (x_4 - x_1)(y_3 - y_1)(z_2 - z_1) - \\ & (x_3 - x_1)(y_2 - y_1)(z_4 - z_1) - (x_2 - x_1)(y_4 - y_1)(z_3 - z_1). \end{aligned}$$

On the other hand, denoting by $\mathcal{N}_i(\boldsymbol{\xi})$ for $(1 \leq i \leq 4)$ the nodal basis functions on the coordinate system (ξ, η, ζ) for the reference tetrahedron τ_0, and by $\widehat{\mathcal{N}}$ the following mapping

$$\widehat{\mathcal{N}}(\boldsymbol{\xi}) = \begin{bmatrix} \mathcal{N}_1(\boldsymbol{\xi}) \\ \mathcal{N}_2(\boldsymbol{\xi}) \\ \mathcal{N}_3(\boldsymbol{\xi}) \\ \mathcal{N}_4(\boldsymbol{\xi}) \end{bmatrix}, \quad \boldsymbol{\xi} \in \tau_0,$$

then, a simple calculation (recall the expression of the basis function in (A.7)–(A.8)) provides that

$$\widehat{\mathcal{N}}(\boldsymbol{\xi}) = \begin{bmatrix} 1-\xi-\eta-\zeta \\ \xi \\ \eta \\ \zeta \end{bmatrix}. \tag{A.23}$$

Moreover, the affine transformation $\Psi(\boldsymbol{\xi})$ allows to express the nodal basis functions $\widehat{\varphi}(\mathbf{x})$ with respect to the reference tetrahedron τ_0 as follows

$$\widehat{\varphi}(\mathbf{x}) = \widehat{\mathcal{N}}(\boldsymbol{\xi}) \circ \Psi^{-1}, \tag{A.24}$$

so that, applying the chain rule in (A.24), the differential of the nodal basis functions $\widehat{\varphi}(\mathbf{x})$ with respect to $\mathbf{x}$ can be written in the following form

$$\begin{aligned} \widehat{\varphi}_x &= \widehat{\mathcal{N}}_\xi \xi_x + \widehat{\mathcal{N}}_\eta \eta_x + \widehat{\mathcal{N}}_\zeta \zeta_x, \\ \widehat{\varphi}_y &= \widehat{\mathcal{N}}_\xi \xi_y + \widehat{\mathcal{N}}_\eta \eta_y + \widehat{\mathcal{N}}_\zeta \zeta_y, \\ \widehat{\varphi}_z &= \widehat{\mathcal{N}}_\xi \xi_z + \widehat{\mathcal{N}}_\eta \eta_z + \widehat{\mathcal{N}}_\zeta \zeta_z, \end{aligned}$$

which implies that

$$\begin{aligned} \widehat{\varphi}_x \widehat{\varphi}_x^T = \xi_x^2 (\widehat{\mathcal{N}}_\xi \widehat{\mathcal{N}}_\xi^T) + \eta_x^2 (\widehat{\mathcal{N}}_\eta \widehat{\mathcal{N}}_\eta^T) + \zeta_x^2 (\widehat{\mathcal{N}}_\zeta \widehat{\mathcal{N}}_\zeta^T) + \xi_x \eta_x (\widehat{\mathcal{N}}_\xi \widehat{\mathcal{N}}_\eta^T + \\ \widehat{\mathcal{N}}_\eta \widehat{\mathcal{N}}_\xi^T) + \xi_x \zeta_x (\widehat{\mathcal{N}}_\xi \widehat{\mathcal{N}}_\zeta^T + \widehat{\mathcal{N}}_\zeta \widehat{\mathcal{N}}_\xi^T) + \eta_x \zeta_x (\widehat{\mathcal{N}}_\eta \widehat{\mathcal{N}}_\zeta^T + \widehat{\mathcal{N}}_\zeta \widehat{\mathcal{N}}_\eta^T), \end{aligned}$$

$$\widehat{\varphi}_y \widehat{\varphi}_y^T = \xi_y^2 (\widehat{\mathcal{N}}_\xi \widehat{\mathcal{N}}_\xi^T) + \eta_y^2 (\widehat{\mathcal{N}}_\eta \widehat{\mathcal{N}}_\eta^T) + \zeta_y^2 (\widehat{\mathcal{N}}_\zeta \widehat{\mathcal{N}}_\zeta^T) + \xi_y \eta_y (\widehat{\mathcal{N}}_\xi \widehat{\mathcal{N}}_\eta^T + \tag{A.25}$$

$$\widehat{\mathcal{N}}_\eta\widehat{\mathcal{N}}_\xi^T) + \xi_y\zeta_y(\widehat{\mathcal{N}}_\xi\widehat{\mathcal{N}}_\zeta^T + \widehat{\mathcal{N}}_\zeta\widehat{\mathcal{N}}_\xi^T) + \eta_y\zeta_y(\widehat{\mathcal{N}}_\eta\widehat{\mathcal{N}}_\zeta^T + \widehat{\mathcal{N}}_\zeta\widehat{\mathcal{N}}_\eta^T),$$

$$\begin{aligned}\widehat{\varphi}_z\widehat{\varphi}_z^T = \xi_z^2(\widehat{\mathcal{N}}_\xi\widehat{\mathcal{N}}_\xi^T) + \eta_z^2(\widehat{\mathcal{N}}_\eta\widehat{\mathcal{N}}_\eta^T) + \zeta_z^2(\widehat{\mathcal{N}}_\zeta\widehat{\mathcal{N}}_\zeta^T) + \xi_z\eta_z(\widehat{\mathcal{N}}_\xi\widehat{\mathcal{N}}_\eta^T + \\ \widehat{\mathcal{N}}_\eta\widehat{\mathcal{N}}_\xi^T) + \xi_z\zeta_z(\widehat{\mathcal{N}}_\xi\widehat{\mathcal{N}}_\zeta^T + \widehat{\mathcal{N}}_\zeta\widehat{\mathcal{N}}_\xi^T) + \eta_z\zeta_z(\widehat{\mathcal{N}}_\eta\widehat{\mathcal{N}}_\zeta^T + \widehat{\mathcal{N}}_\zeta\widehat{\mathcal{N}}_\eta^T).\end{aligned}$$

Notice that, $\widehat{\mathcal{N}}_\xi$, $\widehat{\mathcal{N}}_\eta$ and $\widehat{\mathcal{N}}_\zeta$ are constant vectors obtained by deriving the expression (A.23) with respect to ξ, η and ζ respectively, which are as follows

$$\widehat{\mathcal{N}}_\xi = \begin{bmatrix}-1\\1\\0\\0\end{bmatrix}, \quad \widehat{\mathcal{N}}_\eta = \begin{bmatrix}-1\\0\\1\\0\end{bmatrix}, \quad \widehat{\mathcal{N}}_\zeta = \begin{bmatrix}-1\\0\\0\\1\end{bmatrix}.$$

Thus, expression (A.25) can be substituted into the bilinear form $a_\tau(v,v)$ in (A.20), which can be expressed in terms of the reference tetrahedron τ_0 as follows

$$\begin{aligned}\int_\tau \left(\widehat{\varphi}_x\widehat{\varphi}_x^T + \widehat{\varphi}_y\widehat{\varphi}_y^T + \widehat{\varphi}_z\widehat{\varphi}_z^T\right)\, d\mathbf{x} = \\ c_1\int_{\tau_0}\widehat{\mathcal{N}}_\xi\widehat{\mathcal{N}}_\xi^T\, d\boldsymbol{\xi} + c_2\int_{\tau_0}\widehat{\mathcal{N}}_\eta\widehat{\mathcal{N}}_\eta^T\, d\boldsymbol{\xi} + c_3\int_{\tau_0}\widehat{\mathcal{N}}_\zeta\widehat{\mathcal{N}}_\zeta^T\, d\boldsymbol{\xi} + \\ c_4\int_{\tau_0}(\widehat{\mathcal{N}}_\xi\widehat{\mathcal{N}}_\eta^T + \widehat{\mathcal{N}}_\eta\widehat{\mathcal{N}}_\xi^T)\, d\boldsymbol{\xi} + \\ c_5\int_{\tau_0}(\widehat{\mathcal{N}}_\xi\widehat{\mathcal{N}}_\zeta^T + \widehat{\mathcal{N}}_\zeta\widehat{\mathcal{N}}_\xi^T)\, d\boldsymbol{\xi} + \\ c_6\int_{\tau_0}(\widehat{\mathcal{N}}_\eta\widehat{\mathcal{N}}_\zeta^T + \widehat{\mathcal{N}}_\zeta\widehat{\mathcal{N}}_\eta^T)\, d\boldsymbol{\xi},\end{aligned} \tag{A.26}$$

where the constants c_i for $(i = 1, \ldots, 6)$ are given by

$$\begin{aligned}c_1 &= |J|(\xi_x^2 + \xi_y^2 + \xi_z^2),\\ c_2 &= |J|(\eta_x^2 + \eta_y^2 + \eta_z^2),\\ c_3 &= |J|(\zeta_x^2 + \zeta_y^2 + \zeta_z^2),\end{aligned}$$

$$c_4 = |J|(\xi_x\eta_x + \xi_y\eta_y + \xi_z\eta_z),$$
$$c_5 = |J|(\xi_x\zeta_x + \xi_y\zeta_y + \xi_z\zeta_z),$$
$$c_6 = |J|(\zeta_x\eta_x + \zeta_y\eta_y + \zeta_z\eta_z)$$

and $|J|$ is the absolute value of the determinant of the Jacobian matrix. Since $\widehat{\mathcal{N}}_{\boldsymbol{\xi}}$, $\widehat{\mathcal{N}}_\eta$ and $\widehat{\mathcal{N}}_\zeta$ are constant vectors and the integral over τ_0 of the constant function one is the volume of τ_0, which is equal to $1/6$ (see [209] for further details), then the integrals in the right hand of (A.26) denoted by $S_1, \ldots, S_6$ respectively, are the following

$$S_1 = \int_{\tau_0} \widehat{\mathcal{N}}_\xi \widehat{\mathcal{N}}_\xi^T \, d\boldsymbol{\xi} = \frac{1}{6}\widehat{\mathcal{N}}_\xi \widehat{\mathcal{N}}_\xi^T,$$
$$S_2 = \int_{\tau_0} \widehat{\mathcal{N}}_\eta \widehat{\mathcal{N}}_\eta^T \, d\boldsymbol{\xi} = \frac{1}{6}\widehat{\mathcal{N}}_\eta \widehat{\mathcal{N}}_\eta^T,$$
$$S_3 = \int_{\tau_0} \widehat{\mathcal{N}}_\zeta \widehat{\mathcal{N}}_\zeta^T \, d\boldsymbol{\xi} = \frac{1}{6}\widehat{\mathcal{N}}_\zeta \widehat{\mathcal{N}}_\zeta^T,$$
$$S_4 = \int_{\tau_0} (\widehat{\mathcal{N}}_\xi \widehat{\mathcal{N}}_\eta^T + \widehat{\mathcal{N}}_\eta \widehat{\mathcal{N}}_\xi^T) \, d\boldsymbol{\xi} = \frac{1}{6}(\widehat{\mathcal{N}}_\xi \widehat{\mathcal{N}}_\eta^T + \widehat{\mathcal{N}}_\eta \widehat{\mathcal{N}}_\xi^T),$$
$$S_5 = \int_{\tau_0} (\widehat{\mathcal{N}}_\xi \widehat{\mathcal{N}}_\zeta^T + \widehat{\mathcal{N}}_\zeta \widehat{\mathcal{N}}_\xi^T) \, d\boldsymbol{\xi} = \frac{1}{6}(\widehat{\mathcal{N}}_\xi \widehat{\mathcal{N}}_\zeta^T + \widehat{\mathcal{N}}_\zeta \widehat{\mathcal{N}}_\xi^T),$$
$$S_6 = \int_{\tau_0} (\widehat{\mathcal{N}}_\eta \widehat{\mathcal{N}}_\zeta^T + \widehat{\mathcal{N}}_\zeta \widehat{\mathcal{N}}_\eta^T) \, d\boldsymbol{\xi} = \frac{1}{6}(\widehat{\mathcal{N}}_\eta \widehat{\mathcal{N}}_\zeta^T + \widehat{\mathcal{N}}_\zeta \widehat{\mathcal{N}}_\eta^T).$$

Therefore, the elementary matrix E can be computed by a linear combination of the constants c_i and matrices S_i for $(i = 1, \ldots, 6)$ in the following form

$$E = \sum_{i=1}^{6} c_i S_i.$$

Finally, it should be noted that the matrix A_τ of an arbitrary tetrahedron $\tau \in \mathcal{T}_h$ with vertices $\mathbf{x}_i$, $\mathbf{x}_j$, $\mathbf{x}_k$ and $\mathbf{x}_l$ can be obtained from the corresponding elementary matrix E. Thus, the stiffness matrix A_h in (A.12) can be sequentially assembled as a sum of the matrices A_τ of tetrahedrons $\tau \in \mathcal{T}_h$. See Figure A.3 for a

representation of the eventually nonzero elements of a matrix A_τ.

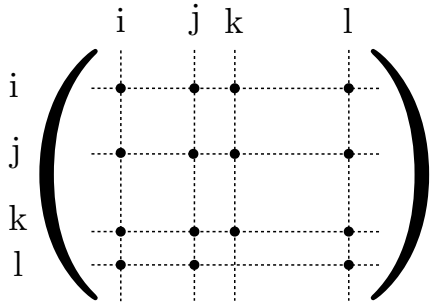

Figure A.3. Representation of the eventually nonzero elements of the matrix A_τ, corresponding to the tetrahedron τ with vertices $\mathbf{x}_i$, $\mathbf{x}_j$, $\mathbf{x}_k$ and $\mathbf{x}_l$.

A.6 Computation of integrals of a general nonlinear functional

Similarly to computations described in the previous Section, using the affine transformation $\Psi(\boldsymbol{\xi})$ in (A.22) and the nodal basis functions $\widehat{\mathcal{N}}(\boldsymbol{\xi})$ in (A.23), the value of the integral in (A.14) over an arbitrary tetrahedron $\tau \in \mathcal{T}_h$ can be computed as an integral on the reference tetrahedron τ_0 by means of the change of variables given by

$$F_\tau(v) = \int_\tau f\left(\underline{v}^T \widehat{\varphi}(\mathbf{x})\right)\, d\mathbf{x} = |J| \int_{\tau_0} f\left(\underline{v}^T \widehat{\mathcal{N}}(\boldsymbol{\xi})\right)\, d\boldsymbol{\xi},$$

where $|J|$ is the absolute value of the determinant of the Jacobian matrix.

However, quite frequently these integrals cannot be expressed in terms of elementary functions, so that, a quadrature formula (a method to approximate the value of integrals) can be used to approximate their values [210], [211]. In this case, a quadrature formula of $s = 15$ nodes $[\mathbf{c}_1, \ldots, \mathbf{c}_s]$ and the corresponding nonnegative weights $[w_1, \ldots, w_s]$ to approximate the value of an integral $\int_{\tau_0} g\, d\boldsymbol{\xi}$, which integrates exactly all polynomials of degree less than and equal to five, has been considered. The values of the corresponding nodes and weights for this quadrature formula are given in Table A.1.

i	w_i	ξ_i	η_i	ζ_i
1	$0.602678571428571597 \times 10^{-2}$	0.333333333333333333	0.333333333333333333	0.000000000000000000
2	$0.602678571428571597 \times 10^{-2}$	0.333333333333333333	0.000000000000000000	0.333333333333333333
3	$0.602678571428571597 \times 10^{-2}$	0.000000000000000000	0.333333333333333333	0.333333333333333333
4	$0.602678571428571597 \times 10^{-2}$	0.333333333333333333	0.333333333333333333	0.333333333333333333
5	$0.302836780970891856 \times 10^{-1}$	0.250000000000000000	0.250000000000000000	0.250000000000000000
6	$0.116452490860289742 \times 10^{-1}$	$0.909090909090909091 \times 10^{-1}$	$0.909090909090909091 \times 10^{-1}$	0.727272727272727273
7	$0.116452490860289742 \times 10^{-1}$	$0.909090909090909091 \times 10^{-1}$	0.727272727272727273	$0.909090909090909091 \times 10^{-1}$
8	$0.116452490860289742 \times 10^{-1}$	0.727272727272727273	$0.90909090909090909 \times 10^{-1}$	$0.909090909090909091 \times 10^{-1}$
9	$0.116452490860289742 \times 10^{-1}$	$0.909090909090909091 \times 10^{-1}$	$0.909090909090909091 \times 10^{-1}$	$0.909090909090909091 \times 10^{-1}$
10	$0.109491415613864534 \times 10^{-1}$	$0.665501535736642813 \times 10^{-1}$	0.433449846426335728	0.433449846426335728
11	$0.109491415613864534 \times 10^{-1}$	0.433449846426335728	$0.665501535736642813 \times 10^{-1}$	0.433449846426335728
12	$0.109491415613864534 \times 10^{-1}$	$0.665501535736642813 \times 10^{-1}$	$0.665501535736642813 \times 10^{-1}$	0.433449846426335728
13	$0.109491415613864534 \times 10^{-1}$	0.433449846426335728	$0.665501535736642813 \times 10^{-1}$	$0.665501535736642813 \times 10^{-1}$
14	$0.109491415613864534 \times 10^{-1}$	0.433449846426335728	0.433449846426335728	$0.665501535736642813 \times 10^{-1}$
15	$0.109491415613864534 \times 10^{-1}$	$0.665501535736642813 \times 10^{-1}$	0.433449846426335728	$0.665501535736642813 \times 10^{-1}$

Table A.1. The ($s = 15$) nodes and the corresponding weights of a quadrature (cubature) formula to approximate the value of an integral defined on the reference tetrahedron τ_0 in the coordinate system (ξ, η, ζ) [211], [212]. Notice that, this formula integrates exactly all polynomials of degree less than and equal to five.

Therefore, by means of the quadrature formula described above, a definite integral on the reference tetrahedron τ_0 can be approximated in the following form

$$\int_{\tau_0} g(\boldsymbol{\xi})\, d\boldsymbol{\xi} \approx \sum_{j=0}^{s} w_j g(\mathbf{c}_j) = [w_1, \ldots, w_s] \begin{bmatrix} g(\mathbf{c}_1) \\ \vdots \\ g(\mathbf{c}_s) \end{bmatrix}.$$

Then, an approximation of the value of $F_\tau(v)$ can be obtained as follows

$$F_\tau(v) \approx |J| \sum_{i=1}^{s} w_i f\left(\underline{v}^T \widehat{\mathcal{N}}(\mathbf{c}_i)\right) \quad . \tag{A.27}$$

In particular, notice that the value of $F(v)$ in (A.13) can be approximated by a sum of the contributions of the tetrahedrons $\tau \in \mathcal{T}_h$ by means of the expression (A.27).

A.7 Computation of the functional and constraints

The goal of this Section is to describe the discrete formulation of the variational problem (2.6)–(2.11) in the finite dimensional function space V_h defined by piecewise linear continuous functions (the well-known Lagrange elements), where a triangulation $\mathcal{T}_h = \{\tau_i\}_{i=1}^{n_t}$ of the domain $\Omega \in \mathbb{R}^3$ has been considered.

As before, the key idea is to express the integrals defined on Ω in terms of the tetrahedrons of the triangulation $\mathcal{T}_h$. Let us begin denoting by $T1$ the first term of the functional (2.6), which is given by

$$T1 \equiv \int_{\Omega} X_{\Omega_i} SF_i(D(\mathbf{x}))\, d\mathbf{x} = \int_{\Omega_i} \left(e^{-\alpha_i D(\mathbf{x}) - \beta_i D(\mathbf{x})^2}\right) d\mathbf{x}.$$

Then, the value of $T1$ can be obtained by a finite sum of integrals over each tetrahedron $\tau \subset \Omega_i$, that is

$$T1 = \sum_{\tau \subset \Omega_i} \int_{\tau} e^{-\alpha_i D(\mathbf{x}) - \beta_i D(\mathbf{x})^2} \, d\mathbf{x} = \sum_{\tau \subset \Omega_i} T1_{\tau}, \tag{A.28}$$

where

$$T1_{\tau} = \int_{\tau} e^{-\alpha_i D(\mathbf{x}) - \beta_i D(\mathbf{x})^2} \, d\mathbf{x}. \tag{A.29}$$

In a similar way, the second term of the functional (2.6) can be expressed as follows

$$T2 \equiv \int_{\Omega_j} \left(1 - e^{-\alpha_j D(\mathbf{x}) - \beta_j D(\mathbf{x})^2}\right) d\mathbf{x} = \sum_{\tau \subset \Omega_j} T2_{\tau}, \tag{A.30}$$

where

$$T2_{\tau} = \int_{\tau} \left(1 - e^{-\alpha_j D(\mathbf{x}) - \beta_j D(\mathbf{x})^2}\right) \, d\mathbf{x}. \tag{A.31}$$

On the other hand, it should be noted that the discrete formulation of the last term of the functional (2.6) in the finite dimensional function space V_h has been described in the previous Sections (see (A.11) in Section A.4 for further details).

Therefore, in order to obtain a whole discrete formulation of the problem (P) defined by (2.6)–(2.11), the inequality constraints (2.10) and (2.11) should be also expressed in the finite dimensional function space V_h. Similarly, the gradient vectors and Hessian matrices should be computed for the functional (2.6) and constraints (2.7), (2.10) and (2.11) of the problem (P) to look for the minimizer function through an optimization algorithm. In particular, the following Sections are devoted to provide a detailed description of these issues. Finally, existence and uniqueness properties of solutions of the problem (P) in the discrete formulation are also discussed.

A.7.1 Computation of the gradient vector and Hessian matrix of the nonlinear functional

To begin with, let $\tau \in \mathcal{T}_h$ be an arbitrary tetrahedron with vertices $\mathbf{x}_1$, $\mathbf{x}_2$, $\mathbf{x}_3$ and $\mathbf{x}_4$, and $d \in V_h$ the linear function restricted to τ, which is expressed as

$d(\mathbf{x}) = \underline{d}^T \widehat{\varphi}(\mathbf{x})$ for $\mathbf{x} \in \tau$, where $\underline{d} \in \mathbb{R}^4$ is the vector whose components are the values of the function $d(\mathbf{x})$ at the vertices of τ, that is

$$\underline{d} = \begin{bmatrix} d(\mathbf{x}_1) \\ d(\mathbf{x}_2) \\ d(\mathbf{x}_3) \\ d(\mathbf{x}_4) \end{bmatrix}.$$

Then, using the affine transformation $\Psi(\boldsymbol{\xi})$ in (A.22), the integrals of $T1_\tau$ in (A.29) and $T2_\tau$ in (A.31) can be expressed in terms of the reference tetrahedron τ_0 on the nodal basis functions $\widehat{\mathcal{N}}(\boldsymbol{\xi})$ and approximated by means of the quadrature formula as follows

$$\begin{aligned} T1_\tau &\approx |J| \sum_{k=1}^{s} w_k \, e^{-\alpha_i(\underline{d}^T \widehat{\mathcal{N}}(\mathbf{c}_k)) - \beta_i(\underline{d}^T \widehat{\mathcal{N}}(\mathbf{c}_k))^2}, \\ T2_\tau &\approx |J| \sum_{k=1}^{s} w_k \, \left(1 - e^{-\alpha_j(\underline{d}^T \widehat{\mathcal{N}}(\mathbf{c}_k)) - \beta_j(\underline{d}^T \widehat{\mathcal{N}}(\mathbf{c}_k))^2}\right). \end{aligned} \tag{A.32}$$

On the other hand, the gradient vector and Hessian matrix of $T1$ in (A.28) and $T2$ in (A.30) can be assembled from the first and the second derivatives of $T1_\tau$ and $T2_\tau$ in (A.32) with respect to $\underline{d}$ for all tetrahedron $\tau \in \Omega_i$ and $\tau \in \Omega_j$ respectively. In what follows, the expressions of such gradient vectors and Hessian matrices are described.

The differential of $T1_\tau$ with respect to $\underline{d}$ is given by

$$(T1_\tau)_{\underline{d}} = |J| \sum_{k=1}^{s} w_k \, e^{-\alpha_i(\underline{d}^T \widehat{\mathcal{N}}(\mathbf{c}_k)) - \beta_i(\underline{d}^T \widehat{\mathcal{N}}(\mathbf{c}_k))^2} \left(-\alpha_i - 2\beta_i(\underline{d}^T \widehat{\mathcal{N}}(\mathbf{c}_k))\right) \widehat{\mathcal{N}}^T(\mathbf{c}_k)$$

and similarly, the differential of $T2_\tau$ can be expressed as follows

$$(T2_\tau)_{\underline{d}} = |J| \sum_{k=1}^{s} w_k \, \left(1 - e^{-\alpha_j(\underline{d}^T \widehat{\mathcal{N}}(\mathbf{c}_k)) - \beta_j(\underline{d}^T \widehat{\mathcal{N}}(\mathbf{c}_k))^2}\right) \left(\alpha_j + 2\beta_j(\underline{d}^T \widehat{\mathcal{N}}(\mathbf{c}_k))\right) \widehat{\mathcal{N}}^T(\mathbf{c}_k).$$

On the other hand, the Hessian matrix of $T1_\tau$ and $T2_\tau$ are given by

$$(T1_\tau)_{\underline{d},\underline{d}} = |J| \sum_{k=1}^{s} w_k \, e^{-\alpha_i(\underline{d}^T\widehat{\mathcal{N}}(\mathbf{c}_k))-\beta_i(\underline{d}^T\widehat{\mathcal{N}}(\mathbf{c}_k))^2} \left(\left(\alpha_i + 2\beta_i(\underline{d}^T\widehat{\mathcal{N}}(\mathbf{c}_k))\right)^2 - 2\beta_i \right) \widehat{\mathcal{N}}(\mathbf{c}_k)\widehat{\mathcal{N}}^T(\mathbf{c}_k)$$

and

$$(T2_\tau)_{\underline{d},\underline{d}} = |J| \sum_{k=1}^{s} w_k \, \left(1 - e^{-\alpha_j(\underline{d}^T\widehat{\mathcal{N}}(\mathbf{c}_k))-\beta_j(\underline{d}^T\widehat{\mathcal{N}}(\mathbf{c}_k))^2}\right) \left(2\beta_j - \left(\alpha_j + 2\beta_j(\underline{d}^T\widehat{\mathcal{N}}(\mathbf{c}_k))\right)^2\right) \widehat{\mathcal{N}}(\mathbf{c}_k)\widehat{\mathcal{N}}^T(\mathbf{c}_k).$$

To conclude this Section, observe that the gradient vector and Hessian matrix of the last term in the functional (2.6) restricted to an arbitrary tetrahedron τ can be easily obtained from (A.19) in Section A.5, which are respectively

$$(a_\tau(d,d))_{\underline{d}} = 2A_\tau\underline{d},$$

where $A_\tau = E$, being E the matrix defined in (A.21), and

$$(a_\tau(d,d))_{\underline{d},\underline{d}} = 2A_\tau.$$

A.7.2 The constraint on the gradient

The constraint on the gradient (2.7) should be also formulated in the finite dimensional function space V_h respect to every tetrahedron τ of the triangulation $\mathcal{T}_h$. To do that, for an arbitrary tetrahedron $\tau \in \mathcal{T}_h$, let us consider the linear function $d(\mathbf{x}) = \underline{d}^T\widehat{\varphi}(\mathbf{x})$ for $\mathbf{x} \in \tau$, where as before $\underline{d}$ denotes the vector $\underline{d} = [d(\mathbf{x}_1), d(\mathbf{x}_2), d(\mathbf{x}_3), d(\mathbf{x}_4)]^T \in \mathbb{R}^4$ and $\widehat{\varphi}$ the mapping whose components are the nodal basis functions associated to the vertices of τ, that is, $\widehat{\varphi}(\mathbf{x}) = [\varphi_1(\mathbf{x}), \varphi_2(\mathbf{x}), \varphi_3(\mathbf{x}), \varphi_4(\mathbf{x})]^T$. Then, the constraint (2.7) can be written as follows

$$|\nabla d(\mathbf{x})| \leq C_1 \;\Rightarrow\; \sqrt{(\underline{d}^T\widehat{\varphi}_x(\mathbf{x}))^2 + (\underline{d}^T\widehat{\varphi}_y(\mathbf{x}))^2 + (\underline{d}^T\widehat{\varphi}_z(\mathbf{x}))^2} \leq C_1,$$

where using the property (A.18) in Section A.5 can be expressed in the following form

$$\underline{d}^T(\widehat{\varphi}_x\widehat{\varphi}_x^T + \widehat{\varphi}_y\widehat{\varphi}_y^T + \widehat{\varphi}_z\widehat{\varphi}_z^T)\underline{d} \leq C_1^2, \tag{A.33}$$

which can be easily computed by means of the affine transformation $\Psi(\boldsymbol{\xi})$ in (A.22) to the reference tetrahedron τ_0 in the nodal basis functions $\widehat{\mathcal{N}}(\boldsymbol{\xi})$ in (A.23).

Then, the gradient vector is the first derivative of inequality (A.33) with respect to $\underline{d}$ and given by

$$2(\widehat{\varphi}_x\widehat{\varphi}_x^T + \widehat{\varphi}_y\widehat{\varphi}_y^T + \widehat{\varphi}_z\widehat{\varphi}_z^T)\underline{d},$$

where hence the Hessian matrix is the second derivative of (A.33) and defined as follows

$$2(\widehat{\varphi}_x\widehat{\varphi}_x^T + \widehat{\varphi}_y\widehat{\varphi}_y^T + \widehat{\varphi}_z\widehat{\varphi}_z^T).$$

A.7.3 The volumetric constraints

In particular, this Section is devoted to present the discretization in the finite dimensional function space V_h, as well as the procedure to compute the gradient vector and Hessian matrix, of the volumetric constraints (2.10)–(2.11). As described before, the gradient vector and Hessian matrix are assembled from the contributions of the tetrahedrons τ in the triangulation $\mathcal{T}_h$. For the sake of simplicity, let us only consider the volumetric constraint (2.10) given by

$$|\{\mathbf{x} \in \Omega_i : \ D(\mathbf{x}) > C_{V_i}\}| \geq \delta_i|\Omega_i|, \tag{A.34}$$

where it should be noted that the arguments presented in this Section can be similarly used for the volumetric constraint (2.11).

As a matter of fact, the volumetric constraint (A.34) can be interpreted as the portion of the volume $|\Omega_i|$ that receives a radiation dose higher than C_{V_i} must be at least the δ_i percent of the total volume $|\Omega_i|$ for $(0 \leq \delta_i \leq 1)$. Therefore, the volume $|\Omega_i|$ and the portion of $|\Omega_i|$ that receives a radiation dose higher than C_{V_i} (denoted in what follows as $|\widehat{\Omega}_i|$) should be computed.

The volume $|\Omega_i|$ can be computed by the finite sum of the volume of the tetra-

hedrons in Ω_i. Thus, for an arbitrary tetrahedron $\tau \in \Omega_i$ in the triangulation $\mathcal{T}_h$ with vertices $\mathbf{x}_1$, $\mathbf{x}_2$, $\mathbf{x}_3$ and $\mathbf{x}_4$, the volume $|\tau|$ can be computed by means of the determinant of the matrix, whose columns are $\mathbf{x}_2 - \mathbf{x}_1$, $\mathbf{x}_3 - \mathbf{x}_1$ and $\mathbf{x}_4 - \mathbf{x}_1$, and denoted by $[\mathbf{x}_2 - \mathbf{x}_1, \mathbf{x}_3 - \mathbf{x}_1, \mathbf{x}_4 - \mathbf{x}_1]$, as follows

$$|\tau| = \frac{|\det([\mathbf{x}_2 - \mathbf{x}_1, \mathbf{x}_3 - \mathbf{x}_1, \mathbf{x}_4 - \mathbf{x}_1])|}{6}.$$

In a similar way, the volume $|\widehat{\Omega}_i|$ can be computed by the finite sum of the portions of the volume that receive a radiation dose higher than C_{V_i} of the tetrahedrons in Ω_i. To do that, let us take the same arbitrary tetrahedron $\tau \in \Omega_i$ defined above, and let $d(\mathbf{x}) = \underline{d}^T \widehat{\varphi}(\mathbf{x})$ be a linear function in τ, and $\underline{d} = [d_1, d_2, d_3, d_4]^T$ be the constant vector whose components are the values of the radiation dose in the vertices of τ, that is, $d_i = d(\mathbf{x_i})$ for $(1 \leq i \leq 4)$. Then, the following four general cases in terms of the radiation dose in the vertices of τ can be considered:

1. No vertex of τ receives a radiation dose higher than C_{V_i}.
2. Every vertex of τ receives a radiation dose higher than C_{V_i}.
3. Only one vertex (respectively, the opposite three vertices) of τ receives a radiation dose higher than C_{V_i} (see Figure A.4).
4. Exactly two vertices (respectively, the opposite two vertices) of τ receive a radiation dose higher than C_{V_i} (see Figure A.5).

In the first case, the portion of τ that receives a radiation dose higher than C_{V_i} is equal to zero, while in the second case is the total volume, $|\tau|$. Since that in both cases the radiation dose in all vertices is higher or lower than C_{V_i} respectively, the contribution of this tetrahedron τ to the gradient vector and Hessian matrix of the volumetric constraint (A.34) is zero.

Let us now consider the third case, where only one vertex of a tetrahedron τ receives a radiation dose higher than C_{V_i}, say for instance $\mathbf{x}_1$. Then, the portion of τ that receives a radiation dose higher than C_{V_i} is the volume of the tetrahedron with vertices $\mathbf{x}_1$, $\mathbf{p}_{12}$, $\mathbf{p}_{13}$ and $\mathbf{p}_{14}$ (see Figure A.6), where $\mathbf{p}_{12}$, $\mathbf{p}_{13}$ and $\mathbf{p}_{14}$ are the points on the edges between $\mathbf{x}_1$ and the remaining three vertices respectively, for

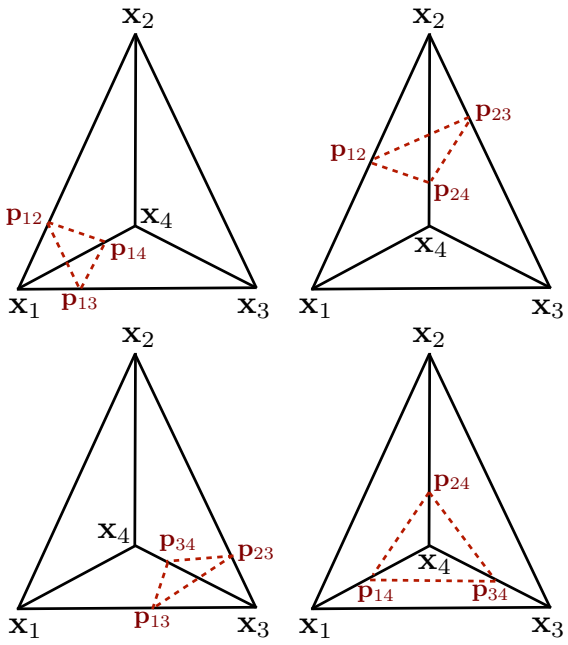

Figure A.4. Representation of the possible combinations where only one vertex (respectively, the opposite three vertices) of τ receives a radiation dose higher than C_{V_i}. Notice that, in the points $\mathbf{p}_{ij}$ for $(1 \leq i, j \leq 4 \text{ and } i \neq j)$ the radiation doses are equal to C_{V_i}.

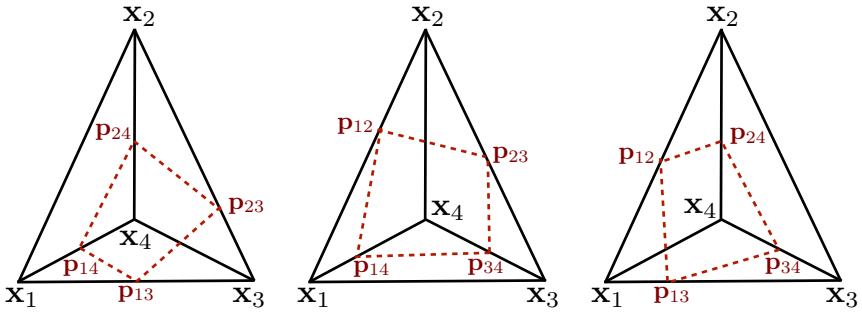

Figure A.5. Representation of the possible combinations where exactly two vertices (respectively, the opposite two vertices) of τ receive a radiation dose higher than C_{V_i}. Notice that, in the points $\mathbf{p}_{ij}$ for $(1 \leq i, j \leq 4 \text{ and } i \neq j)$ the radiation doses are equal to C_{V_i}.

which the radiation doses are equal to C_{V_i}. Observe that, the equations of these points are given by

$$\begin{aligned}
\mathbf{p}_{12} &= \mathbf{x}_1 + \frac{C_{V_i} - d_1}{d_2 - d_1}(\mathbf{x}_2 - \mathbf{x}_1), \\
\mathbf{p}_{13} &= \mathbf{x}_1 + \frac{C_{V_i} - d_1}{d_3 - d_1}(\mathbf{x}_3 - \mathbf{x}_1), \\
\mathbf{p}_{14} &= \mathbf{x}_1 + \frac{C_{V_i} - d_1}{d_4 - d_1}(\mathbf{x}_4 - \mathbf{x}_1),
\end{aligned}$$

where, for instance, the equation of the point $\mathbf{p}_{12} \in [\mathbf{x}_1, \mathbf{x}_2]$ is obtained as follows. Let $\mathbf{x} = \mathbf{x}_1 + t(\mathbf{x}_2 - \mathbf{x}_1)$ be the parametric equation of the line passing through points $\mathbf{x}_1$ and $\mathbf{x}_2$, where $d_2 \leq C_{V_i} < d_1$. Then, the radiation dose in the line $[\mathbf{x}_1, \mathbf{x}_2]$ is equal to C_{V_i} when $d_1 + t(d_2 - d_1) = C_{V_i}$ holds, which implies that the value of the parameter t is $\frac{C_{V_i} - d_1}{d_2 - d_1}$. Then, $\mathbf{p}_{12} = \mathbf{x}_1 + \frac{C_{V_i} - d_1}{d_2 - d_1}(\mathbf{x}_2 - \mathbf{x}_1)$. Notice that, the equations of $\mathbf{p}_{13}$ and $\mathbf{p}_{14}$ are obtained in a similar way.

Therefore, the contribution to $|\widehat{\Omega}_i|$ of the tetrahedron τ is computed as follows

$$V_c \equiv \frac{|(\mathbf{p}_{12} - \mathbf{x}_1)\ (\mathbf{p}_{13} - \mathbf{x}_1)\ (\mathbf{p}_{14} - \mathbf{x}_1)|}{6} = \left(\frac{C_{V_i} - d_1}{d_2 - d_1}\right) \cdot \left(\frac{C_{V_i} - d_1}{d_3 - d_1}\right) \cdot \left(\frac{C_{V_i} - d_1}{d_4 - d_1}\right) \cdot |\tau|, \quad \text{(A.35)}$$

where V_c is the volume of the tetrahedron with vertices $\mathbf{x}_1$, $\mathbf{p}_{12}$, $\mathbf{p}_{13}$ and $\mathbf{p}_{14}$.

Analogously, if the vertices $\mathbf{x}_2$, $\mathbf{x}_3$ and $\mathbf{x}_4$ receive a radiation dose higher than C_{V_i} and $\mathbf{x}_1$ less than C_{V_i}, the portion of the volume $|\tau|$ that receives a radiation dose higher than C_{V_i} is given by $(|\tau| - V_c)$ (see Figure A.6).

The next step is to describe the form of the gradient vector restricted to an arbitrary tetrahedron τ, which satisfies the third case stated above. To obtain it, the first derivative of equation (A.35) with respect to $\underline{d}$ should be computed, which is given by

$$\partial_{d_1}(V_c) = |\tau| \cdot \left(\frac{1}{C_{V_i} - d_1}\right) \cdot \left[\left(\frac{C_{V_i} - d_2}{d_2 - d_1}\right) + \left(\frac{C_{V_i} - d_3}{d_2 - d_1}\right) + \left(\frac{C_{V_i} - d_4}{d_2 - d_1}\right)\right],$$

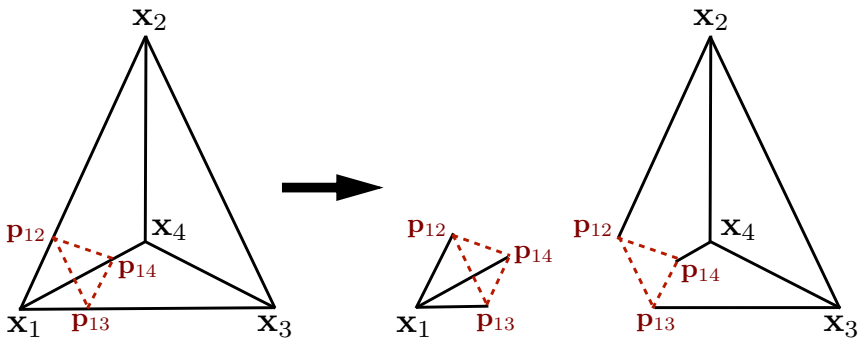

Figure A.6. Representation of the combination where only the node $\mathbf{x}_1$ receives a radiation dose higher than C_{V_i}, or the vertices $\mathbf{x}_2$, $\mathbf{x}_3$ and $\mathbf{x}_4$ receive a radiation dose higher than C_{V_i} and $\mathbf{x}_1$ less than C_{V_i}. Notice that, in the points $\mathbf{p}_{ij}$ for ($i = 1$ and $j = 2, 3, 4$) the radiation doses are equal to C_{V_i}.

$$\partial_{d_2}(V_c) = |\tau| \cdot \left(\frac{1}{C_{V_i} - d_1}\right) \cdot \left(-\frac{C_{V_i} - d_1}{d_2 - d_1}\right),$$
$$\partial_{d_3}(V_c) = |\tau| \cdot \left(\frac{1}{C_{V_i} - d_1}\right) \cdot \left(-\frac{C_{V_i} - d_1}{d_3 - d_1}\right),$$
$$\partial_{d_4}(V_c) = |\tau| \cdot \left(\frac{1}{C_{V_i} - d_1}\right) \cdot \left(-\frac{C_{V_i} - d_1}{d_4 - d_1}\right).$$

Notice that, the Hessian matrix can be easily obtained from the second derivative of equation (A.35) with respect to $\underline{d}$. In summary, for any other combination of vertices as shown in Figure A.4, the calculation of the portion of the volume $|\tau|$ that receives a radiation dose higher than C_{V_i}, as well as the gradient vector and Hessian matrix, can be obtained in a similar way.

Finally, let us consider the last case where exactly two vertices of τ receive a radiation dose higher than C_{V_i}, for instance $\mathbf{x}_1$ and $\mathbf{x}_2$ (see Figure A.7). Then, the portion of the volume $|\tau|$ that receives a radiation dose higher than C_{V_i} is the volume of the polyhedron given by $\mathbf{x}_1$, $\mathbf{x}_2$, $\mathbf{p}_{13}$, $\mathbf{p}_{14}$, $\mathbf{p}_{23}$ and $\mathbf{p}_{24}$, where $\mathbf{p}_{13}$, $\mathbf{p}_{14}$, $\mathbf{p}_{23}$ and $\mathbf{p}_{24}$ are the points on the edges between vertices $\mathbf{x}_1$, $\mathbf{x}_2$ and $\mathbf{x}_3$, $\mathbf{x}_4$ respectively, for which the radiation dose is equal to C_{V_i}. Notice that, the volume of this polyhedron can be computed by the sum of the volume of the following three tetrahedrons with vertices $\mathbf{x}_2$, $\mathbf{p}_{14}$, $\mathbf{p}_{23}$ and $\mathbf{p}_{24}$; $\mathbf{x}_1$, $\mathbf{x}_2$, $\mathbf{p}_{14}$ and $\mathbf{p}_{23}$; and $\mathbf{x}_1$, $\mathbf{p}_{13}$, $\mathbf{p}_{14}$ and $\mathbf{p}_{23}$ respectively (see Figure A.7). Therefore, in this case the contribution to $|\widehat{\Omega}_i|$ of the tetrahedron τ can be computed as follows

$$\left(\frac{|(\mathbf{p}_{14}-\mathbf{x}_2)\,(\mathbf{p}_{23}-\mathbf{x}_2)\,(\mathbf{p}_{24}-\mathbf{x}_2)|}{6}\right)+\left(\frac{|(\mathbf{x}_2-\mathbf{x}_1)\,(\mathbf{p}_{14}-\mathbf{x}_1)\,(\mathbf{p}_{23}-\mathbf{x}_1)|}{6}\right)$$
$$+\left(\frac{|(\mathbf{p}_{13}-\mathbf{x}_1)\,(\mathbf{p}_{14}-\mathbf{x}_1)\,(\mathbf{p}_{23}-\mathbf{x}_1)|}{6}\right), \tag{A.36}$$

where

$$\begin{aligned}
\mathbf{p}_{13} &= \mathbf{x}_1+\frac{C_{V_i}-D_1}{D_3-D_1}(\mathbf{x}_3-\mathbf{x}_1),\\
\mathbf{p}_{14} &= \mathbf{x}_1+\frac{C_{V_i}-D_1}{D_4-D_1}(\mathbf{x}_4-\mathbf{x}_1),\\
\mathbf{p}_{23} &= \mathbf{x}_2+\frac{C_{V_i}-D_2}{D_3-D_2}(\mathbf{x}_3-\mathbf{x}_2),\\
\mathbf{p}_{24} &= \mathbf{x}_2+\frac{C_{V_i}-D_2}{D_4-D_3}(\mathbf{x}_4-\mathbf{x}_3).
\end{aligned}$$

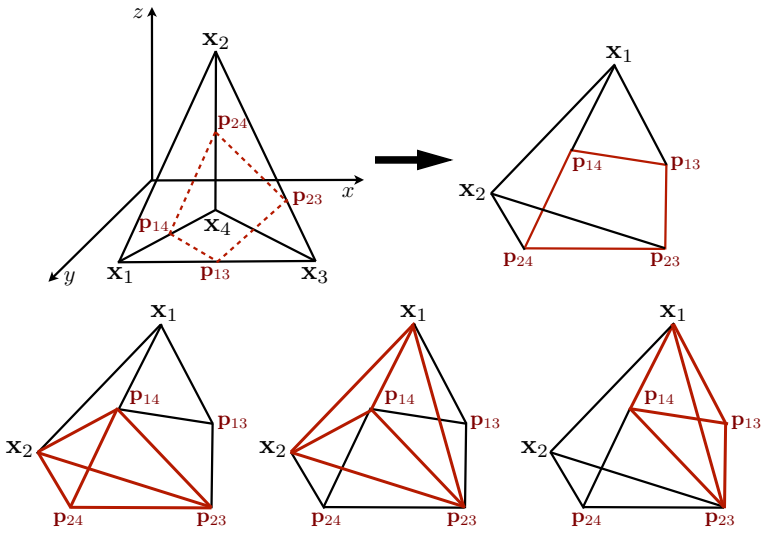

Figure A.7. Representation of the combination where exactly two vertices $\mathbf{x}_1$ and $\mathbf{x}_2$ receive a radiation dose higher than C_{V_i}. Notice that, in the points $\mathbf{p}_{ij}$ for ($i = 1, 2$ and $j = 3, 4$) the radiation doses are equal to C_{V_i} and the polyhedron with vertices $\mathbf{x}_1$, $\mathbf{x}_2$, $\mathbf{p}_{13}$, $\mathbf{p}_{14}$, $\mathbf{p}_{23}$ and $\mathbf{p}_{24}$ can be divided in the following three tetrahedrons with vertices $\mathbf{x}_2$, $\mathbf{p}_{14}$, $\mathbf{p}_{23}$ and $\mathbf{p}_{24}$; $\mathbf{x}_1$, $\mathbf{x}_2$, $\mathbf{p}_{14}$ and $\mathbf{p}_{23}$; and $\mathbf{x}_1$, $\mathbf{p}_{13}$, $\mathbf{p}_{14}$ and $\mathbf{p}_{23}$.

To conclude, observe that the gradient vector and Hessian matrix for this case can be computed from equation (A.36) in a similar way as that discussed for the previous case. In particular, notice that for any other combination of this case as shown in Figure A.5 the calculations are similar.

A.7.4 Existence and uniqueness of solutions in the finite dimensional function space

Let us take the positive radiosensitivity parameters (α, β) of the LQ model described in Chapter 1 and the function $f(d(\mathbf{x}))$ defined as follows

$$f(d(\mathbf{x})) = e^{-\alpha d(\mathbf{x}) - \beta d(\mathbf{x})^2}.$$

Then, it is easy to check that $f(d(\mathbf{x}))$ is a strictly convex function in the interval

$$C_2 \leq d(\mathbf{x}) \leq C_3,$$

if the following condition is satisfied

$$C_2 > \left(-\frac{\alpha}{2\beta} + \sqrt{\frac{1}{2\beta}} \right), \tag{A.37}$$

and the function $(1 - f(d(\mathbf{x})))$ is also strictly convex if, on the contrary,

$$C_3 < \left(-\frac{\alpha}{2\beta} + \sqrt{\frac{1}{2\beta}} \right). \tag{A.38}$$

See the proof of Theorem 3 in Chapter 2 for further details.

Therefore, by means of the affine transformation $\Psi(\underline{\boldsymbol{\xi}})$ in (A.22) the linear function $d \in V_h$ in an arbitrary tetrahedron $\tau \in \mathcal{T}_h$ with vertices $\mathbf{x}_1$, $\mathbf{x}_2$, $\mathbf{x}_3$ and $\mathbf{x}_4$ can be expressed in the reference tetrahedron τ_0 as follows

$$d(\mathbf{x}) = \underline{d}^T \widehat{\mathcal{N}}(\boldsymbol{\xi}), \qquad \mathbf{x} \in \tau, \;\; \boldsymbol{\xi} \in \tau_0,$$

where $\underline{d} = [d(\mathbf{x}_1), d(\mathbf{x}_2), d(\mathbf{x}_3), d(\mathbf{x}_4)]^T \in \mathbb{R}^4$ and the components of $\widehat{\mathcal{N}}(\boldsymbol{\xi})$ are the nodal basis functions on τ_0 given by

$$\mathcal{N}(\underline{\boldsymbol{\xi}}) = \begin{bmatrix} 1-\xi-\eta-\zeta \\ \xi \\ \eta \\ \zeta \end{bmatrix}, \qquad \boldsymbol{\xi} = \begin{bmatrix} \xi \\ \eta \\ \zeta \end{bmatrix} \in \tau_0,$$

so that, the components of the constant vector $\underline{d}$ are the values of $d \in V_h$ at the vertices of τ_0.

Let us now consider the nonnegative weights $[w_1, \ldots, w_s]$ of a quadrature formula based on s nodes $[c_1, \ldots, c_s]$, which is assumed to integrate exactly all polynomials of degree at least two (see Table A.1 in Section A.6). Then, it is possible to prove that the expression

$$I(d(\mathbf{x})) = \sum_{i=1}^{s} w_i f(\underline{d}^T \widehat{\mathcal{N}}(\mathbf{c}_i)), \tag{A.39}$$

which is an approximation of the integral

$$\int_{\tau_0} f(\underline{d}^T \widehat{\mathcal{N}}(\boldsymbol{\xi}))\, d\boldsymbol{\xi},$$

is a convex function of $\underline{d}$ if condition (A.37) holds, which is particularly satisfied if

$$d(\mathbf{x}_1), d(\mathbf{x}_2), d(\mathbf{x}_3), d(\mathbf{x}_4) > \left(-\frac{\alpha}{2\beta} + \sqrt{\frac{1}{2\beta}}\right).$$

In addition, notice that the arguments developed below can also be used to show that

$$1 - I(d(\mathbf{x})) = \sum_{i=1}^{s} w_i \left(1 - f(\underline{d}^T \widehat{\mathcal{N}}(\mathbf{c}_i))\right)$$

is convex if condition (A.38) holds.

In order to prove these results, the differential $\left(f(\underline{d}^T N)\right)_{\underline{d}}$ of $f(\underline{d}^T N)$ with respect to $\underline{d}$ should be computed, where the vector N represents any of the vectors $\widehat{\mathcal{N}}(\mathbf{c}_i)$ for $(i = 1, \ldots, s)$. Thus, applying the chain rule, then

$$\left(f(\underline{d}^T N)\right)_{\underline{d}} = f(\underline{d}^T N)\left(-\alpha - 2\beta(\underline{d}^T N)\right)\left(\underline{d}^T N\right)_{\underline{d}},$$

where $\left(\underline{d}^T N\right)_{\underline{d}}$ is the differential of $\left(\underline{d}^T N\right)$ with respect to $\underline{d}$, which is given by

$$\left(\underline{d}^T N\right)_{\underline{d}} = N^T.$$

Therefore, the differential $\left(f(\underline{d}^T N)\right)_{\underline{d}}$ is obtained as follows

$$\left(f(\underline{d}^T N)\right)_{\underline{d}} = f(\underline{d}^T N)\left(-\alpha - 2\beta(\underline{d}^T N)\right) N^T$$

and the Hessian is expressed in the following form

$$f(\underline{d}^T N)\left(\left(\alpha + 2\beta(\underline{d}^T N)\right)^2 - 2\beta\right) NN^T.$$

Since $f(\underline{d}^T N) = e^{\left(-\alpha(\underline{d}^T N) - \beta(\underline{d}^T N)^2\right)} > 0$ and (NN^T) is a rank one positive semidefinite matrix, then Hessian of $f(\underline{d}^T N)$ is positive semidefinite if

$$\left(\alpha + 2\beta(\underline{d}^T N)\right)^2 - 2\beta > 0,$$

which holds if (A.37) is satisfied.

Therefore, the Hessian of $I(d(\mathbf{x}))$, which is given by

$$\left(I(d(\mathbf{x}))\right)_{\underline{d},\underline{d}} = \sum_{i=1}^{s} w_i f(\underline{d}^T \widehat{\mathcal{N}}(\mathbf{c}_i)) \left(\left(\alpha + 2\beta(\underline{d}^T \widehat{\mathcal{N}}(\mathbf{c}_i))\right)^2 - 2\beta\right) \widehat{\mathcal{N}}(\mathbf{c}_i)\, \widehat{\mathcal{N}}(\mathbf{c}_i)^T, \quad \text{(A.40)}$$

is positive definite if for every vector $\underline{v} \in \mathbb{R}^4$ with $\underline{v} \neq 0$, then

$$\underline{v}^T \left(\sum_{i=1}^{s} w_i f(\underline{d}^T \widehat{\mathcal{N}}(\mathbf{c}_i)) \left(\left(\alpha + 2\beta(\underline{d}^T \widehat{\mathcal{N}}(\mathbf{c}_i))\right)^2 - 2\beta\right) \widehat{\mathcal{N}}(\mathbf{c}_i)\, \widehat{\mathcal{N}}(\mathbf{c}_i)^T\right) \underline{v} > 0,$$

that is, if

$$\sum_{i=1}^{s} w_i f(\underline{d}^T \widehat{\mathcal{N}}(\mathbf{c}_i)) \left(\left(\alpha + 2\beta(\underline{d}^T \widehat{\mathcal{N}}(\mathbf{c}_i))\right)^2 - 2\beta\right) \left(\underline{v}^T \widehat{\mathcal{N}}(\mathbf{c}_i)\right)^2 > 0,$$

where $\left(\underline{v}^T \widehat{\mathcal{N}}(\mathbf{c}_i)\right)^2 = \underline{v}^T \left(\widehat{\mathcal{N}}(\mathbf{c}_i)\, \widehat{\mathcal{N}}(\mathbf{c}_i)^T\right) \underline{v}$ (see equation (A.18) for further details).

Therefore, as argued before, if (A.37) holds then $\left(\alpha + 2\beta(\underline{d}^T\widehat{\mathcal{N}}(\mathbf{c}_i))\right)^2 - 2\beta > 0$, so that, $\underline{v}^T\left((I(d(\mathbf{x})))_{\underline{d},\underline{d}}\right)\underline{v} \geq 0$. Then, $\underline{v}^T\left((I(d(\mathbf{x})))_{\underline{d},\underline{d}}\right)\underline{v} = 0$, which implies that

$$\left(\underline{v}^T\widehat{\mathcal{N}}(\mathbf{c}_i)\right)^2 = 0, \quad i = 1, \ldots, s$$

and

$$\sum_{i=1}^{s} w_i \left(\underline{v}^T\widehat{\mathcal{N}}(\mathbf{c}_i)\right)^2 = 0. \tag{A.41}$$

But since that, the quadrature formula considered integrates exactly all polynomials of degree at least two, then the expression on the left-hand side of (A.41) coincides with

$$\int_{\tau_0} \left(\underline{v}^T\widehat{\mathcal{N}}(\boldsymbol{\xi})\right)^2 d\boldsymbol{\xi},$$

where this integral can only be zero if and only if $\underline{v}^T\widehat{\mathcal{N}}(\boldsymbol{\xi}) = 0$ for all $\boldsymbol{\xi} \in \tau_0$, which being $\underline{v}^T\widehat{\mathcal{N}}(\boldsymbol{\xi}) = 0$ a linear function of $\boldsymbol{\xi}$ can only hold if $v = 0$. Thus, the Hessian $(I(d(\mathbf{x})))_{\underline{d},\underline{d}}$ (A.40) is positive definite and the function $I(d(\mathbf{x}))$ (A.39) is convex.

To conclude this Section, it should be noted that the last term of the functional (2.6) is not strictly convex, because the second derivative is equal to zero for constant functions. However, the sum of all terms of such functional is strictly convex, due to its nonlinear terms are strictly convex as described above.

A.7.5 Computational implementation

Before concluding this Appendix, some comments on the programming routines are appropriate. It should be noted that errors in the implementation of subroutines involving the gradient and the Hessian of objective functions are common and often difficult to detect. Therefore, it is essential to check these routines before applying optimization algorithms. For this purpose, a test has been developed using the Taylor expansion to check the implementation of the gradient and the Hessian of the functional and constraints involved in the problem (P).

In order to briefly explain this procedure, let us consider a Taylor expansion of a

function $f(\mathbf{x}) : \mathbb{R}^n \to \mathbb{R}$ around a given point $\mathbf{x}_0 \in \mathbb{R}^n$, which is formulated at $\mathbf{x}_0 + \epsilon\,\mathbf{x}_1$ for $\epsilon > 0$ and $\mathbf{x}_1 \in \mathbb{R}^n$, that is

$$f(\mathbf{x}_0 + \epsilon\,\mathbf{x}_1) = f(\mathbf{x}_0) + \epsilon\, g(\mathbf{x}_0)^T \mathbf{x}_1 + \left(\frac{\epsilon^2}{2}\right) \mathbf{x}_1^T H(\mathbf{x}_0)\mathbf{x}_1 + O(\epsilon^3)$$

where g and H are the gradient and the Hessian, respectively. Notice that, if only the gradient is tested, the second-order Taylor term is set to zero, and the truncation error is $O(\epsilon^2)$.

This test was performed by computing the Taylor approximation at smaller and smaller values of ϵ and checking whether the truncation errors are as expected, $O(\epsilon^2)$ and $O(\epsilon^3)$ if the approximation is correct up to the gradient and the Hessian terms, respectively. Then, for the *ith* step, $\epsilon_{_i} = \frac{\epsilon_{i-1}}{10}$ is taken, and to verify if indeed the truncation errors decrease as they should (in order 10^{-2} for the gradient and 10^{-3} for the Hessian). Observe that the truncation error for the *ith* step is given by

$$\left| f(\mathbf{x}_0 + \epsilon_{_i}\,\mathbf{x}_1) - f(\mathbf{x}_0) - \epsilon_{_i}\, g(\mathbf{x}_0)^T \mathbf{x}_1 - \left(\frac{\epsilon_{_i}^2}{2}\right) \mathbf{x}_1^T H(\mathbf{x}_0)\mathbf{x}_1 \right|.$$

Notice that a small error in the code of these subroutines would produce much different values in the truncation errors. In particular, this test is useful to detect errors that are common in the implementation and very difficult to detect without this procedure.

Appendix B

Computer simulations for minimizers of a constrained optimization problem

B.1 Comparison with a clinical case: additional results

In this Appendix different computer simulations as a complement to the results discussed in Chapter 2 are described.

To begin with, dose volume histograms (DVHs) for different values of the radiosensitivity parameter α for the case considered in Section 2.5 are provided. More precisely, DVHs for numerical simulations where $w_1 = w_j = 1$ (see Figure B.1), and $w_1 = 10$ and $w_j = 1$ (see Figure B.2) for $(2 \leq j \leq m+1)$ in the functional (2.6) are presented. The remaining parameters are selected as described in Tables 2.2 and 2.4 in Chapter 2 respectively (see Sections 2.5.3 and 2.5.5).

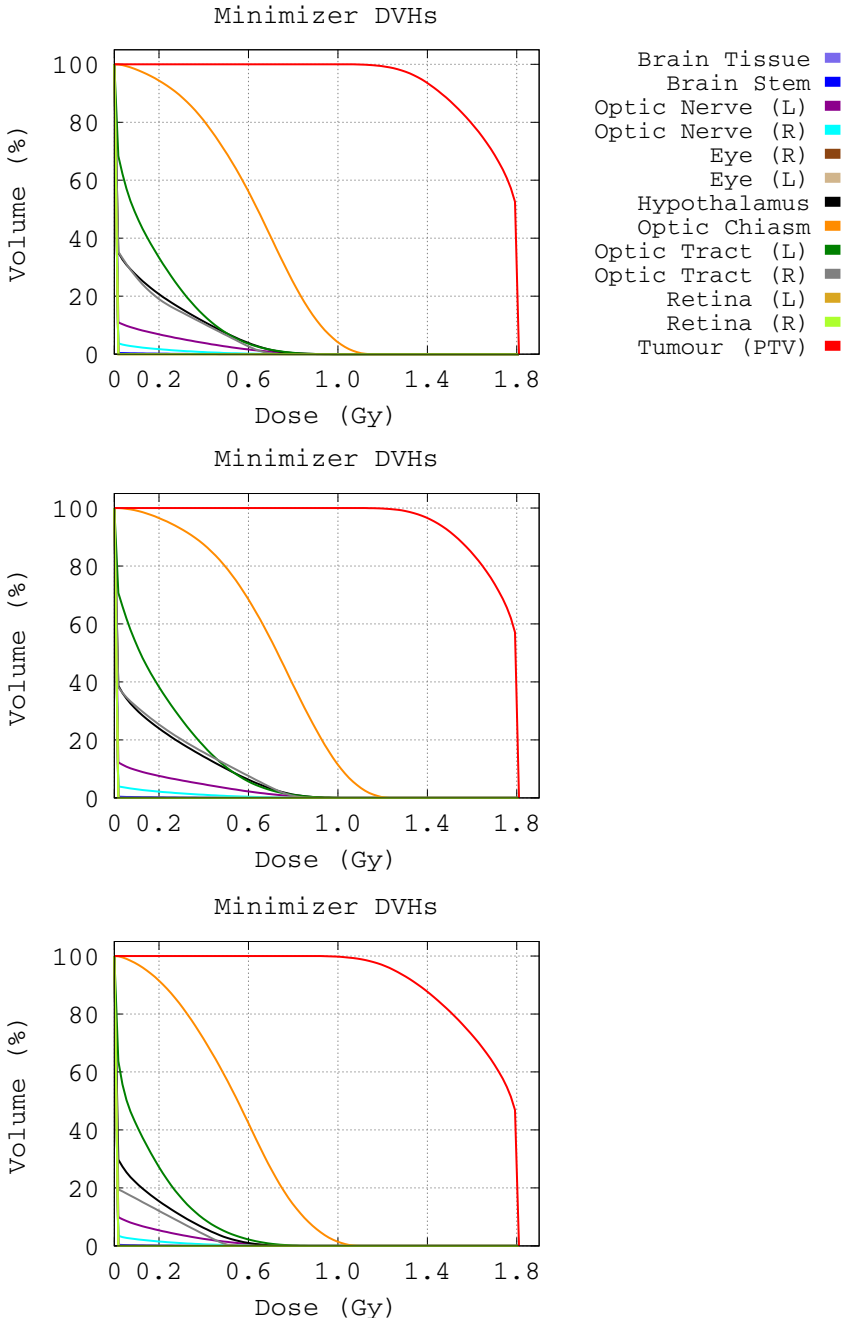

Figure B.1. From top to bottom dose volume histograms (DVHs) for each OAR, healthy tissue (Brain tissue) and the PTV corresponding to numerical simulations of the case $w_1 = w_j = 1$ $(2 \leq j \leq m+1)$ for $\alpha = 0.95Gy^{-1}$, $\alpha = 0.55Gy^{-1}$ and $\alpha = 0.10Gy^{-1}$ respectively.

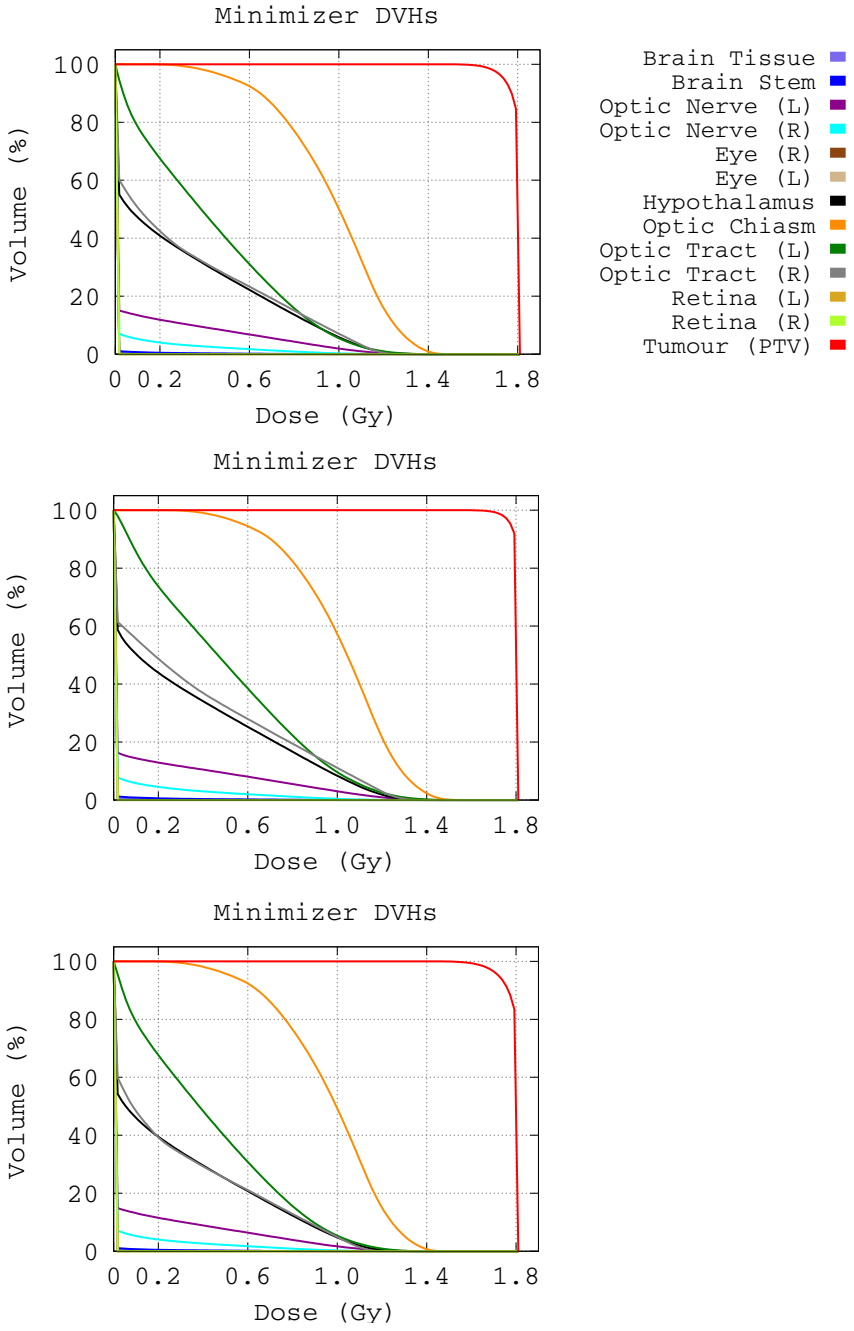

Figure B.2. From top to bottom dose volume histograms (DVHs) for each OAR, healthy tissue (Brain tissue) and the PTV corresponding to numerical simulations of the case $w_1 = 10$ and $w_j = 1$ $(2 \leq j \leq m+1)$ for $\alpha = 0.95Gy^{-1}$, $\alpha = 0.55Gy^{-1}$ and $\alpha = 0.10Gy^{-1}$ respectively.

An inspection of Figures B.1 and B.2 reveals the dependence of the model minimizers with respect to parameters w_1 and α. As described in Chapter 2 and shown in Figure B.1 for the case $w_1 = w_j = 1$ with $(2 \leq j \leq m+1)$ the minimizer provides in all cases low radiation doses on the organs at risk (OARs) and healthy tissue (Brain tissue), but also low radiation dose conformation for the isodose corresponding to 95% of the prescription dose on the planning target volume (PTV), than that obtained with the applied treatment plan (see Table 2.2 in Chapter 2). On the other hand, when the weight corresponding to the PTV dosimetry increases (say, when $w_1 = 10$ and $w_j = 1$ for $(2 \leq j \leq m+1)$) the radiation coverage on the tumor also increases, and so does the radiation doses delivered to OARs and healthy tissue (HT). However, in all cases the maximum radiation dose on the OARs and HT is lower than that delivered with the applied treatment plan (see Figure B.2 and Table 2.4 in Chapter 2). Moreover, for all values of the parameter α considered the coverage of the PTV is also better. Therefore, these simulations support the strategy suggested in Section 2.5 to select an optimal radiation dose distribution as a standard for comparison with radiotherapy tentative treatment plans.

B.2 Description of results for different clinical cases

To continue, numerical simulations corresponding to the remaining nine clinical cases included in this study of patients diagnosed with centrally-located brain tumors (Meningioma) are provided, of which a single case has been discussed in detail in Chapter 2. These will be referred to as Case 2 to 10 in the sequel. All of them were treated in the same Hospital and treatment planning system (TPS) with Intensity Modulated Radiation Therapy (IMRT). For any of them a total prescription dose of $50.4Gy$, scheduled in 28 daily sessions, 5 days a week, of $1.8Gy$ with weekend interruptions, was planned and delivered. For any patient a reconstruction of the PTV and OARs, drawn from the TPS used during the treatment planning process is provided. Furthermore, DVHs corresponding respectively to *i)* the radiation dose distribution actually applied and *ii)* that corresponding to

one minimizer obtained as described in Sections 2.3 and 2.5 are given. Concerning the latter, parameters are selected as follows: $w_1 = 10$ for the PTV dosimetry, $w_j = 1$ with $(2 \leq j \leq m+1)$ for OARs and HT (Brain tissue) terms in (2.6), set $\alpha/\beta = 3.7Gy$ as before and then pick $\alpha = 0.55Gy^{-1}$. As to the bounds (2.7) and (2.8), (2.7) is selected as in the case considered in Section 2.5, and values $C_2 = 0.0Gy$, $C_3 = 1.8Gy$ in (2.8) are also taken in agreement with clinical requirements. For simplicity, only solutions to (2.6)-(2.8) are considered.

A description of the clinical cases considered is provided below. Notice that all studies made share some common properties. In particular, the Homogeneity Index (HI) (see equation (2.2) in Chapter 2) of the proposed minimizers is always equal to one (the optimal homogeneity case on the PTV), whereas for most of the actually applied treatments the corresponding value is different from one. On the other hand, the portion of the PTV receiving the prescribed radiation dose ($1.8Gy$) and the value of the Conformity Index (CI) (see equation (2.3) in Chapter 2) for the isodose corresponding to 95% of the prescription radiation dose on the PTV are always better or equal for the proposed minimizer when compared with the applied treatments. Finally, such minimizers always induce lower side effects on OARs than the applied treatments considered (see Tables and Figures below).

CASE 2:

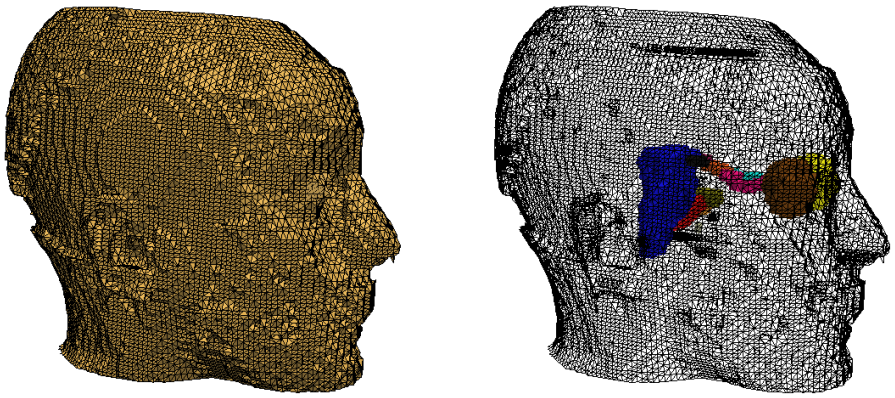

Figure B.3. From left to right a three-dimensional domain reconstruction for the case considered, the three-dimensional Delaunay triangulation created over the whole domain of simulation, and the representation of the PTV and OARs involved.

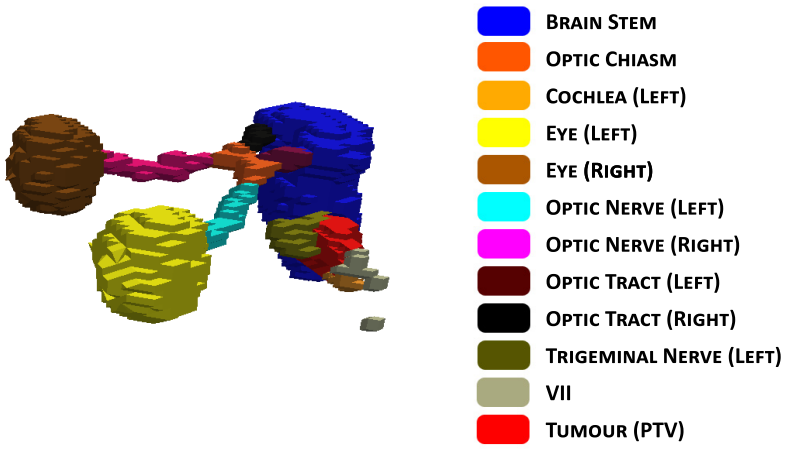

Figure B.4. Three-dimensional reconstruction of the PTV and OARs involved. Notice that the PTV is represented in red.

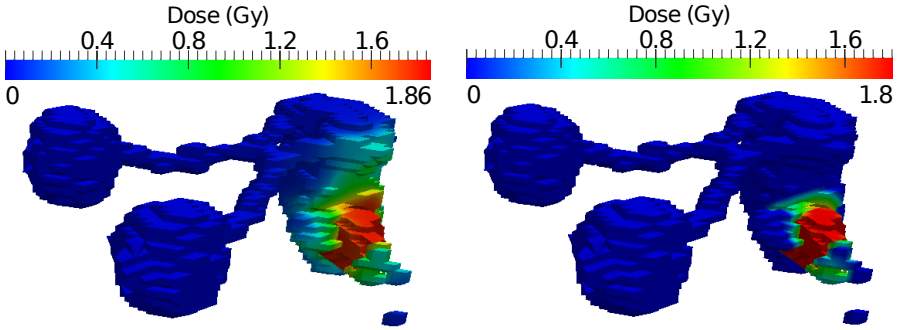

Figure B.5. A comparison of the applied radiation dose distribution (left) and the minimizer radiation dose distribution (right). From left to right the radiation dose distributions (3D) over the PTV and OARs.

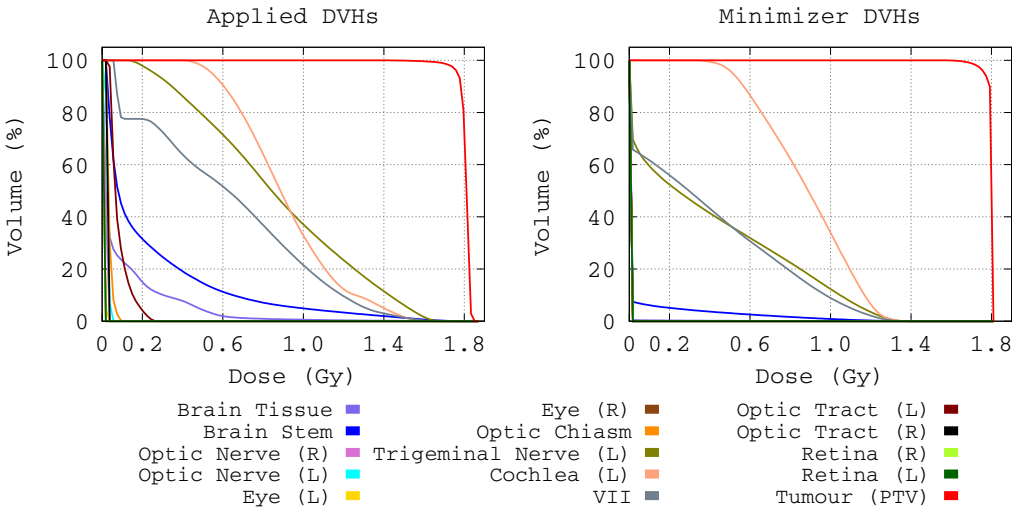

Figure B.6. Dose volume histograms (DVHs) of the applied (left) and minimizer (right) radiation dose distributions for each OAR, healthy tissue (Brain tissue) and the PTV.

Parameter	Applied	Minimizer
PTV_{D_M}	$1.86Gy$	$1.80Gy$
$D_{PTV100\%}$	$1.5524Gy$	$1.6389Gy$
PTV_{Dp}	71.58%	91.88%
$CI_{Dp95\%}$	0.97	0.98
Brain Tissue*	$1.8143Gy$	$1.6832Gy$
Cochlea (Left)*	$1.5226Gy$	$1.3015Gy$
Brain Stem*	$1.5524Gy$	$1.2874Gy$
VII*	$1.5337Gy$	$1.3570Gy$
Trigeminal Nerve (Left)*	$1.6173Gy$	$1.2932Gy$

Table B.1. A comparison of the applied radiation dose distribution (second column) and the minimizer radiation dose distribution (third column). (PTV_{D_M}) Maximum radiation dose received by the PTV. ($D_{PTV100\%}$) Maximum radiation dose received at least by 100% of the PTV. (PTV_{Dp}) Percentage of the PTV receiving the prescribed radiation dose ($1.8Gy$). ($CI_{Dp95\%}$) Conformity Index (CI) for the isodose corresponding to 95% of the prescription radiation dose on the PTV. (*) Maximum radiation dose received by the OARs considered.

CASE 3:

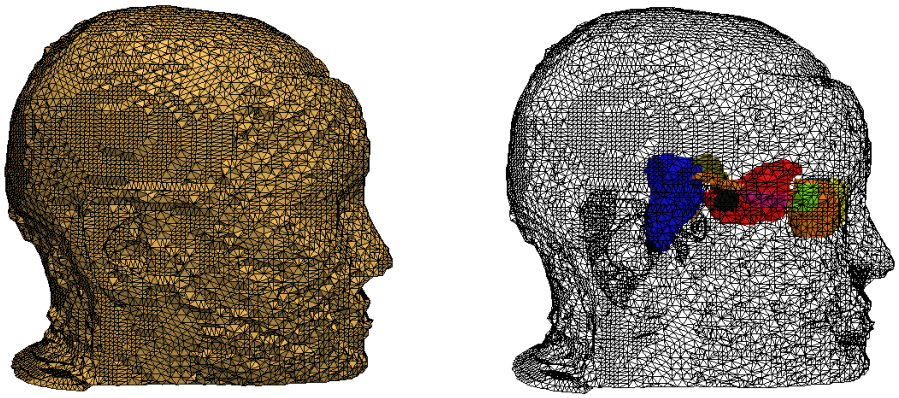

Figure B.7. From left to right a three-dimensional domain reconstruction for the case considered, the three-dimensional Delaunay triangulation created over the whole domain of simulation, and the representation of the PTV and OARs involved.

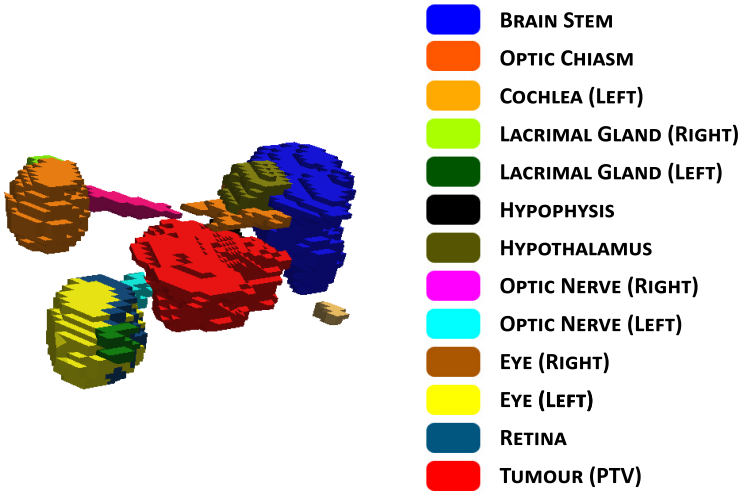

Figure B.8. Three-dimensional reconstruction of the PTV and OARs involved. Notice that the PTV is represented in red.

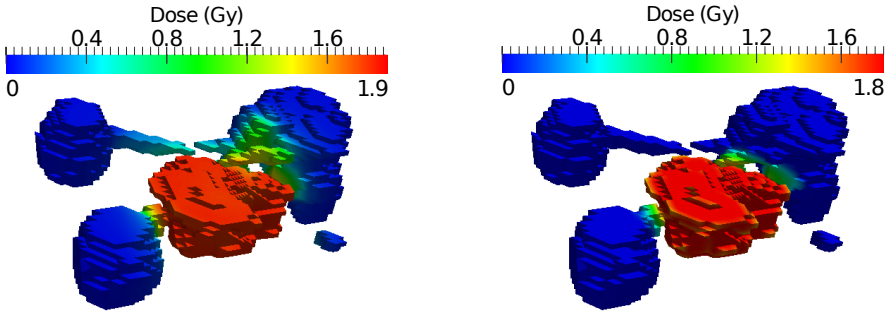

Figure B.9. A comparison of the applied radiation dose distribution (left) and the minimizer radiation dose distribution (right). From left to right the radiation dose distributions (3D) over the PTV and OARs.

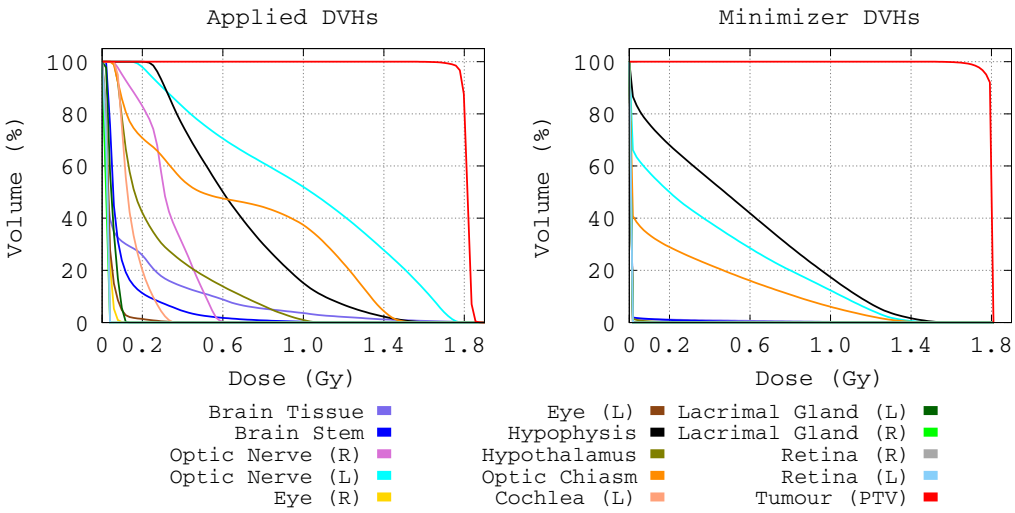

Figure B.10. Dose volume histograms (DVHs) of the applied (left) and minimizer (right) radiation dose distributions for each OAR, healthy tissue (Brain tissue) and the PTV.

Parameter	**Applied**	**Minimizer**
PTV_{D_M}	$1.90Gy$	$1.80Gy$
$D_{PTV100\%}$	$1.6626Gy$	$1.6274Gy$
PTV_{Dp}	78.68%	92.14%
$CI_{Dp95\%}$	0.98	0.98
Brain Tissue*	$1.8876Gy$	$1.7094Gy$
Hypophysis*	$1.5043Gy$	$1.4479Gy$
Optic Nerve (Left)*	$1.7583Gy$	$1.4256Gy$
Optic Chiasm*	$1.4748Gy$	$1.3813Gy$

Table B.2. A comparison of the applied radiation dose distribution (second column) and the minimizer radiation dose distribution (third column). (PTV_{D_M}) Maximum radiation dose received by the PTV. ($D_{PTV100\%}$) Maximum radiation dose received at least by 100% of the PTV. (PTV_{Dp}) Percentage of the PTV receiving the prescribed radiation dose ($1.8Gy$). ($CI_{Dp95\%}$) Conformity Index (CI) for the isodose corresponding to 95% of the prescription radiation dose on the PTV. (*) Maximum radiation dose received by the OARs considered.

CASE 4:

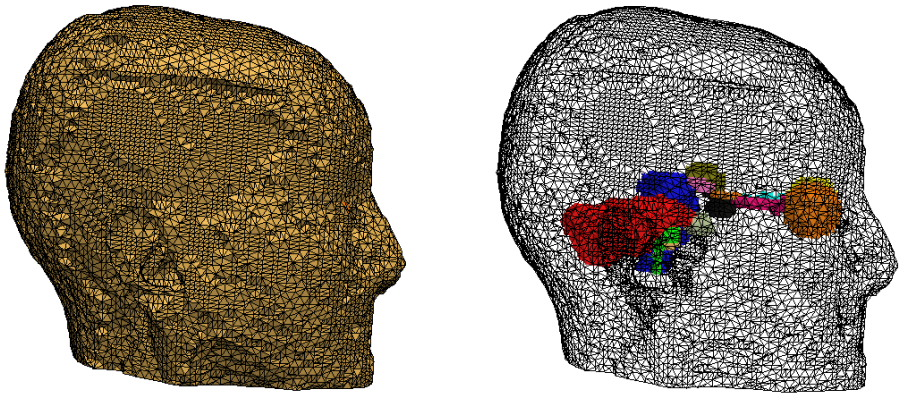

Figure B.11. From left to right a three-dimensional domain reconstruction for the case considered, the three-dimensional Delaunay triangulation created over the whole domain of simulation, and the representation of the PTV and OARs involved.

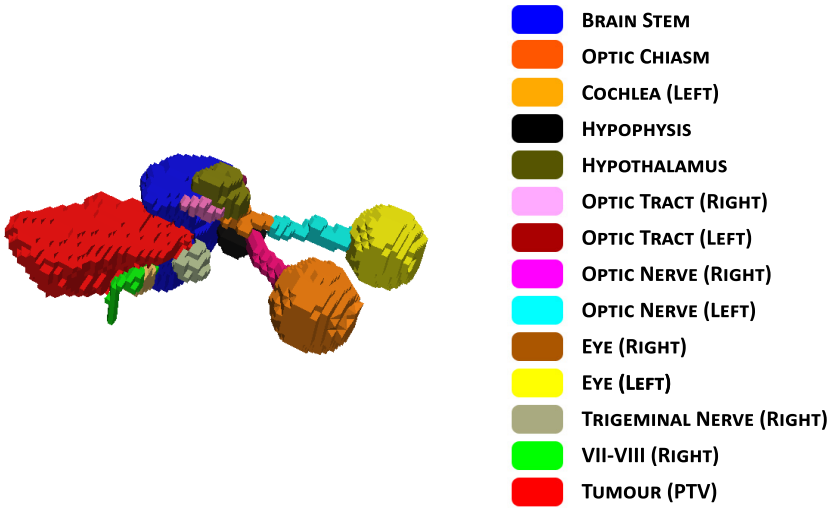

Figure B.12. Three-dimensional reconstruction of the PTV and OARs involved. Notice that the PTV is represented in red.

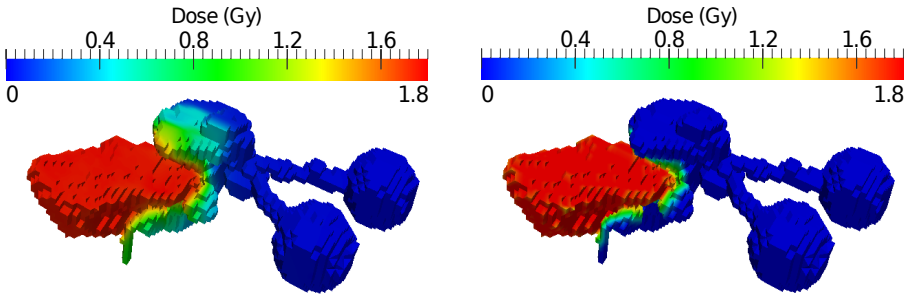

Figure B.13. A comparison of the applied radiation dose distribution (left) and the minimizer radiation dose distribution (right). From left to right the radiation dose distributions (3D) over the PTV and OARs.

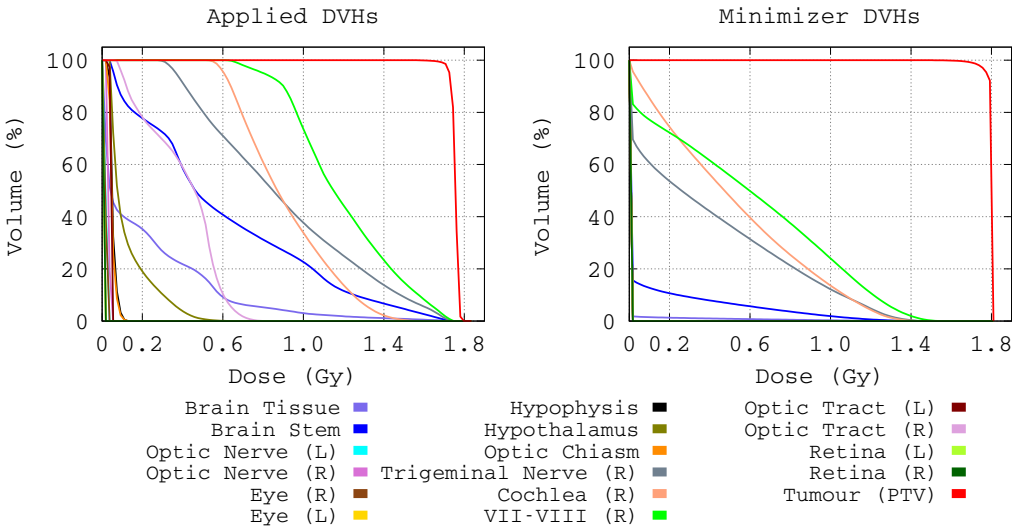

Figure B.14. Dose volume histograms (DVHs) of the applied (left) and minimizer (right) radiation dose distributions for each OAR, healthy tissue (Brain tissue) and the PTV.

Parameter	Applied	Minimizer
PTV_{D_M}	$1.80Gy$	$1.80Gy$
$D_{PTV100\%}$	$1.6334Gy$	$1.6489Gy$
PTV_{Dp}	2.56%	92.18%
$CI_{Dp95\%}$	0.95	0.98
Brain Tissue*	$1.7782Gy$	$1.6651Gy$
VII-VIII (Right)*	$1.7452Gy$	$1.4580Gy$
Cochlea (Right)*	$1.4682Gy$	$1.3813Gy$
Trigeminal Nerve (Right)*	$1.7168Gy$	$1.3975Gy$
Brain Stem*	$1.6885Gy$	$1.3203Gy$

Table B.3. A comparison of the applied radiation dose distribution (second column) and the minimizer radiation dose distribution (third column). (PTV_{D_M}) Maximum radiation dose received by the PTV. ($D_{PTV100\%}$) Maximum radiation dose received at least by 100% of the PTV. (PTV_{Dp}) Percentage of the PTV receiving the prescribed radiation dose ($1.8Gy$). ($CI_{Dp95\%}$) Conformity Index (CI) for the isodose corresponding to 95% of the prescription radiation dose on the PTV. (*) Maximum radiation dose received by the OARs considered.

CASE 5:

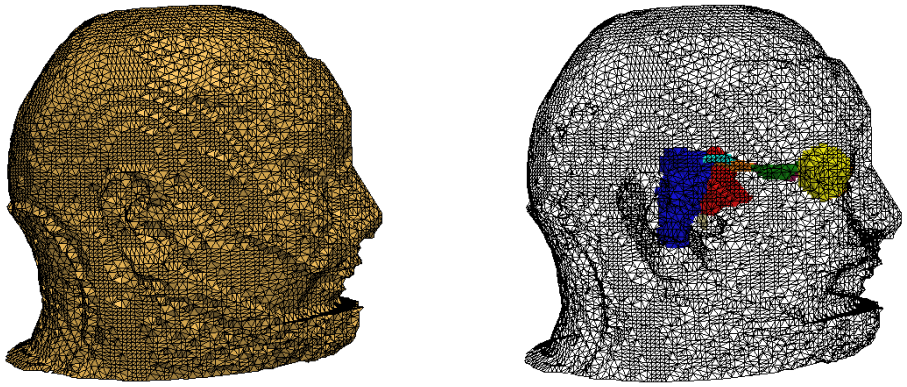

Figure B.15. From left to right a three-dimensional domain reconstruction for the case considered, the three-dimensional Delaunay triangulation created over the whole domain of simulation, and the representation of the PTV and OARs involved.

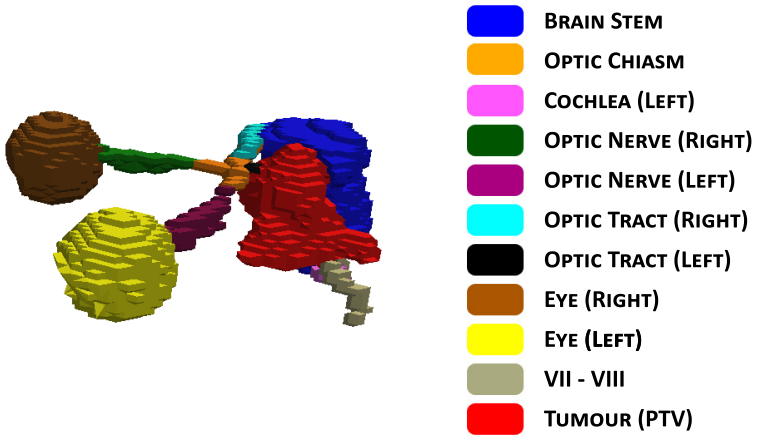

Figure B.16. Three-dimensional reconstruction of the PTV and OARs involved. Notice that the PTV is represented in red.

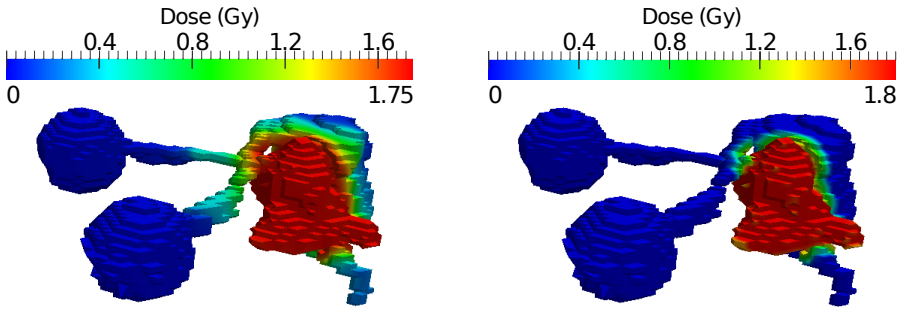

Figure B.17. A comparison of the applied radiation dose distribution (left) and the minimizer radiation dose distribution (right). From left to right the radiation dose distributions (3D) over the PTV and OARs.

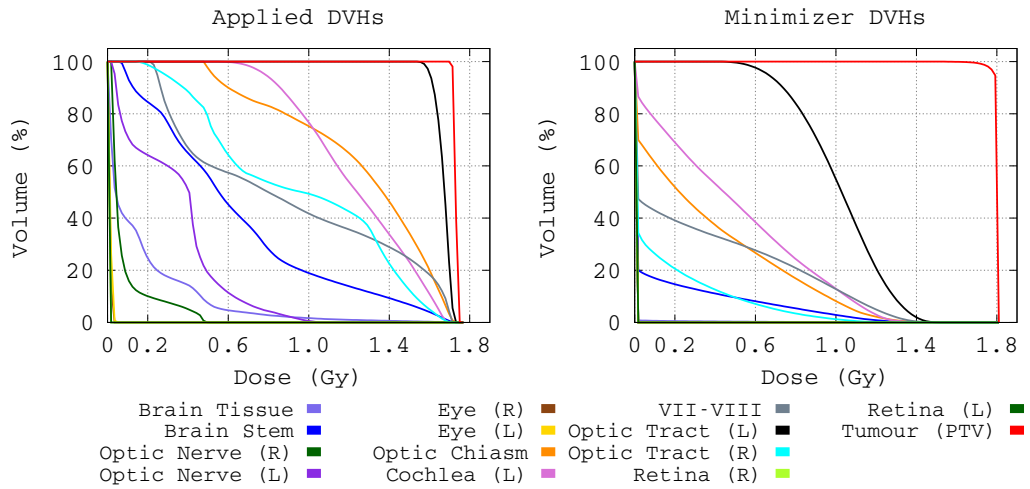

Figure B.18. Dose volume histograms (DVHs) of the applied (left) and minimizer (right) radiation dose distributions for each OAR, healthy tissue (Brain tissue) and the PTV.

Parameter	**Applied**	**Minimizer**
PTV_{D_M}	$1.75Gy$	$1.80Gy$
$D_{PTV100\%}$	$1.6948Gy$	$1.6570Gy$
PTV_{Dp}	0%	94.69%
$CI_{Dp95\%}$	0.98	0.99
Brain Tissue*	$1.7402Gy$	$1.6651Gy$
Brain Stem*	$1.6871Gy$	$1.3146Gy$
Optic Chiasm*	$1.7148Gy$	$1.2951Gy$
Cochlea (Left)*	$1.6754Gy$	$1.2730Gy$
VII-VIII*	$1.7056Gy$	$1.3976Gy$
Optic Tract (Left)*	$1.7202Gy$	$1.4299Gy$
Optic Tract (Right)*	$1.6995Gy$	$1.2817Gy$

Table B.4. A comparison of the applied radiation dose distribution (second column) and the minimizer radiation dose distribution (third column). (PTV_{D_M}) Maximum radiation dose received by the PTV. ($D_{PTV100\%}$) Maximum radiation dose received at least by 100% of the PTV. (PTV_{Dp}) Percentage of the PTV receiving the prescribed radiation dose ($1.8Gy$). ($CI_{Dp95\%}$) Conformity Index (CI) for the isodose corresponding to 95% of the prescription radiation dose on the PTV. (*) Maximum radiation dose received by the OARs considered.

CASE 6:

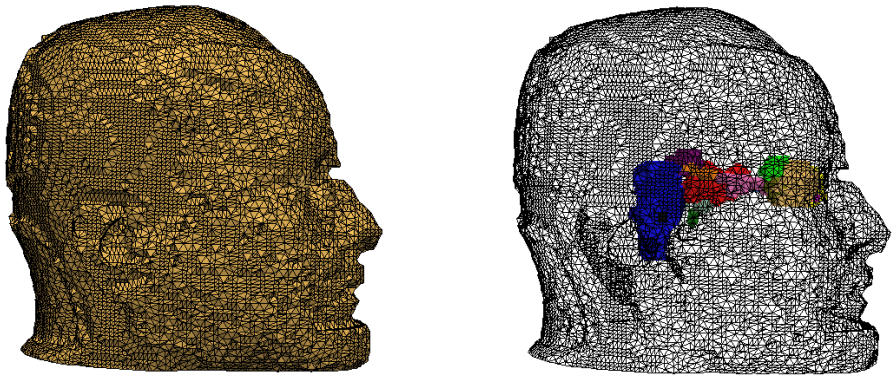

Figure B.19. From left to right a three-dimensional domain reconstruction for the case considered, the three-dimensional Delaunay triangulation created over the whole domain of simulation, and the representation of the PTV and OARs involved.

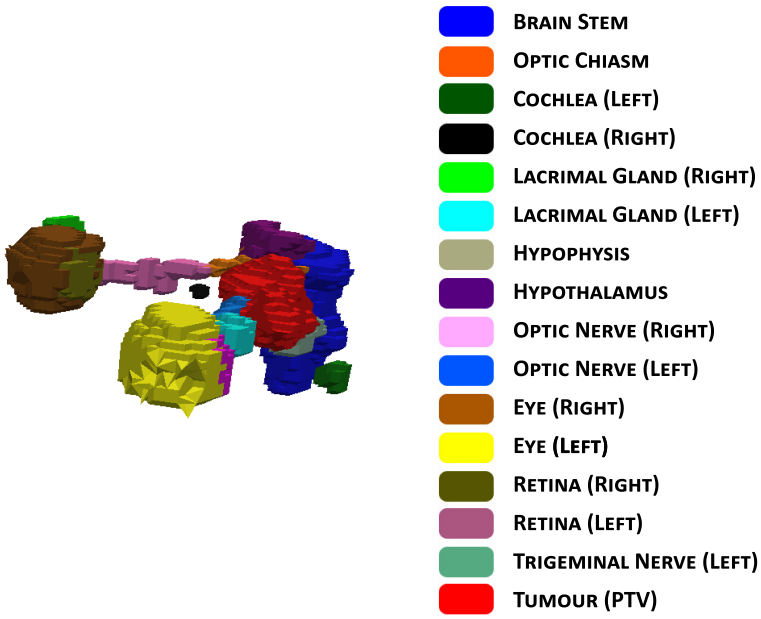

Figure B.20. Three-dimensional reconstruction of the PTV and OARs involved. Notice that the PTV is represented in red.

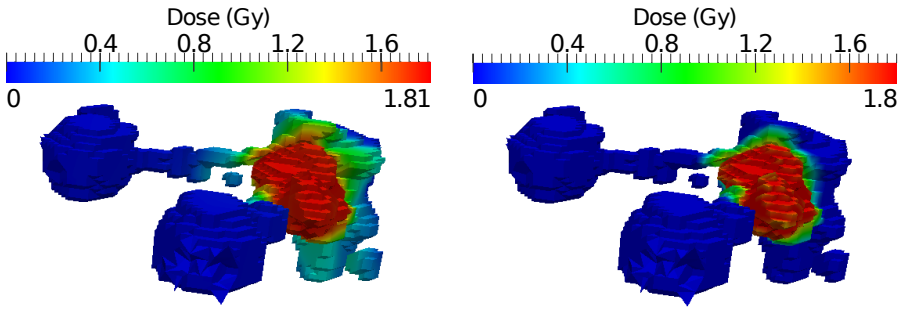

Figure B.21. A comparison of the applied radiation dose distribution (left) and the minimizer radiation dose distribution (right). From left to right the radiation dose distributions (3D) over the PTV and OARs.

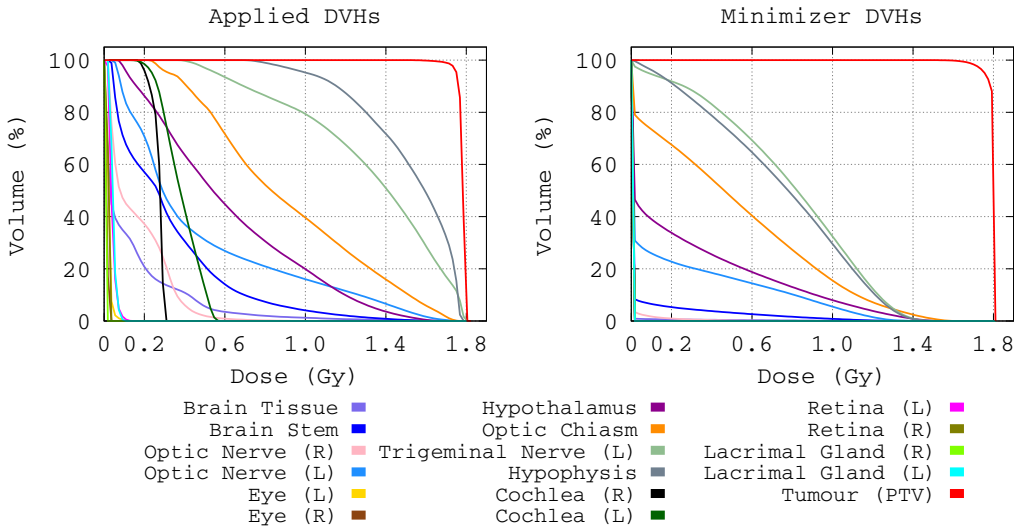

Figure B.22. Dose volume histograms (DVHs) of the applied (left) and minimizer (right) radiation dose distributions for each OAR, healthy tissue (Brain tissue) and the PTV.

Parameter	Applied	Minimizer
PTV_{D_M}	$1.81Gy$	$1.80Gy$
$D_{PTV100\%}$	$1.6226Gy$	$1.6108Gy$
PTV_{Dp}	6.45%	88.69%
$CI_{Dp95\%}$	0.97	0.98
Brain Tissue*	$1.8049Gy$	$1.6832Gy$
Brain Stem*	$1.7037Gy$	$1.3942Gy$
Optic Nerve (Left)*	$1.6409Gy$	$1.3789Gy$
Hypothalamus*	$1.5879Gy$	$1.4437Gy$
Optic Chiasm*	$1.7337Gy$	$1.5022Gy$
Trigeminal Nerve (Left)*	$1.7967Gy$	$1.4218Gy$
Hypophysis*	$1.7767Gy$	$1.4037Gy$

Table B.5. A comparison of the applied radiation dose distribution (second column) and the minimizer radiation dose distribution (third column). (PTV_{D_M}) Maximum radiation dose received by the PTV. ($D_{PTV100\%}$) Maximum radiation dose received at least by 100% of the PTV. (PTV_{Dp}) Percentage of the PTV receiving the prescribed radiation dose ($1.8Gy$). ($CI_{Dp95\%}$) Conformity Index (CI) for the isodose corresponding to 95% of the prescription radiation dose on the PTV. (*) Maximum radiation dose received by the OARs considered.

CASE 7:

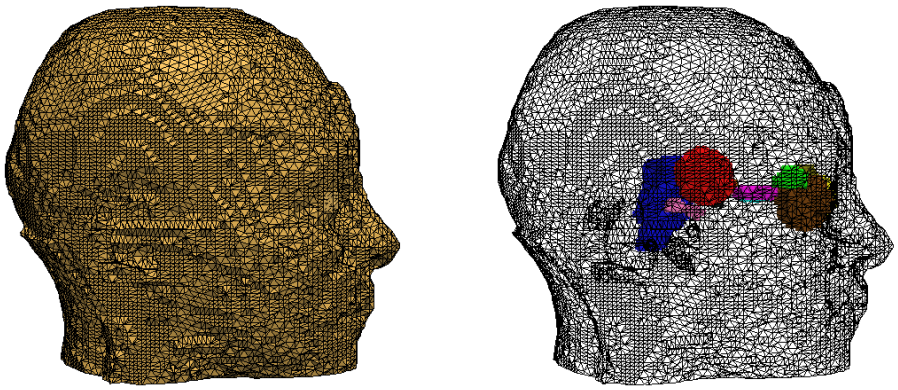

Figure B.23. From left to right a three-dimensional domain reconstruction for the case considered, the three-dimensional Delaunay triangulation created over the whole domain of simulation, and the representation of the PTV and OARs involved.

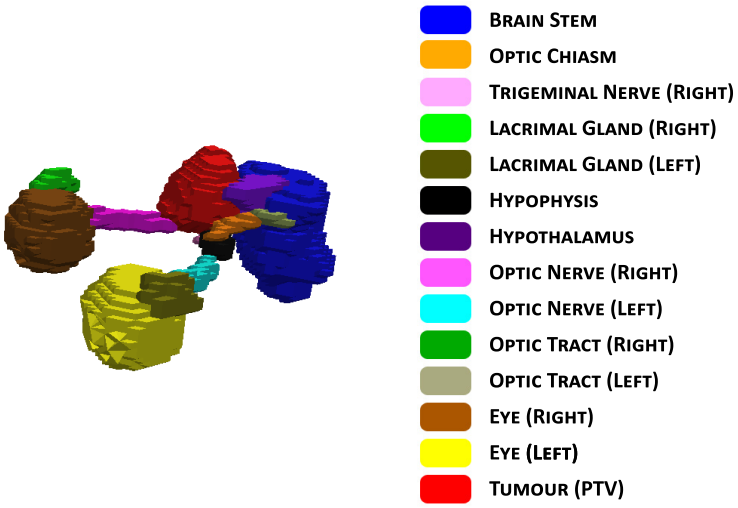

Figure B.24. Three-dimensional reconstruction of the PTV and OARs involved. Notice that the PTV is represented in red.

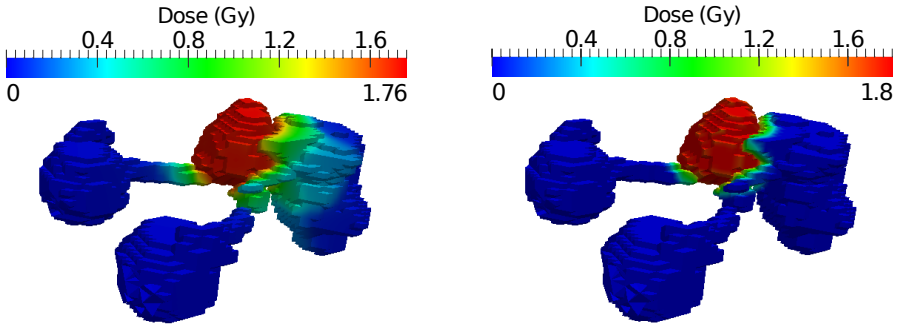

Figure B.25. A comparison of the applied radiation dose distribution (left) and the minimizer radiation dose distribution (right). From left to right the radiation dose distributions (3D) over the PTV and OARs.

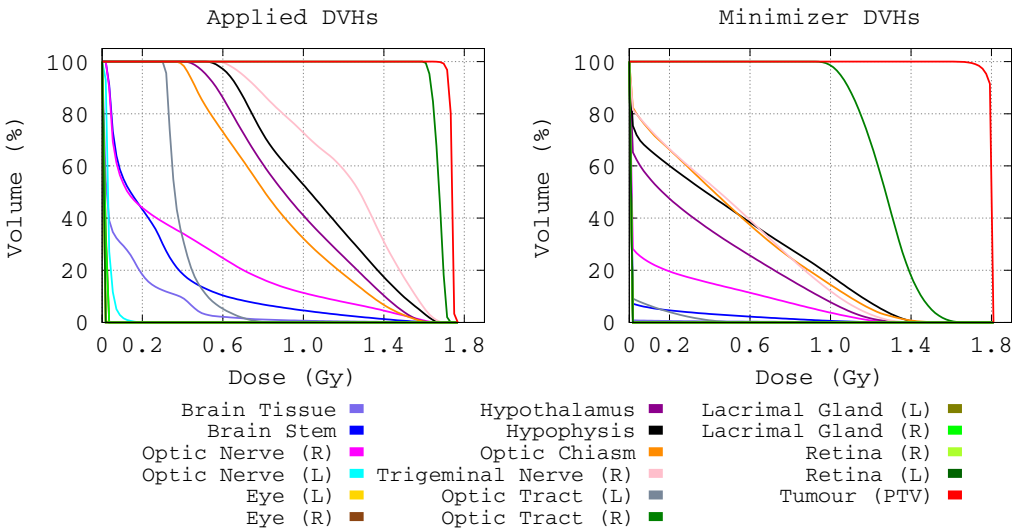

Figure B.26. Dose volume histograms (DVHs) of the applied (left) and minimizer (right) radiation dose distributions for each OAR, healthy tissue (Brain tissue) and the PTV.

Parameter	**Applied**	**Minimizer**
PTV_{D_M}	$1.76Gy$	$1.80Gy$
$D_{PTV100\%}$	$1.6814Gy$	$1.6733Gy$
PTV_{Dp}	0%	92.47%
$CI_{Dp95\%}$	0.96	0.99
Brain Tissue*	$1.7323Gy$	$1.6852Gy$
Brain Stem*	$1.5563Gy$	$1.3842Gy$
Optic Nerve (Right)*	$1.5909Gy$	$1.2946Gy$
Hypothalamus*	$1.5632Gy$	$1.3489Gy$
Hypophysis*	$1.6439Gy$	$1.3955Gy$
Optic Chiasm*	$1.5748Gy$	$1.4437Gy$
Trigeminal Nerve (Right)*	$1.6616Gy$	$1.3651Gy$
Optic Tract (Right)*	$1.7146Gy$	$1.5928Gy$

Table B.6. A comparison of the applied radiation dose distribution (second column) and the minimizer radiation dose distribution (third column). (PTV_{D_M}) Maximum radiation dose received by the PTV. ($D_{PTV100\%}$) Maximum radiation dose received at least by 100% of the PTV. (PTV_{Dp}) Percentage of the PTV receiving the prescribed radiation dose ($1.8Gy$). ($CI_{Dp95\%}$) Conformity Index (CI) for the isodose corresponding to 95% of the prescription radiation dose on the PTV. (*) Maximum radiation dose received by the OARs considered.

CASE 8:

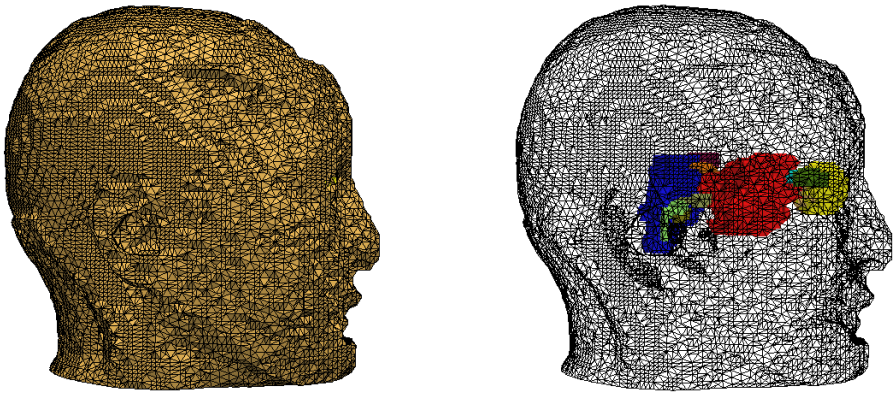

Figure B.27. From left to right a three-dimensional domain reconstruction for the case considered, the three-dimensional Delaunay triangulation created over the whole domain of simulation, and the representation of the PTV and OARs involved.

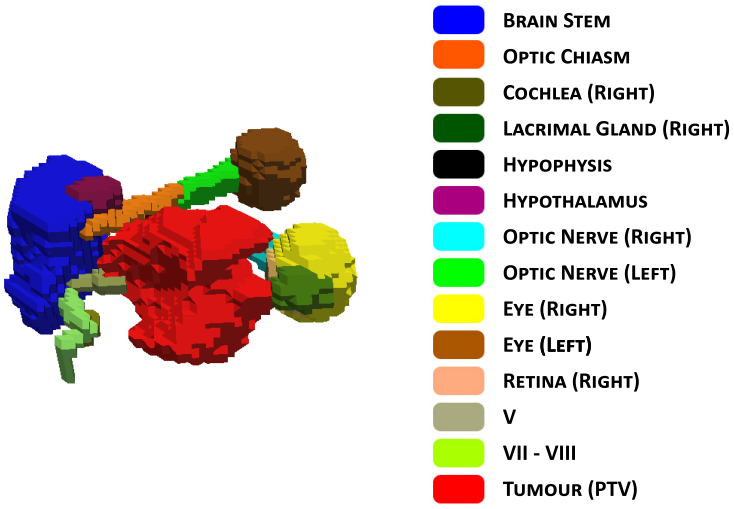

Figure B.28. Three-dimensional reconstruction of the PTV and OARs involved. Notice that the PTV is represented in red.

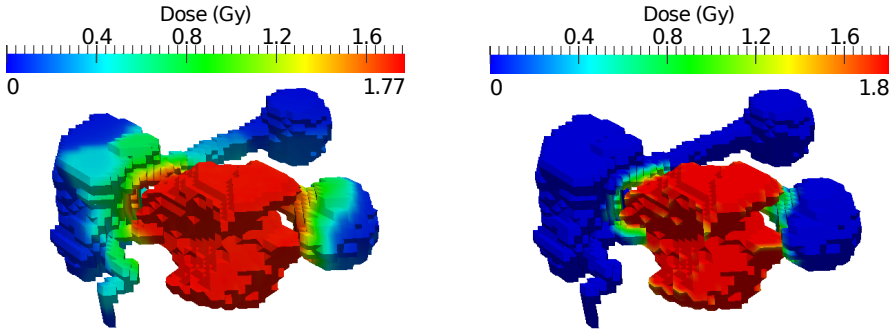

Figure B.29. A comparison of the applied radiation dose distribution (left) and the minimizer radiation dose distribution (right). From left to right the radiation dose distributions (3D) over the PTV and OARs.

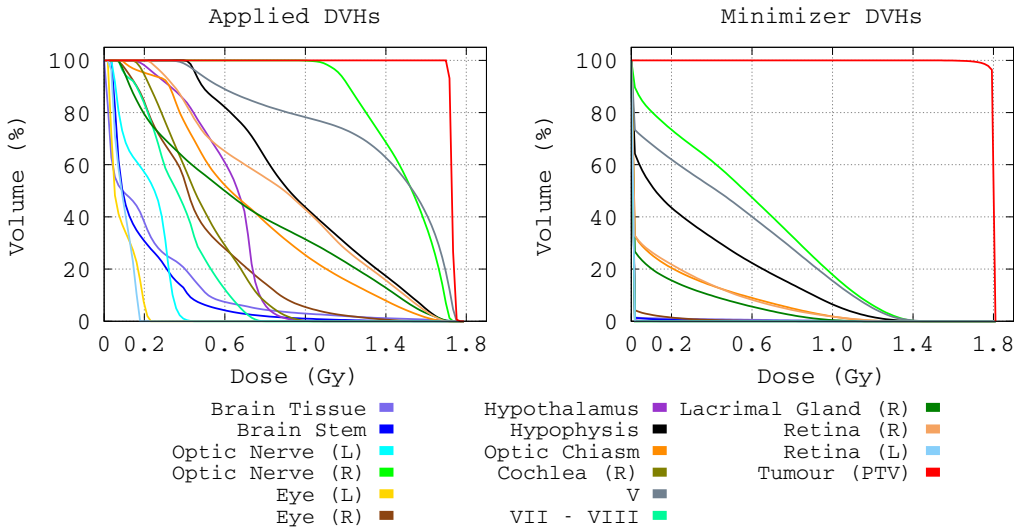

Figure B.30. Dose volume histograms (DVHs) of the applied (left) and minimizer (right) radiation dose distributions for each OAR, healthy tissue (Brain tissue) and the PTV.

Parameter	**Applied**	**Minimizer**
PTV_{D_M}	$1.77Gy$	$1.80Gy$
$D_{PTV100\%}$	$1.6865Gy$	$1.6651Gy$
PTV_{Dp}	0%	96.36%
$CI_{Dp95\%}$	0.96	0.99
Brain Tissue*	$1.7402Gy$	$1.6832Gy$
Optic Nerve (Right)*	$1.7165Gy$	$1.4261Gy$
Hypophysis*	$1.6808Gy$	$1.3789Gy$
Optic Chiasm*	$1.6271Gy$	$1.3560Gy$
V*	$1.7344Gy$	$1.3994Gy$
Lacrimal Gland (Right)*	$1.6794Gy$	$1.2823Gy$
Retina (Right)*	$1.6629Gy$	$1.3441Gy$

Table B.7. A comparison of the applied radiation dose distribution (second column) and the minimizer radiation dose distribution (third column). (PTV_{D_M}) Maximum radiation dose received by the PTV. ($D_{PTV100\%}$) Maximum radiation dose received at least by 100% of the PTV. (PTV_{Dp}) Percentage of the PTV receiving the prescribed radiation dose ($1.8Gy$). ($CI_{Dp95\%}$) Conformity Index (CI) for the isodose corresponding to 95% of the prescription radiation dose on the PTV. (*) Maximum radiation dose received by the OARs considered.

CASE 9:

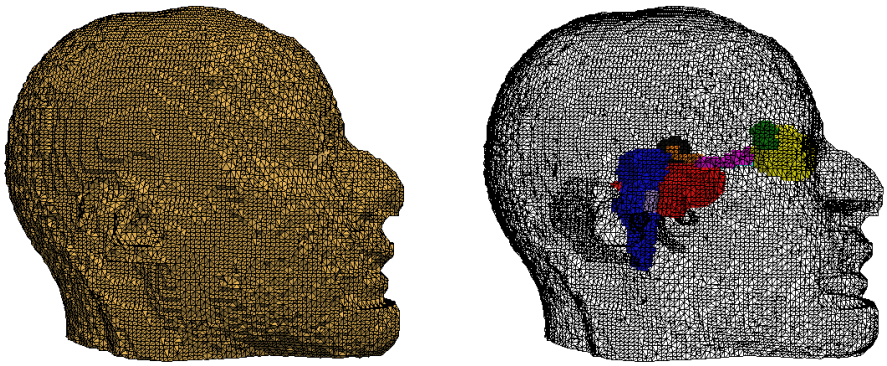

Figure B.31. From left to right a three-dimensional domain reconstruction for the case considered, the three-dimensional Delaunay triangulation created over the whole domain of simulation, and the representation of the PTV and OARs involved.

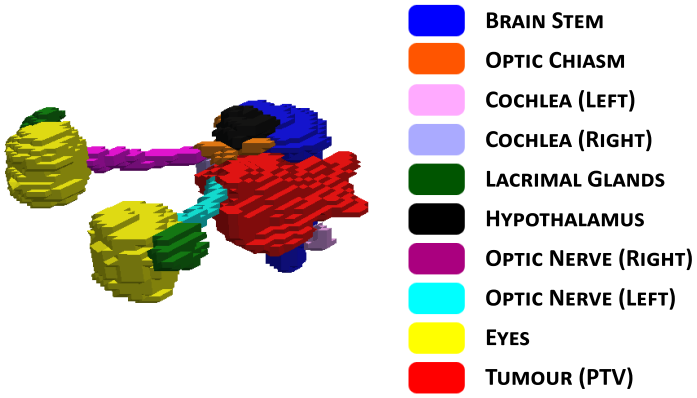

Figure B.32. Three-dimensional reconstruction of the PTV and OARs involved. Notice that the PTV is represented in red.

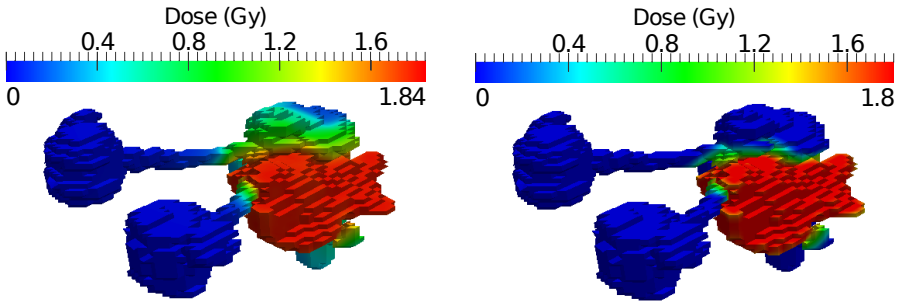

Figure B.33. A comparison of the applied radiation dose distribution (left) and the minimizer radiation dose distribution (right). From left to right the radiation dose distributions (3D) over the PTV and OARs.

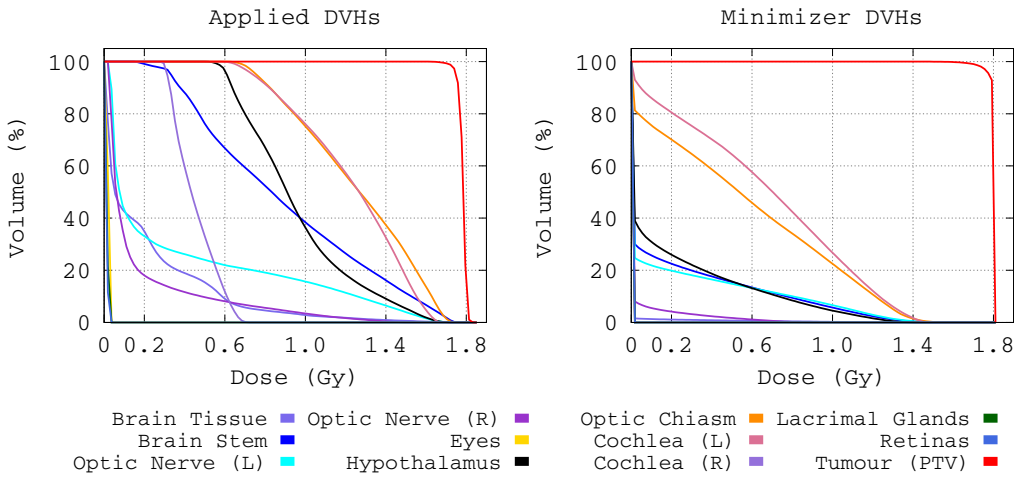

Figure B.34. Dose volume histograms (DVHs) of the applied (left) and minimizer (right) radiation dose distributions for each OAR, healthy tissue (Brain tissue) and the PTV.

Parameter	**Applied**	**Minimizer**
PTV_{D_M}	$1.84Gy$	$1.80Gy$
$D_{PTV100\%}$	$1.6657Gy$	$1.6109Gy$
PTV_{Dp}	19.93%	93.87%
$CI_{Dp95\%}$	0.97	0.98
Brain Tissue*	$1.7952Gy$	$1.6571Gy$
Brain Stem*	$1.7212Gy$	$1.3813Gy$
Optic Nerve (Left)*	$1.6671Gy$	$1.3894Gy$
Hypothalamus*	$1.6983Gy$	$1.3670Gy$
Optic Chiasm*	$1.7135Gy$	$1.4399Gy$
Cochlea (Left)*	$1.6876Gy$	$1.4157Gy$

Table B.8. A comparison of the applied radiation dose distribution (second column) and the minimizer radiation dose distribution (third column). (PTV_{D_M}) Maximum radiation dose received by the PTV. ($D_{PTV100\%}$) Maximum radiation dose received at least by 100% of the PTV. (PTV_{Dp}) Percentage of the PTV receiving the prescribed radiation dose ($1.8Gy$). ($CI_{Dp95\%}$) Conformity Index (CI) for the isodose corresponding to 95% of the prescription radiation dose on the PTV. (*) Maximum radiation dose received by the OARs considered.

CASE 10:

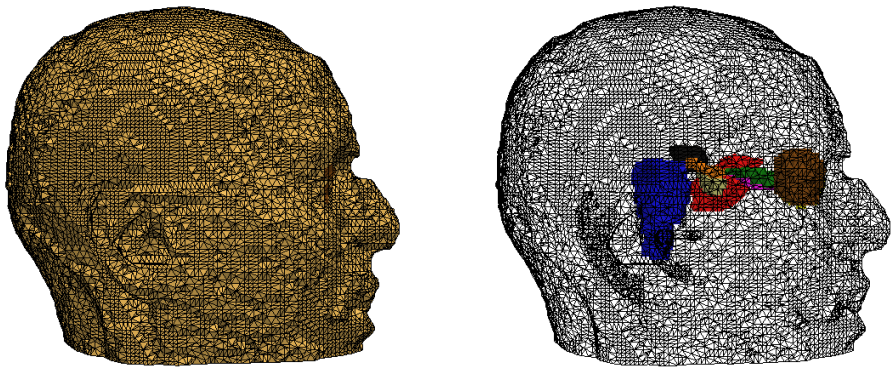

Figure B.35. From left to right a three-dimensional domain reconstruction for the case considered, the three-dimensional Delaunay triangulation created over the whole domain of simulation, and the representation of the PTV and OARs involved.

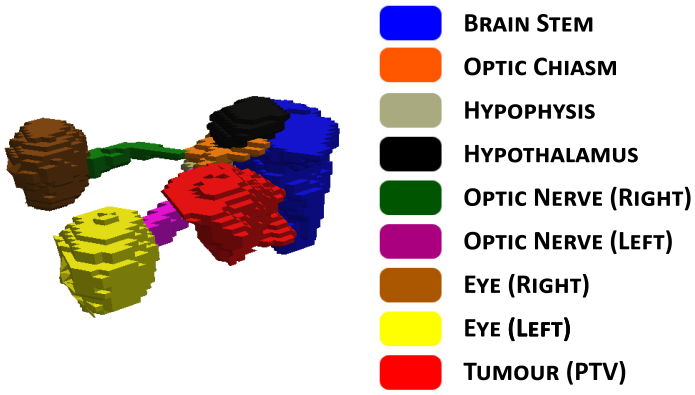

Figure B.36. Three-dimensional reconstruction of the PTV and OARs involved. Notice that the PTV is represented in red.

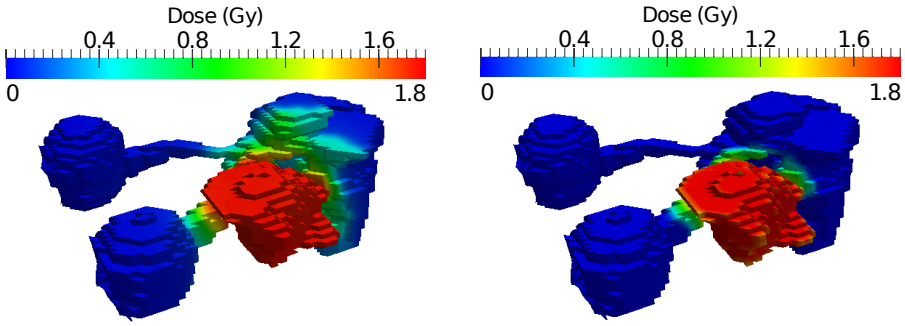

Figure B.37. A comparison of the applied radiation dose distribution (left) and the minimizer radiation dose distribution (right). From left to right the radiation dose distributions (3D) over the PTV and OARs.

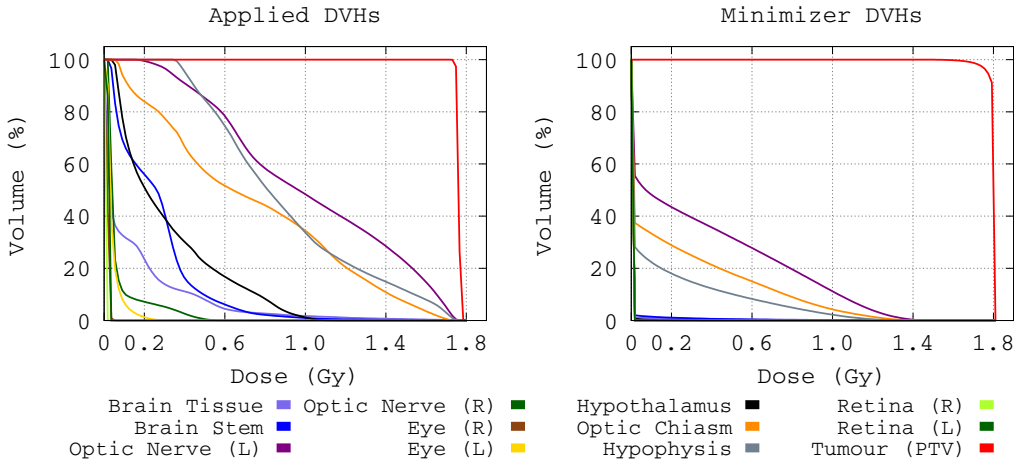

Figure B.38. Dose volume histograms (DVHs) of the applied (left) and minimizer (right) radiation dose distributions for each OAR, healthy tissue (Brain tissue) and the PTV.

Parameter	**Applied**	**Minimizer**
PTV_{D_M}	$1.80Gy$	$1.80Gy$
$D_{PTV100\%}$	$1.6954Gy$	$1.6128Gy$
PTV_{Dp}	0%	92.14%
$CI_{Dp95\%}$	0.99	0.98
Brain Tissue*	$1.7767Gy$	$1.6433Gy$
Optic Nerve (Left)*	$1.7687Gy$	$1.4394Gy$
Optic Chiasm*	$1.7246Gy$	$1.4189Gy$
Hypophysis*	$1.7507Gy$	$1.3624Gy$

Table B.9. A comparison of the applied radiation dose distribution (second column) and the minimizer radiation dose distribution (third column). (PTV_{D_M}) Maximum radiation dose received by the PTV. ($D_{PTV100\%}$) Maximum radiation dose received at least by 100% of the PTV. (PTV_{Dp}) Percentage of the PTV receiving the prescribed radiation dose ($1.8Gy$). ($CI_{Dp95\%}$) Conformity Index (CI) for the isodose corresponding to 95% of the prescription radiation dose on the PTV. (*) Maximum radiation dose received by the OARs considered.

Appendix C

Model of tumor growth and radiotherapy treatments: details of computer simulations and additional results

C.1 Details of computer simulations

In this Section, details of computer simulations of the model of tumor growth and radiotherapy treatments considered in Chapter 3 are described. Moreover, the flowchart of a cell in the model of tumor growth and the pseudo-code guidelines of the algorithm implemented are also provided.

C.1.1 Cell processes and model parameters

In Chapter 3 a three-dimensional (3D) cellular automata (CA) model for tumor growth has been developed, where each cell is considered as an individual agent (cf. for instance [144], [191] and [192]). For computer simulations of the model of tumor growth, a three-dimensional Voronoi tessellation is implemented, where each lattice point will host only one cell at any time. The construction points of the Voronoi tessellation are defined by first generating a regular cubic lattice with lattice constant a, and then placing exactly one point at an arbitrary position

within each cube of that lattice (resulting in an unstructured lattice with no rotational or translational symmetry, thus avoiding symmetry artifacts). Constant a is chosen such that the average volume of a Voronoi cell, $E[V] = a^3$, corresponds to that of a biological cell, $V = (\pi/6)d^3$. In this work the average cell diameter d will be assumed equal to $20\,\mu m$ (i.e. $a = (\pi/6)^{1/3}\,d = 16.12\,\mu m$). Thus, the domain of computer simulations is divided into $200 \times 200 \times 200$ lattice points, which corresponds to a total volume of about $33.51\,mm^3$. Actually, the modeling framework selected permits simulations to be scaled up to cubic centimeter sizes, though at the expense of lower spatial and functional resolution. Alternatively, hybrid models might be used, zooming in at the cell scale in regions of interest. However, a CA model representing each cell individually has been chosen to better understand the relation between tumor heterogeneity and simulated radiation treatment outcomes.

This model accounts for heterogeneous tumor growth. Specifically, two different tumor cell phenotypes (called, cancer cell (CC) and cancer stem cell (CSC)), which have markedly different biological and radiobiological properties, are allowed to coexist. The initial configuration of computer simulations is composed by 10^5 cells, out of which approximately 85% are CCs and 15% are CSCs. Tumor growth is kept track of until a size of about 10^6 cells is reached. At this time, the impact of different (homogeneous and heterogeneous) radiation therapies is simulated and discussed. In the case of tumor recurrence after radiation therapy, regrowth is allowed until a size of about 10^6 cells is attained, and then computer simulations are stopped.

The cell processes considered in the model of tumor growth are summarized as follows:

∘ **Cell Division (symmetric or asymmetric):** Cell replication on the lattice depends on the doubling time of the tumor cell phenotypes involved (τ). In the multi-cellular model the cell cycle is mimicked by a chain of Poisson processes. A Poisson process implies exponentially distributed waiting times. Moreover, a chain of m consecutive Poisson processes leads to an Erlang-distributed waiting time of the whole chain [213]. The integer parameter m determines the sharpness of the distribution around the average waiting time. This enables the model to

capture a variety of different cell cycle time distribution shapes from exponentially distributed cell cycle times ($m = 1$) to very sharp Erlang-distributed cell cycle times ($m \to \infty$). In this case, the cell cycle is modeled as such a chain of 4 consecutive cell cycle phases ($G1$, S, $G2$ and M) which themselves are subdivided into a number of subprocesses (m_{G1}, m_S, m_{G2}, m_M). Each of the cell cycle phases has an average duration (τ_{G1}, τ_S, τ_{G2}, τ_M). This construction permits to control the average duration τ_p as well as the sharpness of the distribution of τ_p for each phase p individually (see Figure C.1). Beginning in cycle step $i = 1$, a cell progresses in the cell cycle from i to $i + 1$ with rate m_p/τ_p, where p is the associated cell cycle phase. When $i = m_{G1} + m_S + m_{G2} + m_M$, the cell divides and both daughter cells reenter in the cell cycle with $i = 1$.

In the proposed model of tumor growth, division of CCs is always supposed to be symmetric giving two identical daughter cells and with a limited replication capability. However, CSCs will be assumed to sustain either symmetric or asymmetric division, in which case one CSC and one CC will result from replication. Proliferation is only possible for cells located at a point having at least one free neighbor in the lattice (which is randomly chosen for replication). During cell division, the daughter cell is placed on this randomly selected free neighbor site. A cell with no free neighbors temporarily loses its ability to divide and becomes quiescent due to contact inhibition. The quiescence state is abandoned as soon as one of the surrounding lattice points becomes free. The duration of cell cycle for CCs is assumed to be significantly shorter than that of CSCs (see Table 3.1).

∘ **Migration:** In this work, both tumor cell phenotypes considered are able to move to a randomly chosen free neighbor site with same (hopping) rate k_{mig}. Indeed, two different migration rates have been considered, a comparatively low rate obtained from the cell diffusion constant (cf. for instance [144] and [214]) and a higher rate as estimated *in vitro* in [111] for a Glioblastoma Multiforme (GBM) cell line (see Table 3.1). The cell diffusion rate is estimated as $D = 6.5 \times 10^{-11}\, cm^2/s - 4.7 \times 10^{-12}\, cm^2/s$ (see Table of parameters in [144]). The diffusion coefficient depends on the properties of the cell and the surrounding media. Since $D = l^2\lambda$ (λ = hopping rate = k_{mig}) and l the hopping distance (= cell diameter), then considering a cell diameter of $20\mu m$, this implies that $\lambda =$

$D/l^2 = D \cdot 2.5 \times 10^5\ cm^2 = 2.5 \times 10^{-7}\ s^{-1} - 1.5 \times 10^{-5}\ s^{-1} = 0.009\ h^{-1} - 0.054\ h^{-1}$. Therefore, for the low migration case, a $k_{mig} = 0.025\ h^{-1}$ has been selected, which is in the range estimated. On the other hand, for the high migration case, a $k_{mig} = 1.75\ h^{-1}$ has been assumed. Similar estimates of this last migration rate have been independently derived for a GBM cell line in [111] and references therein.

◦ **Death by radiation:** The effect of radiation on tumor cells (in terms of the corresponding surviving cell fraction) is estimated by means of the standard Linear Quadratic (LQ) model (see Section 3.3.2 in Chapter 3 and [53], [54], [55], [56]). In this work has been considered that CSCs are more resistant to radiation than CCs. Moreover, for any of these two tumor cell phenotypes, quiescent cells are more radioresistant than proliferating ones. When a radiation dose is delivered on the tumor, four estimates on dying fractions (corresponding to proliferating / quiescent CC phenotype and to proliferating / quiescent CSC phenotype) for the total tumor volume or for the inner and outer tumor regions are computed and a corresponding amount of cells (randomly chosen) is then declared as being dead.

◦ **Apoptosis (programmed cell death):** In this model, both tumor cell phenotypes considered are subject to apoptosis, a programmed cell death. When this process occurs, cells activate the apoptotic pathway, which will lead to cell shrinkage, nuclear fragmentation, chromatin condensation, chromosomal DNA fragmentation and cell fragmentation into apoptotic bodies. The corresponding process is accounted for in the model of tumor growth by changing from a proliferating or quiescent state to an apoptotic state (cell death) at a rate k_{apt} (see Table 3.1).

◦ **Lysis:** Disposal of cellular debris resulting from apoptosis is carried out by a lysis process [193], for which a lysis rate $k_{lys} = 0.035\ h^{-1}$ (about $30\,h$) has been assumed (see Table 3.1). This rate is about 10-fold less than phagocytosis (digestion of cellular debris by macrophages) observed *in vivo* [194], but within the range reported for *in vitro* cultures ($0.002\ h^{-1}$ for *Hybridoma VO 208* cell line [195] to $0.07\ h^{-1}$ for *Fibrobacter succinogenes* [196]). It should be noted in this context that tumor growth within the size limits considered in this work is closer to *in vitro* cultures than to *in vivo* situations. Lysis is mimicked in the model of tumor growth by means of a Poisson process, which removes dead cells from the lattice.

C.1.2 Time evolution of the system

A version of the Gillespie algorithm [197] has been implemented and adapted to the cell population system considered in this work. To this end, some explanations are in order. The class of processes that cells can perform will be indexed by μ, say proliferation, migration, apoptosis and lysis. The related process rate, denoted by r_μ needs not be constant for all cells. For example, proliferating rates depend on the tumor cell phenotypes considered. Therefore, a process $P_{c,\mu}$ is specified by its process class μ, but also by the cell c where it takes place. For instance, if μ represents proliferation, the corresponding replication process can be summarized as follows

$$P_{c,\mu} : c - [r_{c,\mu}] \rightarrow 2c,$$

where $r_{c,\mu}$ is the rate at which the cell c implements the process μ (in this example, proliferation) and $2c$ represents the two daughter cells arising from c.

The algorithm describing the temporal evolution of the system is shortly described in the pseudo-code provided in Section C.1.3 (see also Figure C.1 for further details). Lines within braces at each step refer to the procedure sketched at the end of the description.

• **Step 0 (lines 1 to 10 - Initialization):** Read the initial set of cells (C) and the list of all possible processes at this stage of the system (P) from a data file (see lines 1 and 2). The initial tumor stage is composed by 10^5 cells, where about 85% are CCs and the remaining 15% are CSCs randomly distributed. Set the time variable t to zero and initialize the unit-interval uniform random number generator (URN) (see lines 3 and 4). When a size of about 10^6 cells is reached, a radiotherapy treatment is applied. Then the frequency and total number of sessions (r_{sf} and n_s), the dying cell fraction for each tumor cell phenotype (CC and CSC) after each session, and the respective cell states (proliferating and quiescent) are computed (see input parameters and lines 5 to 9). Moreover, the maximum number of cells allowed (mn_c) in computer simulations is also defined. On the other hand, the proportion of CSCs (p_{in}) to define the inner region for the case of high migration, when heterogeneous therapies are delivered, should be established (80% in the

simulations performed). Notice that, for the case of low migration, p_{in} is equal to 100% which corresponds with the inner region where all CSCs are located.

• **Steps 1 to 5 (lines 11 to 79 - Time evolution):** A step-by-step time evolution is processed within the global loop. The following Steps 1 to 5 are repeated until the system reaches the end time t_{max} of simulation, when there are no more processes to execute (for instance, all cells are dead) or the maximum number of cells considered is reached ($mn_c = 10^6$) at the end of the recurrence tumor stage after radiation therapy.

• **Step 1 (line 12 - Rates):** Calculate and store as r_Σ the sum of rates $r_{c,\mu}$ of all processes $P_{c,\mu} \in P$.

• **Step 2 (lines 13 and 14 - Time increment):** Generate a random number u_1 using the unit-interval uniform random number generator (URN), and calculate the time increment $\tau = -\frac{\ln(u_1)}{r_\Sigma}$.

• **Step 3 (lines 15 to 23 - Process selection):** The process $P_{b,v}$ to perform during this iteration is chosen randomly from the list of all processes P taking into account that the probability of each process $P_{c,\mu} \in P$ to be chosen is proportional to its rate $r_{c,\mu}$. As proposed by Gillespie [197], this can be done as follows: generate a second random number u_2 using the unit-interval uniform random number generator (URN). Then step-by-step sum up as r'_Σ the rates $r_{c,\mu}$ of all processes $P_{c,\mu} \in P$ until the condition $r'_\Sigma - r_{c,\mu} < u_2 \cdot r_\Sigma \leq r'_\Sigma$ is satisfied. Then store $P_{c,\mu}$ as the selected process in $P_{b,v}$.

• **Step 4 (lines 24 and 25 - Update):** Increase the time t by τ, and adjust the cell set to account for what has happened during process $P_{b,v}$ (e.g. remove cells, add cells, move cells and/or change environment of a cell). Update the list of possible processes according to the new cell set (e.g. add/remove processes after an environmental change).

• **Step 5 (lines 26 to 78 - Radiation therapy):** Radiation therapy starts when the tumor reaches a size greater than or equal to mn_c. Radiation is delivered over the time corresponding with the number and frequency of sessions selected. Notice that in the case of weekend interruptions the variable rs_f should be incremented in 72 hours after weekly consecutive sessions, and afterwards this period

will be changed back to the initial frequency of sessions. For homogeneous therapies a number of cells is randomly selected on the whole tumor corresponding with the dying cell fraction of proliferating and quiescent states for CCs and CSCs respectively. However, for heterogeneous therapies this selection is separately made within the inner sphere and in the rest of the tumor, and the dying cell fractions are computed for the corresponding radiation dose delivered on each region. At the end of each session, the cell state of this set of cells is updated to dead. Alternatively, one might introduce the death process by radiation as a rate. However, a common and accepted assumption is that this process is very fast, in which case the algorithm chosen is much more efficient.

C.1.3 Pseudo-code guidelines

In this Section the pseudo-code guidelines of the algorithm implemented is described (see Section C.1.2 above for further details).

Input parameters:

t_{max} := maximum duration of simulations
rs_f := frequency of radiation sessions
n_s := total number of radiation sessions
mn_c := maximum number of cells allowed in simulations
p_{in} := proportion of CSCs to define the inner region (for heterogeneous therapies with the high migration rate)

Initialization:

1 – Input the initial set of cells $C := \{c \mid c$ is a cell within the volume V where $c \in \{CC, CSC\}\}$
2 – Determine the processes array $P := \{P_{c,\mu} \mid$ if $c \in C$ and c is reactant of $\mu\}$
3 – Set $t := 0$
4 – Initialize URN
5 – Initialize the dying cell fraction for each tumor cell phenotype (CC and CSC) and cell state (proliferating and quiescent), where D is the radiation dose for homogeneous therapies:

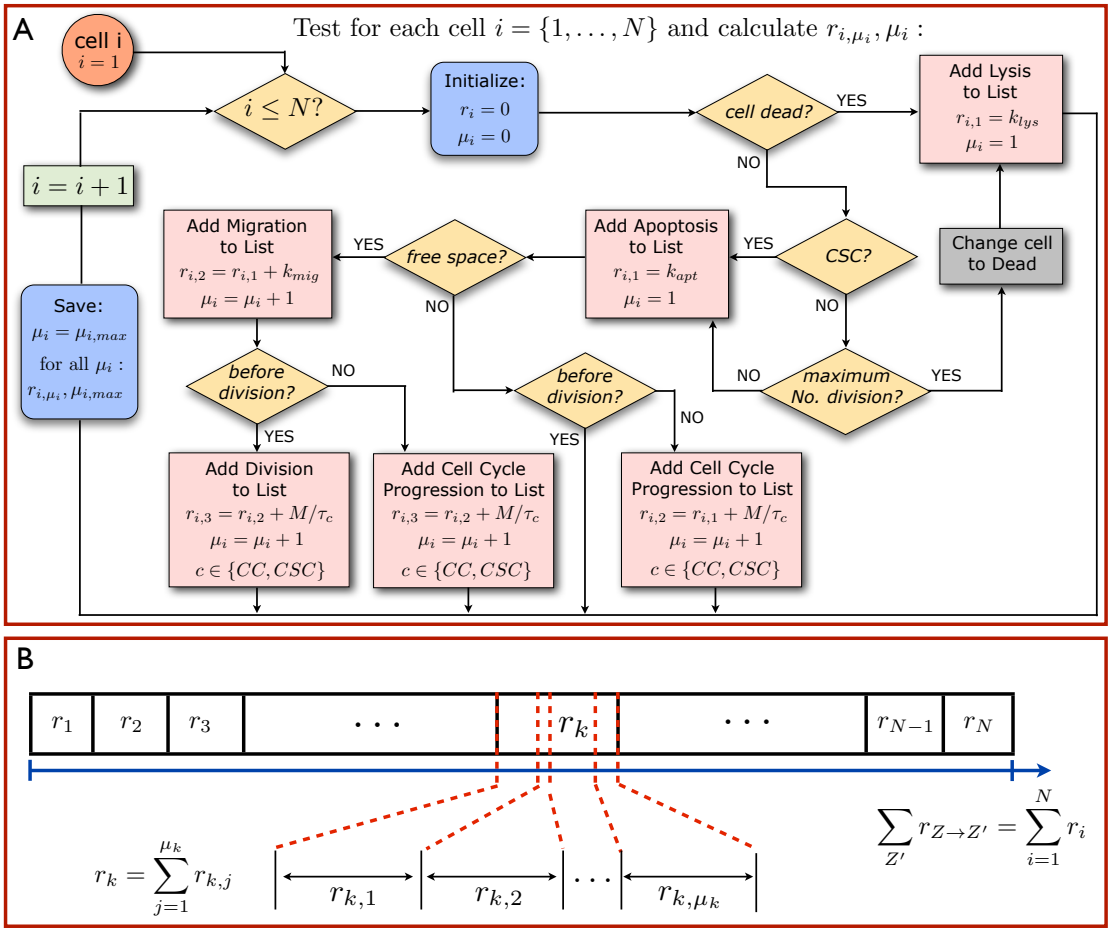

Figure C.1. The flowchart of a cell in the model of tumor growth. (A) The flowchart illustrates how the accessible states and rates for the respective transition for a configuration of N cells, both CCs and CSCs, are determined algorithmically in the computer program. Here, $M = m_{G_1} + m_S + m_{G_2} + m_M$. The possible transitions are investigated cell by cell. For each cell ($i = 1, \ldots, N$) all processes that cell i can perform are determined and saved in a list. If cell i is dead, it can only undergo lysis with rate k_{lys}. Accordingly, the rate $r_{i,1}$ with which cell i can change its state becomes equal to the lysis rate. Notice that this includes cells of tumor phenotype CC which reached its maximum number of cell cycles and consequently die. If cell i is alive, apoptosis is added as every cell can undergo apoptosis in the model, so that $r_{i,1} = k_{apt}$. If in addition a lattice site is free next to the cell, it may migrate, so $r_{i,2} = r_{i,1} + k_{mig}$. In this way the total $r_{i,\mu}$ of cell i is computed, and all intermediate values, ($r_{i,1}$, $r_{i,2}$, ...) are saved. The total rate at which the current cell configuration changes is then given by $r_{tot} = \sum_{i=0}^{N} r_{i,\mu_{i,max}}$. (B) To select a process, a random number ξ is chosen in $[0, r_{tot})$, and that process p of cell k is performed, for which either $\sum_{i=1}^{k-1} r_{i,\mu_{i,max}} + r_{k,p} \leq \xi < \sum_{i=1}^{k-1} r_{i,\mu_{i,max}} + r_{k,p+1}$, or $p = \mu_{k,max}$ and $\sum_{i=1}^{k} r_{i,\mu_{i,max}} \leq \xi < \sum_{i=1}^{k} r_{i,\mu_{i,max}} + r_{k+1,1}$. Concerning radiation effects, cells are picked randomly and killed according to the corresponding surviving cell fraction estimate.

6 – Set $p_{CC} := \left(1 - e^{-\xi_{p1}\left(\alpha D + \beta D^2\right)}\right)$

7 – Set $q_{CC} := \left(1 - e^{-\xi_{q1}\left(\alpha D + \beta D^2\right)}\right)$

8 – Set $p_{CSC} := \left(1 - e^{-\xi_{p2}\left(\alpha D + \beta D^2\right)}\right)$

9 – Set $q_{CSC} := \left(1 - e^{-\xi_{q2}\left(\alpha D + \beta D^2\right)}\right)$

 # Notice that in the case of heterogeneous therapies, D_{in} and D_{out} should be defined with the corresponding dying cell fractions for each tumor cell phenotype (CC and CSC) and cell state (proliferating and quiescent) respectively.

10 – Define r_{rad}, s_{rad}, d_s and d_r (auxiliary variables):

Set $r_{rad} :=$ *false* *# conditional: start irradiation*

Set $s_{rad} :=$ *false* *# conditional: stop irradiation*

Set $d_s := 0$ *# delivered number of radiation sessions*

Set $d_r := 0$ *# radius partitions to define the inner region (for heterogeneous therapies with the high migration rate)*

11 – **REPEAT**

Sum over all process rates:

12 – Calculate $r_\Sigma := \sum_{P_{c,\mu} \in P} r_{c,\mu}$

Calculate time step τ:

13 – Generate u_1 from URN

14 – Take $\tau := -\frac{\ln(u_1)}{r_\Sigma}$

Select process $P_{b,v}$ regarding to its probability $P_{b,v} = \frac{r_{b,v}}{r_\Sigma}$:

15 – Generate u_2 from URN

16 – Set $r_\Sigma^{'} := 0$

17 – for all $P_{c,\mu} \in P$ do

18 – if $(r_\Sigma^{'} < u_2 \cdot r_\Sigma \leq r_\Sigma^{'} + r_{c,\mu})$ then

Select cell b and process class v:

19 – $b := c$

20 – $v := \mu$

21 – end if

22 – Put $r_\Sigma^{'} := r_\Sigma^{'} + r_{c,\mu}$

23 – end for

Execute process $P_{b,v}$:

24 – Put $t := t + \tau$

25 – Adjust C and P according to $P_{b,v}$

Applying radiation therapy:

26 – if ((length$(C) \geq mn_c$) or ($r_{rad} == true$) and ($s_{rad} == false$)) then

27 – if (($d_s == 0$) or (($t - t_s$) == rs_f))

(taking into account weekend interruptions if it is the case) then

28 – if ($d_s == 0$) then

Compute the center-of-mass:

29 – $m_x := \frac{\sum_{c \in C} x_i}{\text{length}(C)}$; $m_y := \frac{\sum_{c \in C} y_i}{\text{length}(C)}$; $m_z := \frac{\sum_{c \in C} z_i}{\text{length}(C)}$

Compute the diameter of tumor regions:

30 – Set $r_{out} := 0$

31 – Set $r_{in} := 0$

32 – for all $c \in C$ do

33 – $c_d := \sqrt{(c_x - m_x)^2 + (c_y - m_y)^2 + (c_z - m_z)^2}$

34 – if ($c_d > r_{out}$) then

35 – $r_{out} := c_d$

36 – end if

37 – end for

38 – if (Heterogeneous therapy) then

39 – N_{CSC} := Compute the number of CSCs in C

40 – if (Low migration rate) then

41 – for all $c \in C$ and c is CSC do

42 – $c_d := \sqrt{(c_x - m_x)^2 + (c_y - m_y)^2 + (c_z - m_z)^2}$

43 – if ($c_d > r_{in}$) then

44 – $r_{in} := c_d$

45 – end if

46 – end for

47 – else # *High migration rate*

48 – for ($i = d_r$; $i > 0$; $i - -$) do

49 – Set $c_{in} := 0$

50 – for all $c \in C$ and c is CSC do

51 – $c_d := \sqrt{(c_x - m_x)^2 + (c_y - m_y)^2 + (c_z - m_z)^2}$

52 – if $(c_d \leq (r_{out}/d_r) * i)$ then

53 – $c_{in} := c_{in} + 1$

54 – end if

55 – end for

56 – if $(c_{in} \geq p_{in} * N_{CSC})$ then

57 – $r_{in} := (r_{out}/d_r) * i$

58 – *break*

59 – end if

60 – end for

61 – end if

62 – end if

63 – end if

For homogeneous therapies select randomly on the whole tumor:

64 – A number of proliferating CCs corresponding to:

p_{CC}

65 – A number of quiescent CCs corresponding to:

q_{CC}

66 – A number of proliferating CSCs corresponding to:

p_{CSC}

67 – A number of quiescent CSCs corresponding to:

q_{CSC}

 # Notice that for heterogeneous therapies this selection is separately made within the inner sphere (center-of-mass to r_{in}) and in the rest of the tumor (r_{in} to r_{out}) for the corresponding radiation dose delivered on each region (D_{in} and D_{out}) respectively

68 – Change cell state of the selected set of cells to dead

69 – Adjust P for all selected cells

70 – $d_s := d_s + 1$

71 – $r_{rad} := true$

72 – if ($d_s == n_s$) then
73 – $r_{rad} := false$
74 – $s_{rad} := true$
75 – end if
76 – $t_s := t$ # *update time of the last delivered treatment session*
77 – end if
78 – end if
79 – **UNTIL** ($t \geq t_{max}$) or ($P = \varnothing$) or ((length(C) $\geq mn_c$) and ($s_{rad} == true$))

C.2 Additional results: radiotherapy treatments and number of CSCs at the pre-treatment and recurrence tumor stages

In this Section, additional results for heterogeneous and homogeneous radiation therapies considered in Chapter 3 are presented and other model properties are investigated.

C.2.1 Heterogeneous vs. homogeneous therapies for the low and high migration cases

To begin with, in Tables C.1 and C.2 (to be compared to Tables 3.4 and 3.5 in Chapter 3 respectively) the number of CSCs at the recurrence tumor stage (with the corresponding standard deviation) for heterogeneous and the corresponding averaged homogeneous radiation therapies considered in Chapter 3 are provided. Moreover, heterogeneous and homogeneous radiation therapies required to achieve tumor control are also shown. This is done for the values of p_a (0.75, 0.50 and 0.25), CSC cycle duration ($96h$, $72h$ and $48h$) and migration rate k_{mig} ($0.025h^{-1}$, $1.75h^{-1}$) considered in Table 3.1.

		Heterogeneous therapy		Homogeneous therapy	
p_a	τ_{csc}	No Control	Control	No Control	Control
0.75	**96h**	$---$	$2.0Gy - 2.5Gy^{(1)}$	$2.10Gy^{(1)}$	$2.5Gy$
				(83/7.87)	
	72h	$---$	$2.0Gy - 2.5Gy^{(2)}$	$2.10Gy^{(2)}$	$2.5Gy$
				(264/14.82)	
	48h	$2.0Gy - 2.5Gy^{(3)}$	$2.0Gy - 2.7Gy^{(4)}$	$2.10Gy^{(3)}/2.12Gy^{(4)}$	$2.7Gy$
		(107/8.53)		(603/41.22)/(514/13.65)	
0.50	**96h**	$---$	$2.0Gy - 2.9Gy^{(5)}$	$2.15Gy^{(5)}$	$2.9Gy$
				(814/37.57)	
	72h	$---$	$2.0Gy - 2.9Gy^{(6)}$	$2.17Gy^{(6)}$	$2.9Gy$
				(2130/86.68)	
	48h	$2.0Gy - 2.9Gy^{(7)}$	$2.0Gy - 3.4Gy^{(8)}$	$2.19Gy^{(7)}/2.30Gy^{(8)}$	$3.4Gy$
		(1785/78.31)		(16757/243.46)/(12208/456.08)	
0.25	**96h**	$---$	$2.0Gy - 3.3Gy^{(9)}$	$2.23Gy^{(9)}$	$3.3Gy$
				(3961/171.88)	
	72h	$---$	$2.0Gy - 3.3Gy^{(10)}$	$2.27Gy^{(10)}$	$3.3Gy$
				(14495/274.86)	
	48h	$2.0Gy - 3.3Gy^{(11)}$	$2.0Gy - 3.9Gy^{(12)}$	$2.32Gy^{(11)}/2.47Gy^{(12)}$	$3.9Gy$
		(4457/232.67)		(113546/1393.2)/(96346/1141.3)	

Table C.1. Classification of heterogeneous and homogeneous radiation therapies for the low migration case. In all cases, treatment sessions were scheduled along 6 weeks separated by 24 hours intervals except for weekends, where a 72 hours interval is allowed. Data corresponding to 20 simulations (with different seeds of a random number generator) are presented. In the heterogeneous therapies, radiation doses are specified both for the outer (left) and inner (right) tumor regions, each case being indexed from (1) to (12). The averaged dose for any of the previous cases is labeled with the same number in the columns corresponding to homogeneous therapies. Within braces, the number of CSCs at the recurrence tumor stage and the corresponding standard deviation are also provided. See Figure 3.10 (A) in Chapter 3 where some of these results are shown.

C.2.2 Consequences of assuming that CSCs cycle faster than CCs

So far, the standard assumption that the duration of cell cycle for CSCs is significantly longer than that of CCs has been considered (cf. for instance [142], [163], [164], [165], [166], [167], [168], [169], [170] and [171]). For completeness, some results provided by this model of tumor growth under the opposite situation that CSCs cycle faster than CCs are shortly described. To do that, consider the cases where CSC cycle lasts 26 hours (respectively 18 hours) which is equal to (respectively less than) the 26 hours cell cycle selected for CCs. In Tables C.3 and C.4 (see also Figures C.2, C.3 and C.4), estimates of the tumor inner region diameter and number of CSCs before radiation treatment starts are provided, both for the low and high migration cases and values of p_a equal to 0.75, 0.50 and 0.25 respectively.

		Heterogeneous therapy		Homogeneous therapy	
p_a	τ_{csc}	No Control	Control	No Control	Control
0.75	**96h**	$---$	$2.0Gy - 2.5Gy^{(1)}$	$2.10Gy^{(1)}$	$2.5Gy$
				(135/11.88)	
	72h	$---$	$2.0Gy - 2.5Gy^{(2)}$	$2.11Gy^{(2)}$	$2.5Gy$
				(216/9.24)	
	48h	$2.0Gy - 2.5Gy^{(3)}$	$2.2Gy - 2.7Gy^{(4)}$	$2.13Gy^{(3)}/2.33Gy^{(4)}$	$2.7Gy$
		(294/16.73)		(536/37.21)/(267/10.61)	
0.50	**96h**	$2.0Gy - 2.9Gy^{(5)}$	$2.3Gy - 2.9Gy^{(6)}$	$2.23Gy^{(5)}/2.45Gy^{(6)}$	$2.9Gy$
		(349/21.89)		(634/43.73)/(251/13.86)	
	72h	$2.0Gy - 2.9Gy^{(7)}$	$2.6Gy - 2.9Gy^{(8)}$	$2.25Gy^{(7)}/2.70Gy^{(8)}$	$2.9Gy$
		(815/36.70)		(1579/85.56)/(466/29.65)	
	48h	$2.0Gy - 2.9Gy^{(9)}$	$2.8Gy - 3.4Gy^{(10)}$	$2.29Gy^{(9)}/3.00Gy^{(10)}$	$3.4Gy$
		(12712/455.01)		(19344/447.66)/(1582/48.38)	
0.25	**96h**	$2.0Gy - 3.3Gy^{(11)}$	$2.4Gy - 3.3Gy^{(12)}$	$2.36Gy^{(11)}/2.65Gy^{(12)}$	$3.3Gy$
		(1448/71.75)		(2419/160.03)/(769/59.82)	
	72h	$2.0Gy - 3.3Gy^{(13)}$	$2.7Gy - 3.3Gy^{(14)}$	$2.43Gy^{(13)}/2.90Gy^{(14)}$	$3.3Gy$
		(2646/136.52)		(11318/335.88)/(2020/77.78)	
	48h	$2.0Gy - 3.3Gy^{(15)}$	$3.4Gy - 3.9Gy^{(16)}$	$2.52Gy^{(15)}/3.60Gy^{(16)}$	$3.9Gy$
		(78073/3054.90)		(191730/3747.03)/(7716/174.66)	

Table C.2. Classification of heterogeneous and homogeneous radiation therapies for the high migration case. In all cases, treatment sessions were scheduled along 6 weeks separated by 24 hours intervals except for weekends, where a 72 hours interval is allowed. Data corresponding to 20 simulations (with different seeds of a random number generator) are presented. In the heterogeneous therapies, radiation doses are specified both for the outer (left) and inner (right) tumor regions, each case being indexed from (1) to (16). The averaged dose for any of the previous cases is labeled with the same number in the columns corresponding to homogeneous therapies. Within braces, the number of CSCs at the recurrence tumor stage and the corresponding standard deviation are also provided. See Figure 3.10 (B) in Chapter 3 where some of these results are shown.

As expected, in these cases the inner core where most CSCs remain concentrated is now larger than when slow-cycling CSCs is assumed, see Tables C.3 and C.4 (to be compared to Tables 3.2 and 3.3 in Chapter 3). In particular, it should be noted that in the slow-cycling CSCs case for the low migration case such inner regions, where 100% of CSCs are located, ranged from 15% to 25% of the total tumor volume. For the case of high migration the volume where at least 80% of CSCs are located ranged from 21% to 40% of the volume where 90% of total cells (CCs and CSCs) are located. Notice that, as reported in Chapter 3, the average diameter of the tumor for the low migration case is about $2680\mu m$, while for the high migration case the average diameter of the region where 90% of total cells (CCs and CSCs) are located is about $3120\mu m$ (with standard deviations of $56\mu m$ and $186\mu m$ over

20 simulation performed for each parameter set considered respectively).

When the assumption that CSCs cycle faster than CCs is made, then the values of the average diameter of the tumor and the region where the 90% of total cells (CCs and CSCs) are located for the low and high migration cases respectively, are exactly those recalled above. This is due to the fact that computer simulations are executed for the same maximum number of cells (10^6) keeping the same migration rates. However, in the case of low migration now considered and CSC cycle duration equal to $26h$ (respectively $18h$) tumor inner regions range from 20% to 83% (respectively 22% to 100%) of the total tumor volume (see Table C.3, and Figures C.2 (A) and C.3 (A)). For the case of high migration and CSC cycle duration equal to $26h$ (respectively $18h$) these inner regions further expand, so that the volume where 80% of CSCs remain confined ranges now from 28% to 44% (respectively 33% to 51%) of the volume where 90% of total cells (CCs and CSCs) are located (see Table C.4, and Figures C.2 (B) and C.3 (B)).

	$p_a = 0.75$		$p_a = 0.50$		$p_a = 0.25$	
τ_{csc}	**Diameter**	**CSCs**	**Diameter**	**CSCs**	**Diameter**	**CSCs**
26h	1567.3 μm	18217	1826.2 μm	21417	2516.3 μm	29873
	[57.16 μm]	[71.82]	[78.22 μm]	[145.66]	[37.87 μm]	[765.80]
18h	1623.5 μm	19151	2412.9 μm	27846	2678.3 μm	84134
	[63.48 μm]	[75.48]	[67.77 μm]	[573.03]	[48.75 μm]	[3104.15]

Table C.3. Estimates of the tumor inner region diameter and number of CSCs before irradiation for the low migration case and fast-cycling CSCs. Diameter is that of an inner sphere where 100% of CSCs are located. CSCs number is computed before radiation therapy treatment starts. Within brackets the corresponding standard deviations are also provided. Data corresponding to 20 simulations (with different seeds of a random number generator) for each case considered. See also Figures C.2 (A), C.3 (A) and C.4 (A) where these results are shown.

	$p_a = 0.75$		$p_a = 0.50$		$p_a = 0.25$	
τ_{csc}	**Diameter**	**CSCs**	**Diameter**	**CSCs**	**Diameter**	**CSCs**
26h	2048.1 μm	23084	2195.0 μm	38081	2365.7 μm	64786
	[72.81 μm]	[485.90]	[84.28 μm]	[1227.08]	[69.15 μm]	[2086.43]
18h	2156.5 μm	25791	2284.4 μm	54628	2495.4 μm	124584
	[62.38 μm]	[584.35]	[93.49 μm]	[1502.97]	[71.36 μm]	[2339.59]

Table C.4. Estimates of the tumor inner region diameter and number of CSCs before irradiation for the high migration case and fast-cycling CSCs. Diameter is that of an inner sphere where 80% of CSCs are located. CSCs number is computed before radiation therapy treatment starts. Within brackets the corresponding standard deviations are also provided. Data corresponding to 20 simulations (with different seeds of a random number generator) for each case considered. See also Figures C.2 (B), C.3 (B) and C.4 (B) where these results are shown.

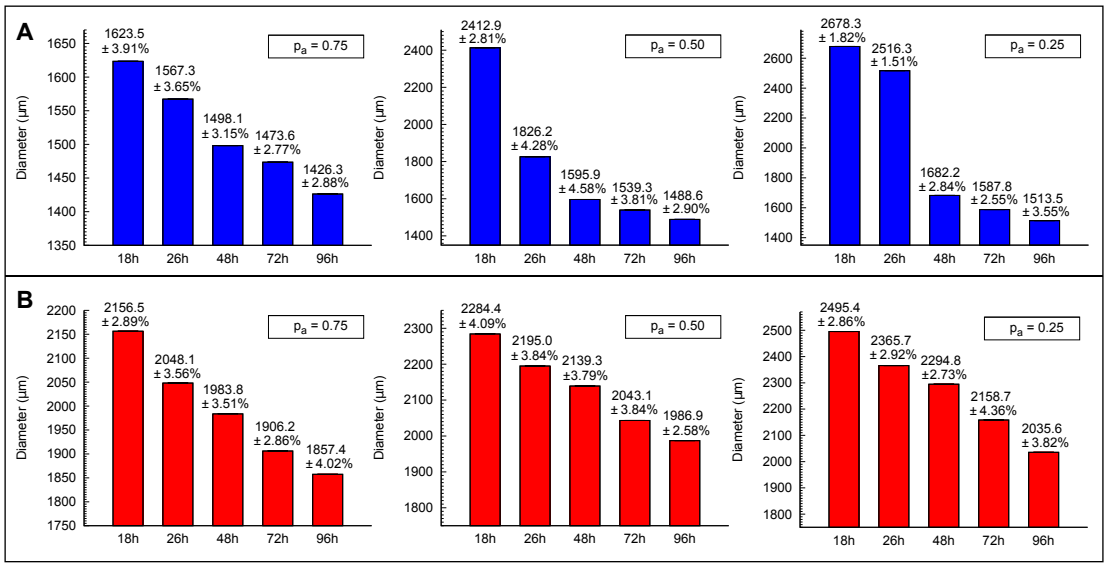

Figure C.2. Representation of the tumor inner region diameter for the low and high migration cases. Diameters of the tumor inner region at the pre-treatment stage (where about 10^6 cells are present) and the corresponding standard deviations after performing 20 simulations in each case (with different seeds of a random number generator) are shown. Results are provided for the cases $p_a = 0.75$, $p_a = 0.50$ and $p_a = 0.25$ (left, middle, right) and CSC cycle durations equal to $18h$, $26h$, $48h$, $72h$ and $96h$. (A) Diameters of the tumor inner sphere where 100% of CSCs are located for the low migration case. (B) Diameters of the tumor inner sphere where 80% of CSCs are located for the high migration case. See Tables 3.2 and 3.3 in Chapter 3, and Tables C.3 and C.4 above.

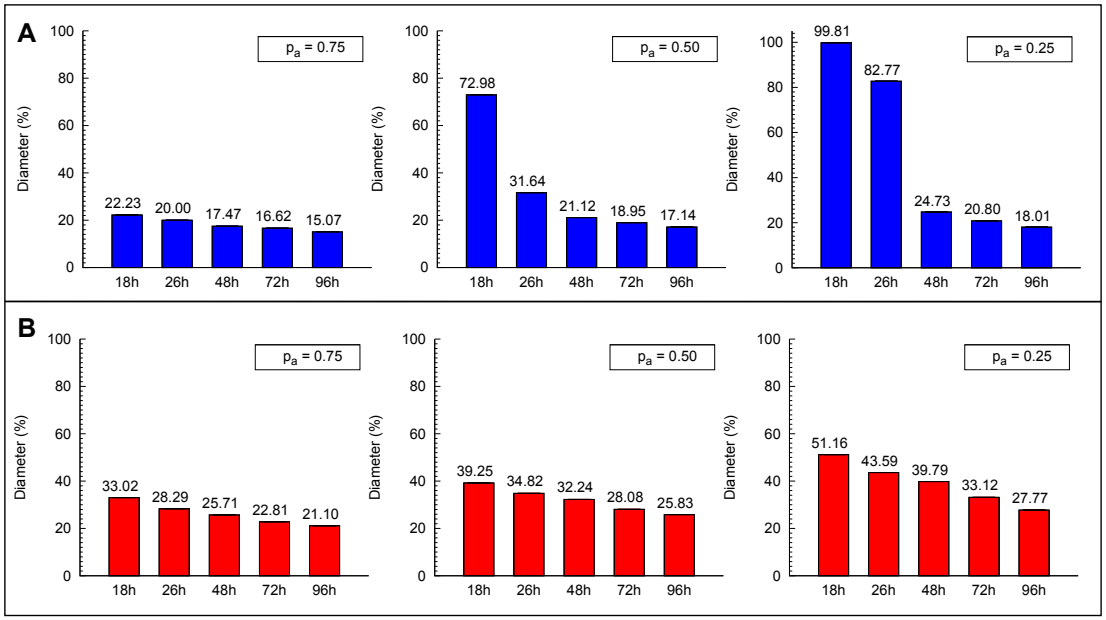

Figure C.3. Representation of the volume proportion of the inner region respect to the volume of the outer region for the low and high migration cases. Volume of the tumor inner region at the pre-treatment stage (where about 10^6 cells are present) and the corresponding standard deviations after performing 20 simulations in each case (with different seeds of a random number generator) are shown. Results are provided for the cases $p_a = 0.75$, $p_a = 0.50$ and $p_a = 0.25$ (left, middle, right) and CSC cycle durations equal to $18h$, $26h$, $48h$, $72h$ and $96h$. (A) Volume proportion of the tumor inner sphere where 100% of CSCs are located for the low migration case with respect to the total tumor volume ($2680\mu m$). (B) Volume proportion of the tumor inner sphere where 80% of CSCs are located for the high migration case with respect to the region where 90% of total cells (CCs and CSCs) are located ($3120\mu m$). See Tables 3.2 and 3.3 in Chapter 3, and Tables C.3 and C.4 above.

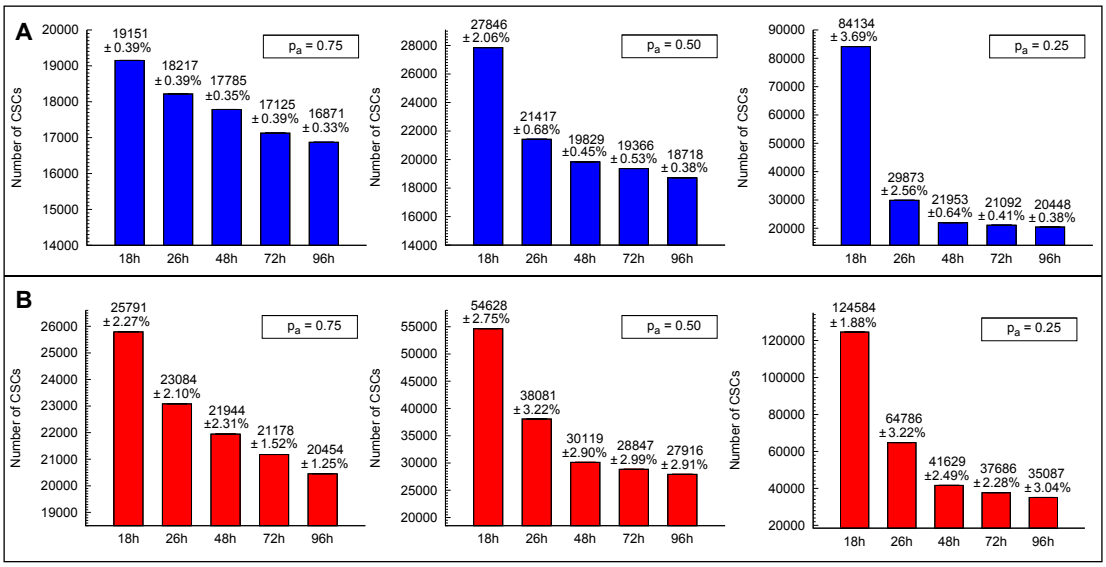

Figure C.4. Representation of the number of CSCs before irradiation for the low and high migration cases. Number of CSCs at the pre-treatment stage (where about 10^6 cells are present) and the corresponding standard deviations after performing 20 simulations in each case (with different seeds of a random number generator) are shown. Results are provided for the cases $p_a = 0.75$, $p_a = 0.50$ and $p_a = 0.25$ (left, middle, right), CSC cycle durations equal to $18h$, $26h$, $48h$, $72h$ and $96h$, for the low (A) and high (B) migration cases. See Tables 3.2 and 3.3 in Chapter 3, and Tables C.3 and C.4 above.

To complete this discussion related to the fast-cycling CSCs situation, some results concerning the performance of heterogeneous and the corresponding averaged homogeneous radiation therapies for CSC cycle durations equal to $26h$ and $18h$ are provided in Tables C.5 and C.6 (see also Figures C.5 and C.6) respectively. Moreover, the number of CSCs at the recurrence tumor stages and radiation doses for heterogeneous and homogeneous therapies needed to obtain tumor control are also shown.

As it turns out, as CSC cycle duration and p_a decrease, the standard fractionation (30 sessions delivered 5 days a week at 24 hours intervals with weekend interruptions) is not enough to treat the resulting tumors with clinically acceptable radiation doses. In both cases, heterogeneous and homogeneous radiation therapies and for some model parameter sets a fractionation protocol delivered in 7

days a week along 30 sessions at 24 hours intervals is advisable instead. Moreover, in the worst scenario, which corresponds to CSC cycle duration equal to $18h$ and $p_a = 0.25$, the total radiation dose needed to achieve tumor control whit any of these fractionation protocols is too high to be considered as a treatment option. However, an inspection of Tables C.5 and C.6 (see Figures C.5 and C.6) reveals that for all model parameter sets used, heterogeneous radiation therapies yield better results than their averaged homogeneous counterparts.

		Heterogeneous therapy		**Homogeneous therapy**	
p_a	τ_{csc}	**No Control**	**Control**	**No Control**	**Control**
0.75	**26h**	$2.0Gy - 2.5Gy^{(1)}$	$2.0Gy - 3.2Gy^{(2)}$	$2.10Gy^{(1)}/2.24Gy^{(2)}$	$3.2Gy$
		$[63Gy]^{\dagger}$	$[67.2Gy]^{\dagger}$	$[63Gy]^{\dagger}/[67.2Gy]^{\dagger}$	$[96Gy]^{\dagger}$
		(3085/116.59)		(11904/232.85)/(7913/224.15)	
	18h	$2.0Gy - 2.5Gy^{(3)}$	$2.0Gy - 3.9Gy^{(4)}$	$2.11Gy^{(3)}/2.42Gy^{(4)}$	$3.9Gy$
		$[63.3Gy]^{\dagger}$	$[72.6Gy]^{\dagger}$	$[63.3Gy]^{\dagger}/[72.6Gy]^{\dagger}$	$[117Gy]^{\dagger}$
		(26579/586.17)		(57890/951.47)/(34675/854.97)	
0.50	**26h**	$2.0Gy - 2.9Gy^{(5)}$	$2.0Gy - 4.3Gy^{(6)}$	$2.28Gy^{(5)}/2.73Gy^{(6)}$	$4.3Gy$
		$[68.4Gy]^{\dagger}$	$[81.9Gy]^{\dagger}$	$[68.4Gy]^{\dagger}/[81.9Gy]^{\dagger}$	$[129Gy]^{\dagger}$
		(96626/1776.42)		(182051/3485.87)/(123683/2601.55)	
	18h	$2.0Gy - 2.9Gy^{(7)}$	$2.0Gy - 4.9Gy^{(8)}$	$2.66Gy^{(7)}/4.12Gy^{(8)}$	$4.9Gy$
		$[79.8Gy]^{\ddagger}$	$[123.6Gy]^{\ddagger}$	$[79.8Gy]^{\ddagger}/[123.6Gy]^{\ddagger}$	$[147Gy]^{\ddagger}$
		(241936/7613.76)		(357911/9430.74)/(30377/1859.44)	
0.25	**26h**	$2.0Gy - 3.3Gy^{(9)}$	$2.0Gy - 4.7Gy^{(10)}$	$3.10Gy^{(9)}/4.23Gy^{(10)}$	$4.7Gy$
		$[93Gy]^{\ddagger}$	$[126.9Gy]^{\ddagger}$	$[93Gy]^{\ddagger}/[126.9Gy]^{\ddagger}$	$[141Gy]^{\ddagger}$
		(192613/5840.14)		(331871/9068.78)/(52201/3183.69)	
	18h	– – –	– – –	– – –	– – –

Table C.5. Performance of heterogeneous and homogeneous radiation therapies for the low migration case and fast-cycling CSCs. Data corresponding to 20 simulations (with different seeds of a random number generator) are presented. Treatment sessions were scheduled along 6 weeks (30 sessions) separated by 24 hours intervals except for weekends, where a 72 hours interval is allowed (†) and 7 days a week along 30 sessions at 24 hours intervals (without weekend interruptions) (‡). In the heterogeneous therapies, radiation doses are specified both for the outer (left) and inner (right) tumor regions, each case being indexed from (1) to (10). The averaged dose for any of the previous cases is labeled with the same number in the columns corresponding to homogeneous therapies. In brackets the total dose of the radiation therapy treatment and within braces the number of CSCs at the recurrence tumor stage with the corresponding standard deviation. See also Figure C.5 where some of these results are shown.

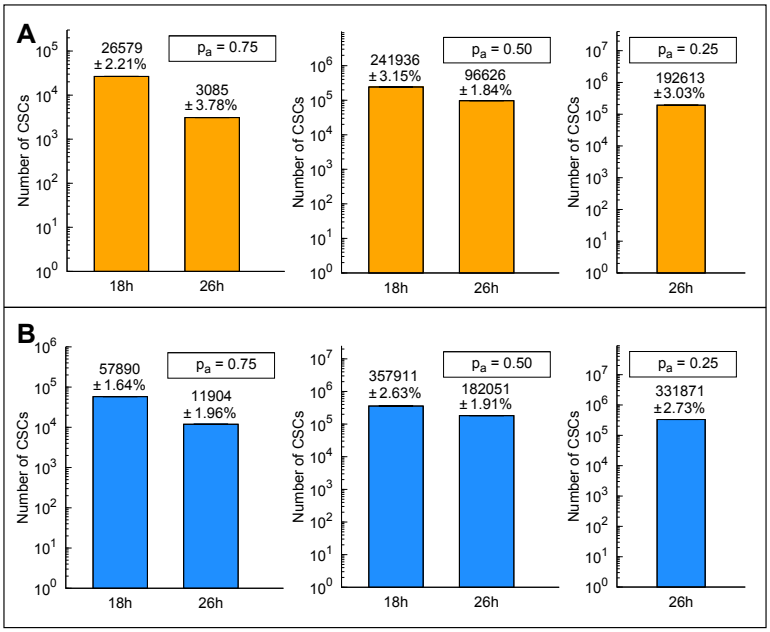

Figure C.5. Total number of fast-cycling CSCs at the end of the recurrence tumor stage for heterogeneous and averaged homogeneous radiation therapies with the low migration rate. Number of CSCs at the end of the recurrence tumor stage (where about 10^6 cells are again present) and the corresponding standard deviations after performing 20 simulations in each case (with different seeds of a random number generator) are shown. (A) For heterogeneous therapies that do not achieve tumor control and (B) for the corresponding averaged homogeneous therapies considered in Table C.5 for the cases $p_a = 0.75$, $p_a = 0.50$ and $p_a = 0.25$ (left, middle, right). The low migration rate and CSC cycle durations equal to $18h$ and $26h$ have been assumed. Notice that the vertical coordinate is represented in a logarithmic scale. See Table C.5 for further details.

		Heterogeneous therapy		Homogeneous therapy	
p_a	τ_{csc}	**No Control**	**Control**	**No Control**	**Control**
0.75	**26h**	$2.0Gy - 2.5Gy^{(1)}$	$2.8Gy - 3.4Gy^{(2)}$	$2.14Gy^{(1)}/2.97Gy^{(2)}$	$3.4Gy$
		$[64.2Gy]^{\dagger}$	$[89.1Gy]^{\dagger}$	$[64.2Gy]^{\dagger}/[89.1Gy]^{\dagger}$	$[102Gy]^{\dagger}$
		(11050/484.08)		(18967/326.68)/(2269/189.34)	
	18h	$2.0Gy - 2.5Gy^{(3)}$	$3.6Gy - 4.3Gy^{(4)}$	$2.17Gy^{(3)}/3.83Gy^{(4)}$	$4.3Gy$
		$[65.1Gy]^{\dagger}$	$[114.9Gy]^{\dagger}$	$[65.1Gy]^{\dagger}/[114.9Gy]^{\dagger}$	$[129Gy]^{\dagger}$
		(159982/5495.70)		(197218/5508.36)/(3826/319.69)	
0.50	**26h**	$2.0Gy - 2.9Gy^{(5)}$	$3.5Gy - 4.1Gy^{(6)}$	$2.31Gy^{(5)}/3.70Gy^{(6)}$	$4.1Gy$
		$[69.3Gy]^{\ddagger}$	$[111Gy]^{\ddagger}$	$[69.3Gy]^{\ddagger}/[111Gy]^{\ddagger}$	$[123Gy]^{\ddagger}$
		(218770/5954.86)		(282412/6544.93)/(9844/562.32)	
	18h	$2.0Gy - 2.9Gy^{(7)}$	$4.4Gy - 4.9Gy^{(8)}$	$2.35Gy^{(7)}/4.60Gy^{(8)}$	$4.9Gy$
		$[70.5Gy]^{\ddagger}$	$[138Gy]^{\ddagger}$	$[70.5Gy]^{\ddagger}/[138Gy]^{\ddagger}$	$[147Gy]^{\ddagger}$
		(594483/8063.34)		(831328/18256.43)/(48205/2468.33)	
0.25	**26h**	$2.0Gy - 3.3Gy^{(9)}$	$4.3Gy - 4.8Gy^{(10)}$	$2.57Gy^{(9)}/4.52Gy^{(10)}$	$4.8Gy$
		$[77.1Gy]^{\ddagger}$	$[135.6Gy]^{\ddagger}$	$[77.1Gy]^{\ddagger}/[135.6Gy]^{\ddagger}$	$[144Gy]^{\ddagger}$
		(689546/11268.43)		(896248/19376.56)/(96035/4090.75)	
	18h	$---$	$---$	$---$	$---$

Table C.6. Performance of heterogeneous and homogeneous radiation therapies for the high migration case and fast-cycling CSCs. Data corresponding to 20 simulations (with different seeds of a random number generator) are presented. Treatment sessions were scheduled along 6 weeks (30 sessions) separated by 24 hours intervals except for weekends, where a 72 hours interval is allowed (†) and 7 days a week along 30 sessions at 24 hours intervals (without weekend interruptions) (‡). In the heterogeneous therapies, radiation doses are specified both for the outer (left) and inner (right) tumor regions, each case being indexed from (1) to (10). The averaged dose for any of the previous cases is labeled with the same number in the columns corresponding to homogeneous therapies. In brackets the total dose of the radiation therapy treatment and within braces the number of CSCs at the recurrence tumor stage with the corresponding standard deviation. See also Figure C.6 where some of these results are shown.

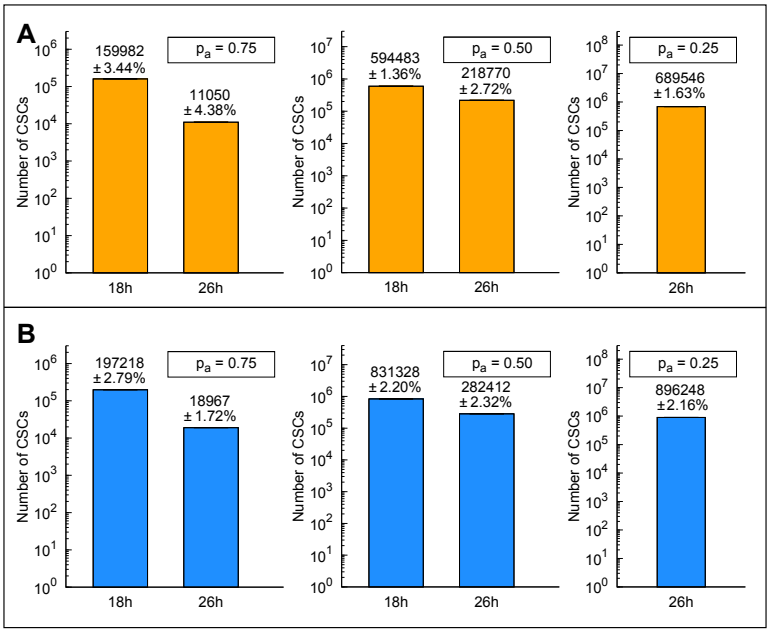

Figure C.6. Total number of fast-cycling CSCs at the end of the recurrence tumor stage for heterogeneous and averaged homogeneous radiation therapies with the high migration rate. Number of CSCs at the end of the recurrence tumor stage (where about 10^6 cells are again present) and the corresponding standard deviations after performing 20 simulations in each case (with different seeds of a random number generator) are shown. (A) For heterogeneous therapies that do not achieve tumor control and (B) for the corresponding averaged homogeneous therapies considered in Table C.6 for the cases $p_a = 0.75$, $p_a = 0.50$ and $p_a = 0.25$ (left, middle, right). The high migration rate and CSC cycle durations equal to $18h$ and $26h$ have been assumed. Notice that the vertical coordinate is represented in a logarithmic scale. See Table C.6 for further details.

C.2.3 A particular case of cancer cell plasticity

To conclude this Appendix, an example of cancer cell plasticity is described, a hypothesis that has been proposed to better understand the onset of resistance after therapy (cf. for instance [203], [204] and [205]). To address this issue, suppose that in addition to CSCs giving raise to CCs by asymmetric division, a (assumed small) percentage of CCs may transform to a CSC phenotype, possibly as a reaction to radiation therapy. In particular, consider the cases of CSC cycle duration equal

to $48h$ and p_a equal to 0.75 and 0.25, both for the low and high migration cases respectively. Then, assume that a small percentage of CCs (5%) are transformed to CSCs after sessions 5, 15 and 25 of a standard fractionation protocol (5 days a week along 30 sessions at 24 hours intervals except for weekends, where a 72 hours interval is allowed). As one can expect, any increase in the number of CSCs results in increased malignancy, measured in terms of higher radioresistance to therapy. However, the conclusion obtained that heterogeneous, tumor-adapted radiation therapies fare better than their corresponding averaged, homogeneous versions continues to hold. To show that, in Table C.7 (respectively, Table C.8) a comparison is provided of the same cases with and without the cancer cell plasticity effect for the low (respectively high) migration case. See also Figures C.7 and C.8 where some results provided in Tables C.7 and C.8 are shown respectively.

		Heterogeneous therapy		**Homogeneous therapy**	
p_a		**No Control**	**Control**	**No Control**	**Control**
0.75	**No CC Plasticity**	$---$	$2.0Gy - 2.7Gy^{(1)}$	$2.12Gy^{(1)}$	$2.7Gy$
			[63.6Gy]	[63.6Gy]	[81Gy]
				(514/13.65)	
	CC Plasticity	$2.0Gy - 2.7Gy^{(2)}$	$2.4Gy - 3.2Gy^{(3)}$	$2.12Gy^{(2)}/2.54Gy^{(3)}$	$3.2Gy$
		[63.6Gy]	[76.2Gy]	[63.6Gy]/[76.2Gy]	[96Gy]
		(771/24.37)		(1256/43.42)/(197/26.14)	
0.25	**No CC Plasticity**	$---$	$2.0Gy - 3.9Gy^{(4)}$	$2.47Gy^{(4)}$	$3.9Gy$
			[74.1Gy]	[74.1Gy]	[117Gy]
				(96346/1141.30)	
	CC Plasticity	$2.0Gy - 3.9Gy^{(5)}$	$3.2Gy - 4.3Gy^{(6)}$	$2.47Gy^{(5)}/3.47Gy^{(6)}$	$4.3Gy$
		[74.1Gy]	[104.1Gy]	[74.1Gy]/[104.1Gy]	[129Gy]
		(143242/4084.60)		(297794/6467.14)/(5144/280.49)	

Table C.7. Estimating cancer cell plasticity effects for the low migration case and CSC cycle duration equal to 48 hours. In all cases, treatment sessions were scheduled along 6 weeks separated by 24 hours intervals except for weekends, where a 72 hours interval is allowed. Data corresponding to 20 simulations (with different seeds of a random number generator) are presented. In the heterogeneous therapies, radiation doses are specified both for the outer (left) and inner (right) tumor regions, each case being indexed from (1) to (6). The averaged dose for any of the previous cases is labeled with the same number in the columns corresponding to homogeneous therapies. In brackets the total dose of the radiation therapy treatment and within braces the number of CSCs at the recurrence tumor stage with the corresponding standard deviation. See also Figure C.7 where some of these results are shown.

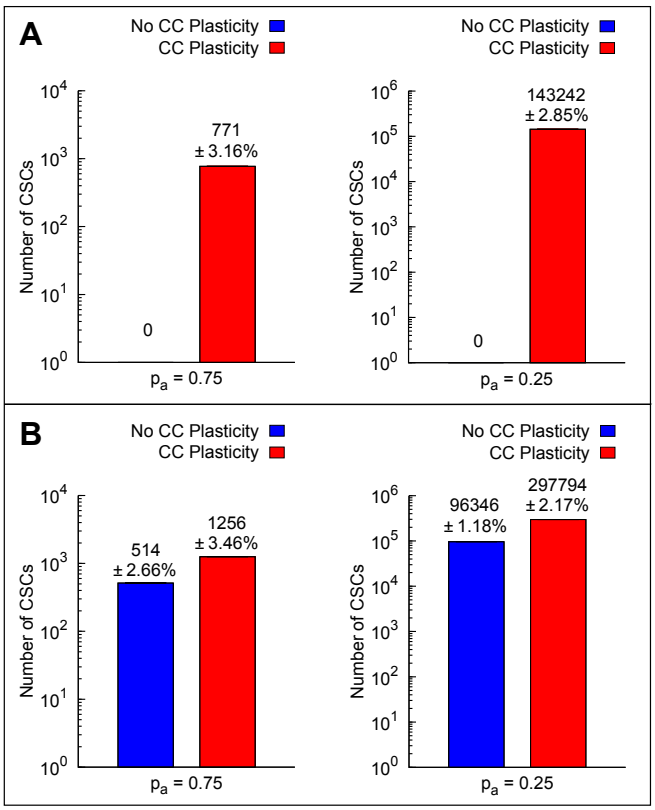

Figure C.7. Cancer cell plasticity effects on the total number of CSCs at the end of the recurrence tumor stage for heterogeneous and averaged homogeneous radiation therapies. The low migration rate and CSC cycle duration equal to $48h$ have been assumed. Number of CSCs at the end of the recurrence tumor stage (where about 10^6 cells are again present) and the corresponding standard deviations after performing 20 simulations in each case (with different seeds of a random number generator) are shown. Results are provided for radiation therapies with and without cell plasticity effects. (A) For heterogeneous therapies that do not achieve tumor control and (B) for the corresponding averaged homogeneous therapies considered in Table C.7 for the cases $p_a = 0.75$ and $p_a = 0.25$ (left and right). Notice that the vertical coordinate is represented in a logarithmic scale. See Table C.7 for further details.

		Heterogeneous therapy		Homogeneous therapy	
p_a		**No Control**	**Control**	**No Control**	**Control**
0.75	**No CC Plasticity**	$---$	$2.2Gy - 2.7Gy^{(1)}$	$2.33Gy^{(1)}$	$2.7Gy$
			$[69.9Gy]$	$[69.9Gy]$	$[81Gy]$
				(267/10.61)	
	CC Plasticity	$2.2Gy - 2.7Gy^{(2)}$	$2.6Gy - 3.2Gy^{(3)}$	$2.33Gy^{(2)}/2.75Gy^{(3)}$	$3.2Gy$
		$[69.9Gy]$	$[82.5Gy]$	$[69.9Gy]/[82.5Gy]$	$[96Gy]$
		(953/37.45)		(2487/92.83)/(526/34.56)	
0.25	**No CC Plasticity**	$---$	$3.4Gy - 3.9Gy^{(4)}$	$3.60Gy^{(4)}$	$3.9Gy$
			$[108Gy]$	$[108Gy]$	$[117Gy]$
				(7716/174.66)	
	CC Plasticity	$3.4Gy - 3.9Gy^{(5)}$	$3.7Gy - 4.3Gy^{(6)}$	$3.60Gy^{(5)}/3.94Gy^{(6)}$	$4.3Gy$
		$[108Gy]$	$[118.2Gy]$	$[108Gy]/[118.2Gy]$	$[129Gy]$
		(8116/251.09)		(17212/592.21)/(3501/278.34)	

Table C.8. Estimating cancer cell plasticity effects for the high migration case and CSC cycle duration equal to 48 hours. In all cases, treatment sessions were scheduled along 6 weeks separated by 24 hours intervals except for weekends, where a 72 hours interval is allowed. Data corresponding to 20 simulations (with different seeds of a random number generator) are presented. In the heterogeneous therapies, doses are specified both for the outer (left) and inner (right) tumor regions, each case being indexed from (1) to (6). The averaged dose for any of the previous cases is labeled with the same number in the columns corresponding to homogeneous therapies. In brackets the total dose of the radiation therapy treatment and within braces the number of CSCs at the recurrence tumor stage with the corresponding standard deviation. See also Figure C.8 where some of these results are shown.

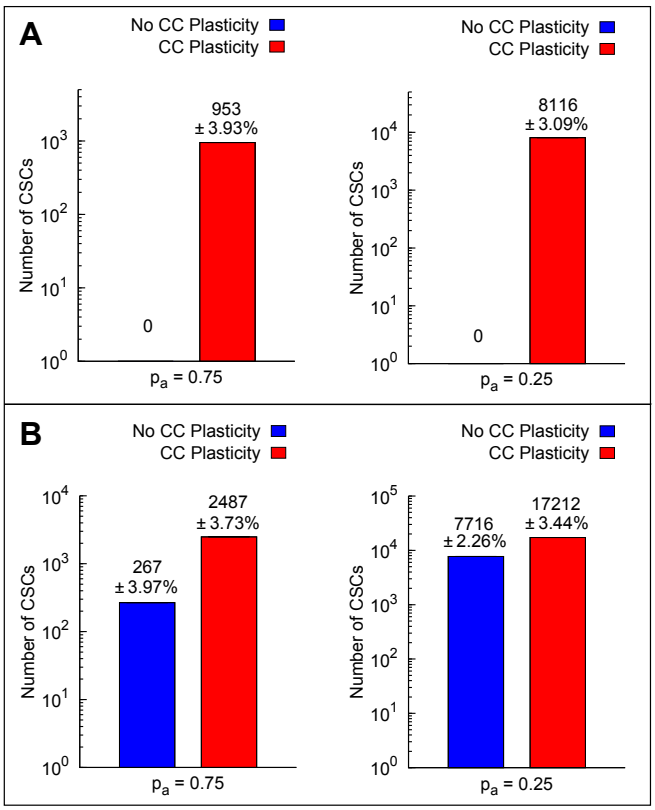

Figure C.8. Cancer cell plasticity effects on the total number of CSCs at the end of the recurrence tumor stage for heterogeneous and averaged homogeneous radiation therapies. The high migration rate and CSC cycle duration equal to $48h$ have been assumed. Number of CSCs at the end of the recurrence tumor stage (where about 10^6 cells are again present) and the corresponding standard deviations after performing 20 simulations in each case (with different seeds of a random number generator) are shown. Results are provided for radiation therapies with and without cell plasticity effects. (A) For heterogeneous therapies that do not achieve tumor control and (B) for the corresponding averaged homogeneous therapies considered in Table C.8 for the cases $p_a = 0.75$ and $p_a = 0.25$ (left and right). Notice that the vertical coordinate is represented in a logarithmic scale. See Table C.8 for further details.

Bibliography

[1] World Health Organization, "Annex Table 2: Deaths by cause, sex and mortality stratum in WHO regions, estimates for 2002", *The world health report 2004 - changing history*, 2004.

[2] American Cancer Society, "Global Cancer Facts & Figures", 2nd Edition. Atlanta, 2011.

[3] J. Ferlay, I. Soerjomataram, M. Ervik, R. Dikshit, S. Eser, C. Mathers, M. Rebelo, D. M. Parkin, D. Forman and F. Bray, "GLOBOCAN 2012 v1.0, Cancer Incidence and Mortality Worldwide: IARC", CancerBase No. 11 [Internet]. Lyon, France: International Agency for Research on Cancer; 2013. Available from: *http://globocan.iarc.fr*, accessed on 24/01/2014.

[4] A. C. Begg, F. A. Stewart and C. Vens, "Strategies to improve radiotherapy with targeted drugs", *Nat. Rev. Cancer*, 11, 2011 pp. 239–53.

[5] E. J. Moding, M. B. Kastan and D. G. Kirsch, "Strategies for optimizing the response of cancer and normal tissues to radiation", *Nat. Rev. Drug Discov.*, 12, 2013 pp. 526–42.

[6] G. Delaney, S. Jacob, C. Featherstone and M. Barton, "The role of radiotherapy in cancer treatment: estimating optimal utilization from a review of evidence-based clinical guidelines", *Cancer*, 104, 2005 pp. 1129–37.

[7] W. C. Röntgen, "Ueber eine neue Art von Strahlen", *Sitzungsberichte der Physikalisch-Medizinischen Gesellschaft zu Wrzburg, Sitzung*, 30, 1895 pp. 132–41.

[8] W. C. Röntgen, "On a new kind of rays", *Nature*, 23(53), 1896 pp. 274–76.

[9] E. Grubbe, "X-rays in the treatment of cancer and other malignant diseases", *Med. Rec.*, 62, 1902 pp. 692–95.

[10] F. H. Williams, "The Roentgen rays in medicine and surgery", Macmillan, 1902.

[11] J. Belot, "Radiotherapy in skin disease", Rebman, 1905.

[12] H.S. Kaplan, "Basic principles in radiation oncology", *Cancer*, 39(2), 1977 pp. 689–93.

[13] J. Bernier, E. J. Hall and A. Giaccia, "Radiation oncology: a century of achievements", *Nat. Rev. Cancer*, 4(9), 2004 pp. 737–47.

[14] International Commission on Radiation Units and Measurements, ICRU Report 62, "Prescribing, recording, and reporting photon beam therapy", *(Supplement to ICRU report 50)*, Bethesda MD, USA, 1999.

[15] International Commission on Radiation Units and Measurements, ICRU Report 83, "Prescribing, recording, and reporting IMRT", Washington D.C., USA, 2010.

[16] R. Baskar, K. A. Lee, R. Yeo and K. W. Yeoh, "Cancer and radiation therapy: current advances and future directions", *Int. J. Med. Sci.*, 9(3), 2012 pp. 193–9.

[17] J. R. Williams and D. I. Thwaites, "Radiotherapy physics in practice", 2nd Edition. Oxford University Press UK, 2000.

[18] R. Timmerman and L. Xing, "Image Guided and Adaptive Radiation Therapy", Wolters Kluwer Lippincott Williams & Wilkins Health in Philadelphia, 2010.

[19] J. R. Palta and T. R. Mackie, "Intensity Modulated Radiation Therapy: The State of the Art", Medical Physics Publishing, Madison, Wisconsin, 2003.

[20] J. Grimm, T. LaCouture, R. Croce, I. Yeo, Y. Zhu and J. Xue, "Dose tolerance limits and dose volume histogram evaluation for stereotactic body radiotherapy", *J. Appl. Clin. Med. Phys.*, 12(2), 2011 pp. 3368.

[21] A. Marusyk and K. Polyak, "Tumor heterogeneity: causes and consequences", *Biochim. Biophys. Acta*, 1805, 2010 pp. 105–17.

[22] A. Marusyk, V. Almendro and K. Polyak, "Intra-tumour heterogeneity: a looking glass for cancer?", *Nat. Rev. Cancer*, 12, 2012 pp. 323–34.

[23] S. Bao, Q. Wu, R. E. McLendon, Y. Hao, Q. Shi , A. B. Hjelmeland, M. W. Dewhirst, D. D. Bigner and J. N. Rich, "Glioma stem cells promote radioresistance by preferential activation of the dna damage response", *Nature*, 444, 2006 pp. 756–60.

[24] U. A. van der Heide, A. C. Houweling, G. Groenendaal, R. G. Beets-Tan and P. Lambin, "Functional mri for radiotherapy dose painting", *Magn. Reson. Imaging*, 30, 2012 pp. 1216–23.

[25] S. M. Bentzen and V. Gregoire, "Molecular imaging-based dose painting: a novel paradigm for radiation therapy prescription", *Semin. Radiat. Oncol.*, 21, 2011 pp. 101–10.

[26] E. Malinen, A. Søvik, D. Hristov, Ø. S. Bruland and D. R. Olsen, "Adapting radiotherapy to hypoxic tumours", *Phys. Med. Biol.*, 51(19), 2006 pp. 4903–21.

[27] E. Shaw, R. Kline, M. Gillin, L. Souhami, A. Hirschfeld, R. Dinapoli and L. Martin, "Radiation therapy oncology group: radiosurgery quality assurance guidelines", *Int. J. Radiat. Oncol. Biol. Phys.*, 27(5), 1993 pp. 1231–9.

[28] T. Knöös, I. Kristensen and P. Nilsson, "Volumetric and dosimetric evaluation of radiation treatment plans: radiation conformity index", *Int. J. Radiat. Oncol. Biol. Phys.*, 42(5), 1998 pp. 1169–76.

[29] M. Yoon, S. Y. Park, D. Shin, S. B. Lee, H. R. Pyo, D. Y. Kim and K. H. Cho, "A new homogeneity index based on statistical analysis of the dose-volume histogram", *J. Appl. Clin. Med. Phys.*, 8(2), 2007 pp. 9–17.

[30] I. Paddick, "A simple scoring ratio to index the conformity of radiosurgical treatment plans", *J. Neurosurg.*, 93(3), 2000 pp. 219–22.

[31] J. Menhel, D. Levin, D. Alezra, Z. Symon and R. Pfeffer, "Assessing the quality of conformal treatment planning: a new tool for quantitative comparison", *Phys. Med. Biol.*, 51(20), 2006 pp. 5363–75.

[32] L. Feuvret, G. Noël, J. J. Mazeron and P. Bey, "Conformity index: a review", *Int. J. Radiat. Oncol. Biol. Phys.*, 64(2), 2006 pp. 333–42.

[33] Q. R. Wu, B. W. Wessels, D. B. Einstein, R. J. Maciunas, E. Y. Kim and T. J. Kinsella, "Quality of coverage: conformity measures for stereotactic radiosurgery", *J. Appl. Clin. Med. Phys.*, 4(4), 2003 pp. 374–81.

[34] T. H. Wagner, F. J. Bova, W. A. Friedman, J. M. Buatti, L. G. Bouchet and S. L. Meeks, "A simple and reliable index for scoring rival stereotactic radiosurgery plans", *Int. J. Radiat. Oncol. Biol. Phys.*, 57(4), 2003 pp. 1141–9.

[35] N. J. Lomax and S. G. Scheib, "Quantifying the degree of conformity in radiosurgery treatment planning", *Int. J. Radiat. Oncol. Biol. Phys.*, 55(5), 2003 pp. 1409–19.

[36] V. W. Wu, D. L. Kwong and J. S. Sham, "Target dose conformity in 3-dimensional conformal radiotherapy and intensity modulated radiotherapy", *Radiother. Oncol.*, 71(2), 2004 pp. 201–6.

[37] H. Akpati, C. Kim, B. Kim, T. Park and A. Meek, "Unified dosimetry index (UDI): a figure of merit for ranking treatment plans", *J. Appl. Clin. Med. Phys.*, 9(3), 2008 pp. 2803.

[38] R. R. Meyer, H. H. Zhang, L. Goadrich, D. P. Nazareth, L. Shi and W. D. D'Souza, "A multiplan treatment-planning framework: a paradigm shift for intensity-modulated radiotherapy", *Int. J. Radiat. Oncol. Biol. Phys.*, 68(4), 2007 pp. 1178–89.

[39] M. M. Miften, S. K. Das, M. Su and L. B. Marks, "A dose-volume-based tool for evaluating and ranking imrt treatment plans", *J. Appl. Clin. Med. Phys.*, 5(4), 2004 pp. 1–14.

[40] I. J. Kalet and M. M. Austin-Seymour, "The Use of Medical Images in Planning and Delivery of Radiation Therapy", *J. Am. Med. Inform. Assoc.*, 4(5), 1997 pp. 327–39.

[41] W. G. Bradley, "History of medical imaging", *P. Am. Philos. Soc.*, 152(3), 2008 pp. 349–61.

[42] F. Tixier, C. C. Le Rest, M. Hatt, N. Albarghach, O. Pradier, J. P. Metges, L. Corcos and D. Visvikis, "Intratumor heterogeneity characterized by textural features on baseline 18F-FDG PET images predicts response to concomitant radiochemotherapy in esophageal cancer", *J. Nucl. Med.*, 52(3), 2011 pp. 369–78.

[43] H. R. Withers, "The four rs of radiotherapy", *Adv. Radiat. Biol.*, 5, 1975 pp. 241–47.

[44] G. G. Steel, T. J. McMillan and J. H. Peacock, "The 5rs of radiobiology", *Int. J. Radiat. Biol.*, 56, 1989 pp. 1045–48.

[45] F. D. Malkinson, "Some principles of radiobiology: A selective review", *J. Invest. Dermatol.*, 76, 1981 pp. 32–6.

[46] T. M. Pawlik and K. Keyomarsi, "Role of cell cycle in mediating sensitivity to radiotherapy", *Int. J. Radiat. Oncol. Biol. Phys.*, 59(4), 2004 pp. 928–42.

[47] E. J. Hall and A. J. Giaccia, "Radiobiology for the radiologist", 6th Edition. JB Lippincott, Philadelphia, 2006.

[48] G. Minniti, M. Amichetti and R. M. Enrici, "Radiotherapy and radiosurgery for benign skull base meningiomas", *Radiat. Oncol.*, 4(42), 2009.

[49] C. D. Fuller, M. Choi, B. Forthuber, S. J. Wang, N. Rajagiriyil, B. J. Salter and M. Fuss, "Standard fractionation intensity modulated radiation therapy (IMRT) of primary and recurrent glioblastoma multiforme", *Radiat. Oncol.*, 2(26), 2007.

[50] International Commission on Radiation Units and Measurements, ICRU Report 33, "Radiation Quantities and Units", Washington D.C., USA, 1980.

[51] S. A. Bhide and C. M. Nutting, "Recent advances in radiotherapy", *BMC Medicine*, 8(25), 2010.

[52] T. Gupta and C. A. Narayan, "Image-guided radiation therapy: Physician's perspectives", *J. Med. Phys.*, 37(4), 2012 pp. 174–82.

[53] R. G. Dale and B. Jones, "Radiobiological Modelling in Radiation Oncology", The British Institute of Radiology, London, UK, 2007.

[54] S. F. O'Rourke, H. McAneney and T. Hillen, "Linear quadratic and tumour control probability modelling in external beam radiotherapy", *J. Math. Biol.*, 58(4-5), 2009 pp. 799–817.

[55] J. F. Fowler, "The linear-quadratic formula and progress in fractionated radiotherapy", *Br. J. Radiol.*, 62(740), 1989 pp. 679–94.

[56] A. Cappuccio, M. A. Herrero and L. Núñez, "Tumour radiotherapy and its mathematical modelling", *Contemporary Mathematics*, 492, 2009 pp. 77–102.

[57] W. K. Sinclair, "The shape of radiation survival curves of mammalian cells cultured in vitro", *Bio-physical Aspects of Radiation Quality, International Atomic Energy Agency, Technical Reports Series*, 58, 1966 pp. 21–43.

[58] R. Sachs, P. Hahnfeld and D. Brenner, "The link between low-LET dose-response relations and the underlying kinetics of damage production/repair/misrepair", *Int. J. Rad. Biol.*, 72, 1997 pp. 351–74.

[59] G. Steel, "Basic Clinical Radiobiology", Hodder Arnold, London, UK, 2002.

[60] D. J. Brenner, L. R. Hlatky, P. J. Hahnfeldt, Y. Huang and R. K. Sachs, "The linear-quadratic model and most other common radiobiological models result in similar predictions of time-dose relationships", *Radiat. Res.*, 150(1), 1998 pp. 83–91.

[61] L. Jones, P. Hoban and P. Metcalfe, "The use of the linear quadratic model in radiotherapy: a review", *Australas Phys. Eng. Sci. Med.*, 24(3), 2001 pp. 132–46.

[62] D. M. Shepard, M. C. Ferris, G. H. Olivera and T. R. Mackie, "Optimizing the delivery of radiation therapy to cancer patients", *Siam Review*, 41, 1999 pp. 721–44.

[63] A. Brahme, "Development of radiation therapy optimization", *Acta Oncol.*, 39(5), 2000 pp. 579–95.

[64] C. G. Orton, T. R. Bortfeld, A. Niemierko and J. Unkelbach, "The role of medical physicists and the AAPM in the development of treatment planning and optimization", *Med. Phys.*, 35(11), 2008 pp. 4911–23.

[65] A. E. Nahum and J. Uzan, "(Radio)biological optimization of external-beam radiotherapy", *Comput. Math. Methods Med.*, 329214, 2012.

[66] X. Allen Li, M. Alber, J. O. Deasy, A. Jackson, K. W. Ken Jee, L. B. Marks, M. K. Martel, C. Mayo, V. Moiseenko, A. E. Nahum, A. Niemierko, V. A. Semenenko and E. D. Yorke, "The use and QA of biologically related models for treatment planning: short report of the TG-166 of the therapy physics committee of the AAPM", *Med. Phys.*, 39(3), 2012 pp. 1386–409.

[67] A. Niemierko, M. Urie and M. Goitein, "Optimization of 3D radiation-therapy with both physical and biological end-points and constraints", *Int. J. Radiat. Oncol. Biol. Phys.*, 23(1), 1992 pp. 99–108.

[68] T. Bortfeld, "Optimized planning using physical objectives and constraints", *Semin. Radiat. Oncol.*, 9(1), 1999 pp. 20–34.

[69] M. Alber and F. Nusslin, "An objective function for radiation treatment optimization based on local biological measures", *Phys. Med. Biol.*, 44(2), 1999 pp. 479–93.

[70] A. Brahme, "Individualizing cancer treatment: biological optimization models in treatment planning and delivery", *Int. J. Radiat. Oncol. Biol. Phys.*, 49(2), 2001 pp. 327–37.

[71] Q. W. Wu, R. Mohan, A. Niemierko and R. Schmidt-Ullrich, "Optimization of intensity-modulated radiotherapy plans based on the equivalent uniform dose", *Int. J. Radiat. Oncol. Biol. Phys.*, 52(1), 2002 pp. 224–35.

[72] L. Strigari, M. D'Andrea, C. L. Maini, R. Sciuto and M. Benassi, "Biological optimization of heterogeneous dose distributions in systemic radiotherapy", *Med. Phys.*, 33(6), 2006 pp. 1857–66.

[73] J. Stein, R. Mohan, X. Wang, T. Bortfeld, Q. Wu, K. Preiser, C. Ling and W. Schlegel, "Number and orientations of beams in intensity-modulated radiation treatments", *Med. Phys.*, 24(2), 1997 pp. 149–60.

[74] Q. Hou, J. Wang, Y. Chen and J. Galvin, "Beam orientation optimization for IMRT by a hybrid method of the genetic algorithm and the simulated dynamics", *Med. Phys.*, 30(9), 2003 pp. 2360–67.

[75] E. Schreibmann, M. Lahanas, L. Xing and D. Baltas, "Multiobjective evolutionary optimization of number of beams, their orientations and weights for IMRT", *Phys. Med. Biol.*, 49(5), 2004 pp. 747–70.

[76] W. D'Souza, R. Meyer and L. Shi, "Selection of beam orientations in intensity modulated radiation therapy using single-beam indices and integer programming", *Phys. Med. Biol.*, 49(15), 2004 pp. 3465–81.

[77] R. J. Yang, J. R. Dai, Y. Yang and Y. M. Hu, "Beam orientation optimization for intensity-modulated radiation therapy using mixed integer programming", *Phys. Med. Biol.*, 51(15), 2006 pp. 3653–66.

[78] J. L. Bedford and S. Webb, "Direct-aperture optimization applied to selection of beam orientations in intensity-modulated radiation therapy", *Phys. Med. Biol.*, 52(2), 2007 pp. 479–98.

[79] S. Webb, "The physical basis of imrt and inverse planning", *Br. J. Radiol.*, 76(910), 2007 pp. 678–89.

[80] K. S. Chuang, T. J. Chen, S. C. Kuo, M. L. Jan, I. M. Hwang, S. Chen, Y. C. Lin and J. Wu, "Determination of beam intensity in a single step for IMRT inverse planning", *Phys. Med. Biol.*, 48(3), 2003 pp. 293–306.

[81] M. A. Earl, D. M. Shepard, S. Naqvi, X. A. Li and C. X. Yu, "Inverse planning for intensity-modulated arc therapy using direct aperture optimization", *Phys. Med. Biol.*, 48(8), 2003 pp. 1075–89.

[82] L. Lee, Y. Z. Ma, Y. Y. Ye and L. Xing, "Conceptual formulation on fourdimensional inverse planning for intensity modulated radiation therapy", *Phys. Med. Biol.*, 54(13), 2009 pp. 255–66.

[83] J. St-Hilaire, C. Sévigny, F. Beaulieu, L. Gingras, D. Tremblay and L. Beaulieu, "Optimization of photon beam energy in aperture-based inverse planning", *J. Appl. Clin. Med. Phys.*, 10(4), 2009 pp. 36–54.

[84] E. K. Lee, T. Fox and I. Crocker, "Optimization of radiosurgery treatment planning via mixed integer programming", *Med. Phys.*, 27(5), 2000 pp. 995–1004.

[85] H. W. Hamacher and K. H. Küfer, "Inverse radiation therapy planning - a multiple objective optimization approach", *Discrete Applied Mathematics*, 118(1-2), 2002 pp. 145–61.

[86] G. Bednarz, D. Michalski, C. Houser, M. S. Huq, Y. Xiao, P. R. Anne and J. M. Galvin, "The use of mixed-integer programming for inverse treatment planning with pre-defined field segments", *Phys. Med. Biol.*, 47(13), 2002 pp. 2235–45.

[87] M. C. Ferris, R. R. Meyer and W. DSouza, "Radiation treatment planning: Mixed integer programming formulations and approaches", *In G. Appa, L. Pitsoulis, H. P. Williams, eds., Handbook on Modelling for Discrete Optimization*, Springer-Verlag, NY, 2006 pp. 317–40.

[88] G. W. Barendsen, "Dose fractionation, dose rate and iso-effect relationships for normal tissue responses", *Int. J. Radiat. Oncol. Biol. Phys.*, 8(11), 1982 pp. 1981–97.

[89] T. S. Kehwar, "Analytical approach to estimate normal tissue complication probability using best fit of normal tissue tolerance doses into the NTCP equation of the linear quadratic model", *J. Cancer Res. Ther.*, 1(3), 2005 pp. 168–79.

[90] D. D. Dionysiou, G. S. Stamatakos, D. Gintides, N. Uzunoglu and K. Kyriaki, "Critical parameters determining standard radiotherapy treatment outcome for glioblastoma multiforme: a computer simulation", *Open Biomed. Eng. J.*, 2, 2008 pp. 43–51.

[91] D. J. Carlson, R. D. Stewart, X. A. Li, K. Jennings, J. Z. Wang and M. Guerrero, "Comparison of in vitro and in vivo α/β ratios for prostate cancer", *Phys. Med. Biol.*, 49(19), 2004 pp. 4477–91.

[92] B. Jones, R. G. Dale, C. Deehan, K. I. Hopkins and D. A. Morgan, "The role of biologically effective dose (BED) in clinical oncology", *Clin. Oncol. (R. Coll. Radiol.)*, 13(2), 2001 pp. 71–81.

[93] P. Mayles, A. Nahum and J. C. Rosenwald, "Handbook of Radiotherapy Physics: Theory and Practice", Taylor & Francis Group 2007.

[94] M. V. Williams, J. Denekamp and J. F. Fowler, "A review of alpha/beta ratios for experimental tumors: implications for clinical studies of altered fractionation", *Int. J. Radiat. Oncol. Biol. Phys.*, 11(1), 1985 pp. 87–96.

[95] H. McAneney and S. F. O'Rourke, "Investigation of various growth mechanisms of solid tumour growth within the linear-quadratic model for radiotherapy", *Phys. Med. Biol.*, 52(4), 2007 pp. 1039–54.

[96] H. D. Thames, S. M. Bentzen, I. Turesson, M. Overgaard and W. van den Bogaert, "Time-dose factors in radiotherapy: a review of the human data", *Radiother. Oncol.*, 19(3), 1990 pp. 219–35.

[97] H. Byrne and L. Preziosi, "Modelling solid tumour growth using the theory of mixtures", *Math. Med. Biol.*, 20(4), 2003 pp. 341–66.

[98] P. Macklin, S. McDougall, A. R. Anderson, M. A. Chaplain, V. Cristini and J. Lowengrub, "Multiscale modelling and nonlinear simulation of vascular tumour growth", *J. Math. Biol.*, 58(4-5), 2009 pp. 765–98.

[99] I. Ramis-Conde, M. A. Chaplain, A. R. Anderson and D. Drasdo, "Multi-scale modelling of cancer cell intravasation: the role of cadherins in metastasis", *Phys. Biol.*, 6(1), 016008, 2009.

[100] N. K. Martin, E. A. Gaffney, R. A. Gatenby and P. K. Maini, "Tumour-stromal interactions in acid-mediated invasion: a mathematical model", *J. Theor. Biol.*, 267(3), 2010 pp. 461–70.

[101] V. Andasari, A. Gerisch, G. Lolas, A. P. South and M. A. Chaplain, "Mathematical modeling of cancer cell invasion of tissue: biological insight from mathematical analysis and computational simulation", *J. Math. Biol.*, 63(1), 2011 pp. 141–71.

[102] H. Perfahl, H. M. Byrne, T. Chen, V. Estrella, T. Alarcón, A. Lapin, R. A. Gatenby, R. J. Gillies, M. C. Lloyd, P. K. Maini, M. Reuss and M. R. Owen, "Multiscale modelling of vascular tumour growth in 3D: the roles of domain size and boundary conditions", *PLoS One*, 6(4), e14790, 2011.

[103] N. Bellomo, A. Bellouquid and M. Delitala, "Mathematical topics on the modelling complex multicellular systems and tumor immune cells competition", *Math. Mod. Meth. in Applied Sciences*, 14(11), 2004 pp. 1683–1733.

[104] R. P. Araujo and D. L. McElwain, "A history of the study of solid tumour growth: the contribution of mathematical modelling", *Bull. Math. Biol.*, 66(5), 2004 pp. 1039–91.

[105] H. M. Byrne, T. Alarcón, M. R. Owen, S. D. Webb and P. K. Maini, "Modelling aspects of cancer dynamics: a review", *Philos. Trans. A Math. Phys. Eng. Sci.*, 364(1843), 2006 pp. 1563–78.

[106] A. Cappuccio, M. A. Herrero and L. Núñez, "Biological optimization of tumor radiosurgery", *Med. Phys.*, 36(1), 2009 pp. 98–104.

[107] H. Enderling, D. Park, L. Hlatky and P. Hahnfeldt, "The importance of spatial distribution of stemness and proliferation state in determining tumor radioresponse", *Mathematical Modelling of Natural Phenomena*, 4(3), 2009 pp. 117–33.

[108] H. Enderling, M. A. Chaplain and P. Hahnfeldt, "Quantitative modeling of tumor dynamics and radiotherapy", *Acta Biotheor.*, 58(4), 2010 pp. 341–53.

[109] A. Bertuzzi, C. Bruni, A. Fasano, A. Gandolfi, F. Papa and C. Sinisgalli, "Response of tumor spheroids to radiation: modeling and parameter estimation", *Bull. Math. Biol.*, 72(5), 2010 pp. 1069–91.

[110] J. C. L. Alfonso, G. Buttazzo, B. García-Archilla, M. A. Herrero and L. Núñez, "A class of optimization problems in radiotherapy dosimetry planning", *Discr. Cont. Dyn. Systems B.*, 17(6), 2012 pp. 1651–72.

[111] X. Gao, J. T. McDonald, L. Hlatky and H. Enderling, "Acute and fractionated irradiation differentially modulate glioma stem cell division kinetics", *Cancer Res.*, 73(5), 2013 pp. 1481–90.

[112] H. Kempf, M. Bleicher and M. Meyer-Hermann, "Spatio-temporal cell dynamics in tumour spheroid irradiation", *Eur. Phys. J. D.*, 60(1), 2010 pp. 177–93.

[113] G. Schaller and M. Meyer-Hermann, "Continuum versus discrete model: a comparison for multicellular tumour spheroids", *Philos. Trans. A Math. Phys. Eng. Sci.*, 364(1843), 2006 pp. 1443–64.

[114] A. Bertuzzi, A. Fasano, A. Gandolfi and C. Sinisgalli, "Reoxygenation and split-dose response to radiation in a tumour model with krogh-type vascular geometry", *Bull. Math. Biol.*, 70(4), 2008 pp. 992–1012.

[115] M. Chao, Y. Xie, E. G. Moros, Q.T. Le and L. Xing, "Image-based modeling of tumor shrinkage in head and neck radiation therapy", *Med. Phys.*, 37(5), 2010 pp. 2351–58.

[116] R. Rockne, E. C. Jr Alvord, J. K. Rockhill and K. R. Swanson, "A mathematical model for brain tumor response to radiation therapy", *J. Math. Biol.*, 58(4-5), 2009 pp. 561–78.

[117] R. Rockne, J. K. Rockhill, M. Mrugala, A. M. Spence, I. Kalet, K. Hendrickson, A. Lai, T. Cloughesy, E. C. Jr Alvord and K. R. Swanson, "Predicting the efficacy of radiotherapy in individual glioblastoma patients in vivo: a mathematical modeling approach", *Phys. Med. Biol.*, 55(12), 2010 pp. 3271–85.

[118] G. Buttazzo, "Semicontinuity, Relaxation and Integral Representation in the Calculus of Variations", *Pitman Res. Notes Math. Ser., 207, Longman Scientific & Technical, Harlow; copublished in the United States with John Wiley & Sons, Inc.*, New York, 1989.

[119] G. Buttazzo, M. Giaquinta and S. Hildebrandt, "One-Dimensional Variational Problems: An Introduction", *Oxford Lecture Series in Mathematics and its Applications, 15, The Clarendon Press, Oxford University Press*, New York, 1998.

[120] H.Brezis, "Functional Analysis, Sobolev Spaces and Partial Differential Equations", Springer New York, 2010.

[121] M. Y. Law and B. Liu, "Informatics in radiology: DICOM-RT and its utilization in radiation therapy", *Radiographics*, 29(3), 2009 pp. 655–67.

[122] J. O. Deasy, A. I. Blanco and V. H. Clark, "CERR: a computational environment for radiotherapy research", *Med. Phys.*, 30(5), 2003 pp. 979–85.

[123] M. de Berg, O. Cheong, M. van Kreveld and M. Overmars, "Computational Geometry: Algorithms and Applications", 3rd ed. Springer-Verlag TELOS Santa Clara, CA, USA 2008.

[124] "CGAL, Computational Geometry Algorithms Library", *http://www.cgal.org*.

[125] J. D. Boissonnat, O. Devillers, S. Pion, M. Teillaud and M. Yvinec, "Triangulations in CGAL", *Comput. Geom. Theory Appl.*, 22, 2002 pp. 5–19.

[126] P. G. Ciarlet, "The Finite Element Method for Elliptic Problems", *Classics in Applied Mathematics 40, SIAM*, Philadelphia, 2002.

[127] C. Johnson, "Numerical Solution of Partial Differential equations by the Finite Element Method", Cambridge University Press, 1994.

[128] H. R. Schwarz, "Finite element methods", Academic Press, London, 1988.

[129] O. C. Zienkiewicz and R. L. Taylor, "The Finite Element Method", London: McGraw-Hill 1989.

[130] J. Nocedal and S. J. Wright, "Numerical Optimization", 2nd edition. Springer, New York 2006.

[131] A. Wachter and L. T. Biegler, "On the implementation of a primal-dual interior point filter line search algorithm for large-scale nonlinear programming", *Mathematical Programming*, 106(1), 2006 pp. 25–57.

[132] O. Schenk, M. Bollhöfer and R. A. Römer, "On large-scale diagonalization techniques for the anderson model of localization", *SIAM J. Sci. Comput.*, 28(3), 2008 pp. 963–83.

[133] O. Schenk, A. Wächter and M. Hagemann, "Matching-based preprocessing algorithms to the solution of saddle-point problems in large-scale nonconvex interior-point optimization", *Comput. Optim. Appl.*, 36(2-3), 2007 pp. 321–41.

[134] F. J. Vernimmen and J. P. Slabbert, "Assessment of the alpha/beta ratios for arteriovenous malformations, meningiomas, acoustic neuromas, and the optic chiasma", *Int. J. Radiat. Biol.*, 86(6), 2010 pp. 486–98.

[135] D. C. Shrieve, L. Hazard, K. Boucher and R. L. Jensen, "Dose fractionation in stereotactic radiotherapy for parasellar meningiomas: radiobiological considerations of efficacy and optic nerve tolerance", *J. Neurosurg.*, 101(3), 2004 pp. 390–5.

[136] J. Debus, M. Wuendrich, A. Pirzkall, A. Hoess, W. Schlegel, I. Zuna, R. Engenhart-Cabillic and M. Wannenmacher, "High efficacy of fractionated stereotactic radiotherapy of large base-of-skull meningiomas: long-term results", *J. Clin. Oncol.*, 19(15), 2001 pp. 3547–53.

[137] A. Amini, F. Lou, A. M. Correa, R. Baldassarre, A. Rimner, J. Huang, J. A. Roth, S. G. Swisher, A. A. Vaporciyan and S. H. Lin, "Predictors for locoregional recurrence for clinical stage III-N2 non-small cell lung cancer with nodal downstaging after induction chemotherapy and surgery", *Ann. Surg. Oncol.*, 20(6), 2013 pp. 1934–40.

[138] A. K. Paulsson and K. P. McMullen and A. M. Peiffer, W. H. Hinson, W. T. Kearns, A. J. Johnson, G. J. Lesser, T. L. Ellis, S. B. Tatter, W. Debinski, E. G. Shaw and M. D. Chan, "Limited margins using modern radiotherapy techniques does not increase marginal failure rate of glioblastoma", *Am. J. Clin. Oncol.*, 2012.

[139] M. Gerlinger, A. J. Rowan, S. Horswell, J. Larkin, D. Endesfelder, E. Gronroos, P. Martinez, N. Matthews, A. Stewart, P. Tarpey, I. Varela, B. Phillimore, S. Begum, N. Q. McDonald, A. Butler, D. Jones, K. Raine, C. Latimer, C. R. Santos, M. Nohadani, A. C. Eklund, B. Spencer-Dene, G. Clark, L. Pickering, G. Stamp, M. Gore, Z. Szallasi, J. Downward, P. A. Futreal and C. Swanton, "Intratumor heterogeneity and branched evolution revealed by multiregion sequencing", *N. Engl. J. Med.*, 366(10), 2012 pp. 883–92.

[140] A. Sottoriva, I. Spiteri, S. G. Piccirillo, A. Touloumis, V. P. Collins, J. C. Marioni, C. Curtis, C. Watts and S. Tavaré, "Intratumor heterogeneity in human glioblastoma reflects cancer evolutionary dynamics", *Proc. Natl. Acad. Sci. U S A*, 110(10), 2013 pp. 4009–14.

[141] S. G. Piccirillo, R. Combi, L. Cajola, A. Patrizi, S. Redaelli, A. Bentivegna, S. Baronchelli, G. Maira, B. Pollo, A. Mangiola, F. DiMeco, L. Dalprá and A. L. Vescovi, "Distinct pools of cancer stem-like cells coexist within human glioblastomas and display different tumorigenicity and independent genomic evolution", *Oncogene*, 28(15), 2009 pp. 1807–11.

[142] N. Moore and S. Lyle, "Quiescent, slow-cycling stem cell populations in cancer: a review of the evidence and discussion of significance', *J. Oncol.*, 396076, 2011.

[143] E. Vlashi, C. Lagadec, L. Vergnes, T. Matsutani, K. Masui, M. Poulou, R. Popescu, L. D. Donna, P. Evers, C. Dekmezian, K. Reue, H. Christofk, P. S. Mischel and F. Pajonk, "Metabolic state of glioma stem cells and nontumorigenic cells", *Proc. Natl. Acad. Sci. U S A*, 108(38), 2011 pp. 16062–7.

[144] D. Drasdo and S. Höhme, "A single-cell-based model of tumor growth in vitro: monolayers and spheroids", *Phys. Biol.*, 2(3), 2005 pp. 133–47.

[145] A. R. Anderson and K. Rejniak, "Single-cell-based models in biology and medicine", Birkhäuser-Verlag, Basel, Boston and Berlin 2007.

[146] I. Ramis-Conde, D. Drasdo, A. R. Anderson and M. A. Chaplain, "Modeling the influence of the E-cadherin-beta-catenin pathway in cancer cell invasion: a multiscale approach", *Biophys. J.*, 1(95), 2008 pp. 155–65.

[147] E. A. Rietman, D. E. Friesen, P. Hahnfeldt, R. Gatenby, L. Hlatky and J. A. Tuszynski, "An integrated multidisciplinary model describing initiation of cancer and the Warburg hypothesis", *Theor. Biol. Med. Model.*, 10(39), 2013.

[148] R. J. Gillies, D. Verduzco and R. A. Gatenby, "Evolutionary dynamics of carcinogenesis and why targeted therapy does not work", *Nat. Rev. Cancer*, 12(7), 2012 pp. 487–93.

[149] L. Preziosi and G. Vitale, "A multiphase model of tumor and tissue growth including cell adhesion and plastic reorganization", *Math. Models Methods Appl.*, 21(9), 2011 pp. 1901–32.

[150] N. Bellomo and M. Delitala, "From the mathematical kinetic, and stochastic game theory to modelling mutations, onset, progression and immune competition of cancer cells", *Physics of Life Reviews*, 5(4), 2008 pp. 183–206.

[151] A. R. Anderson and V. Quaranta, "Integrative mathematical oncology", *Nat. Rev. Cancer*, 8(3), 2008 pp. 227–34.

[152] A. R. Anderson, A. M. Weaver, P. T. Cummings and V. Quaranta, "Tumor morphology and phenotypic evolution driven by selective pressure from the microenvironment", *Cell*, 127(5), 2006 pp. 905–15.

[153] Z. Agur and S. Vuk-Pavlović, "Mathematical modeling in immunotherapy of cancer: personalizing clinical trials", *Mol. Ther.*, 20(1), 2012 pp. 1–2.

[154] A. S. Silva and R. A. Gatenby, "A theoretical quantitative model for evolution of cancer chemotherapy resistance", *Biol. Direct*, 5(25), 2010

[155] S. Höhme, M. Brulport, A. Bauer, E. Bedawy, W. Schormann, M. Hermes, V. Puppe, R. Gebhardt, S. Zellmer, M. Schwarz, E. Bockamp, T. Timmel, J. G. Hengstler and D. Drasdo, "Prediction and validation of cell alignment along microvessels as order principle to restore tissue architecture in liver regeneration", *Proc. Natl. Acad. Sci. U S A*, 107(23), 2010 pp. 10371–6.

[156] E. I. Zacharaki, G. S. Stamatakos, K. S. Nikita and N. K. Uzunoglu, "Simulating growth dynamics and radiation response of avascular tumour spheroids-model validation in the case of an EMT6/Ro multicellular spheroid", *Comput. Methods Programs Biomed.*, 76(3), 2004 pp. 193–206.

[157] W. Düchting and T. Vogelsaenger, "Recent progress in modelling and simulation of three-dimensional tumor growth and treatment", *Biosystems*, 18(1), 1985 pp. 79–91.

[158] H. Enderling, A. R. Anderson, M. A. Chaplain, A. J. Munro and J. S. Vaidya, "Mathematical modeling of radiotherapy strategies for early breast cancer", *J. Theor. Biol.*, 241(1), 2006 pp. 158–71.

[159] H. Enderling, M. A. Chaplain, A. R. Anderson and J. S. Vaidya, "A mathematical model of breast cancer development, local treatment and recurrence", *J. Theor. Biol.*, 246(2), 2007 pp. 245–259.

[160] V. Vainstein, O. U. Kirnasovsky, Y. Kogan and Z. Agur, "Strategies for cancer stem cell elimination: insights from mathematical modeling", *J. Theor. Biol.*, 298, 2012 pp. 32–41.

[161] W. K. Dahlberg, E. I. Azzam, Y. Yu and J. B. Little, "Response of human tumor cells of varying radiosensitivity and radiocurability to fractionated irradiation", *Cancer Res.*, 59(20), 1999 pp. 5365–9.

[162] A. Allam, A. Taghian, D. Gioioso, M. Duffy and H. D. Suit, "Intratumoral heterogeneity of malignant gliomas measured in vitro", *Int. J. Radiat. Oncol. Biol. Phys.*, 27(2), 1993 pp. 303–8.

[163] R. Stupp and M. E. Hegi, "Targeting brain-tumor stem cells", *Nat. Biotechnol.*, 25(2), 2007 pp. 193–4.

[164] M. F. Clarke, J. E. Dick, P. B. Dirks, C. J. Eaves, C. H. Jamieson, D. L. Jones, J. Visvader, I. L. Weissman and G. M. Wahl, "Cancer stem cells–perspectives on current status and future directions: AACR Workshop on cancer stem cells", *Cancer Res.*, 66(19), 2006 pp. 9339–44.

[165] D. Bonnet and J. E. Dick, "Human acute myeloid leukemia is organized as a hierarchy that originates from a primitive hematopoietic cell", *Nat. Med.*, 3(7), 1997 pp. 730–7.

[166] L. Li and W. B. Neaves, "Normal stem cells and cancer stem cells: the niche matters", *Cancer Res.*, 66(9), 2006 pp. 4553–57.

[167] J. L. Dembinski and S. Krauss, "Characterization and functional analysis of a slow cycling stem cell-like subpopulation in pancreas adenocarcinoma", *Clin. Exp. Metastasis*, 26(7), 2009 pp. 611–23.

[168] A. Roesch, M. Fukunaga-Kalabis, E. C. Schmidt, S. E. Zabierowski, P. A. Brafford, A. Vultur, D. Basu, P. Gimotty, T. Vogt and M. Herlyn, "A temporarily distinct subpopulation of slow-cycling melanoma cells is required for continuous tumor growth", *Cell*, 141(4), 2010 pp. 583–94.

[169] N. Moore, J. Houghton and S. Lyle, "Slow-cycling therapy-resistant cancer cells", *Stem Cells Dev.*, 21(10), 2012 pp. 1822–30.

[170] C. Richichi, P. Brescia, V. Alberizzi, L. Fornasari and G. Pelicci, "Marker-independent method for isolating slow-dividing cancer stem cells in human glioblastoma", *Neoplasia*, 15(7), 2013 pp. 840–7.

[171] A. Bansal, S. Ramalingam and S. Anant, "Cancer Stem Cells in the Origin and Transformation of Barrett's Esophagus: Current Knowledge and Areas of Uncertainty", *Immunogastroenterology*, 2(1), 2013 pp. 9–21.

[172] J. Chen, Y. Li, T. S. Yu, R. M. McKay, D. K. Burns, S. G. Kernie and L. F. Parada, "A restricted cell population propagates glioblastoma growth after chemotherapy", *Nature*, 488, 2012 pp. 522–26.

[173] B. Hegedüs, A. Czirók, I. Fazekas, T. B'abel, E. Madar'asz and T. Vicsek, "Locomotion and proliferation of glioblastoma cells in vitro: statistical evaluation of videomicroscopic observations", *J. Neurosurg.*, 92(3), 2000 pp. 428–34.

[174] G. S. Stamatakos, V. P. Antipas, N. K. Uzunoglu and R. G. Dale, "A four-dimensional computer simulation model of the in vivo response to radiotherapy of glioblastoma multiforme: studies on the effect of clonogenic cell density", *Br. J. Radiol.*, 79(941), 2006 pp. 389–400.

[175] M. Baumann, M. Krause and R. Hill, "Exploring the role of cancer stem cells in radioresistance", *Nat. Rev. Cancer*, 8(7), 2008 pp. 545–54.

[176] H. Enderling, L. Hlatky and P. Hahnfeldt, "Cancer Stem Cells: A Minor Cancer Subpopulation that Redefines Global Cancer Features", *Front. Oncol.*, 3(76), 2013.

[177] H. Enderling, L. Hlatky and P. Hahnfeldt, "Migration rules: tumours are conglomerates of self-metastases", *Br. J. Cancer*, 100(12), 2009 pp. 1917–25.

[178] S. R. Pine, B. M. Ryan, L. Varticovski, A. I. Robles and C. C. Harris, "Microenvironmental modulation of asymmetric cell division in human lung cancer cells", *Proc. Natl. Acad. Sci. U S A*, 107(5), 2010 pp. 2195–200.

[179] J. A. Knoblich, "Asymmetric cell division: recent developments and their implications for tumour biology", *Nat. Rev. Mol. Cell Biol.*, 11(12), 2010 pp. 849–60.

[180] J. E. Visvader and G. J. Lindeman, "Cancer stem cells in solid tumours: accumulating evidence and unresolved questions", *Nat. Rev. Cancer*, 8(10), 2008 pp. 755–68.

[181] S. Das, M. Srikanth and J. A. Kessler, "Cancer stem cells and glioma", *Nat. Clin. Pract. Neurol.*, 4(8), 2008 pp. 427–35.

[182] G. W. Barendsen, C. van Bree and N. A. Franken, "Importance of cell proliferative state and potentially lethal damage repair on radiation effectiveness: implications for combined tumor treatments (review)", *Int. J. Oncol.*, 19(2), 2001 pp. 247–56.

[183] M. J. Allalunis-Turner, G. M. Barron, R. S. 3rd Day, D. S. Fulton and R. C. Urtasun, "Radiosensitivity testing of human primary brain tumor specimens", *Int. J. Radiat. Oncol. Biol. Phys.*, 23(2), 1992 pp. 339–43.

[184] A. Taghian, J. Ramsay, M. J Allalunis-Turner, W. Budach, D. Gioioso, F. Pardo, P. Okunieff, N. Bleehen, R. Urtasun and H. Suit, "Intrinsic radiation sensitivity may not be the major determinant of the poor clinical outcome of glioblastoma multiforme", *Int. J. Radiat. Oncol. Biol. Phys.*, 25(2), 1993 pp. 243–9.

[185] J. S. Lowengrub, H. B. Frieboes, F. Jin, Y. L. Chuang, X. Li, P. Macklin, S. M. Wise and V. Cristini, "Nonlinear modelling of cancer: bridging the gap between cells and tumours", *Nonlinearity*, 23(1), 2010 pp. 1–9.

[186] J. Moreira and A. Deutsch, "Cellular automaton models of tumor development: a critical review", *Advs. Complex Syst.*, 5(247), 2002 pp. 1–21.

[187] A. Sottoriva, J. J. Verhoeff, T. Borovski, S. K. McWeeney, L. Naumov, J. P. Medema, P. M. Sloot and L. Vermeulen, "Cancer stem cell tumor model reveals invasive morphology and increased phenotypical heterogeneity", *Cancer Res.*, 70(1), 2010 pp. 46–56.

[188] W. Düchting, R. Lehrig, G. Rademacher and W. Ulmer, "Computer simulation of clinical irradiation schemes applied to in vitro tumor spheroids", *Strahlenther Onkol.*, 165(12), 1989 pp. 873–8.

[189] S. Dormann and A. Deutsch, "Modeling of self-organized avascular tumor growth with a hybrid cellular automaton", *In Silico Biol.*, 2(3), 2002 pp. 393–406.

[190] B. Ribba, K. Marron, Z. Agur, T. Alarcón and P. K. Maini, "A mathematical model of Doxorubicin treatment efficacy for non-Hodgkin's lymphoma: investigation of the current protocol through theoretical modelling results", *Bull. Math. Biol.*, 67(1), 2005 pp. 79–99.

[191] M. Radszuweit, M. Block, J. G. Hengstler, E. Schöll and D. Drasdo, "Comparing the growth kinetics of cell populations in two and three dimensions", *Phys. Rev. E Stat. Nonlin. Soft Matter Phys.*, 79(5 Pt 1), 051907, 2009.

[192] M. Block, E. Schöll and D. Drasdo, "Classifying the growth kinetics and surface dynamics in growing cell populations", *Phys. Rev. Lett.*, 99(24), 2007 pp. 248101–104.

[193] S. van Cruchten and W. van den Broeck, "Morphological and biochemical aspects of apoptosis, oncosis and necrosis", *Anat. Histol. Embryol.*, 31(4), 2002 pp. 214–23.

[194] W. Bursch, L. Kleine and M. Tenniswood, "The biochemistry of cell death by apoptosis", *Biochem. Cell Biol.*, 68(9), 1990 pp. 1071–4.

[195] J. L. Goergen, A. Marc and J. M. Engasser, "Determination of cell lysis and death kinetics in continuous hybridoma cultures from the measurement of lactate dehydrogenase release", *Cytotechnology*, 11(3), 1993 pp. 189–95.

[196] J. E. Wells and J. B. Russell, "The effect of growth and starvation on the lysis of the ruminal cellulolytic bacterium Fibrobacter succinogenes", *Appl. Environ. Microbiol.*, 62(4), 1996 pp. 1342–6.

[197] D. T. Gillespie, "Exact stochastic simulation of coupled chemical reactions", *J. Phys. Chem.*, 81(25), 1977 pp. 2340–61.

[198] A. B. Bortz, M. H. Kalos and J. L. Lebowitz, "New algorithm for Monte-Carlo simulations of Ising spin systems", *J. Comput. Phys.*, 17, 1975 pp. 10–18.

[199] A. Narayana, J. Yamada, S. Berry, P. Shah, M. Hunt, P. H. Gutin and S. A. Leibel, "Intensity-modulated radiotherapy in high-grade gliomas: clinical and dosimetric results", *Int. J. Radiat. Oncol. Biol. Phys.*, 64(3), 2006 pp. 892–7.

[200] R. Stupp, J. C. Tonn, M. Brada and G. Pentheroudakis, "ESMO Guidelines Working Group. High-grade malignant glioma: ESMO Clinical Practice Guidelines for diagnosis, treatment and follow-up", *Ann. Oncol.*, 21(5), 2010.

[201] K. S. Korolev, M. J. I. Müller, N. Karahan, A. W. Murray, O. Hallatschek and D. R. Nelson, "Selective sweeps in growing microbial colonies", *Phys. Biol.*, 9(2), 026008, 2012.

[202] J. M. Buatti, R. B. Marcus, W. M. Mendenhall, W. A. Friedman and F. J. Bova, "Accelerated hyperfractionated radiotherapy for malignant gliomas", *Int. J. Radiat. Oncol. Biol. Phys.*, 34(4), 1996 pp. 785–92.

[203] C. L. Chaffer, I. Brueckmann, C. Scheel, A. J. Kaestli, P. A. Wiggins, L. O. Rodrigues, M. Brooks, F. Reinhardt, Y. Su, K. Polyak, L. M. Arendt, C. Kuperwasser, B. Bierie and R. A. Weinberg, "Normal and neoplastic nonstem cells can spontaneously convert to a stem-like state", *Proc. Natl. Acad. Sci. U S A*, 108(19), 2011 pp. 7950–5.

[204] D. G. Tang, "Understanding cancer stem cell heterogeneity and plasticity", *Cell Res.*, 22(3), 2012 pp. 457–72.

[205] C. E. Meacham and S. J. Morrison, "Tumour heterogeneity and cancer cell plasticity", *Nature*, 501(7467), 2013 pp. 328–37.

[206] C. Lengauer, K. W. Kinzler and B. Vogelstein, "Genetic instabilities in human cancers", *Nature*, 396(6712), 1998 pp. 643–9.

[207] J. Wang, L. P. Guo, L. Z. Chen, Y. X. Zeng and S. H. Lu, "Identification of cancer stem cell-like side population cells in human nasopharyngeal carcinoma cell line", *Cancer Res.*, 67(8), 2007 pp. 3716–24.

[208] R. A. Gatenby, "A change of strategy in the war on cancer", *Nature*, 459(7246), 2009 pp. 508–9.

[209] T. M. Apostol, "Calculus", Volume 2 (Second Edition), Editorial Reverté, 1997.

[210] A. H. Stroud and D. Secrest, "Gaussian Quadrature Formulas", Englewood Cliffs, NJ: Prentice-Hall, 1966.

[211] P. Keast, "Moderate-degree tetrahedral quadrature formulas", *Comput. Methods Appl. Mech. Eng.*, 55, 1986 pp. 339.

[212] Y. Jinyun, "Symmetric Gaussian quadrature formulae for tetrahedronal regions", *Comput. Methods Appl. Mech. Eng.*, 43, 1984 pp. 349–53.

[213] J. Honerkamp, "Stochastic Dynamical Systems", Wiley-VCH 1993.

[214] D. Drasdo, "Coarse Graining In Simulated Cell Populations", *Advances in Complex Systems (ACS)*, 8(2), 2005 pp. 319–63.